Dissertation

submitted to the

Combined Faculties of the Natural Sciences and Mathematics

of the Ruperto-Carola-University of Heidelberg. Germany

for the degree of

Doctor of Natural Sciences

Put forward by

Yulong Zhuang

born in Xi'an, China

Oral examination: 26, June, 2019

Diversity of Galactic Stellar Metallicity Gradients and their Origins

Referees: Prof. Dr. Glenn van de Ven

Prof: Dr. Andreas Koch

Abstract

In this thesis we use integral field spectroscopic observations, semi-analytic models and state of the art cosmological simulations to study the diverse formation and evolutionary mechanisms setting stellar population gradients in the inner regions of galaxies. We find a clear link between the shape of the radial stellar metallicity profiles and the stellar surface mass density profiles within the inner ($< 1\,R_e$) regions of galaxies; independent of their mass ($10^9 \leq M_{gal} \leq 10^{12.5}$) or morphological type (E to Sd). The stellar metallicity profiles are well described by a Sérsic function, and we show that the Sérsic indices of the stellar mass density and metallicity profiles are tightly correlated, with $n_Z = 1.51 \times n_S - 0.53$ and intrinsic scatter of ~ 0.25. The expected signatures of radial migration (bars, spiral arms, mergers) do not appear to correlate with the metallicity gradient strength, nor do the present day stellar kinematics. We show with a semi-analytic chemical evolution model that the angular momentum of the infalling gas is an important factor in developing the metallicity and surface mass density correlations. Together, these results suggest that the in-situ, time-integrated stellar mass build-up is the predominant factor setting the metallicity gradients of the inner regions of galaxies.

Zusammenfassung

In dieser Dissertation verwenden wir integralfeldspektroskopische Beobachtungen, semi-analytische Modelle und moderne kosmologische Simulationen, um die verschiedenen Mechanismen zu untersuchen, die für die Entstehung und Entwicklung von Gradienten der stellaren Populationen in den inneren Gebieten von Galaxien entscheidend sind. Wir können zeigen, dass ein klarer Zusammenhang zwischen der Form des Radialprofils der stellaren Metallizität und dem Profil der stellaren Flächendichte in der inneren Region einer Galaxie ($< 1\,R_e$) besteht. Dieser Zusammenhang ist unabhängig von der Masse der Galaxie ($10^9 \leq M_{gal} \leq 10^{12.5}$) oder ihrem morphologischen Typ (E bis Sd). Die Profile der stellaren Metallizität können gut mit einer Sérsic-Funktion beschrieben werden. Außerdem korrelieren die Sérsic-Indizes der Profile für die stellare Massendichte und Metallizität stark miteinander, $n_Z = 1.51 \times n_S - 0.53$ und mit einer intrinsischen Streuung von ~ 0.25. Weder die erwarteten Signaturen radialer Migration (Balken, Spiralarme, Merger) noch die heutigen Orbits von Sternen scheinen mit der Stärke der Metallizitätsgradienten zu korrelieren. Wie wir mit einem semi-analytischen Modell für die chemische Entwicklung zeigen, ist der Drehimpuls des hereinfallenden Gases ein wichtiger Faktor für die Entstehung der Korrelation zwischen Metallizität und Flächendichte. Zusammengenommen deuten diese Ergebnisse darauf hin, dass der in-situ, zeitintegrierte Aufbau der stellaren Masse der dominante Faktor für die Herausbildung von Metallizitätsgradienten in den inneren Regionen von Galaxien ist.

Contents

List of Figures

List of Tables

"You can’t wake a person who is pretending to be asleep."

Navajo Proverb

Chapter 1

Introduction

1.1 Galaxies

Galaxies are gravitationally bound systems that consist of stars, gas, dust, and dark matter. They are the building blocks of our Universe. A typical galaxy contains from ten million to a hundred trillion stars that are orbiting the galaxy's center of mass. The number of galaxies in the observable Universe is considered to be more than 2 trillion (Conselice et al., 2016). Most of the galaxies have scales from 1 to 100 kpc (or $\sim 3\times10^3$ to 3×10^6 light years) and distances of the order of millions of parsecs.

Our own galaxy, the Milky Way, appears as a giant hazy stream of light in the night sky and is the most well studied galaxy. It contains around 100-400 billion stars and many of those may host planets of their own (Cassan et al., 2012). It consists of a stellar disk with size of around 15 kiloparsecs (kpc) and a stellar bulge with a few kiloparsecs in radius which is located in the centre (López-Corredoira et al., 2018). Both the disk and bulge are embedded in a large, extended dark matter halo which contains 75% of our Galaxy's total mass. Few hundreds of globular clusters are scattered in the halo. These are old and massive gravitationally bound stellar systems (Harris, 1996). In between the stars there is the interstellar medium (ISM), which includes gas in ionic, atomic, and molecular form, as well as dust (Herbst, 1995). The center of the Milky Way Galaxy hosts a radio source known as Sagittarius A^*, which is believed to be a supermassive black hole with around 4×10^6 solar masses (Ghez et al., 1998; Schödel et al., 2002).

Our Milky Way galaxy is not isolated. It has 59 known satellite galaxies (e.g. Small and Large Magellanic Clouds, Sculptor Dwarf, Draco Dwarf, etc) and together they belong to the local galaxy cluster - the Local Group (Turner, 2014; van den Bergh, 2003).

Galaxies are the fundamental units of our Universe. Studies of the properties and evolutionary histories of galaxies provide us with a crucial tool to explore the formation and evolution of our Universe. On the other hand, galaxies are also the birth place of stars, which provide basic materials and energies for life. Understading their formation and evolution helps us to trace the origin of elements and of life. Therefore the nature of galaxies is one of the most important topic in science. In this section, we provide a general overview on galaxies, starting from their observational properties, their classification, and conclude with a description of their formation and evolution.

TABLE 1.1: Different wavelengths of light and typical sources.

Wavelength	**Temperature**	**Typical Sources**
Gamma-rays	> 10^8 Kelvin (K)	accretion disks around black holes
X-rays	10^6-10^8 K	stellar coronae, wind-blown bubbles surrounding massive stars, gas in clusters of galaxies, supernova remnants
Ultraviolet	10^4-10^6 K	hot stars, supernova remnants
Visible	10^3-10^4 K	stars
Infrared	10-10^3 K	planets, cool ISM clouds
Microwave	1-10 K	cool ISM clouds, cosmic microwave background
Radio	< 1 K	radio emission produced by electrons moving in magnetic fields

1.1.1 Observations of galaxies

Although our ancestors have been looking at the night sky for thousands of years, it was not until the beginning of the 20th century that we started to understand the nature of galaxies, as most of them are too far away from us to study in detail.

Apart from the Milky Way there are only a few galaxies which are visible on a dark night with naked eyes, including the Andromeda Galaxy, the Large Magellanic Cloud, the Small Magellanic Cloud, and the Triangulum Galaxy. As they show appearances not comparable to our Milky Way (which we only observe from the inside), for a long time they were considered to be some kinds of gaseous "Nebulae" or "celestial dome clouds" inside our Milky Way. At the end of the 18th century, Charles Messier compiled a catalog containing the 109 "nebulous" apparent objects. Later, William Herschel assembled a catalog including 5,000 nebulae. In 1845, Lord Rosse was, for the first time, able to distinguish between elliptical and spiral nebulae with his telescope.

Not until the great debate between Harlow Shapley and Heber Curtis in the early last century (Shapley and Curtis, 1921) people started to realize there are other "Milky Ways" (galaxies) outside of our Milky Way Galaxy. In 1922, Edwin Hubble resolved the outer parts of some spiral nebulae as collections of individual stars and identified some Chepheid variables. By estimating the distance to these “nebulae” using the proportionality between the intrinsic luminosity and the periods of chepheids, he realized they were too distant to be part of the Milky Way (Hubble, 1929). In 1936 Hubble classified galaxies according to their morphology, and this classification is still in use today (Sandage, 1989).

In modern times, thanks to the extraordinary improvements of observational techniques and instrumentation, we are now able to observe galaxies with different tracers (e.g. different wavelengths), leading to a more complete understanding of these objects..

For the majority of remote galaxies, the primary information we get is from their light - that is the electromagnetic radiation mostly from their stars. In astronomy, we have two major ways to detect light, photometry and spectroscopy.

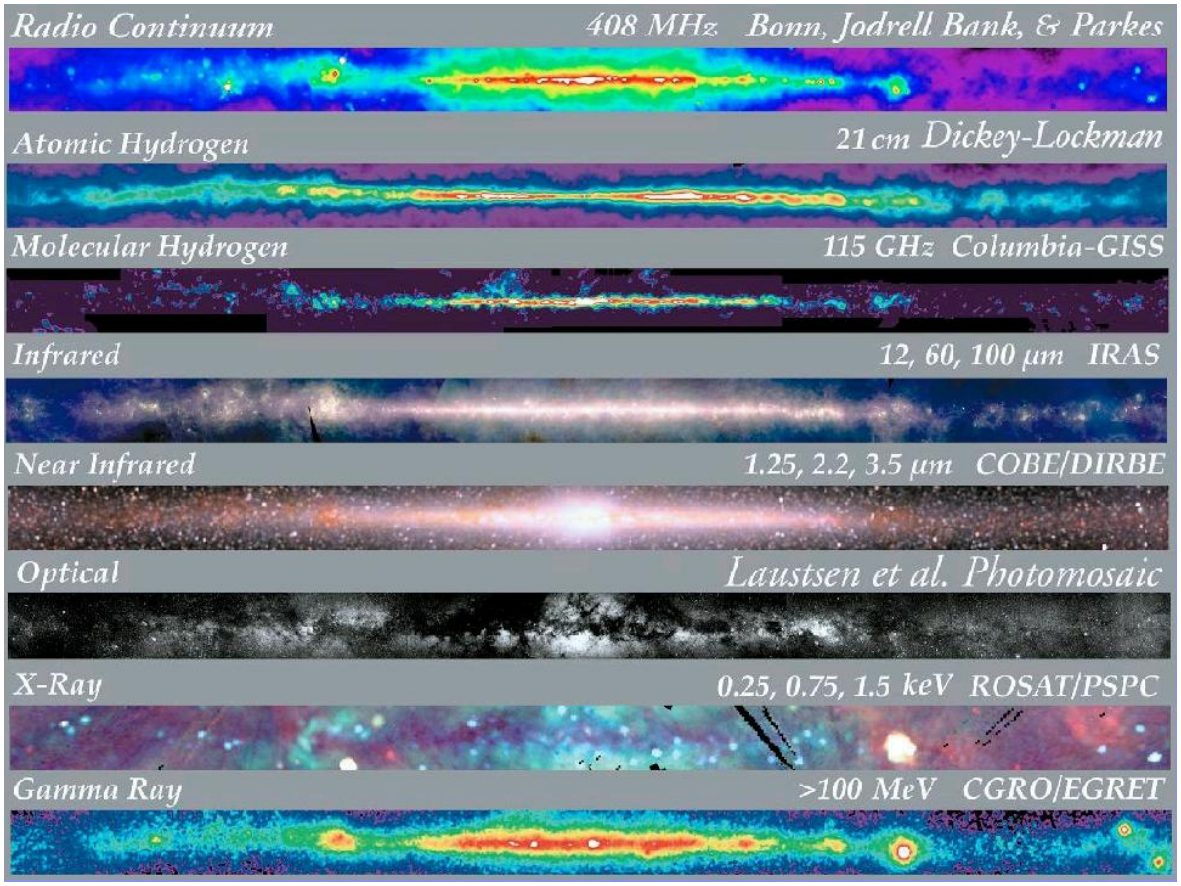

FIGURE 1.1: Images of our Milky Way in different wavelength bands.
Image credit: NASA's Goddard Space Flight Center.

Photometric observations

Photometric observations serve to get the brightness (or flux) of target objects within a given wavelength band, by collecting their light that passes through specialized photometric optical bandpass filters. In simpler terms, this corresponds to taking a picture of the galaxy, as we would do with a modern cell phone. For optical wavelengths, CCD cameras are the most commonly used receiver to gather photons. A CCD camera is a grid of photometers that is able to measure the flux density of incoming photons and simultaneously image objects in a certain wavelength range.

Depending on the feature of filters, photons with a certain range of frequencies or wavelengths can pass through a filter. A set of well-defined passbands is a photometric system. There are many photometric systems in astronomy, one of the most commonly used is the UBV photometric system, which is the first known standardized photometric system or Johnson-Cousins system (Johnson and Morgan, 1953). It contains five filters with effective central wavelengths: 365.6 nm (U) 435.3 nm (U) 547.7 nm (U) 634.9 nm (U) 879.7 nm (U). The letters U, B, V, R and I stand for ultraviolet, blue, visual, red and infrared.

Our Earth's atmosphere will reduce the intensity of light that is received by a telescope, and this reduction can change with time and location. For the same celestial object, the intensity of photons received by our CCD cameras can be different

at different time and locations on Earth. Although we cannot measure the absolute brightness of an object, we can measure its relative brightness compared to some standard reference stars. In photometric observations, we use apparent magnitude (m) to represent the brightness of a celestial object that is observed from Earth. It is defined as:

$$m_x = -2.5\log_{10}\Big(\frac{F_x}{F_{x,0}}\Big) \tag{1.1}$$

m_x is the apparent magnitude of an object at wavelength band x. F_x and $F_{x,0}$ are the observed flux density of the object and the standard reference star at wavelength band x. The standard reference star is also called photometric zeropoint.

Depending on the definition of photometric zeropoint there are different apparent magnitude systems. The most commonly used are the Vega system which uses the flux density of Vega at different band as zeropoints and AB magnitude system which uses a hypothetical reference spectrum with constant flux density per unit frequency interval, with its V band flux density equals to the V band flux density of Vega (Oke and Gunn, 1983).

As described in the name, the apparent magnitude provides a way to measure the "apparent" brightness of an celestial as viewed from earth. It doesn't represent the intrinsic brightness of the object, because the flux decreases with distance - e.g. a distant brighter star can have a smaller flux density received on Earth than that from a closer but dimmer star. The absolute magnitude (M) is used to describe the intrinsic brightness of an astronomical object, which is defined as the apparent magnitude it would have when seen from a distance of 10 parsecs ($\sim$ 32.6 light-years). Equation 1.2 shows the relation between absolute magnitude (M), apparent magnitude (m) and distance d.

$$M = m - 5\log_{10}(d_{pc}) + 5 \tag{1.2}$$

In this way, once we know the apparent magnitude and the distant of a star we will be able to get its absolute magnitude. On the other side, once we know the apparent magnitude and the absolute magnitude of an object, we will be able to know how far it is from us.

Galaxies are extended objects on the sky, with various structures and substructures. From photometric images, we are able to characterize the structural features of galaxies from the light distribution, for example decomposing the radial luminosity profiles into central bulges and extended disks.

Besides, galaxies are complicated systems that contain stars of different ages and metallicities, stellar remnants, gas, dust, super-massive black holes as well as many other substructures, and are subject to various physical processes. Different components may have their unique emission features (e.g. emitting most of their light at different wavelength ranges, or lack of emission in certain wavelength ranges). Some typical emitting sources in each wavelength range are shown in Table 1.1. Images from different bands therefore reveal the distributions and features of different galactic components, and analyzing these greatly increases are knowledge on structures of galaxies.

The photons received by our CCD may also be partially absorbed by the ISM on the way to us. Depending on the nature of the ISM, photons are absorbed at a different wavelength. This absorption can provide indirect information on the spatial distribution and chemical composition of the ISM. This, in turn, means that stars in different regions of a galaxy can be observed at different wavelengths, depending on the nature of the ISM along the line of sight. For instance, we cannot see through the Milky Way disk at optical wavelengths because of the extinction of the dust-rich disk, but we can observe the Milky Way centre through the dusty disk at IR and radio wavelengths. Figure 1.1 shows images of our Milky Way at different wavelengths. From this image it is clear that the same galaxy shows very different appearances at different wavelengths. For example, the near-infrared image shows the distribution of old stars, the near UV image provides the distribution of massive young stars (star-forming regions) and the 21 cm wavelength image contains information on the distribution of neutral hydrogen (HI).

In addition, photometric observations can also inform us about the intrinsic features of the light source. For example, as the radiation of stars is dominated by blackbody radiation, by knowing the difference between light intensities observed at different wavelength bands (which is the defined as the color index: $x1 - x2 = m_{x1} - m_{x2}$.) we will get a constraint on a star's surface temperature. Comparing the location of stars in the color-magnitude diagram (CMD, as shown in Figure 1.2.) can reveal their physical properties (age, mass, amongst others). This is because it is possible to estimate the mass and size as well as the surface temperature of a star at a certain age with certain metallicity and initial mass by using stellar evolution theories. Therefore colors and magnitudes of galaxies can also indicate some coarse properties of their stellar population components, as the light of most galaxies is dominated by stars.

Spectroscopic observations

Photometric observations only tell us the light intensity of a galaxy within a broad wavelength range defined in a particular filter. Spectroscopic observations on the other hand, can provide us with the light composition of a galaxy by dispersing the light through a grating or a prism and measuring the spectrum of the collected electromagnetic radiation. Figure 1.3 shows several typical stellar spectra, and the corresponding wavelength ranges of several common photometric filters for comparison. In fact, a multi-bands photometric observation is like a crude form of spectroscopic observation, with much lower wavelength resolution. Stars emit light characterized by continuous spectra whose peak wavelengths are linked to the temperature of the emitting object. Just like we use the color index to estimate the temperature of the light source in photometric observations, we could extract more accurate temperatures from the spectrum of the object.

Another advantage of spectroscopic observations is their capability of retaining the information contained in the spectral lines. A spectrum of a galaxy's stellar light may show multiple types of spectral lines. When a photon emitted from a broad spectrum source passes through a cooler medium, its flux will be absorbed at certain wavelengths, producing absorption lines in the spectrum. On the other hand, some medium may also re-emit energy at certain wavelengths, when a photon emitted from a broad spectrum source passes through such medium, the emission from

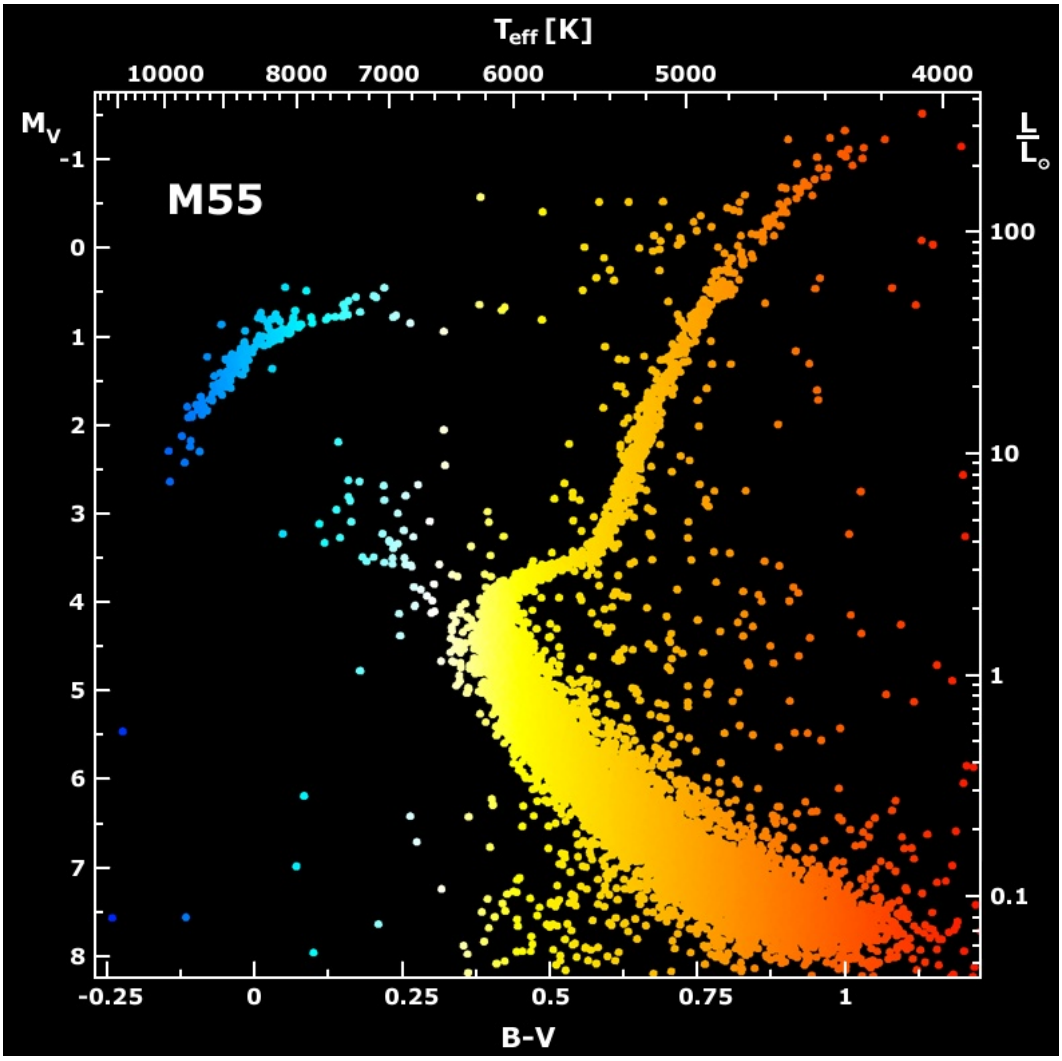

FIGURE 1.2: The color-magnitude diagram of the globular star cluster M55. Each dot represents a star with its color coded by its surface temperature. Image credit: B.J. Mochejska, J. Kaluzny (CAMK), 1m Swope Telescope.

the medium will increase the flux at certain wavelengths, producing emission lines. Different elements may emit or absorb photons at specific wavelengths. Therefore, by comparing the absorption lines from an object's spectrum with emission spectra of known gas, one can determine the chemical composition of the object. Consequently, with a stellar spectrum we are able to extract the age and chemical composition of the star. To complement this, certain spectral lines enable us to obtain the chemical composition of interstellar gas at different phases (atmoic, ionized, molecular). As the majority of the galactic light is from stars, spectroscopic observations could help us to get the distribution of its stellar populations and the chemical abundance distributions of ISM with different compositions. This provides a good window for us to study the evolution history of a galaxy.

Apart from chemical properties, spectroscopic observations also provide us with the kinematic structure of a galaxy. From the shape and position of spectra lines,

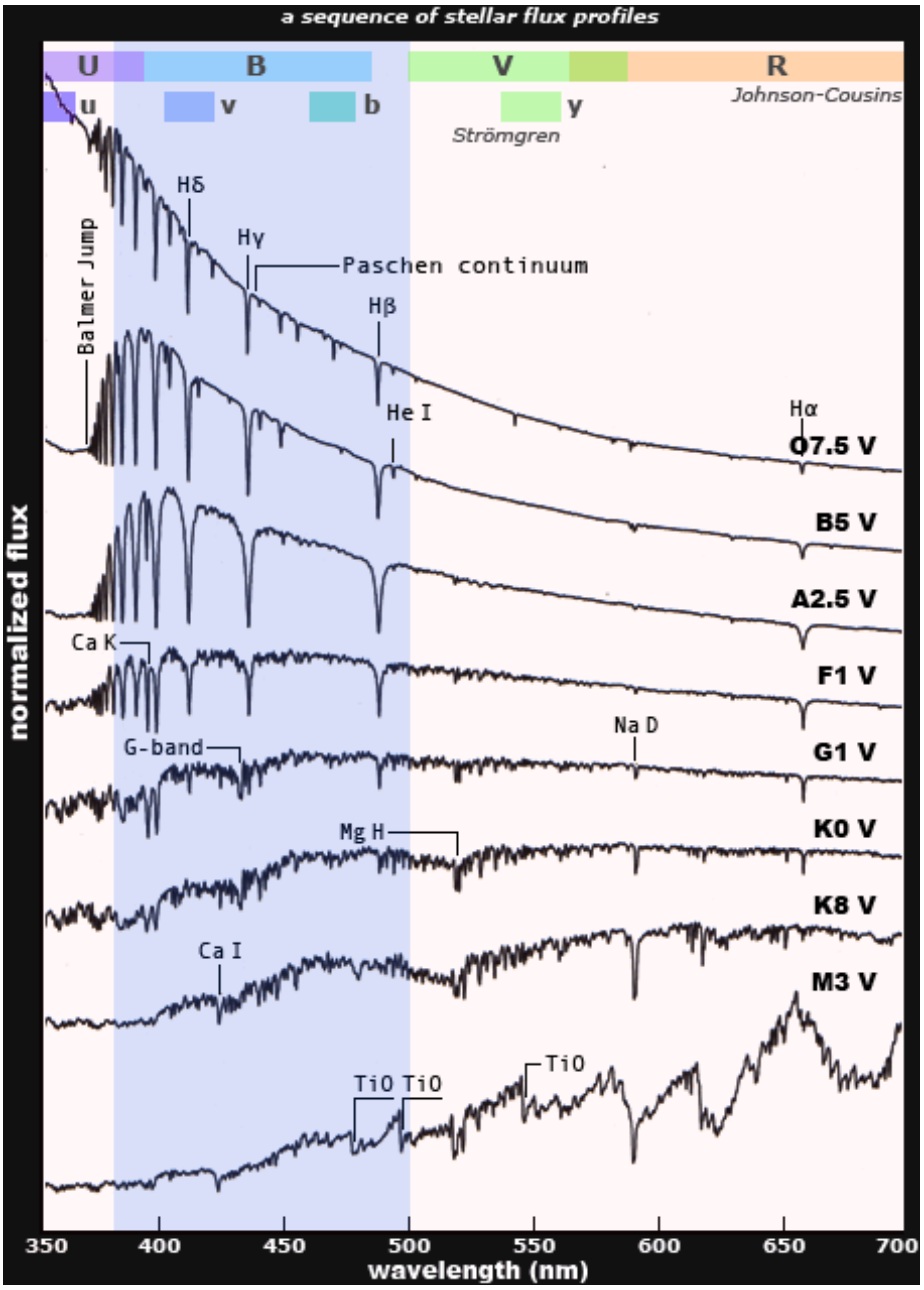

FIGURE 1.3: The spectra of stars with different effective temperatures, colorful bands on the top of the plot shows the wavelength ranges of different sets (Johnson-Cousins and Strömgren) of photometric passbands. Image Credit: Bruce MacEvoy [https://www.handprint.com/ASTRO/specclass.html].

we are able to derive the line-of-sight velocity (V_{los}) and velocity dispersion (σ_{los}) of the object. Modelling these quantities allows us to study the mass distribution and dynamical structure of a galaxy. In addition, the spectral features could also reveal us the properties of other light sources in a galaxy, e.g active galactic nuclei (AGN) through the synchrotron radiation from the high speed charged particles.

A significant advancement in spectroscopy occurred with the introduction of Integral field units (IFU) spectroscopic instruments. IFU observations allow the acquisition of spatially resolved 2-dimensional spectroscopy of a target in a single astronomical exposure, by dispersing the light of discrete spatial units (pixels) covering the field of view with a spectrograph. Through this technique, it is therefore possible to obtain the spectra of each pixel in the image, which is equivalent to the 2-dimensional photometric images at all wavelengths.

Applying this technique to galaxies, we can get spectra of every locations in an observed galaxy. This allows us to derive the spatial distribution (structure) of its stellar populations and gas; chemical abundance and kinematic properties (e.g. V_{los} and σ_{los}) of both stars and gas. Together these observations provide a view of how the dynamical structure and stellar populations were created and evolved over the lifetime of the galaxy.

In recent years, due to the success of IFU surveys such as CALIFA (Sánchez et al., 2012a; Husemann et al., 2013a) or MaNGA (Bundy et al., 2015; Blanton et al., 2017) the wealth of collected IFU data provided a large number of empirical insights and constrains on the nature of galaxies.

1.1.2 Structural, dynamical and chemical properties of galaxies

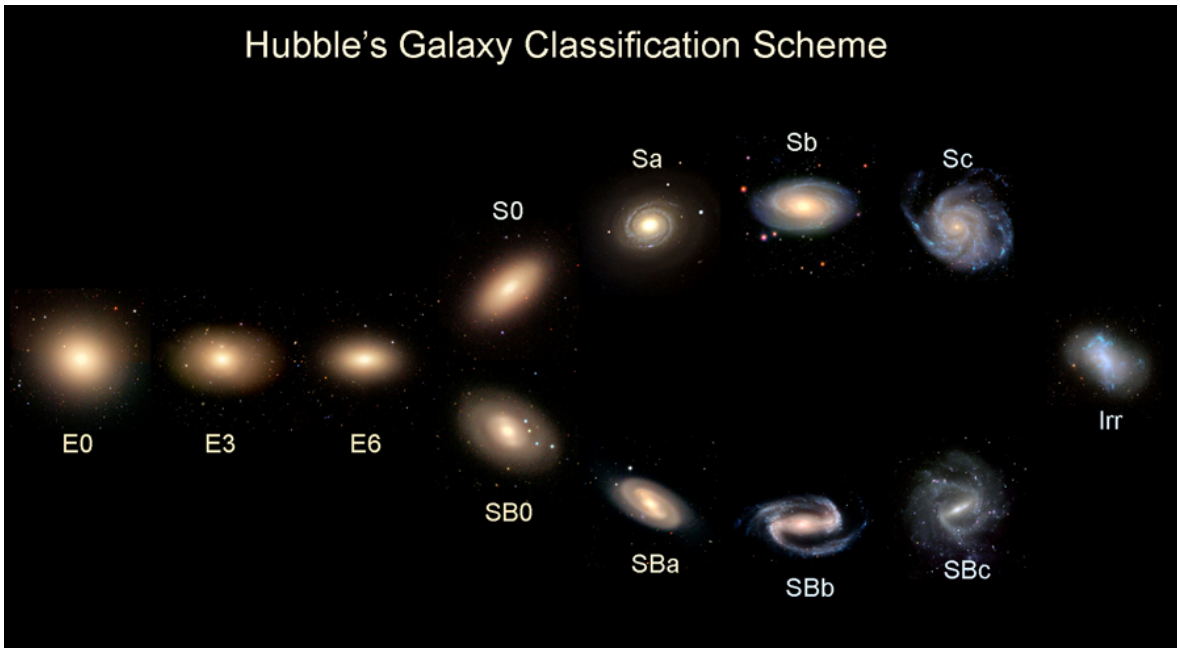

FIGURE 1.4: Hubble's galaxy classification diagram. Image credit: Candels Survey.

Galaxies show a large diversity in many properties including mass, shape, luminosity and color. Historically, researchers use the "visual morphologies" to classify galaxies, as photometric observations used to be the most common way to study external galaxies. Here the term "morphology" means the apparent shape of the galaxy or its stellar structure, also referred to as their visual morphology. Galaxies

can show very different visual morphologies, some are spheroidal-looking, some are disk-shaped like our Milky Way Galaxy.

In 1926 Edwin Hubble first invented the classification system known as the Hubble sequence (Hubble, 1926) or the Hubble tuning-fork because of the way it is traditionally presented, as shown in Figure 1.4. The left side of the graphical representation includes elliptical galaxies (En) which show ellipsoidal shapes. These galaxies are divided according to their ellipticity $\eta = 1 - b/a$, where a and b are the semi-major and semi-minor axes of the projected galaxy. As η becomes larger, galaxies become more disky as seen going rigthward in Figure 1.4. Lenticular galaxies (S0) are located in the middle of the panel. These galaxies, which are at the transition between ellipticals and spirals, consist of a large bulge and a flattened disk-like envelop region, but with no clear substructures, and typically devoid of young stellar populations. The right side of the panel shows spiral galaxies, divided according to the ratio between the luminosities of their bulges and disks. Going rightward we find galaxies which are increasingly dominated by their disk and which show more prominent substructure (bar, spiral arms). In addition, according to the shape of the bulge spiral galaxies show two subsequences, the unbarred spiral (upper sequence with letter Sn) with normal bulges in their centres and barred spiral (SBn) galaxies with bar structures in their centres. The right end of the panel is populated by irregular galaxies that do not show any regular structures.

Traditionally, the left side galaxies are also called "early type" galaxies, while the right side are called "late type" galaxies. This is because scientists used to think that the early type galaxies are the early stage of a galaxy which will become a late type galaxies in the future. However, that was a mistake in our way of understanding the Universe, and today those names are only historical and are not related to the evolutionary history of galaxies (See Schneider, 2015, Section 3).

Elliptical galaxies

Elliptical galaxies have spheroidal-looking shapes and relatively smooth, featureless light distributions, and mostly lack of gas. Most elliptical galaxies appear redder compared to other types of galaxies, which indicates those galaxies consist of older stellar populations. In addition, stars in elliptical galaxies tend to have higher velocity dispersion (σ) compared with their circular velocities (V_{rot}). Elliptical galaxies cover a very large mass ranges. According to their masses and sizes, there are 5 types of elliptical galaxies (Carroll and Ostlie, 2006):

- cD galaxies (cD) are extreme large (R $\sim$ 1 Mpc) massive ($M_* \sim 10^{13}$) and luminous ($M_B \sim$ -25) elliptical galaxies, which mostly exist in the centre of big galaxy clusters.
- Normal elliptical galaxies (E), which are the most common elliptical galaxies with stellar mass from 10^8 - 10^{13} $M_\odot$ also covers a larger range of absolute magnitudes M_B from -23 to -15.
- Dwarf elliptical galaxies (dE) are very low mass elliptical galaxies with stellar mass from 10^7 - 10^9 $M_\odot$ different from low mass normal elliptical galaxies they also have a much smaller surface brightness, with absolute magnitude M_B range from -13 to -19.

- Dwarf spheroidals (dSph) are the dimmest elliptical galaxies, with absolute magnitude M_B from -15 to -8 and stellar mass from 10^7 - 10^9 $M_\odot$.
- Blue compact dwarf galaxies (BCD) are bluer and more compact than other ellipticals, with typical stellar mass $\sim 10^7$ -10^8 $M_\odot$, they also contain considerate amount of gas.

Different elliptical galaxies also show different surface brightness profiles. The brightness profile of normal elliptical galaxies mostly follow the *de Vaucouleurs* profile (de Vaucouleurs, 1948):

$$I(R) = I_e \exp(-7.669[(R/R_e)^{1/4} - 1]) \tag{1.3}$$

Here I is the surface brightness which is a function of the projected distance R from the center of the galaxy, R_e is the effective radius also called half light radius, as it is the radius that encloses half of the total luminsity of the galaxy.

$$\int_0^{Re} I(R) R dR = 0.5 \int_0^{\infty} I(R) R dR \tag{1.4}$$

The inner regions of cD galaxies can also be described as a *de Vaucouleurs* profile, while their outskirts are much more extended. A possible explanation could be that cDs are normal E galaxies but embedded in the extended halos of their galaxy clusters. On the other side, some diffuse dwarf elliptical galaxies' profiles are more like to follow an exponential profiles:

$$I(R) = I_0 \exp(R/R_d) \tag{1.5}$$

Here, R_d is the exponential scale length, and I_0 is the central surface brightness (Schneider, 2015). This could be related to a possible different origin of massive and low mass elliptical galaxies.

Spiral galaxies

Spiral galaxies are usually dominated by a rotating disk of stars and considerate amount of molecular, atomic and ionized gas, along with a central bulge or bar consisting of older stars. Extending outward from the bulge, there can be relatively bright spiral arms. Spiral galaxies show rather continuous classifications. Firstly, spiral galaxies can be divided into unbarred (Sn) and barred (SBn) spiral galaxies. Secondly, as shown in the Hubble tuning-fork diagram (Figure 1.4), from the relatively left (early type) to the right (late type) spiral galaxies are called S(B)0, S(B)a, S(B)b, S(B)c and S(B)d, they show rather continuous transitions:

- Decreasing luminosity ratio between bulges and disks.
- More prominent spiral arm structures (increasing open angles).
- Color appearing more blue.
- Increasing gas fractions.
- Decreasing stellar mass and luminosity.

Though early type spiral galaxies tend to be higher in both stellar mass and luminosity. Unlike elliptical galaxies, all subgroups of spiral galaxies do not show large separations in terms of stellar mass (between $10^9 - 10^{12}$ $M_\odot$), luminosity (M_B from -16 to -23) and size.

The bulge lies in the central region of each spirals. Bulges are round shaped structures and relatively redder than disks. This indicates that they contain old stars. Similar to ellipticals they show *de Vaucouleurs* surface brightness profiles (see Equation 1.3). In contrast, disks are relatively bluer and show exponential radial surface brightness profiles.

The surface brightness profiles perpendicular to the disk plane can be studied from some edge-on galaxies. Such studies revealed that disks consist of two parts: the thin disk and the thick disk. Both disks show vertical exponential surface brightness profiles. The thin disk tends to be dominant in terms of stellar mass and gas mass (Allende Prieto, 2010). Stars in the thin disk are relatively younger and more metal-rich, while stars in the thick disk are relatively older and more metal-poor. In addition, thick disk stars show higher velocity dispersion (σ). Some theories suggest that thick disk stars were early formed thin disk stars, with lower metallicity. An alternative is that after experiencing disk instabilities, interactions and other dynamical perturbations their orbits were "heated up" and moved to the thick disk (Villalobos and Helmi, 2008; Steinmetz, 2012).

Irregular galaxies

Irregular galaxies have no regular structures (either disk-like or ellipsoidal) hampering their classification. Typical irregular galaxies have lower stellar mass (between $10^7 - 10^{10}$ $M_\odot$) and luminosity (M_B from -13 to -20). In addition, they usually contain larger gas fractions and appear to be bluer, which shows they contain significant younger stellar populations. Their irregularity may be due to interactions, or star formation episodes.

Concentration and Sérsic brightness profile

As mentioned above, galaxies with different morphological types could have different surface brightness profiles. To generalize their descriptions, J. Sérsic introduced the Sérsic brightness profile:

$$\log(I(R)/I_e) = -b_n[(R/R_e)^{1/n} - 1] \tag{1.6}$$

Here n is called the Sérsic index which decides the shape of the profile (the larger n the steeper the central peak and more extended the outskirt), b_n is the coefficient which follows the relation $\Gamma[2b_n] = 2\,\gamma[2b(n_S), b_n]$, where Γ and γ are respectively the Gamma function and lower incomplete Gamma function (Ciotti and Bertin, 1999). which to high precision can be approximated by:

$$b = 2\,n_S - \frac{1}{3} + \frac{4}{405}\,\frac{1}{n_S} + \frac{46}{25515}\,\frac{1}{n_S^2} \approx 2\,n_S - \frac{1}{3} \tag{1.7}$$

R_e is the effective radius, I_e represents the surface brightness at R_e. When n=4 the profile becomes the *de Vaucouleurs* profile, while for n=1 we get the exponential profiles, as seen in Figure 1.5. Though a single Sérsic profile may not always be able

to provide a perfect fit, it still provides us a way to describe the shape of galactic radial profiles and classify galaxies.

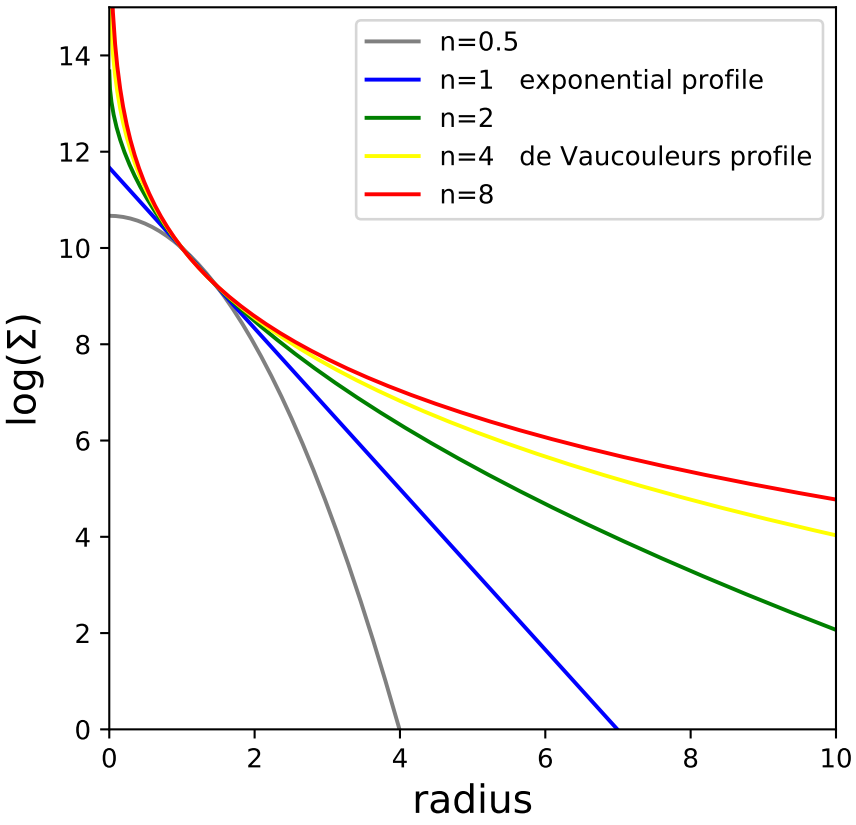

FIGURE 1.5: Radial mass density profiles with different Sérsic indices, n.

Dynamical properties in galaxies

The structural dichotomy in galaxies is also correlated with the distribution of stellar orbits in a galaxy. For example, flat disky structures tend to contain stars that have fast-rotating circularity orbits. These stars are thought to be born and live in quiescent times (White and Rees, 1978). While more elliptical shaped structures (early type galaxies, bulges in late type galaxies, stellar halos and globular clusters) consist of stars with slow-rotating box or radial orbits. These stars may have been born or live in more violent environments (Davies and Illingworth, 1983; Quinn, Hernquist, and Fullagar, 1993; Minchev and Quillen, 2006).

In reality, it is nearly impossible to trace the orbit of each individual stars in galaxies outside our Milky Way. Depending on the approach, there are many tracers which are used to indicate the dynamical structure of a galaxy. Most commonly, people use the ratio between stellar rotation velocity and the velocity dispersion V_{rot}/σ as a proxy for the angular momentum. Observations have shown that elliptical galaxies tend to have more dispersion supported systems ($V_{rot}/\sigma < 1$), while

spiral galaxies show more stellar orbits that are rotationally dominant ($V_{rot}/\sigma > 1$). On the other side, the early type spirals (Sa, Sb) show higher V_{rot}/σ compared with their late type counterparts (Sc, Sd).

V_{rot}/σ is a projected quantity however, and depends on the anisotropy of the velocity dispersion, and the inclination the galaxy is viewed at (for V_{rot}). Therefore, often studies use the orbital circularity λ_z to describe the kinematic properties of an orbit.

$$\lambda_z = J_z / J_{\max}(E) \tag{1.8}$$

Here J_z is the angular momentum of the orbit around the short z-axis, and $J_{\max}$ is the maximum of a circular orbit with the same binding energy E. Thus, $J_z = 1$ represents pure circular orbit, while $J_z = 0$ represents random-motion orbits (radial orbits and box orbits), negative J_z represents counter-rotating orbit. Typically the low J_z random-motion dominant orbits "kinematic hot", and high J_z rotation dominant orbits are referred to as "kinematically cold". In general, kinematically hotter components are more centrally concentrated (with larger Sérsic indices n) and rounder. Besides, both cold and hot components become significantly more concentrated and rounder in higher mass galaxies (Zhu et al., 2018a).

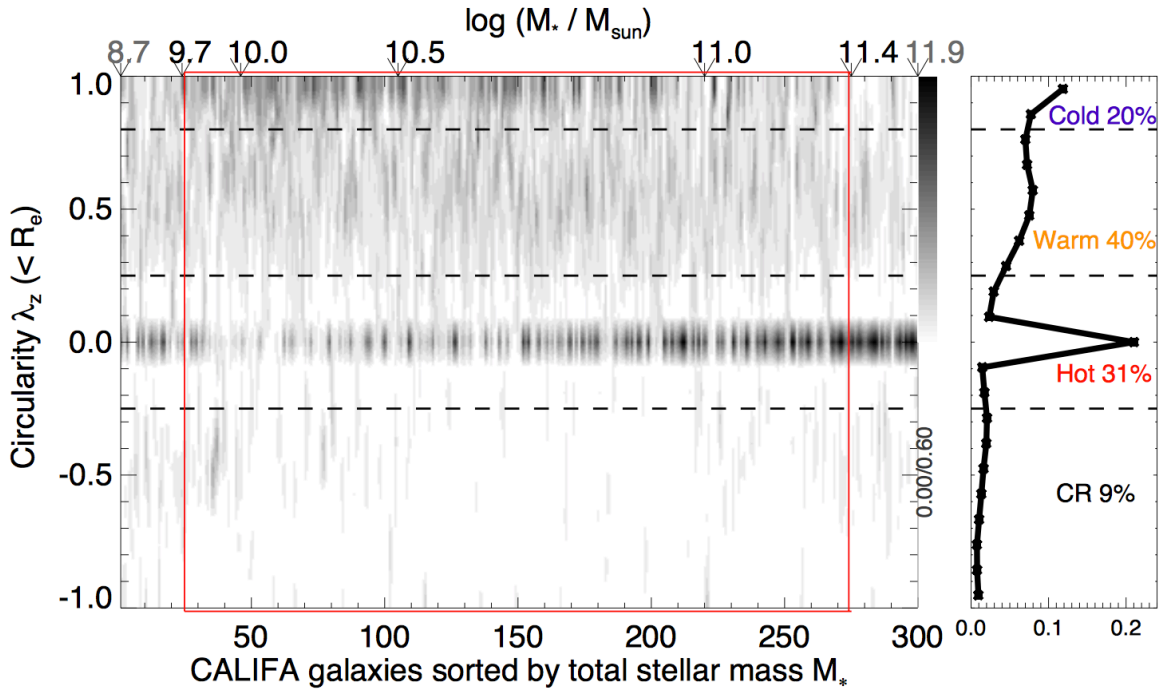

FIGURE 1.6: The λ_z distribution for each of 300 CALIFA galaxies. Each thin vertical slice represents the λ_z distribution of one galaxy, normalized to unity within the half-light-radius Re. From left to right, the galaxies are sorted with increasing total stellar mass log(M_*) (also indicated at the top). The right panel is the volume-corrected average orbit-circularity distribution within the red box. The cold, warm, hot and counter-rotating (CR) components are divided in λ_z indicated by the three horizontal dashed lines. Image credit: Zhu et al., 2018d

Zhu et al., 2018b derived the stellar orbit distribution λ_z by using orbit-superposition Schwarzschild models, and decomposed 300 CALIFA galaxies into four orbital components: cold with strong rotation, warm with weak rotation, hot with dominant random motion, and counter-rotating. Figure 1.6 shows the stellar orbital distributions of those galaxies. We see a clear trend between the dynamical structures and the total stellar mass: with the increasing of total stellar mass, galaxies are more dominanted by hot components, while for very low mass galaxies ($\log(M_*) < 10.0$), galaxies show a stronger contribution of hot orbits. This type of orbital decomposition, allows for insight into when different structures in the galaxy formed and grew (e.g., disk heating).

Stellar population differences among the galaxy sub-types

Though the visual morphology is a widely used way to classify galaxies, its classification is quite subjective. Combined with the limitation of our observations, practically, it can be very hard to obtain the correct morphological type of some galaxies. For instance, some remote galaxies for which it is not possible to get their clear 2D images or in the case of some edge on galaxies it is impossible to obtain their spiral types and bulge shapes.

Therefore the stellar populations of a galaxy can provide another way to study differences in populations of galaxies. As we have mentioned before, early type galaxies are in general redder than late type galaxies, and as such the relative colour distribution of galaxies can be used to understand how many are star forming, what stops them from forming stars and other questions about their evolution. Similar to CMDs for classifying stars, colour-magnitude diagrams of galaxy integrated colours can also be used as a classification scheme.

For example, Strateva et al., 2001; Kauffmann et al., 2003; Baldry et al., 2004 found that the distribution of galaxies in the color-magnitude diagram (U-r vs. M_r) shows two clear density peaks, with a low luminosity blue sequence and a red sequence which covers a broader range of luminosities and extends to higher luminosities (as shown in Figure 1.7). The origin of this bimodality shows some similarity with the morphological classifications, as the early type galaxies are usually redder in color and late type galaxies are bluer. Moreover, the early types galaxies show a larger mass range while also extends to much higher mass compared to late type galaxies.

In addition, besides those normal galaxies, their are also some intermediate or transitory positions for galaxies:

- Interacting galaxies are galaxies that have an encounter with other galaxies (e.g. merger, fly-by, accretion ...). Interactions between galaxies are relatively frequent compared to stars, and could strongly influence galaxies evolution tracks.

- Starburst galaxies are galaxies that undergo very intense star formation processes. This kind of starbursts can quickly consume the gas content within galaxies, thus, the starburst usually lasts for only a short period (10^7 years).

- Active galaxies are galaxies that emit a significant fraction of their total energy output from their active galactic nucleus (AGN), which are accreting super

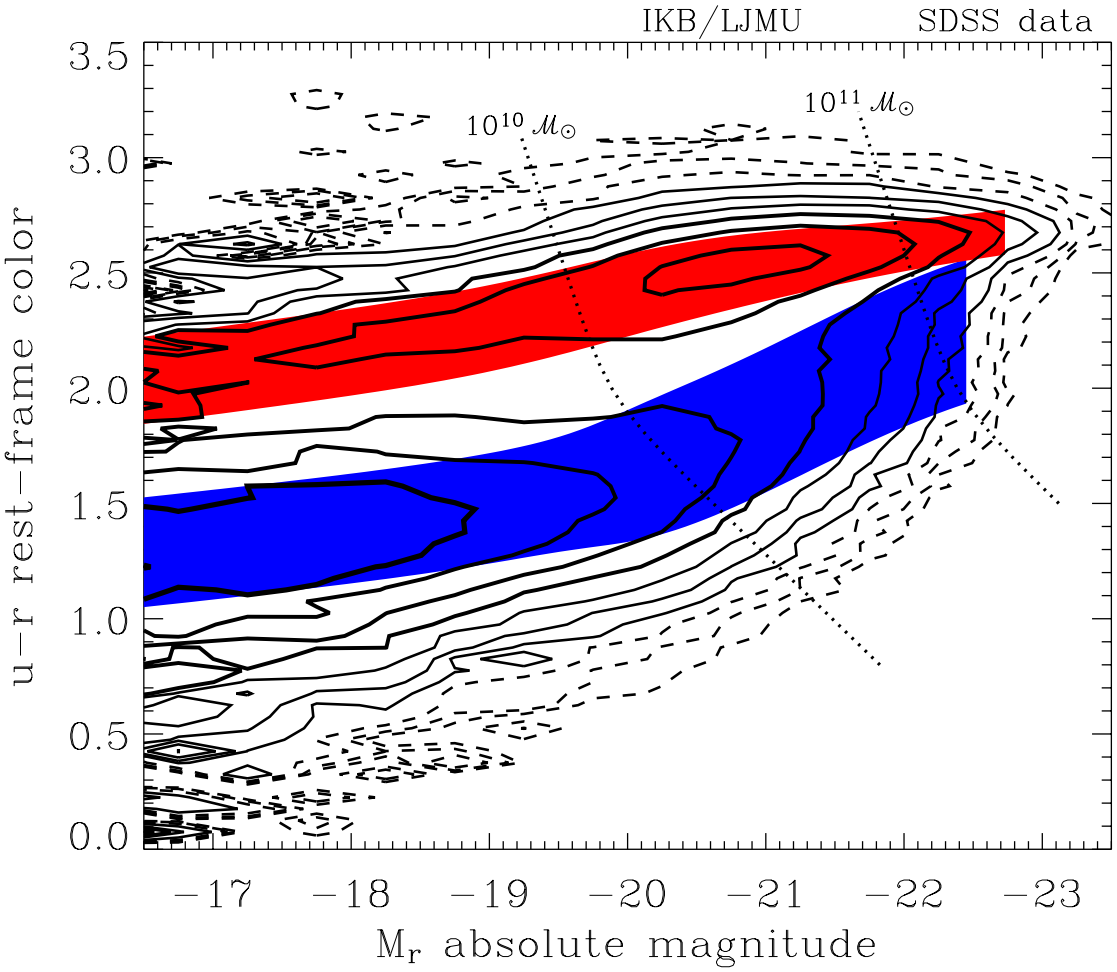

FIGURE 1.7: The color-magnitude distribution of galaxies from the Sloan Digital Sky Survey at z<0.1. Solid and dashed contours represent the number density of galaxies. The red and blue shaded regions show the mean and 1 σ dispersion of the red and blue sequences. The dotted lines represent galaxies of similar stellar masses. Image credit: Baldry et al., 2004.

massive black holes lying in the centre of galaxies. Depending on our viewing angle, those AGNs show different types of spectra and can be further divided to Seyfert galaxy, Blazar, LINER and Quasar.

1.1.3 Formation and evolution

According to the standard Λ-Cold Dark Matter (Λ-CDM) model of Big Bang cosmology, after the decoupling between radiation and matter there were very small density fluctuations in the early Universe (Liddle, 2003; Planck Collaboration et al., 2014; Planck Collaboration et al., 2016b). The large structures in our present-day Universe was originally from those small density fluctuations in the early Universe (Mo, van den Bosch, and White, 2010).

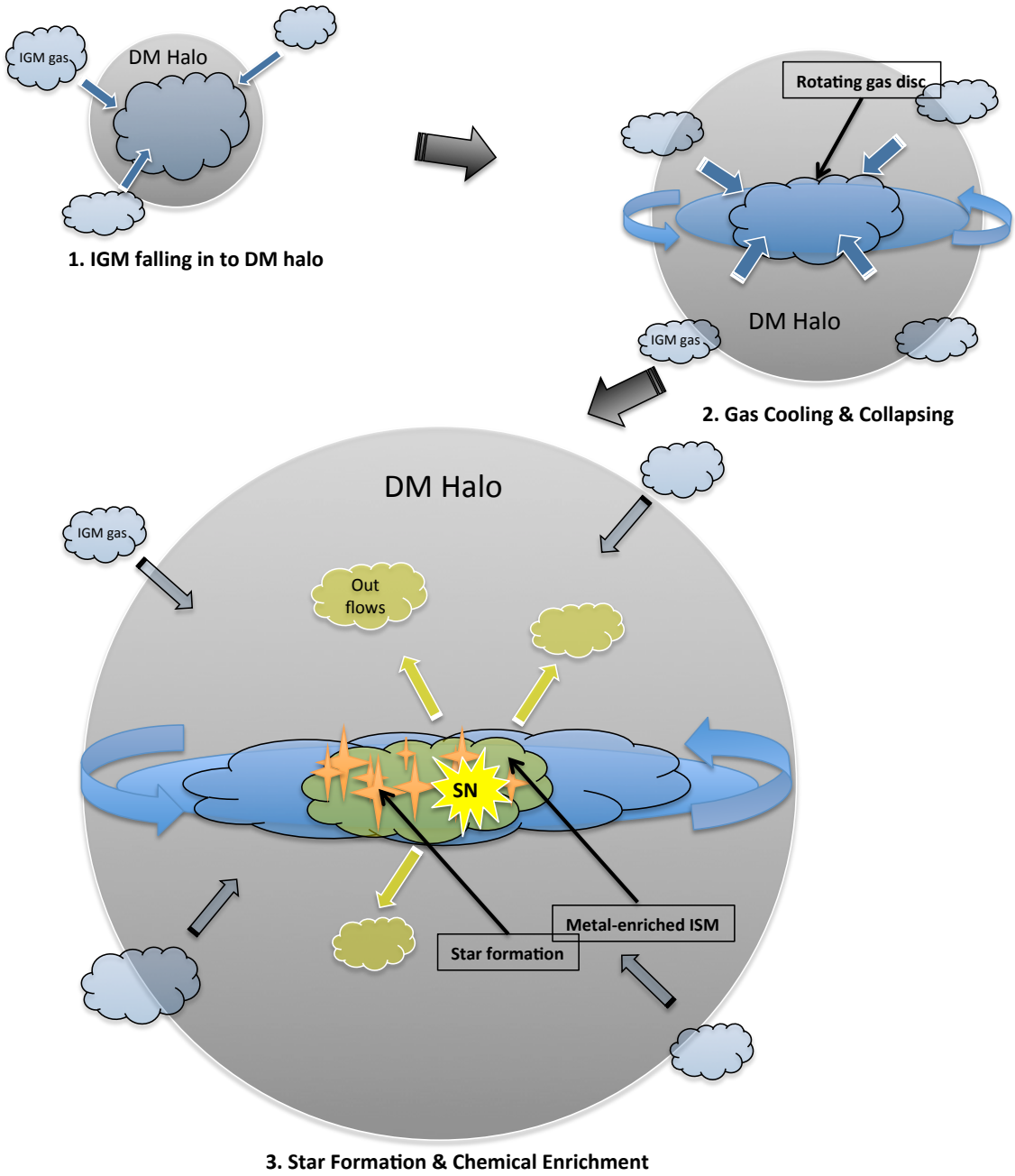

FIGURE 1.8: Cartoon schematic of galaxy formation. In panel 1, gas falls into a small DM halo. In panel 2 the gas within those halos cools and due to the conservation of angular momentum may distribute into a disc. In panel 3, after the formation of first generation stars, the ejected heavy elements start to 'enrich' the surrounding environment, while some gas is blow away from the galaxy.

Due to gravity, the density fluctuations begin to grow in amplitude. As time goes by, those slightly denser areas are becoming denser and slightly emptier areas are becoming more emptier. During this process, dark matter (DM) gradually structures into halos and filaments.

As shown in Figure 1.8, generally, small DM halos appeared first. Due to their

gravity, the baryonic matter (the gas) felt into those halos, and the gas within those halos was then compressed and after cooling down, it could eventually collapse and form stars. After the formation of the first generation stars, their feedback can heat the nearby gas and prevent new star formation processes. If the gravitational potential well of the halo is too shallow, the feedback of the stars can blow the gas out of the halo and the star formation will be halted; if the potential is deep enough to keep the gas, which will eventually cool down and form new stars. Stellar feedback provides an efficient way to regulate the star formation rate. With more and more dark matters and gas falling into the halo, the DM halo grows bigger while more and more gas within forms stars the galaxy is growing up (Schneider, 2015).

Internal processes

For an isolated galaxy, after the first generation stars were formed from the collapse of the "initial" gas, the angular momentum of the gas cloud was preserved in the new born galaxy. Depends on the original angular momentum of the initial cloud, galaxies may begin to show disky structure. Later on, the constant gas inflow from the filaments will also carry more angular momentum into the system, the galaxy will become more 'disky' and the disk structure will also be extended towards outer regions, this is so called inside-out disk formation (Williams et al., 2009; Abdurro'uf, 2018; Spitoni et al., 2019).

With generations of star forming processes, the gas within the galaxy will be exhausted. If there is no new gas inflow from the inter galactic space, the star formation of the galaxies will be halted, and the galaxy will be defined as a quenched galaxy. As young stellar populations contribute more to the bluer bands, a quenched galaxy will become redder in its spectrum and its position on the color-magnitude space (see in Figure 1.7) will move from the blue main sequence to the red sequence.

External processes

In reality, most galaxies are not evolving in isolation as galaxies and their host DM haloes may also grow through merging with other halos/galaxies. Usually, stars that were formed in other galaxies and were accreted to its current host galaxy later are called ex-situ stars, while stars that were formed inside of their own galaxy are called in-situ star.

According to the mass ratio of the merger progenitors, merger can be classified into major merger and minor merger: major mergers happen when the two merging galaxies have similar masses while minor merger are those merger between a big galaxy and a relatively smaller galaxy. According to the gas content, the merger progenitors it can also be classified as dry and wet mergers. Dry mergers take place between progenitor galaxies that do not contain much gas, while wet mergers occur between gas rich galaxies.

Mergers play a very important role in galaxies' evolution. By introducing material from other galaxies, galaxies can rapidly increase their mass. In addition to that, a lot of their properties will be changed. Firstly, the dynamical structure can be strongly influenced through a major merger or constant minor mergers. One result would be the thickening or destruction of the disk structure, shifting galaxies'

FIGURE 1.9: This image captured by Hubble telescope (NASA/ESA) shows two galaxies (NGC 2623 and Arp 243) merging together. The merging system is around 250 million light-years away from us, yet we can observe gravitational interactions producing two beautiful star trails roughly 50,000 light-years long. The speckled patches of bright blue are the star formation regions. In this case the violent merger has stirred up and compressed gas within the two galaxies, triggering intense star formation which can exhaust the gas quickly. Image credit: ESA/Hubble NASA.

morphological types towards early types, massive ellipticals. cDs galaxies are considered to be formed through mergers (Bignone et al., 2017; Rodriguez-Gomez et al., 2017; Martin et al., 2018). Secondly, the chemical structure can also be changed greatly, as mergers introduce ex-situ stars and gas from other galaxies, with different chemical components, and with dynamical processes, both in-situ and ex-situ stars and gas will be redistributed in the galaxy (Di Matteo et al., 2009; Bustamante et al., 2018; Taylor, Kobayashi, and Federrath, 2019). Thirdly, wet merger may also trigger intense star bursts by compressing the ISM through complicated dynamical interactions (losing angular momentum), leading to the quenching of the galaxy (Prieto et al., 2016; Geach et al., 2018), as shown in Figure 1.9.

A real present-day galaxy is a combined result of many different processes, e.g. the properties of the initial DM halo, the properties of initial and later accreted gas, stellar feedback, mergers, AGN, etc. The study of all those different factors could greatly help us to understand the past, present and the future of galaxies and our Universe.

1.2 Chemical Enrichment

Galaxies were formed from primordial gas which consists $\sim$77 % Hydrogen, $\sim$23 % Helium and very small amount of Lithium and no heavier elements. But today,

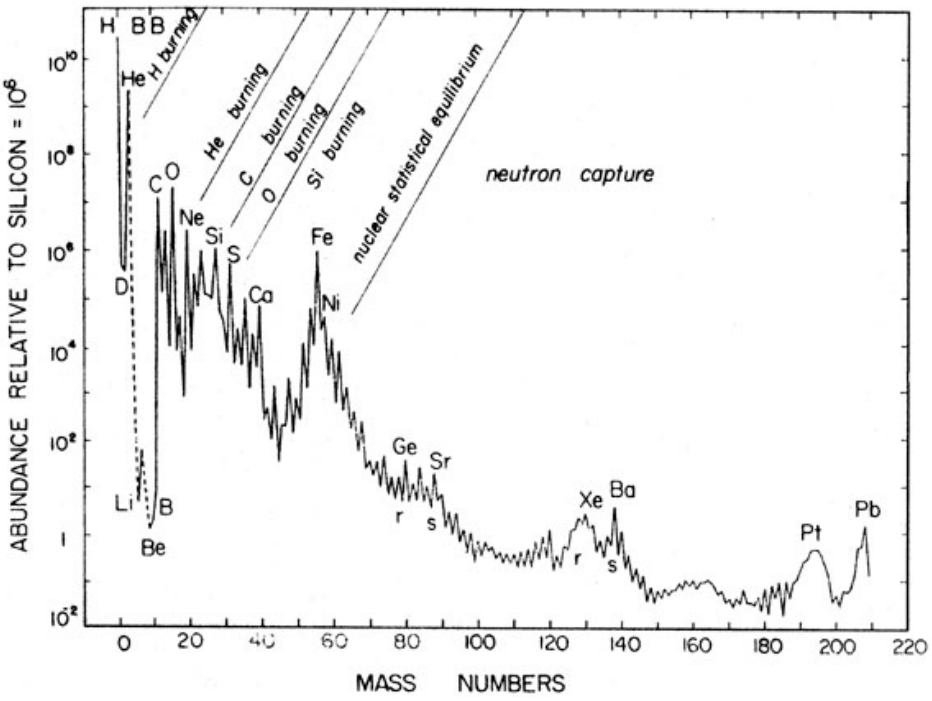

FIGURE 1.10: The solar neighbourhood abundance distribution of different elements, adapted from Cameron (1982). Image credit: Pagel, 1997.

stars and interstellar gas in galaxies exhibit diverse chemical element abundance patterns, e.g. the interstellar medium (ISM) in the solar neighbourhood shows a composition of ∼70 % Hydrogen, ∼28 % Helium and ∼2 % heavier elements (heavier than Helium), as shown in Figure 1.10. The creation of heavier elements lead to the formation of our planet earth and the existence of lives on it, and this process in the interstellar gas is due to the chemical evolution of galaxy.

Since the first generation of stars were formed from molecular gas clouds, they started to enrich the chemical composition of nearby primordial gas by producing heavier elements in their interiors through nucleosynthesis, and then returning a fraction of their material (including heavy elements) to the ISM via various feedback events (stellar winds, planetary nebula ejections and supernova explosions). Later stellar generations then formed out of this enriched gas and evolved, and kept enriching the ISM. This progressive enrichment of heavier elements in the interstellar gas is referred to as galactic chemical evolution.

However, feedback not only influences the chemical composition but also modifies the kinematic properties of the ISM. Various feedback events could inject thermal and kinetic energy to the surrounding gas and cause the expulsion and turbulent mixing of gas. This may trigger more star formation, or destroy the potential star forming clouds. The combined effect of feedback from a number of stars in a large cluster will significantly redistribute the chemically enriched gas and affect the local galactic star formation rate.

In addition, the evolution of the galaxy may also change the dynamical structure and chemical abundance of gas. As mentioned in previous section, the pristine

gas inflow from the inter-galactic spaces can dilute the local chemically enriched gas, while the outflow due to different mechanisms (stellar, AGN feedback, ram-pressure striping, galaxy interactions...) may remove the gas and heavy elements from the galaxy.

A galaxy's present-day chemical environment is thus a result of many different and interacting processes. In this section, we will talk about the basic mechanisms that are important in the chemical evolution of galaxies. We start from the formation of stars, then followed by the production of heavy elements, and the observed empirical relations and theoretical models seen in chemical evolution..

1.2.1 Star formation

Stars are the primary producers of heavy elements in the Universe, and their formation is tightly linked to the chemical enrichment of their surrounding environments. We believe that most stars are formed form molecular clouds. When the mass of the cloud exceeds its 'Jeans mass', the cloud itself can no longer be supported by its internal gas pressure and it will collapse due to the gravity. During the collapse of the cloud, tens to ten thousands of stars are forming from it more or less simultaneously. The cloud eventually becomes a star cluster. Some of these star clusters will remain bound and are observed today as open or globular clusters, while others will quickly disperse and contribute to the field stars of the galaxy.

Schmidt-Law

While the exact details of star formation is a complex field, there are several imprtant empirical relations which inform our broad picture of how gas is converted into stars. Schmidt, 1959 discovered an empirical relation between the gas surface mass density and the star formation rate per area ($\Sigma_{\rm SFR}$) for stars in our Milky Way:

$$\Sigma_{\rm SFR} = v\Sigma_{\rm gas}^{N} \tag{1.9}$$

Here ($\Sigma_{\rm SFR}$) is the star formation rate per area with a unit of $\mathrm{M_\odot\,kpc^{-2}\,}yr^{-1}$, while $\Sigma_{\rm gas}$ is the gas surface mass density with a unit of $\mathrm{M_\odot\,pc^{-2}}$. This relation was then examined by Rob Kennicutt with a sample of stars from ~ 90 nearby galaxies, here the absolute SFR efficiency $v \sim 0.00025$, with the power index N ~ 1.4 (Kennicutt, 1983; Kennicutt, 1998). This relation is called Schmidt-Kennicutt law, or star formation law.

Recent studies show that there could be different star formation laws for different types of galaxies (Bigiel et al., 2008). Moreover, the $\Sigma_{\rm SFR}$ is more correlated with the surface mass density of molecular hydrogen Σ_{H_2} rather than Σ_{HI}. This suggests some correspondence with our ideas on star formation theory, where stars are formed from the collapse of dense molecular gas clouds, as shown in Figure 1.11.

IMF

During the collapse of the molecular cloud, its Jeans mass will also decrease. This leads to the collapse of multiple smaller denser regions within the collapsing cloud; this process is called fragmentation. This is why stars usually from in groups, and those stars that were formed in the same molecular clouds tend to have same

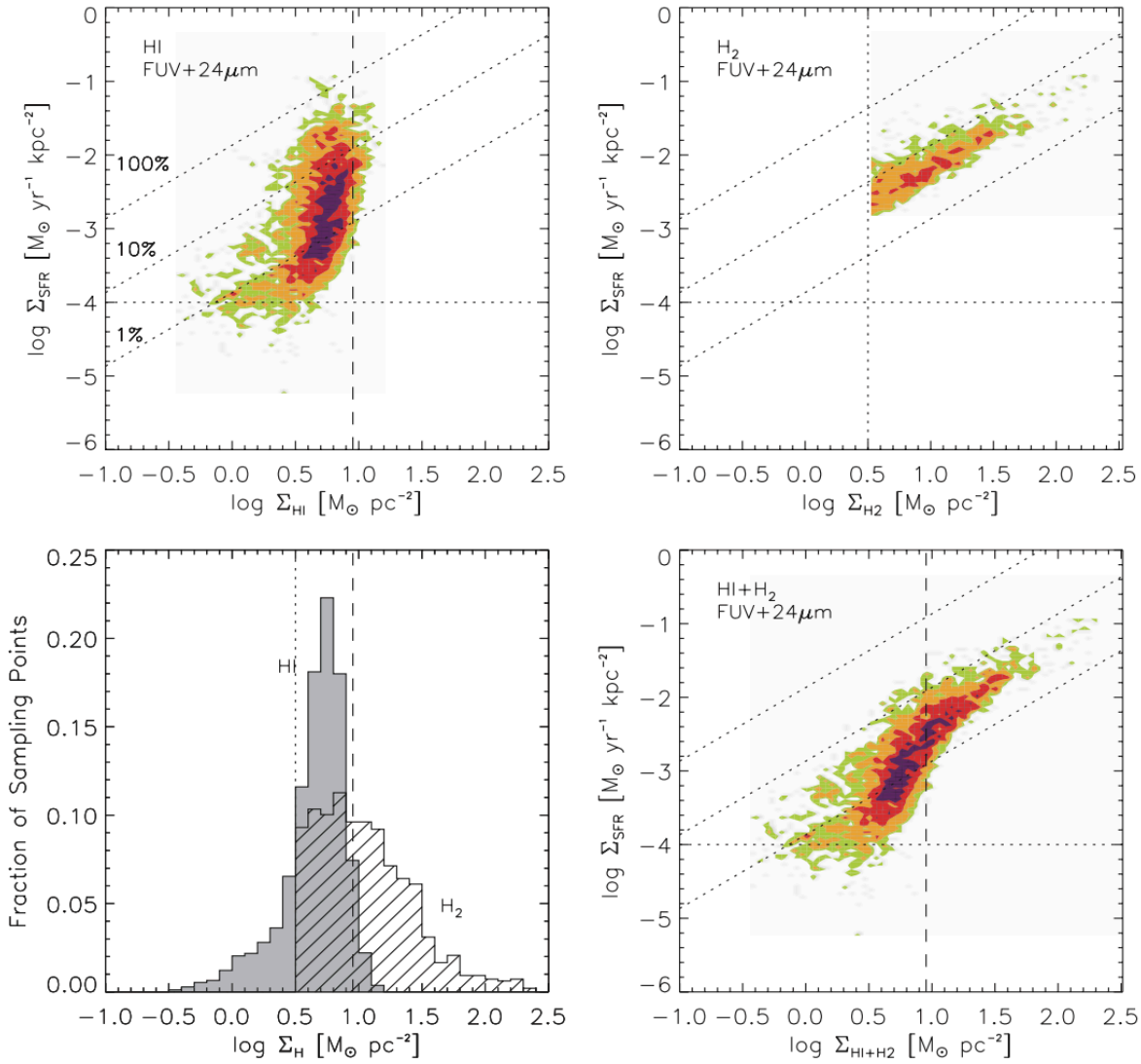

FIGURE 1.11: Relations between SFR surface density and different gas phase surface density from (Bigiel et al., 2008). Top left: $\Sigma_{\rm SFR}$ vs. Σ_{HI}; top right: $\Sigma_{\rm SFR}$ vs. Σ_{H_2}; bottom right: $\Sigma_{\rm SFR}$ vs. $\Sigma_{\rm gas}$. Magenta, red, orange, and green cells show contours of 10, 5, 2, and 1 independent data points. The horizontal dotted line represents the sensitivity limit of each SF tracer. The vertical dashed and dotted lines are the value at which Σ_{HI} saturates the sensitivity limit of the CO data. The bottom-left panel shows the distributions of HI and H_2 surface densities in the sample. Image credit: Figure 8, Bigiel et al., 2008

age and chemical abundance. Moreover, those stars seem also to have similar initial mass distribution. In general, there are many more lower mass stars compared to high mass stars. The initial mass function (IMF) is an empirical function that describes this initial distribution of masses for a stellar population. As stars with different initial masses can have very different evolutionary tracks, it is important to study the IMF of a population.

In 1955 Edwin Salpeter first calculated the IMF of stars with mass higher than

our sun (Salpeter, 1955). He described the IMF with a power law with an exponent of -2.35:

$$\xi(m)\Delta m = \xi_0(m/M_\odot)^{(-2.35)}(\Delta m/M_\odot) \tag{1.10}$$

Here $\xi(m)\Delta m$ represents the number of stars within the mass range m to $m + dm$, $M_\odot$ is the mass of our sun and ξ_0 is a constant representing the local stellar number density. This form of the IMF is called the Salpeter IMF. It shows that the number of stars decreases rapidly with increasing mass.

Kroupa, 2001 refined the IMF by introducing the IMF of stars lower than one solar mass.

$$\begin{gathered} \xi(m) = m^{-\alpha} \\ \alpha = 0.3 \quad \text{for} \quad m < 0.08 \\ \alpha = 1.3 \quad \text{for} \quad 0.08 < m < 0.5 \\ \alpha = 2.3 \quad \text{for} \quad m > 0.5 \end{gathered} \tag{1.11}$$

Chabrier, 2003a provided a new form of IMF for stellar mass lower than solar mass and also extended the IMF to stellar systems (binaries).

For single stars:

$$\begin{gathered} \xi(m)\Delta m = 0.158(1/(ln(10)m))exp[-(log(m) - log(0.08))^2/(2 \times 0.69^2)] \quad \text{for} \quad m < 1, \\ \xi(m) = m^{-\alpha} \quad \text{for} \quad m > 1 \quad \alpha = 2.3 \end{gathered} \tag{1.12}$$

For stellar systems (e.g. binaries):

$$\begin{gathered} \xi(m)\Delta m = 0.86(1/(ln(10)m))exp[-(log(m) - log(0.22))^2/(2 \times 0.57^2)] \quad \text{for} \quad m < 1, \\ \xi(m) = m^{-\alpha} \quad \text{for} \quad m > 1 \quad \alpha = 2.3 \end{gathered} \tag{1.13}$$

The three mostly commonly used IMF are shown in Figure 1.12. Though they show similar shape at the mass higher than 1 $M_\odot$, their IMFs for low mass stars are still quite diversed. In addition, due to the lack of sample, the IMF for very high mass stars (M_* 8 $M_\odot$) is also unclear. As stars of different masses are different in luminosities, ages and release metals on different timescales, knowledge of the form of the IMF is an important ingredient in observations and models of galaxy's chemical evolution.

1.2.2 Stellar nucleosynthesis

For most of the lifetime a star gets its energy through nucleosynthesis. At the beginning, main sequence stars generate their energy through the fusion of hydrogen atoms at their core. Later, depending on the stellar mass the fusion of helium and other heavier elements may take a place. In astronomy, all of these heavier elements (heavier than He) are called "metals", and nucleosynthesis is the major origin of

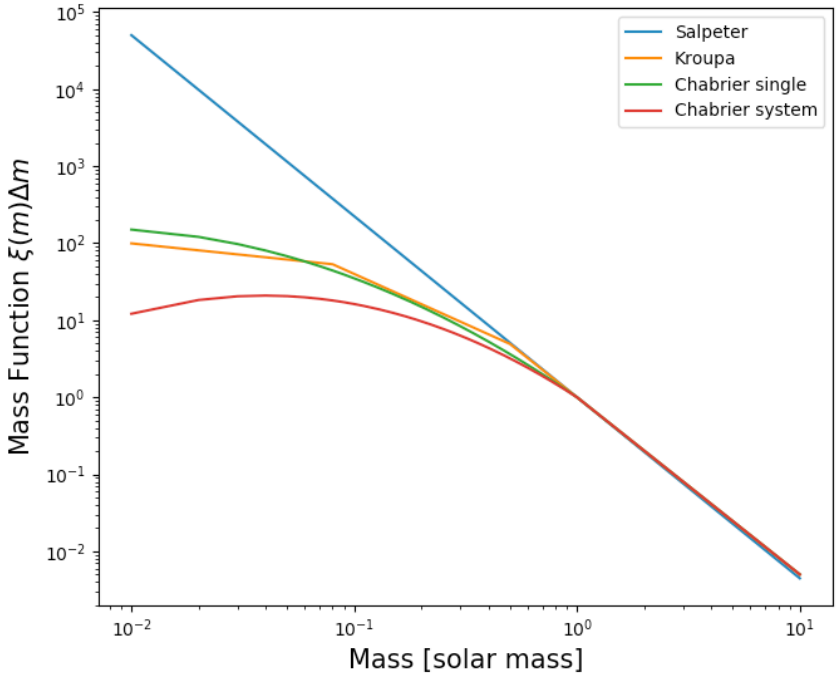

FIGURE 1.12: Three commonly used initial mass functions are shown as coloured lines in a plot of stellar mass versus differential number.

metals in our Universe. In this subSection we will briefly talk about some of the important nucleosynthesis processes in the Universe.

Hydrogen fusion

Hydrogen fusion (also called "hydrogen burning") is the most important process that generates energy to support main-sequence stars. There are two predominant processes for stellar hydrogen fusion the proton-proton chain and the carbon-nitrogen-oxygen (CNO) cycle. ~90% of all stars, with the exception of white dwarfs, are fusing hydrogen through these two processes.

The proton–proton chain reactions (PP-chain) mostly happen in lower mass main-sequence stars (like our sun). The PP-chain reaction has two steps, first is the fusion of two protons to one deuterium nucleus (one proton plus one neutron) and the ejection of a positron and a neutrino. The positron usually annihilates immediately with an electron. Second step is the fusion of the deuterium produced in the first stage can and another proton that produces a light isotope of helium ${}^{3}_{2}\mathrm{He}$.

$$\begin{aligned} {}^{1}_{1}\mathrm{H} + {}^{1}_{1}\mathrm{H} &\rightarrow {}^{2}_{1}\mathrm{H}^{-} + e^{+} + v_e + 0.42\mathrm{MeV} \\ e^{-} + e^{+} &\rightarrow 2\gamma + 1.022\mathrm{MeV} \\ {}^{2}_{1}\mathrm{D} + {}^{1}_{1}\mathrm{H} &\rightarrow {}^{3}_{2}\mathrm{He}^{-} + \gamma + 5.49\mathrm{MeV} \end{aligned} \tag{1.14}$$

The PP-chain is temperature insensitive (the reaction starts at temperatures around $4 \times 10^{6} K$). Thus, it occurs within up to 33% of the star's radius with around half the star's mass, and leads to a radiation dominant heat transfer inside of the star that allows some fusion products to move outward.

The CNO cycle mostly happens in higher mass main-sequence stars. It also produces a helium nucleus but through a catalytic cycle that involves nuclei of carbon, nitrogen and oxygen as intermediaries.

$$4\,{}^{1}_{1}\mathrm{H} + 2e^{-} \quad \rightarrow \quad {}^{4}_{2}\mathrm{He} + 2\nu_e + 3\gamma + 26.7\mathrm{MeV} \tag{1.15}$$

Unlike the PP-chain the CNO cycle is very temperature sensitive (it dominants the energy production at approximately 17×10^6 K). Which only allows the reaction to happen within the inner region of the star. This leads to a strong convective energy transfer that keeps the reactions region well mixed with surrounding regions.

Outside of these two, there are also other ways to fuse hydrogen nuclei, including the Ne-Na chain and the Mg-Al chain which may occur at sufficiently high temperature.

Advanced nuclear burning phases

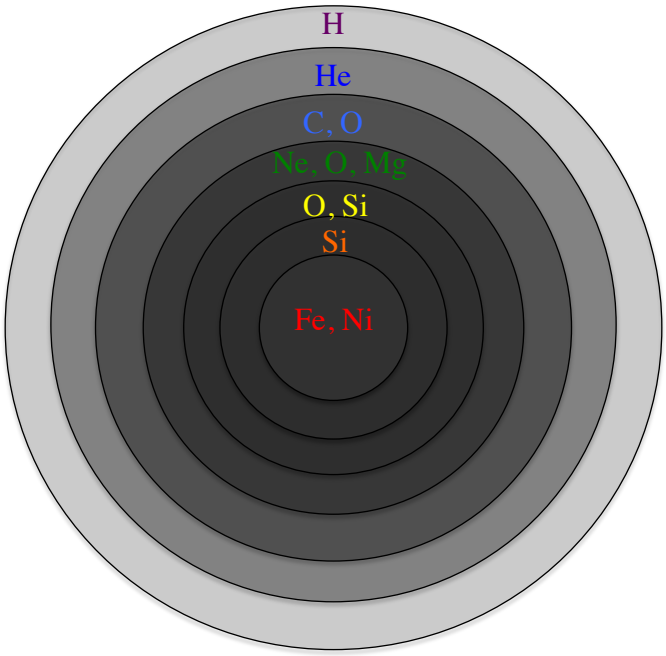

FIGURE 1.13: Onion structure of a fully evolved massive star. Different burning phases take place at the bottom of each layers. The Fe core in the center is accumulated through silicon burning. Note that the relative thicknesses of the layers are not to scale.

After the star is running out of the hydrogen in its centre, the star leaves the main sequence and become a red giant. At this time, the center has accumulated enough helium, but the temperature is not enough to burn the helium until the star leaves the red giant branch the fusion of helium starts.

The main reaction of helium burning is called 3α-reaction. It starts with the fusion of two ${}^{4}_{2}\mathrm{He}$ to form one ${}^{8}_{4}\mathrm{Be}$ and this is a reversible reaction. Then, ${}^{8}_{4}\mathrm{Be}$ fuses with another ${}^{4}_{2}\mathrm{He}$ and becomes a ${}^{12}_{6}\mathrm{C}$:

$$\begin{aligned} 2\,^4_2\mathrm{He} &\leftrightarrow {}^8_4\mathrm{Be} \\ {}^8_4\mathrm{Be} + {}^4_2\mathrm{He} &\rightarrow {}^{12}_6\mathrm{C} + \gamma \end{aligned} \tag{1.16}$$

Out of $^{12}_6$C, the $^4_2$He elements can form heavier elements (e.g. O, Ne and other elements with even numbers of protons, as $^4_2$He has 2 protons). This is called the alpha process. After running out of the helium in the core of a star, the fusion will still continue in a shell around the carbon-oxygen core.

After running out of helium, for massive stars ($M_* > 8\ \mathrm{M}_\odot$) advanced burning phases will take place, which consist of C, Ne, O, and Si burning. Each of these burning phases fuses heavier nuclei, which becomes the fuel for the subsequent burning phases. Meanwhile, due to the lower temperatures and densities the previous fusion phases still continues in the outer layers of the star, leading to a onion shaped structure, with the fusion of heavy elements occurring in the centre while lighter elements burn in outer layers, as shown in Figure 1.13.

Elements beyond the iron

With a sufficiently high neutron supply iron nuclei can accrete the neutrons to form neutron-richer nuclei through the neutron-capture process. Due to the instability, when the neutron number increases the nuclei will undergo β decay through which many elements heavier than Fe can then be formed by transforming a neutron into a proton and emitting an electron and an anti-neutrino. Depending on the relative rate between the neutron capture and β decay, there are two types of neutron-capture processes.

The slow neutron-capture process or s-process is a series of reactions that are believed to occur mostly in asymptotic giant branch (AGB) stars, where the iron group nuclei were not fused in the AGB star itself but left by supernovae from a previous generation of stars. The neutrons mostly comes from the fusion between $^{13}_6$C and $^4_2$He or $^{22}_{10}$Ne and $^4_2$He. So the rate is limited by the initial iron abundance of the star, usually the timescale of s-process is around thousands of years. The typical productions of s-process are Sr, Y and Pb.

The rapid neutron-capture process or r-process happens during the core collapse supernova explosions. Unlike s-process, the r-process is believed to occur over time scales of seconds. After massive star forms its iron core in the centre, due to the fusion of iron does not produce energy, but rather requires absorb energy, the further reactions can no longer support the star against its gravity, leads to the core collapse supernova explosion (SNII and SNIb,c). During the core collapse, the innermost regions of the star are compressed into 10^{12} kg/m^3 nuclear density and the temperature will reach $10^{11}K$. Such environment will break the iron nuclei into neutrons and protons via the high-energy thermal radiation. And then, the pressure will compress the electrons into protons and form neutrons and neutrinos. Part of neutrons will be locked in the remnant of the star (either a neutron star or a black hole), the rest of the neutrons will be bounce outward during the explosion. The r-process occurs when one or more heavy seed nuclei (e.g. ^{5}6Fe) start to rapidly capture neutrons (hence the name) and the typical productions are Se, Br, Kr, Te, I, Xe, Os, Ir and Pt.

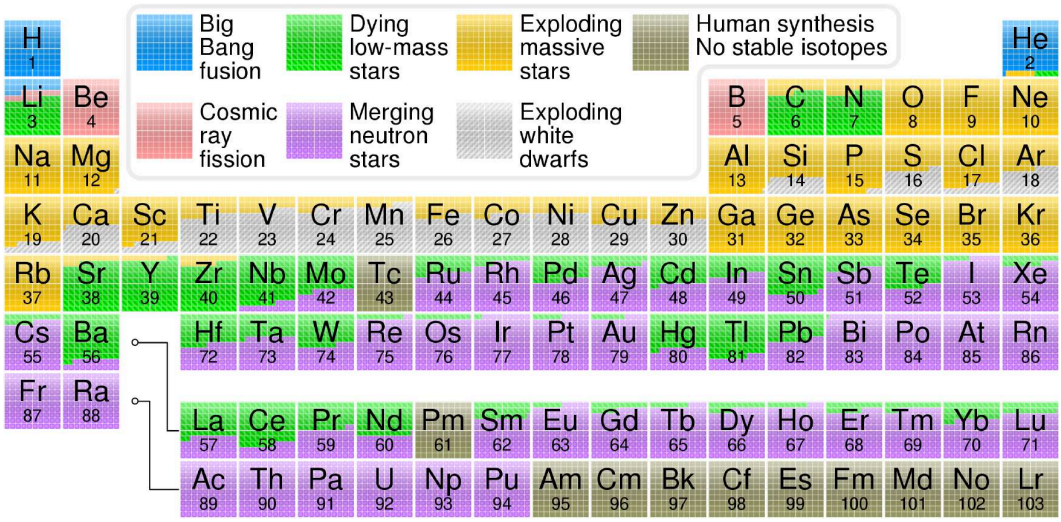

FIGURE 1.14: Periodic Table with the origin of each element. Elements from carbon up to sulfur may be made via α processes in small stars. Elements heavier than iron are made through slow/rapid neutron captures. (Image credit: Wikipedia, made by Cmglee.)

In this subsection we shortly discussed some but not all of the important nucleosynthesis processes. Figure 1.14 shows the origin of each element on the Periodic table. Through nucleosynthesis heavier elements were created in the star, some of them were locked into stellar remnants and some of them were returned to the surrounding ISM through different ways including stellar wind, planetary nebula and supernova explosions.

1.2.3 Mass-metallicity relation

As metals are mostly produced through stellar evolution, we should expect there is a correlation between the metallicity and stellar mass. Indeed, since Lequeux et al., 1979 first found a clear correlation between the two from nearby irregular galaxies, many later observations from the analysis of different samples have shown a similar correlation between stellar mass (luminosity) and metallicity. As shown in Figure 1.15, high-mass (high-luminosity) galaxies tend to have higher metallicities than their lower mass counterparts, though this correlation becomes flatter for massive galaxies (e.g. Zaritsky, Kennicutt, and Huchra, 1994; Tremonti et al., 2004; Zahid et al., 2014; Sánchez et al., 2017).

As one of the most fundamental and early recognized relationships between galaxies and their metal content, the mass-metallicity relation (MMR) is the result of the combined effects of various processes during a galaxy's life: star formation, gas inflow and outflow and galactic mergers amongst others. Though, the basic connection between stellar mass and metallicity can be easily reproduced by a simple "closed-box" model (see Section 1.2.4 and Tinsley, 1980), the nature of the MMR is still not completely understood, as it is washing over many of the spatial trends seen in galaxies.

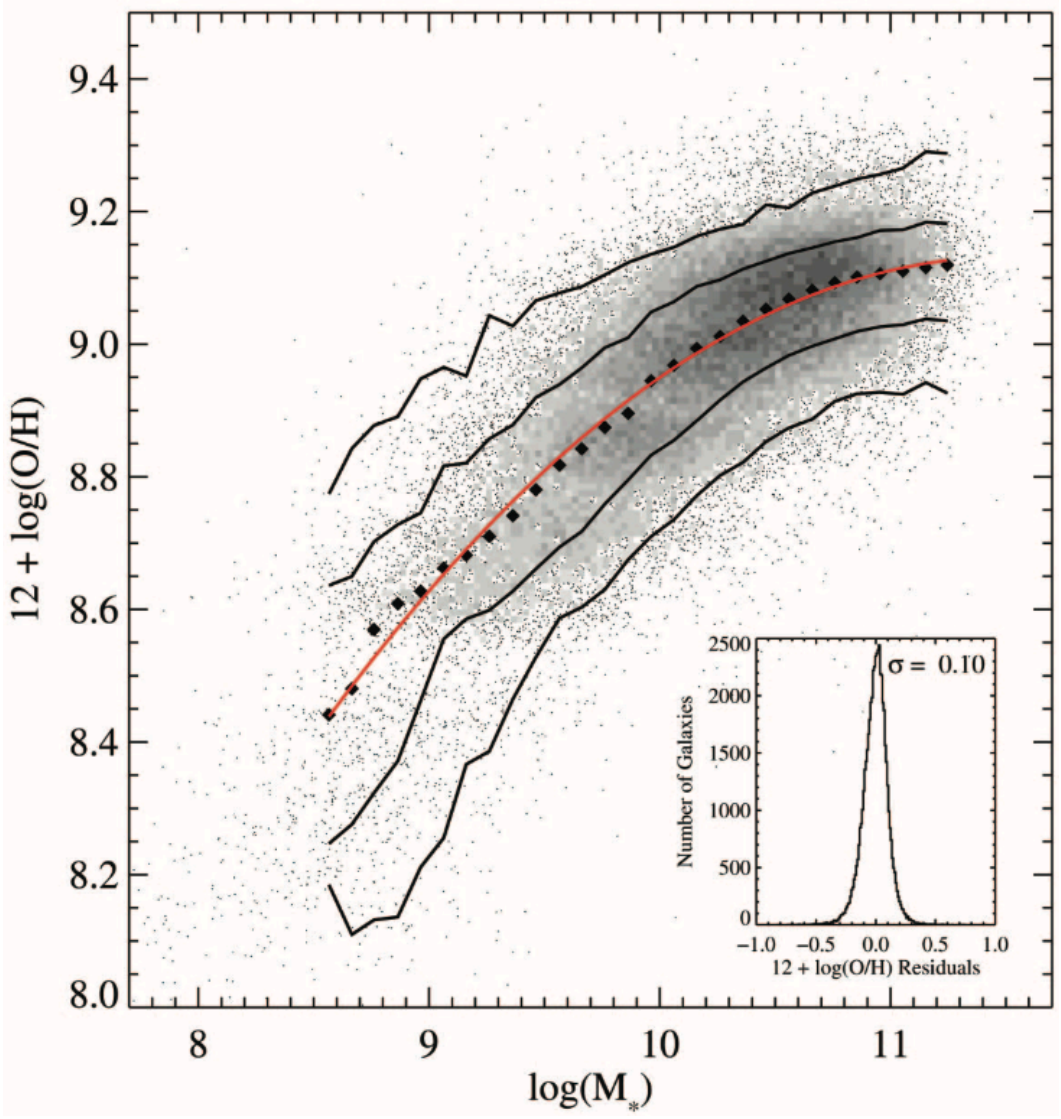

FIGURE 1.15: Relation between stellar mass, in units of solar masses, and gas-phase oxygen abundance for 53,400 star-forming galaxies in the Sloan Digital Sky Survey (SDSS). The large black filled diamonds represent the median in bins of 0.1 dex in mass that include at least 100 data points. The solid lines are the contours that enclose 68% and 95% of the data. The red line shows a polynomial fit to the data. Image credit: Tremonti et al., 2004.

1.2.4 Galactic chemical evolution model

To understand the chemical evolution of galaxies, scientists have used many analytic models to describe the complicated relations of these processes. Here we briefly introduce a simple and classic "closed-box" model, to show some of its principle aspects.

Through stellar feedback, part of those metals that were formed in the core of stars could be ejected out into the surrounding ISM. Then, next generations of stars

were formed from the metal-enriched ISM, which will change their stellar metallicities and evolution tracks. Finally the younger stars will also enrich their surrounding ISM by ejecting part of the metals formed in their cores. Generation by generation, the chemical abundance of the galaxy will be greatly increased. To better understand the chemical evolution of galaxies, researchers use analytical models that describe and predict the metallicity (Z) of galaxies.

Here the metallicity Z, is the mass fraction of metal elements within ISM.

$$Z(t) = m_{Z,\mathrm{gas}}(t)/m_{\mathrm{gas}}(t) \tag{1.17}$$

Here m_Z is the mass of metals in the ISM, m_{gas} is the gas mass.

To build a simple model we assume the galaxy is a closed system, with no interaction or material changes from outside, so the sum of the total stellar mass m_* and the gas mass m_{gas} should be a constant, this is so called a 'closed-box' model. Then, we assume all stars that are formed in our galaxy follow a constant IMF: $\Phi(t) = \Phi$. The total stellar mass that was formed before would be:

$$m_{*,tot}(t) = \int_0^t \Phi \mathrm{d}t \tag{1.18}$$

In addition, we it is typical to adopt an instantaneous recycling approximation (IRA): stellar evolution timescales that introduce the metal enrichment are short enough that for a newly formed star population, the stars immediately evolve and return a fraction R of their evolved (metal-enriched) mass to the ISM through feedback (winds and supernovae). The last assumption is that the returned materials are always well mixed with ISM. Thus, a fraction α=(1-R) of mass will be locked into remnants (note that, in this subsection, remnants includes normal stellar remnants and low mass stars that have too long main sequence lifetimes to enrich the environment). Typically R depends on the IMF of the stellar population, and can be calculated from stellar evolution tracks. So the gas mass equation of the model galaxy is then:

$$\begin{aligned} \mathrm{d}m_{\mathrm{gas}}/\mathrm{d}t &= -\alpha\Psi(t) \\ \text{Due to : } \mathrm{d}m_{\mathrm{gas}} &= M_b - \mathrm{d}m_* \\ \mathrm{d}m_{\mathrm{gas}}/\mathrm{d}t &= -\alpha\Psi(t) = -\mathrm{d}m_*/\mathrm{d}t \end{aligned} \tag{1.19}$$

Here Ψ is the SFR, as we have discussed in 1.2.1, it is determined by the local gas density. And M_b is the total baryonic mass which is constant for a closed-box model. m_* is the total remaining stellar mass $m_* = m_{(*,formed)}\alpha$.

$$\Psi(t) = v \times (\Sigma_{\mathrm{gas}}(t)^k) \tag{1.20}$$

At the beginning (t=0) of the evolution, before the formation of the first generation stars, no metal exists and the metallicity is $Z(0)$=0.

We use q as the mass ratio of the metals that were produced by the star population and returned to the ISM over the starting total mass of the star population $q = m_{(Z,produced)}/(\Psi \mathrm{d}t)$ which is solely depends on IMF. The equation for the metal mass in ISM should be:

$$\mathrm{d}(m_{\mathrm{gas}}Z)/\mathrm{d}t = q\Psi(t) - \alpha\Psi(t)Z(t) \tag{1.21}$$

Here, $\alpha\Psi(t)Z(t)$ are the metals from ISM "old metals" that were locked into remnants. We further define the nucleosynthetic yield $y = q/\alpha$ which is the ratio between the new formed metals that are returned to the ISM and starting total mass of the star population over the fraction of the mass that will be locked into remnants.

$$\mathrm{d}(m_{\mathrm{gas}}Z)/\mathrm{d}t = \alpha\Psi(t)(y - Z) \tag{1.22}$$

Since the $\Psi = dm_{*,formed}/dt$:

$$\begin{aligned} \mathrm{d}(m_{\mathrm{gas}}Z)/\mathrm{d}m_{*,formed} &= \alpha(y - Z) \\ \mathrm{d}(m_{\mathrm{gas}}Z)/\mathrm{d}m_{*} &= (y - Z) \\ Z(\mathrm{d}m_{\mathrm{gas}}/\mathrm{d}m_{*}) + m_{\mathrm{gas}}(\mathrm{d}Z/\mathrm{d}m_{*}) &= y - Z \end{aligned} \tag{1.23}$$

As $\mathrm{d}m_{\mathrm{gas}}/\mathrm{d}m_{*} = -1$:

$$\begin{aligned} m_{\mathrm{gas}}\mathrm{d}Z/\mathrm{d}m_{\mathrm{gas}} = \mathrm{d}Z/\mathrm{dln}(m_{\mathrm{gas}}) &= -y \\ Z(t) = -y\mathrm{ln}(m_{\mathrm{gas}}/M_b) &= -y\mathrm{ln}(\mu_g) \end{aligned} \tag{1.24}$$

Here, $\mu_g = m_{gas}/M_b$ is the gas fraction among all baryonic matter. The yield y depends on the IMF (due to the amount of metal produced and the return fraction). This relation (1.24) produces the trend we found in observed galaxies, e.g. galaxies with higher gas fractions tend to show lower metallicity.

However, this model is not good enough to provide detailed predictions, as the assumptions here are quite simple, and ignore many processes which are crucial for real galaxies. The biggest problem is that galaxies are not closed-boxes, they grow by accreting more materials from filaments, other galaxies, and also they may merge with other galaxies. These processes will cause the inflow of gas, stars and dark matter. Simultaneously, there are mechanisms that trigger the outflow of gas and other materials, internally, the feedback from stellar winds, supernovae and AGN can push the metals and gas out of the galaxy. Externally, the gravitational perturbations or accretion from other galaxies, the ram pressure from hot gas inside of galaxy clusters can also strip metals and gas out of the galaxy.

There are other discrepancies between the model and a real galaxy, e.g. the gas is not perfectly mixed in a real galaxy; the nucleosynthetic yield is incredibely uncertain, depends on model assumptions for explosive models, and may vary with the metallicity of the population; metallicity may also change the star formation rate; the relation (1.24) predicted by the simple model is independent of the SFR and star formation history (SFH).

1.3 Stellar Population Gradients in Galaxies

Stars are the building blocks of galaxies, and importantly the light coming from them encodes chemical information from their birth environment and epochs. Studying the chemical and age properties and spatial distribution of stars in a galaxy can provide hints and constraints on our understanding of the galaxy's formation and

evolution pathways. A galaxy may contain billions of stars, therefore, to systematically study them, we need to characterize the combined integrated chemical signatures contained in the galaxy's spectrum.

1.3.1 Stellar populations

A group of stars with the same age, metallicity and IMF is called a simple stellar population (SSP). For example, an open cluster is a SSP as all its stars formed in the same molecular cloud at the same time. A galaxy consists of a large number of different stellar populations, formed in different regions at different times. By knowing the stellar population compositions, we are able to learn about the evolutionary history of a galaxy. There are two ways to study the stellar population compositions of a galaxy:

1. Individual stars in a galaxy:

As described in Section 1.1.1, from the spectrum of a star we are able to extract its age and metallicity. For nearby galaxies as well as our Milky Way where we are able to resolve the light of individual stars, we can study their stellar population compositions by analyzing the photometric/spectroscopic information of stars.

For stars with same age and metallicity, their locations on a color-magnitude diagram (CMD) should be a single sequence, while stars from different populations (ages, metalliciities) will distribute into multiple sequences on the CMD. As shown in Figure 1.16, the CMD resulting from the complex globular cluster ω Centauri, clearly shows the existence of multiple stellar populations in the cluster.

However CMD analysis is not the perfect solution, as color is just an indicator of the star's effective temperature, and both age and metallicity can influence it - causing a degeneracy between age and metallicity. To break this degeneracy in observations and to separate different stellar populations one usually needs their CMDs from multiple bands, or to derive the accurate chemical abundances through spectroscopy of single star. As we have mentioned before, by measuring the intensity of metal absorbing lines, one can infer the chemical composition of a star.

2. Using stellar population synthesis to study the integrated spectra of a galaxy:

For remote stellar systems like galaxies, we can not resolve the light of individual stars, but instead recover the flux weighted integral of the light of all its stars. Stellar population synthesis therefore can be a useful tool for us to get their stellar population information.

Theoretically, for a SSP with a given IMF and metallicity, with our knowledge of stellar evolution tracks we are able to calculate the mass, size and surface temperature of stars of different initial masses at different ages. Combined with a model of stellar atmospheres or empirical stellar libraries we can predict the integrated spectra of a SSP at different ages. Thus, we can create a spectra library that consists the spectra of SSPs at different ages and with different metallicities:

$$f_{\rm SSP}(t, Z) = \int_{m_{low}}^{m_{high}(t)} f_*[T_{\rm eff}(M), \log g(M)|t, Z]\Phi(M)dM \tag{1.25}$$

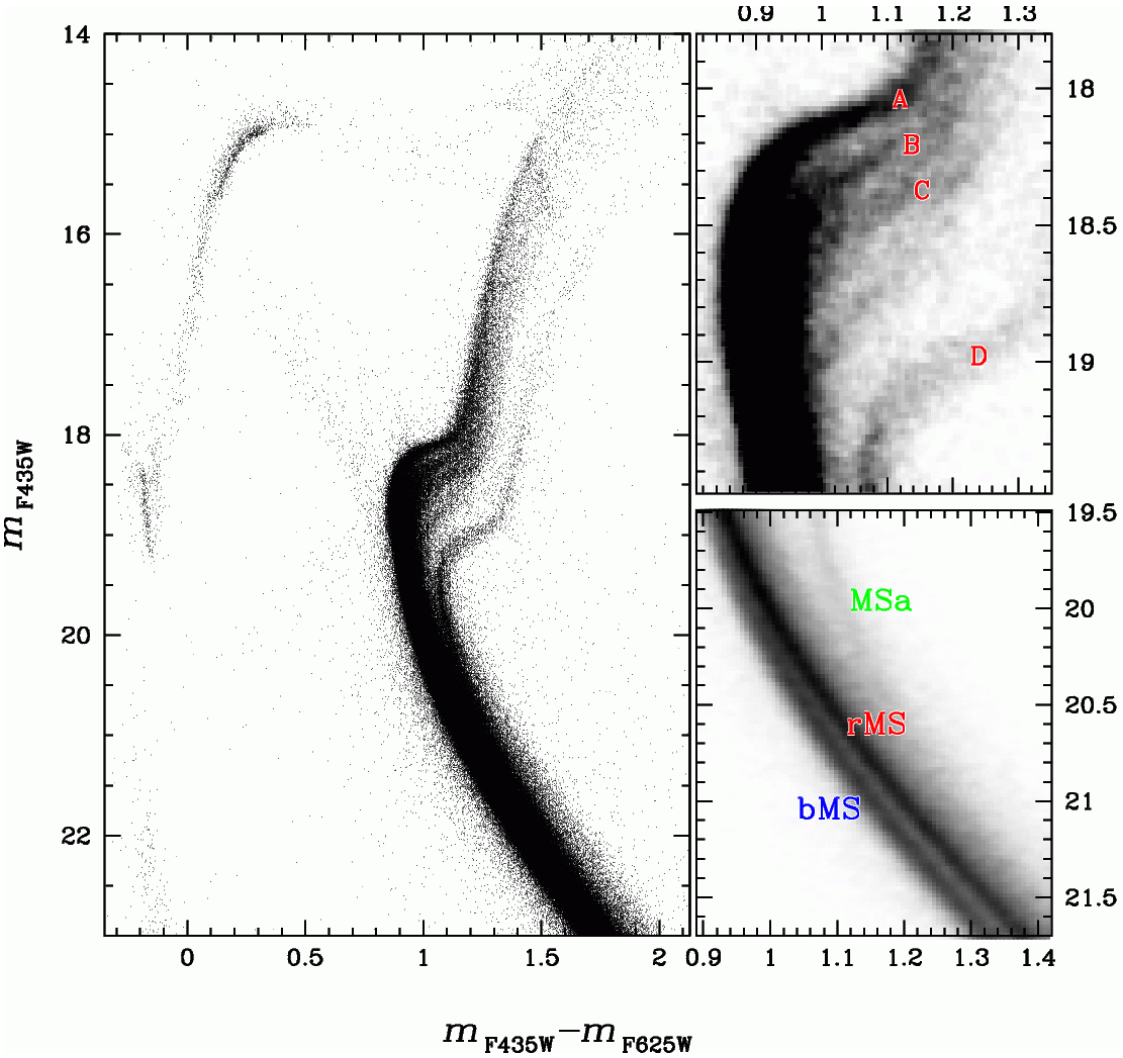

FIGURE 1.16: Left: CMD resulting from the 10×10 arcmin^2 mosaic of HST ACS images centered on the Galactic globular cluster ω Centauri. Top right and bottom right panels show clear sign of multiple populations at the main sequence turn off and main sequence. Image credit: Bellini et al., 2010.

Here, $f_{\rm SSP}$ is the flux as a function of wavelength of the SSP, m_{high} is the upper stellar mass at each time which is determined by stellar evolution tracks, m_{low} is the lower limit of stellar mass (usually choose either 0.08 or 0.1M$_\odot$), f_* is the spectrum of a star at given effective temperature $T_{\rm eff}$, surface gravity log$g(M)$ and metallicity Z, M is the initial stellar mass of the whole population and $\Phi(M)$ is IMF.

A galaxy is a composite stellar populations (CSPs), with old and young, metal poor and metal rich stellar populations, plus it contains dust. It's integrated spectrum is a overlap of the spectra of different SSPs it consists:

$$f_{\mathrm{CSP}}(t) = \int_{t'=t_0}^{t'=t} \int_{Z=Z_{min}}^{Z=Z_{max}} (\Psi(t-t')P(Z,t-t')f_{\mathrm{SSP}}(t,Z)e^{-\tau_d(t')} + Af_{dust}(t',Z))dt'dZ \tag{1.26}$$

Here, the integration variables are the age, t', and metallicity, Z of the stellar population, $P(Z,t)$ is the time-dependent metallicity distribution function, $\tau_d(t')$ represents the dust optical depth and f_{dust} represents the emission of the dust with A as a normalization constant.

By comparing the observed spectrum or its features with the modeled SSPs spectra, one can study its light weighted stellar population information.

One of the most commonly used methods to determine light weighted ages and metallicities of unresolved stellar populations is the Lick spectra indices system (Vazdekis et al., 1997). As the age and metallicity degeneracy can be a big issue in determining the age and metallicity of SPs (both increasing metallicity and age could contribute to the overall reddening of an spectrum with stronger spectroscopic absorption features). Worthey, 1994 found that some spectral line indices are more sensitive to age, e.g. the hydrogen Balmer lines, and some of them are more sensitive to metallicity, e.g. the Fe4668 and Fe5270 indices. Later, Thomas, Maraston, and Bender, 2003 defined a composite metallicity index [MgFe]' $\equiv (\mathrm{Mgb}(0.72 \times \mathrm{Fe5270} + 0.28\mathrm{Fe5335}))^{0.5}$ to be a more robust metallicity estimator.

By computing the indices of our observed and model SSP spectra at different metallicity and age we can constrain the light weighted age and metallicity from observed spectra. As shown in Figure 1.16, the black grid is the spectral indices at different ages and metallicities obtained from SSP models. Comparison with the model grid of indices allows for an inferencee on the age and metallicity of the galaxy's integrated light-weighted age and metallicity information.

Other than using spectra lines, via fitting the observed spectrum with the theoretical SSP spectra library, one could study its stellar population composition - the mass/light fraction of different stellar populations of an CSP spectrum.

1.3.2 Galactic stellar population gradients

A galaxy is not a homogeneous object, it has complicated spatial structures as well as the stellar populations within it. To further understand its evolution, we need the stellar population composition in each spatial areas of a galaxy. The spatial distribution of stellar populations in a galaxy can be an important tracer for us to understand its formation and evolutionary history, as the long-lived stars may record the chemical enrichment history of the environment they formed in. The present day spatial distribution of stars of different chemical abundances and ages can therefore reveal the relevant information on the evolution of galaxies and the role of different physical processes along their evolutionary paths (e.g. Greggio and Tosi, 1986; Mollá, Ferrini, and Díaz, 1997; Chiappini, Matteucci, and Romano, 2001; Pipino, D'Ercole, and Matteucci, 2008; Gibson et al., 2013a; Tissera et al., 2016b).

Observations have already found that galaxies' stellar population distributions show different spatial patterns (Sánchez et al., 2017; Ho et al., 2018), but it is difficult

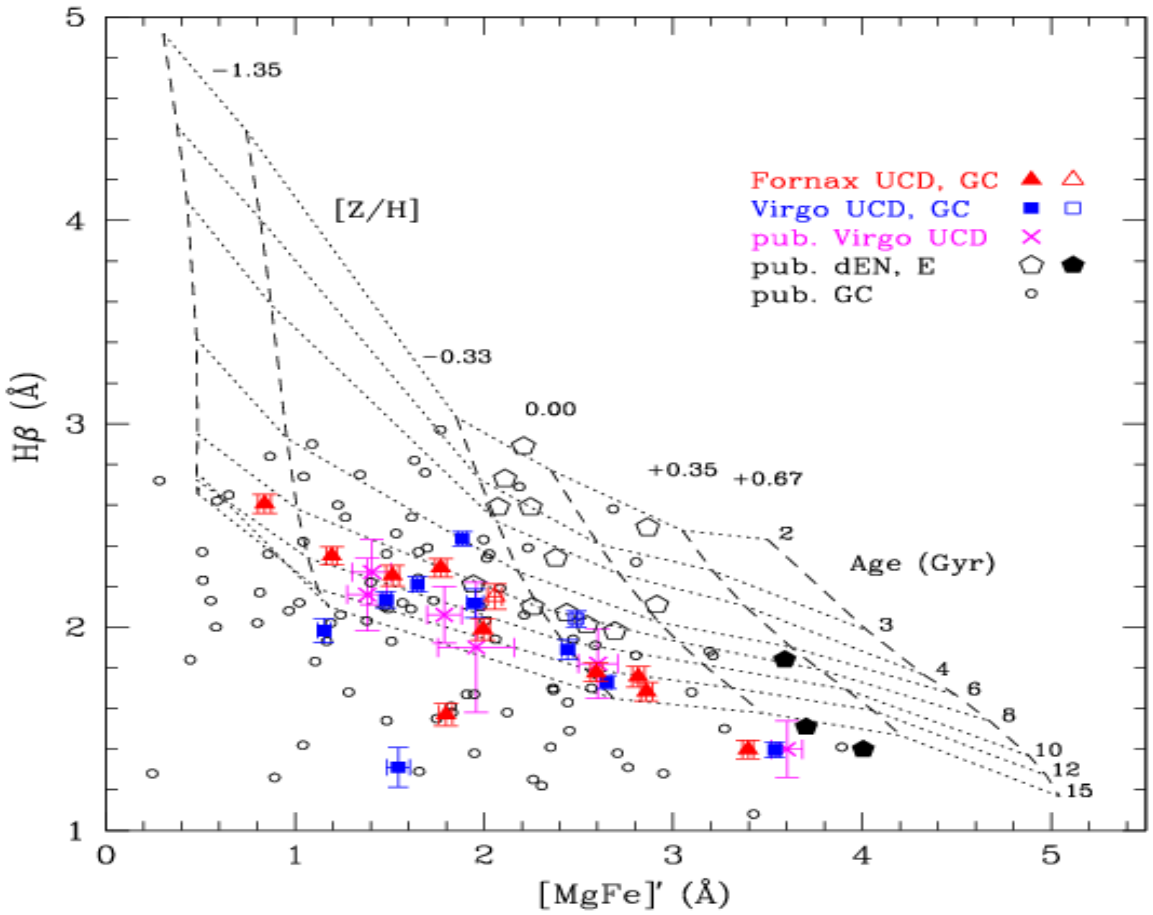

FIGURE 1.17: Age and metallicity of ultra-compact dwarf galaxies, which are indicated by the age sensitive Hβ and metal sensitive [MgFe]' Lick indices. SSP model grids are plotted for [α/Fe]= 0.3 dex from Thomas, Maraston, and Johansson, 2011. The symbols are as in the previous figures with the addition of M87 (Virgo Cluster) globular clusters (circles Cohen, Blakeslee, and Ryzhov, 1998). Image credit: Francis et al., 2012.

to trace all the 2D or 3D spatial distributions of stellar populations for most of the remote extra-galaxies at the moment - not only because of the distance but also because of the complicated mechanisms that shapes the distributions. In this way, the most pragmatic approach has been to study the 1D radial stellar population profiles. One common feature we use to describe radial stellar population profiles are their gradients, basically it describes how difference the values in different radii are. If the value changes fast along the radius, we say the profile has a steep gradient, and vise versa.

Usually radial profiles are measured in some annulli. Once the average value within an annulli is known, the radial gradient can be computed by fitting a line to the profile. This can be done in a variety of ways: with respect to physical radius, scaled radius (e.g., galaxy effective radius), in linear values (e.g., stellar age, circular velocity and velocity dispersion etc.), or logarithmic values (e.g., surface brightness, stellar surface mass density etc.). In this thesis, we will mostly be focusing

on galaxies' stellar metallicity gradients, usually the stellar metallicity gradients are measured in log scale, while my work will be exploring their linear scale gradients.

Basic mechanisms that shapes stellar metallicity gradient

Once we have computed the radial gradient of age or metallicity within a galaxy, it is still necessary to understand what processes could give rise to it.

Gas Flows: Stars are formed from clouds, and carry the same metallicity as clouds they come from, and through their feedback, they also enrich the chemical composition of nearby ISM, influencing the chemical abundances and spatial distribution of subsequent generations of stars. During a galaxy's evolution, the ISM can be relocated by non-axisymmetric structures, stellar winds or supernova driven outflows, which can create radial flows or so-called 'galactic fountains', effectively redistributing metals. In all these cases, the chemical composition of the gas might be additionally changed by mixing with differently enriched ISM, or diluted by infalling intergalactic pristine gas (e.g., Kereš et al., 2005; Brooks et al., 2007a; Gibson et al., 2013b). For example, the existence of a bar can induce the gas to lose angular momentum and lead to a higher star formation rate (SFR) in the galaxy center, which may steepen the gradients and weaken the bar in the meantime (e.g. Combes, 2014). Tissera et al., 2016a analyzed galaxy gas phase metallicity gradients and their relation to stellar masses and star formation rates in a suite of simulated galaxies and found low-mass galaxies tend to show a larger diversity of gas metallicity gradients.

Stellar migration: In addition, stars from existing populations can also be relocated due to orbital modifications (e.g., disk heating or radial migration by bars or spiral arms; c.f., Binney and Tremaine, 1987). Radial migration is supposed to influence the evolution of stellar population gradients. The efficiency of radial migration in galaxies of different morphological types has been difficult to quantify in external galaxies. For example, Sánchez-Blázquez et al., 2014 presented the stellar metallicity and age distributions in a sample of 62 nearly face-on, spiral galaxies with and without bars, using data from the CALIFA survey. They found no difference in the metallicity or age gradients between galaxies with and without bars. Stronger evidence for stellar migratory processes comes primarily from simulations and detailed studies of the Milky Way (MW) (e.g., Sellwood and Binney, 2002; Roediger et al., 2012). In both cases, non-axisymmetric substructures (e.g., bar and spiral arms) seem to efficiently redistribute angular momentum of the galactic stellar populations (e.g., Berentzen et al., 2007). The combined effect of these overdensities can cause a radial displacement of stars (e.g., Roškar et al., 2008; Minchev and Famaey, 2010; Minchev et al., 2011; Minchev et al., 2012). These same non-axisymmetric features can also directly relocate metals in the ISM via streaming motions (e.g. Combes, 2014). Recently El-Badry et al., 2016a also examined the effects of stellar feedback and bursty star formation on low-mass galaxies using the FIRE (Feedback in Realistic Environments) simulations. They found that for low mass galaxies, repeated stellar feedback can rapidly remove gas from the galaxy's center, causing an expansion of the stellar and dark matter components - thus in addition to driving metal-enriched outflows (e.g., Kereš et al., 2005; Brooks et al., 2007a; Pilkington et al., 2012a; Gibson et al., 2013b), feedback can also indirectly modify radial stellar population gradients.

External perturbations: Externally, galaxy accretion events, interactions and mergers can not only strongly influence the gravitational potential of the galaxies,

but also rapidly redistribute the location and angular momenta of stars. Therefore, a galaxy's merger history is considered to play a significant role in determining the shape of the metallicity gradient in the galactic halo (e.g., Hirschmann et al., 2014), while simultaneously altering the angular momentum of its stars. For example, simulations have shown that a major merger could flatten the metallicity gradient efficiently (Rupke, Kewley, and Barnes, 2010; Navarro-González et al., 2013), while continuous minor mergers will steepen the gradient and shape the outskirts of the halo due to the low mass satellites are accreted primarily at large radii (see also, Cooper et al., 2013a; Oogi and Habe, 2013a; Pillepich et al., 2014a). Similarly, Kobayashi, 2004 studied the formation and chemo-dynamical evolution of 124 elliptical galaxies with a GRAPE-SPH simulation code also found that galaxies that form monolithically tend to have steeper gradients than the ones that undergo major mergers.

Towards a complete understanding of stellar population gradient evolution

Identifying the relative strength of *in-situ* star formation (SF), radial stellar migration and accretion events therefore necessitates studying stellar population gradients in a wide range of galaxy masses and morphologically diverse samples. Previous studies have been mainly focused on three approaches: analytical modelling, simulation and observations.

• Semi-analytical models have been used to study the formation and evolution of stellar metallicity gradients for a long time, with good agreement between models predictions and observed properties (Chiappini, Matteucci, and Romano, 2001). By introducing two different gas infall model Chiappini, Matteucci, and Gratton, 1997; Chiappini, Matteucci, and Romano, 2001 reproduced the metallicity gradient of the Milky Way disc. A good agreement between model predictions and observed properties of the Galaxy is generally obtained by models that assume that the disk was formed by the infall of gas (Mott, Spitoni, and Matteucci, 2013). These models have been applied most typically to individual galaxies however.

• Meanwhile, simulations have continued to show the utility of stellar metallicity gradients in understanding the mass growth history of galaxies, and the processes that shape them. (e.g. Brooks et al., 2007b; Pilkington et al., 2012b; Gibson et al., 2013a). Cook et al., 2016 found that the accretion of stars into the stellar halo tends to flatten stellar metallicity and surface-brightness profiles by analysing the result from Illustris simulation(Vogelsberger et al., 2014b; Vogelsberger et al., 2014a; Pillepich et al., 2014b).The ability of the simulations to show the evolution of gradients is useful in understanding how they tracer different processes. However they can be computationally expensive and often are difficult to isolate a single factor.

• Observationally, modern large surveys of galaxies (e.g., MANGA, CALIFA, SAMI) have derived the gradients of stars in galaxies of a wide range of morphological types. For close galaxies, we can resolve the spectra of bright stars and fit the metallicity gradient by calculating the metallicity of individual stars at different radius (Daflon and Cunha, 2004).

For galaxies where it is not possible to resolve enough stars, we can only measure metallicity gradients of different populations. In this case, the integrated color or spectra at several locations along the long axis of a galaxy is measured to then extract the metallicity at each point. Recently, large surveys using integrated field units

(IFUs) such as CALIFA (Sánchez et al., 2012a; Husemann et al., 2013a) or MaNGA (Bundy et al., 2015; Blanton et al., 2017) have provided empirical insights and constrains concerning the diversity of stellar metallicity gradients. Those surveys that observed a large variety of galaxies have found an equally large diversity of observational trends. For example, Zheng et al., 2017a studied the stellar population distributions and the environment of 1105 MaNGA galaxies and found that both the stellar age and metallicity gradients show weak or no correlation with either the large-scale structure type or local environmental density. Goddard et al., 2017a studied the radial stellar population gradients of 721 MaNGA galaxies and suggests higher mass late type galaxies show relatively steeper stellar metallicity gradients. Similarly, Martín-Navarro et al., 2018 found that galaxies with higher velocity dispersion tend to show steeper stellar metallicity gradients, by studying the normalization and the slope of the stellar populations gradients in early type CALIFA galaxies.

In order to reconcile results from both observations and simulations and further clarify the relative strength of different mechanisms in setting stellar metallicity gradients. In the thesis, we study the diversity of stellar metallicity gradients in galaxies with different morphological types and masses, and explore mechanisms that shape the stellar metallicity gradients.

In particular we try to introduce several new aspects: 1) Combining the stellar population gradients with information about the orbital structure of the galaxies. 2) Utilizing new suites of cosmological simulations to understand the local chemical enrichment and mass assembly of galaxies and 3) Producing a semi-analytic model that can be calibrated and flexibly used to describe the local mass-metallicity relations in galaxies in terms of the gas accretion history.

1.4 Summary

In this Chapter, we introduced the basic knowledge of galaxies, their classification, formation and evolution. We then briefly introduced the chemical evolution of galaxies, from different physical processes to theoretical descriptions. Finally, we talked about galaxies' spatial stellar population distributions.

The following Chapters of this thesis are organized as follows: In Chapter 2, we discuss radial stellar metallicity and kinematic profiles out to 1Re in 244 CALIFA galaxies. In Chapter 3, we discuss the stellar metallicity radial profiles of simulated galaxies in the IllustrisTNG simulations. In Chapter 4, based on the result from Chapter 2 and 3, we construct semi-analytical model to explore the evolution of stellar metallicity gradient.

Chapter 2

A CALIFA view of galactic stellar population gradients

This Chapter was published in a refereed article "A dynamical view on stellar metallicity gradient diversity across the Hubble sequence with CALIFA", Yulong Zhuang et al. (2019), where I am the lead author of the article, and was adapted for this thesis.

Overview: In this Chapter, we analyze radial stellar metallicity and kinematic profiles out to one effective radius (Re) in 244 CALIFA galaxies ranging from morphological type E to Sd, to study the evolutionary mechanisms of stellar population gradients. We find that linear metallicity gradients exhibit a clear correlation with galaxy morphological type - with early type galaxies showing the steepest gradients. We show that the metallicity gradients simply reflect the local mass-metallicity relation within a galaxy. This suggests that the radial stellar population distribution within a galaxy's effective radius is primarily a result of the *in-situ* local star formation history. In this simple picture, the dynamically derived stellar surface mass density gradient directly predicts the metallicity gradient of a galaxy. We show that this correlation and its scatter can be reproduced entirely by using independent empirical galaxy structural and chemical scaling relations. Using Schwarzschild dynamical models, we also explore the link between a galaxy's local stellar populations and their orbital structures. We find that galaxies' angular momentum and metallicity gradients show no obvious causal link. This suggests that metallicity gradients in the inner disk are not strongly shaped by radial migration, which is confirmed by the lack of correlation between the metallicity gradients and observable probes of radial migration in the galaxies, such as bars and spiral arms. Finally, we find that galaxies with positive metallicity gradients become increasingly common towards low mass and late morphological types - consistent with stellar feedback more efficiently modifying the baryon cycle in the central regions of these galaxies.

2.1 Introduction

In Chapter 1.3.2 we introduced the complicated processes that take part in the formation and evolution of stellar population gradients. In order to reconcile the role of each process, and further clarify the relative strength of different mechanisms in setting stellar metallicity gradients. In this Chapter we explore a new formalism for understanding stellar metallicity gradients, using a homogeneous analysis of the *chemo-dynamic* signatures present in the inner regions of CALIFA galaxies.

As all theoretical mechanisms presented should simultaneously alter the dynamical and chemical properties of the galaxy, we leverage information on the orbital properties of stars, in the inner regions of galaxies spanning a range of masses and morphological types. This allows us to study the impact of secular processes which may impart signatures on the angular momentum distribution of stars of different metallicities. Specifically, as a new analysis technique, we can incorporate orbit based Schwarzschild dynamical models (Zhu et al., 2018a) to understand and quantify any link between metallicity profiles, migratory signatures and the dynamical structure of the galaxy.

Sections 2 and 3 describe the extraction of the metallicity and kinematic profiles from 244 nearby CALIFA galaxies, which span a large range in mass ($10^9 M_\odot$ to $10^{12} M_\odot$), and morphological type (from E to Sd). The subsequent sections present a simple picture to illustrate the dominant in-situ formation channel for stellar population gradients in our sample, which can naturally recover the observed diversity.

2.2 Observations and Data Analysis

The Calar Alto Legacy Integral Field Area Survey (CALIFA; Sánchez et al., 2012b; Husemann et al., 2013b; Walcher et al., 2014; Sánchez et al., 2016) uses the PMAS/PPAK integral field spectrophotometer to provide the largest and most comprehensive wide-field IFU survey of galaxies. It covers two overlapping spectral regions, one in the red (3745 - 7300) with resolution of R = 850 (V500 setup) and one in the blue (3400 - 4750) with R = 1650 (V1200 setup). Due to the quality and completeness of the data, our final sample includes 244 CALIFA galaxies from E to Sd morphological types, covering stellar mass range ($10^9 M_\odot < M_* < 10^{12} M_\odot$) (for detailed information see Table 1 in Zhuang et al., 2019) and (Walcher et al., 2014). We use the total stellar masses inferred from SED fitting to the photometry from UV to IR.

In a previous work, Falcón-Barroso et al., 2017 extracted the stellar kinematics for every galaxy in a uniform way using both instrumental setups, i.e., V500 and V1200. For this analysis we utilize the derived stellar velocity V_{los}, velocity dispersion σ and their error maps for each galaxy.

Zibetti et al. (in preparation) derive maps of light-weighted stellar metallicity Z as well as of other stellar-population properties from the joint analysis of the CALIFA spectroscopic datacubes and the SDSS 5-band images of the full final data release of CALIFA (DR3 Sánchez et al., 2016). In Zibetti et al., 2017 the method is described in detail regarding the derivation of the maps of light- and mass-weighted ages, but it applies in the same way to the derivation of stellar metallicities, modulo substituting the property to be derived. We therefore refer the reader to Zibetti et al., 2017 and summarize here the main points of the analysis and related uncertainties.

For each spaxel in each galaxy we compute the posterior probability distribution function (PDF) of the light-weighted stellar metallicity $Z \equiv \frac{\sum_j L_j Z_j}{\sum_j L_j}$, where the j index identifies the different Simple Stellar Population (SSP) components, of metallicity Z_j and r-band luminosity L_j, respectively. We characterize the PDF by its median and 16^{th} and 84^{th} percentiles (i.e. $\pm 1\,\sigma$ for a gaussian distribution). We use a large and comprehensive library of 500,000 spectral models to infer Z based on the

comparison between *measured* stellar absorption features and photometric fluxes in SDSS *ugriz* bands and the corresponding *synthetic* quantities measured on the model spectra. The posterior probability function for Z given the data is derived by folding the prior distribution of models in Z with the likelihood of the data given each model i, $\mathcal{L}_i \propto \exp(-\chi_i^2/2)$. In practice, the probability $dP(Z)$ for a metallicity range $[Z - Z + dZ]$ given the data is derived from the sum of the likelihoods of the data over all models i with a metallicity Z_i in the given range.

The set of spectral indices used to compute the likelihood is the one introduced by Gallazzi et al., 2005, namely three (mostly) age-sensitive indices ($D4000_n$), Hβ and $H\delta_A + H\gamma_A$) and two (mostly) metal-sensitive composite indices that show minimal dependence on α-element abundance relative to iron-peak elements (Mg_2Fe] and [MgFe]′).

The spectral library is built based on the SSP spectra provided in the latest revision of the Bruzual and Charlot, 2003 (thereafter BC03), stellar population synthesis models adopting the MILES spectral libraries (Sánchez-Blázquez et al., 2006; Falcón-Barroso et al., 2011) with a Chabrier, 2003b initial mass function. As for the star-formation histories (SFHs) we adopt a Sandage, 1986 model with random bursts:

$$\begin{aligned} SFR(t) &= \frac{(t-t_0)}{\tau} \exp\left(-\frac{(t-t_0)^2}{\tau^2}\right) \\ &+ \sum_{j=1}^{N_{\text{burst}}} A_j \, \delta_{\text{Dirac}}((t-t_0) - t_{\text{burst},j}), (t > t_0) \end{aligned} \tag{2.1}$$

where τ is the time of the maximum SFR in the continuous component, and A_j and $t_{\text{burst},j}$ are the integrated intensity (relative to the integral of the continuous component) and the time of the instantaneous bursts. All these parameters as well as the number of bursts $N_{\text{burst}} \leq 6$ are randomly generated.

Concerning the metallicity, we implement a simple recipe to take its evolution along the SFH into account. Following equation 11 of Erb, 2008 we impose a steady growth of metallicity according to:

$$\begin{aligned} Z(t) &= Z\left(M(t)\right) \\ &= Z_{\text{final}} - (Z_{\text{final}} - Z_0)\left(1 - \frac{M(t)}{M_{\text{final}}}\right)^{\alpha}, \alpha \geq 0 \end{aligned} \tag{2.2}$$

where $M(t)$ and M_{final} denote the stellar mass formed by time t and by the final time of observation, Z_0 and Z_{final} are the initial and final values of stellar metallicity and α is the "swiftness" parameter of the enrichment. Z_{*0} and $Z_{*\,\text{final}}$ are chosen from a logarithmically uniform distribution in the interval 1/50–2.5 $Z_\odot$.

We also implement a dust treatment based on the Charlot and Fall, 2000 2-component interstellar medium (diffuse ISM + birth-cloud, see also da Cunha, Charlot, and Elbaz, 2008).

We adopt a broad range for all random-generated parameters in order to cover a range of SFHs and observable parameters as comprehensive as possible. In fact,

at basically each spaxel we find a best-fit model with reduced $\chi^2 \leq 1$, indicating that our models can reproduce the observations very closely. The input distribution of model-generating parameters translates into non-uniform distributions in the physical parameter space, which however is roughly uniform in *r-band-light-weighted* log(age) between $\sim 5 \times 10^8$ and $\sim 1.5 \times 10^{10}$ years and covers the full range of *r-band-light-weighted* metallicities between $1/50$ and $2.5\ Z_{\odot}$.

Typical errors (i.e. $16^{th} - 84^{th}$ percentile half-range) in $\log(Z)$ are around 0.15 dex in individual spaxels. From Montecarlo simulations which assume the same typical properties of the CALIFA+SDSS dataset we obtain a similar scatter between input and retrieved $\log Z$ (i.e. median value of the PDF) of $\sim$ 0.15 dex. We also quantify possible biases across the age-metallicity plane, which are typically within ± 0.05 dex. Only at the highest metallicities ($Z > 2Z_{\odot}$) there is a clear tendency to underestimate the true metallicity by up to $0.10 - 0.15$ dex, as a consequence of the PDFs being truncated at the high-end of the grid. It must be noted that a significant component of the scatter, between 0.05 and 0.1 dex, is not related to random measurement errors but is systematic and due to the intrinsic degeneracy between the observables and the physical parameters.

To explore the chemodynamical correlations in the galaxies we make use of recent dynamical models of our CALIFA sample. Zhu et al., 2018c constructed triaxial Schwarzschild models (c.f., van den Bosch et al., 2008) of 300 CALIFA galaxies in a uniform way, which simultaneously fit the observed surface brightness and stellar kinematics from the CALIFA survey. The procedure obtains the weights of different orbits that contribute to the best-fitting model. They use the time-averaged radius to represent the size of each orbit; and describe the angular momentum of an orbit by its circularity λ_z, which is defined as the angular momentum around the short axis of the galaxy normalized by the maximum that is allowed by a circular orbit with the same binding energy. The circularity distribution within 1 Re for these 244 galaxies are shown in Zhu et al., 2017; Zhu et al., 2018e. With the best-fitting stellar mass-to-light ratio we can not only estimate a dynamically derived stellar surface mass density, but also the stellar surface mass density maps of each orbital component; the cold, warm and hot orbital components we use here are separated by $\lambda_z > 0.8$, $0.25 < \lambda_z < 0.8$ and $|\lambda_z| < 0.25$, respectively.

2.3 Stellar Kinematic Profiles and Metallicity Gradients

We use the tilted-ring method (Rogstad, Lockhart, and Wright, 1974; Rogstad, Wright, and Lockhart, 1976) to compute radial profiles of a galaxy based on the galaxy's kinematic structure. An axisymmetric galactic dynamic model assumes that besides the system velocity V_{sys}, the disk velocity has three components: the rotation velocity V_{rot}, radial velocity V_{rad} and vertical velocity V_z. In this model, a galaxy's line of sight velocity V_{los} can be written as:

$$\begin{aligned} V_{los}(R, \psi, i) = V_{sys} &+ V_{rot}(R)\cos\psi\sin i \\ &+ V_{rad}(R)\sin\psi\sin i \\ &+ V_z(R)\cos i \end{aligned} \tag{2.3}$$

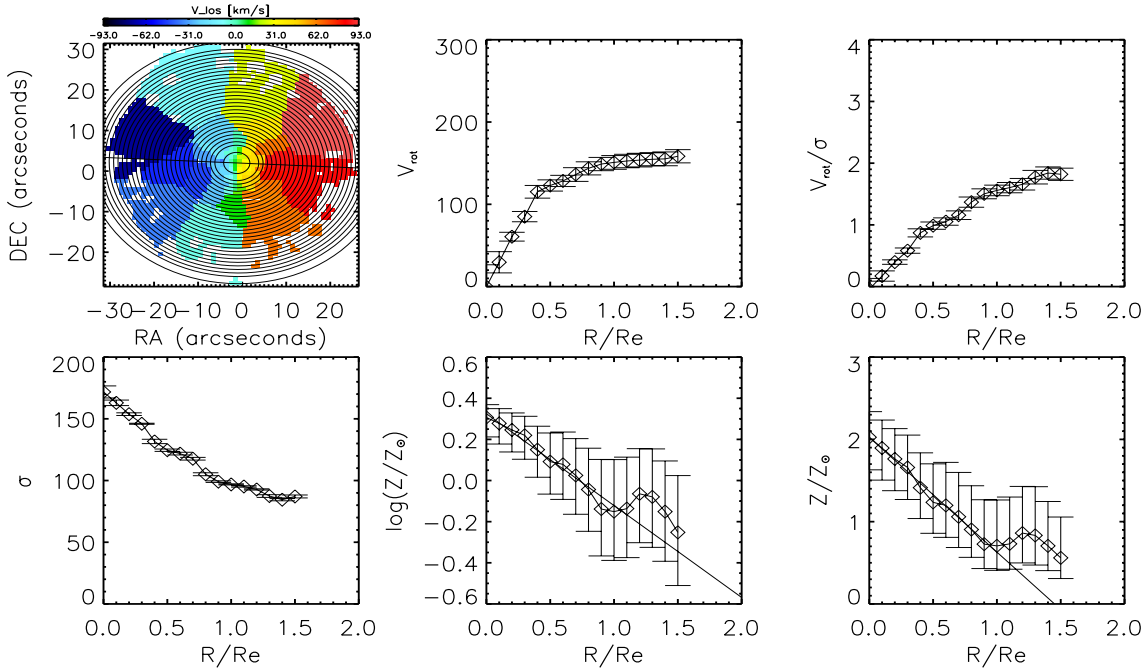

FIGURE 2.1: An example of the V_{los} map based kinematic ellipse system (top left, with color-coding by V_{los}), and derived rotation velocity (top middle), ratio between rotation velocity and velocity dispersion (top right), velocity dispersion (bottom left), logarithmic stellar metallicity (bottom middle) and linear metallicity (bottom right) profiles for NGC0932.

For each point in the polar coordinates system (R, ψ), the three velocity components are projected by the galaxy's inclination angle i.

Using the simplest version of the axisymmetric model with $V_{rad}(R)$ and $V_z(R)$ equal to zero in Eq.(1), we fit the global galaxy parameters (center, PA, inclination) from the V_{los} map. With the best-fit parameters, we can divide the galaxy image into a series of concentric ellipses (see Figure 2.1). Then we apply this ellipse system to other maps including velocity dispersion, log(Z) (and their 84% and 16% confidence maps $\log(Z)_{16\%}$ and $\log(Z)_{84\%}$) to get their radial profiles. We construct the average value of a quantity at elliptical radius R by averaging the spaxels in that annulus. For logarithmic metallicities (log(Z) as well as $\log(Z)_{16\%}$ and $\log(Z)_{84\%}$), we first calculate the linear flux-weighted mean values Z, $Z_{16\%}$, $Z_{84\%}$ from the spaxels within an annulus, then take the log of that value. We do this to ensure that we accurately trace the systematic errors due to e.g. the age-metallicity degeneracy.

We calculate the mean stellar velocity dispersion (σ) value from spaxels within each elliptical ring. The extraction of the rotation velocity (V_{rot}) profile is slightly more complex, because of the existence of non-axisymmetric features (like bars, spiral arms) in the observed data. In order to cope with these detailed morphological structures and perturbations, a harmonic decomposition (HD) method is used in this work, in which we expand the V_{los} into a Fourier series:

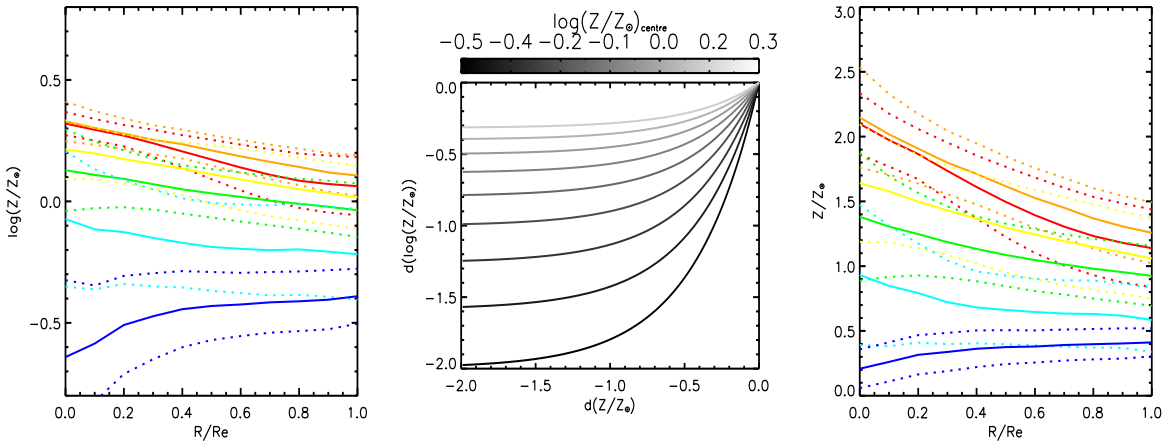

FIGURE 2.2: Average log(Z) (left) and Z (right) profiles of each galaxy morphological type in our sample (solid lines), and standard deviations (dashed lines). Profiles are color-coded by galaxy morphological types: E (Red), S0 (Orange), Sa (Yellow), Sb (Green), Sc (Cyan) and Sd (Blue). The middle panel is the relation between log(Z) gradient and Z gradient for galaxies of different central metallicities. High mass galaxies, with high central metallicity, will show a smaller log(Z) gradients, conversely lower mass galaxies with low central metallicities will show a larger log(Z) gradients at fixed linear metallicity gradient, solely due to the mathematical logarithm transform.

$$V_{los} = V_{sys} + \sum_{n=1}^{k} [c_n(R)\cos(n\psi) + s_n(R)\sin(n\psi)]\sin i \tag{2.4}$$

Here the c_1 term represents V_{rot} while s_1 represents V_{rad}. Compared with an axisymmetric model, this method is better in fitting galaxies with non-axisymmetric features (Sakhibov and Smirnov, 1989; Canzian, Allen, and Tilanus, 1993; Schoenmakers, Franx, and de Zeeuw, 1997; Fridman and Khoruzhii, 2003; Krajnović et al., 2005), which is important when studying the impact of migratory processes. In this work, we fit the V_{rot} at each elliptical annulus by using the HD method from Fathi et al., 2005 .

As the kinematic maps (V_{los}, σ) were Voronoi binned into several superspaxels to increase S/N (see the top left panel of Figure 2.1), for each galaxy, we computed the ellipse system 200 times, each time giving a Gaussian distributed perturbation to the V_{los} map, with standard deviation taken from the V_{los} error map. Then for that ellipse system, we derive all the profiles as described above. The final profile and uncertainties due to stellar population parameters, are taken as the median of the 200 Z, $Z_{16\%}$ and $Z_{84\%}$ profiles. While, the kinematic profiles and uncertainties are taken from the average and standard deviations of the 200 $V_{rot}$and σ profiles.

Our method traces the profiles based on the rotation plane, which may produce differences compared to gradients extracted along the luminosity major axis, if the two planes are not overlapping with each other. However, as we are not considering interacting galaxies, and (Barrera-Ballesteros et al., 2015) has shown that around

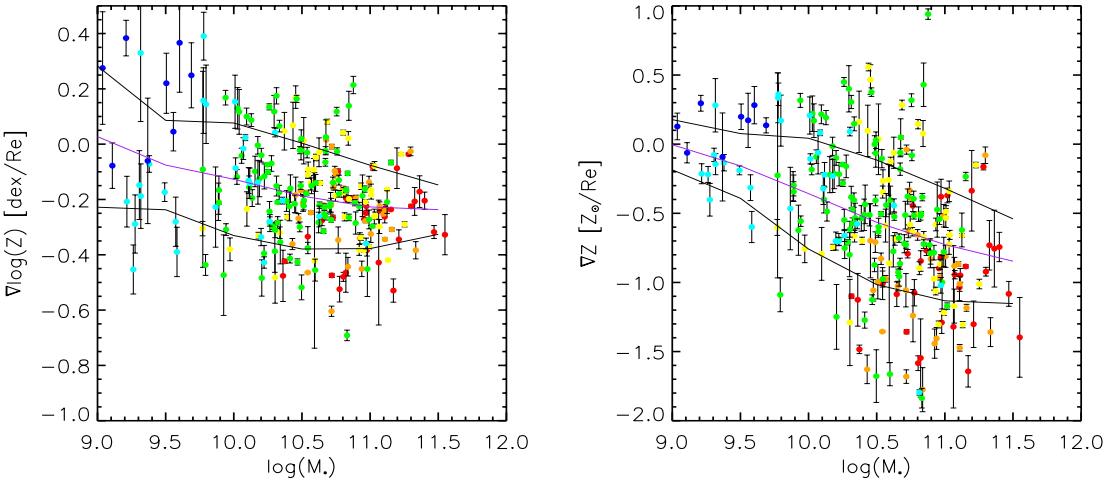

FIGURE 2.3: The log(Z) and Z gradients against galaxy stellar mass, color-coded by galaxy morphological type as in Figure 2.2. Black and grey lines are their mean and $1-\sigma$ intrinsic scatter at each mass range.

90% of non-interacting CALIFA galaxies show differences between their photometric and kinematic position angles of less than 22 degrees, here all galaxies show well defined angular momentum vectors which will be quite similar to the photometric position angles. This is backed up by our Schwarzschild dynamical models (Section 2).

The profiles are derived through the geometry shape of the galaxies' (ellipse systems), which are determined by galaxy's kinematic map (rotation). This means our method would not apply to galaxies with no clear rotation signatures. The E-type galaxies in our sample still contain significant rotational components to permit this. Some galaxies may show different rotation planes at different radii, which could potentially increase the uncertainty. However again, the photometric and kinematic position angle alignment found throughout non-interacting galaxies in CALIFA, suggests the ellipse system will not be significantly different using our method compared to photometrically defined ellipse systems.

2.3.1 Fitting metallicity gradients

To fit the metallicity gradients (∇Z), for each of the 200 trials, we linearly fit the Z profile within certain radial ranges (1 Re) in units of Re with the weighted linear least squares routine MPFIT in IDL (Markwardt, 2009). The weights used in fitting the linear gradient, came from the $Z_{16\%}$ and $Z_{84\%}$ uncertainty profiles in each trial. The final value of the gradient (∇Z), and uncertainty comes from the median and standard deviation of the 200 fits. Thus, the final uncertainty not only takes into account the uncertainties of the metallicity maps but also the uncertainty of the geometrical parameters of the galaxy.

We fit the metallicity gradients from both linear Z profiles and log(Z) profiles. In this project, we focus on the gradients computed from the linear Z profiles (∇Z). These show the difference in metal fraction from the inside to the outside of the

galaxy - as opposed to gradients of log(Z), which represent the ratio of metal fractions. While neither is objectively superior, the former may show a more intuitive visual accounting of the absolute change in metal fraction across galaxy disks when comparing galaxies of a range of masses and absolute metallicities. For example, the value of a log(Z) gradient for a high metallicity, massive galaxy, may be numerically smaller than that of a low metallicity, low mass galaxy - even if the radial difference in Z (linear gradient) is the same. However the primary reason we use the linear Z gradients in this work, is to test the correlations between local metal fraction and local density and kinematics - which is not as easily accomplished with ratios. To conceptualize the differences and aid comparison to previous works, we show comparison of the *profiles* in log(Z) and linear(Z) in Figure 2, with the middle panel showing the numerical equivalence between *gradients* measured on each profile. In addition, given the range of physical galaxy sizes in our sample, we compute the gradients with respect to their relative effective radius, Re.

We note that, all our galaxies have profiles extending to 1 Re and some of them even beyond 1.5 Re. In this paper, unless stated otherwise, we fit the gradient within 1 Re. In certain figures, we also linearly fit the profile between 0.5 to 1.5 Re and label these cases explicitly.

2.4 Results

The left panel of Figure 2.2 shows the average log(Z) profiles for galaxies of different morphological types in our sample. In general, early type galaxies (red) are more metal-rich than late type galaxies (blue), due to the mass-metallicity relation and mass-morphology relations (e.g., González Delgado et al., 2014). It is clear that late type galaxies tend to have a larger diversity in profiles than earlier type galaxies - in agreement with results from gas-phase metallicity gradient studies (Tissera et al., 2016a). The right panel of Figure 2.2 shows the average profiles for different morphological types in linear Z. Compared to the log(Z) profiles, the early type galaxies tend to have steeper Z profiles, and the linear profiles don't show strong decrease in diversity for early type galaxies.

We plot the gradients in both logarithmic and linear metallicity against galaxy stellar mass in Figure 2.3. Though we are mostly focusing on galaxies' linear metallicity gradient in this project, we still calculate the log(Z) gradients (left panel) to show the comparison with other works. The log(Z) gradients show a relatively weak correlation with mass, and an intrinsic scatter which decreases for massive/earlier type galaxies. This is in agreement with previous works on log(Z) gradients in morphologically diverse surveys (González Delgado et al., 2015; Zheng et al., 2017b). Also the correlation between stellar mass and metallicity gradients for late-type galaxies agrees with studies in MANGA galaxies (Goddard et al., 2017b).

The left panel of Figure 3 plots the corresponding linear metallicity Z gradient against stellar mass, which shows a steeper anti-correlation with galaxy mass, and nearly constant intrinsic scatter in gradient value. The difference between the two plots is purely due to the logarithimic effect.

The left panel of Figure 2.4 shows the Z gradients measured within 1 Re, as a function of morphological type. We find a clear correlation between metallicity gradients and galaxy morphological type: the Z gradient becomes steeper as we move

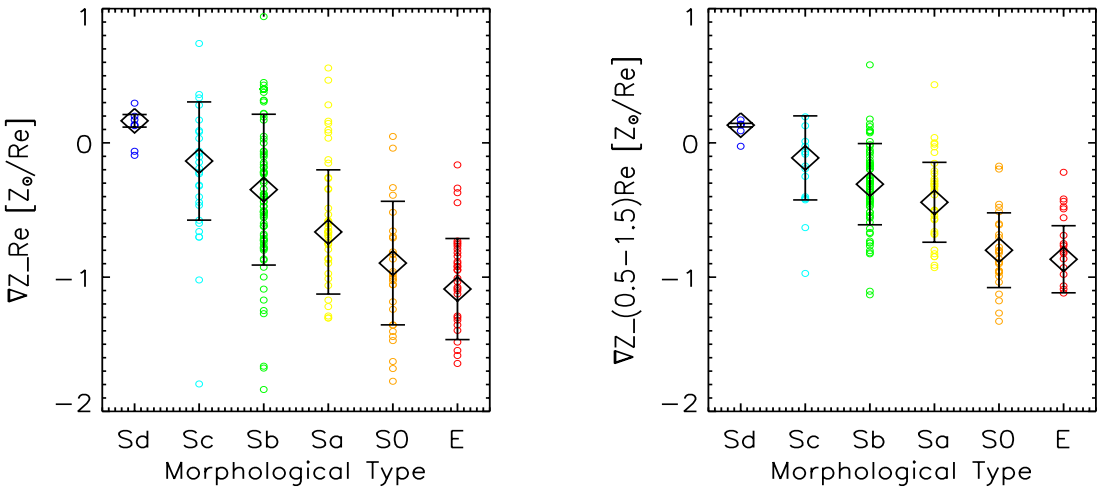

FIGURE 2.4: Radial stellar metallicity gradient ∇Z within 1 Re (left) and (0.5-1.5) Re (right) against different morphological types. Error bars show the average and standard deviation after the volume correction of the CALIFA sample.

towards early type galaxies. By comparing to Figure 2.3, we see that galaxies with different Z gradients are more segregated by morphology than stellar mass.

As in the very central part of galaxies there may exist different structures (Bar, bulge ...) for different morphological types, which may consist of quite different stellar populations (especially in terms of age), this may influence the correlation between Z gradients and morphological types. To rule out this possibility, we also calculate the Z gradients from 0.5 to 1.5 Re (the right panel of Figure 2.4) to test the dependence of this trend on the central substructures. When the central regions are removed, the gradients on average become flatter, though the trend between Z and morphological type still remains equally strong. This suggests the correlation between the Z gradients and morphological type is more likely a general trend with mass concentration than a result of substructures of different formation epochs.

2.5 Discussion

2.5.1 Understanding the morphology and Z gradient correlations

The sample of CALIFA galaxies analyzed here shows a strong correlation between linear metallicity gradient (∇Z) and galaxy morphological type. The most obvious differences between different morphological types should be their average stellar metallicities (due to the morphology-mass and mass-metallicity relations, see also Figure 2.2), their mass/light concentrations (e.g., Holwerda et al., 2014) and their dynamical properties (Zhu et al., 2017).

The right panel of Figure 2.2 shows a clear separation between different galaxy types; as earlier type galaxies (red) are more metal-rich than late type galaxies (blue) and have stronger gradients. This suggests a correlation between a galaxy's average metallicity $< Z/Z_{\odot} >$, and linear metallicity gradient ∇Z. To further explore this

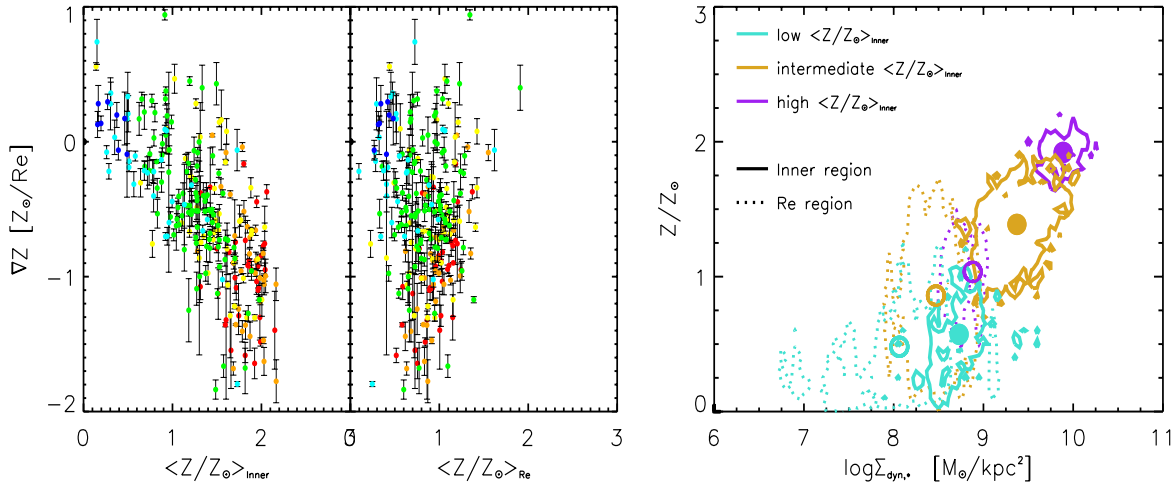

FIGURE 2.5: *Left*: Metallicity Z gradient against average stellar metallicity $<Z/Z_{\odot}>$ for galaxies in an inner region within 0.2 Re (left) and in a Re region within 0.8-1.0 Re (middle). Colour coding is by galaxy morphological type, as in Figure 2.2. *Right*: Local metallicity Z against dynamically derived local surface mass density; contours cover spaxels with densities greater than 0.3 times the maximum density, for the inner region within 0.2 Re, (solid lines and filled circles as mean points) and Re region within 0.8 - 1.0 Re, (dotted lines and open circles as mean points). Here different colors correspond to galaxies of different average central metallicity Z; low ($< Z/Z_{\odot} >_{\mathrm{Inner}} \sim$ 0-0.9; turquoise), intermediate ($< Z/Z_{\odot} >_{\mathrm{Inner}} \sim$ 0.9-1.8; goldenrod) and high ($< Z/Z_{\odot} >_{\mathrm{Inner}} \sim$ 1.8-4; purple).

trend, we can ask what regions of the galaxy are changing to produce the morphological type - ∇Z correlation. For each galaxy, we calculate their average Z within two different regions: an Re region, between 0.8-1.0 Re (relatively outer); and an inner region, within 0.2 Re. The left panel of Figure 2.5 shows the Z gradient against these two average metallicities.

Comparing the two regions, we see that the average metallicity of the *inner region* (left) shows very similar correlations with ∇Z as those seen in Figure 2.4. This suggests the central Z is tightly linked to the strength of Z gradients and a galaxy's morphological type. Conversely, the Z gradient shows no correlation with the metallicity of a galaxy's region around the effective radius. This result is consistent with the average Z *profiles* for galaxies of a given morphological type shown in the right panel of Figure 2.2 - the inner regions are enriched more efficiently with respect to the outskirts in early type galaxies.

The interplay between the mass dependence of a galaxy's morphological type, central concentration, and average metallicity allows for an intuitive description of metallicity gradients when viewed in linear Z space. Previous studies have demonstrated the existence of a *local* mass, gas metallicity, star formation relation (e.g., Rosales-Ortega et al., 2012), hinting that local metal enrichment is the result of integrated star formation/stellar mass accumulation.

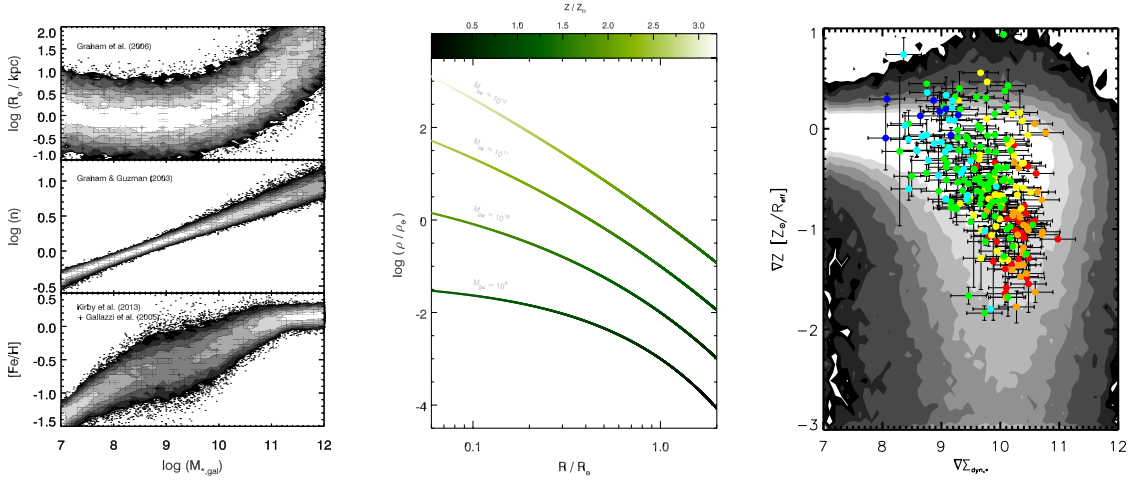

FIGURE 2.6: Left: empirical galaxy scaling relations of size, Sérsic index and stellar metallicity, versus galaxy stellar mass. Middle: Scaling relations are combined to give representative mass density and metallicity profiles for galaxies of different total stellar masses (color-coded by locally predicted galaxy metallicity). Right: Predicted metallicity gradients from the empirical model (contours) naturally accounts for the trend and scatter between stellar mass density gradient and metallicity gradient seen in our data (points color-coded by galaxy morphological type, as in Figure 2.2).

In order to explore a correlation between the local mass density and Z, we divide our sample of galaxies into 3 subgroups according to the average metallicity of their inner regions: (Low: $Z \sim$ 0-0.9, Moderate: $Z \sim$ 0.9-1.8, High: $Z \sim$ 1.8-4). For each group, we compare the galaxies' local metallicities in the inner, and Re regions, with the corresponding dynamically derived stellar surface mass density from Schwarzschild modeling. For each subgroup we plot all the spaxels which lie within inner ($0.0 - 0.2$ Re; solid lines) and outer Re ($0.8 - 1$ Re; dotted lines) regions of all galaxies, in this stellar surface mass density-metallicity parameter space. The right panel of Figure 2.5 shows density contours (greater than 0.3 times the maximum density) for spaxels in the outer regions (dotted contours) and inner regions (solid contours) of galaxies with different central metallicities.

These distributions follow a clear *local* mass-metallicity relation, with Re regions being more metal-poor and having lower surface mass density than the inner regions. Importantly, the Z and surface density *difference* between a galaxy's inner region and Re regions, increases as the average inner Z (and therefore galaxy mass) increases.

In this exercise we have used the dynamically derived stellar surface mass density $\Sigma_{dyn,*}$, which is computed independent of the stellar populations profiles. Similar results for the correlations between local metallicity and stellar surface mass density are found by replacing $\Sigma_{dyn,*}$ with the stellar surface mass density derived via stellar population synthesis modelling from the available spectro-photometry (Zibetti et al., in prep.).

The right panel of Figure 2.5 implies that as a galaxy's local regions also follow the mass$-$metallicity relation, we would expect a steeper Z gradient when there is a

steeper surface mass density gradient. Here we define a dynamically derived stellar surface mass density gradient $\Sigma_{dyn,*}$ as:

$$\nabla\Sigma_{dyn,*} \equiv \log(\Sigma_{dyn,*(r=0)} - \Sigma_{dyn,*(r=Re)}) \tag{2.5}$$

The right panel of Figure 2.6 explicitly quantifies the link between $\nabla\Sigma_{dyn,*}$ and stellar Z gradients, and shows that the Z gradients become steeper as the mass gradients increase in magnitude, though with considerable scatter. In general, early type galaxies with steeper Z gradients also have proportionally higher central Z and steeper mass density gradients, reaffirming the relations, between Z gradient, mass concentration and morphological type.

2.5.2 Empirical model

This simple picture, that stellar metallicity gradients are most clearly observationally connected to, and result from, the time-integrated differences in stellar mass buildup between the inner and outer parts of a galaxy, can be crudely tested using independent empirical scaling relations for galaxy populations. We begin by considering observed relations between galaxy stellar mass and light profile (Sérsic index n, Graham, Jerjen, and Guzmán, 2003), stellar metallicity (Kirby et al., 2013), and effective radius (Graham et al., 2006), as shown in the left panel of Figure 2.6.

In the following exercise we stochastically draw properties which a galaxy of mass M_* would have, from these scaling relations. The mass dependent relations are given a scatter representative of the observations: $\sigma_{logRe} = 0.37$ dex, $\sigma_{logn} = 0.05$ dex (van der Wel et al. 2014), and the $1-\sigma$ spread on [Fe/H] as a function of mass directly from (Gallazzi et al., 2005) and (Kirby et al., 2013).

For a galaxy of a given mass, we use the effective radius and Sérsic index to compute a representative Einasto profile of the 3D stellar mass distribution ($\rho(r)$) for that galaxy. In order to link the global metallicity relations with the local structural relations, at any point r on the radial mass density profile, $\rho(r)$, we compute the mass an idealized spherical galaxy would have if it was this *average* density and size, i.e. $M_*(r) \propto \rho(r)r^3$. That idealized galaxy mass, and thus the corresponding region at r in the composite model galaxy, is then given a homogeneous metallicity following the observed galaxy global mass-metallicity relation (e.g., Gallazzi et al., 2005). The composite galaxy profile is constructed by repeating this exercise at all radii - and the resulting profile can have a metallicity and density gradient computed as per our observations.

The construction of a mock galaxy whose local properties are set by global scaling relations, is physically justified by observations which suggest that the outer regions of disk galaxies are forming stars and enriching chemically in a comparable way to lower mass dwarf galaxies. Hence the local sub-galaxy which is constructed to have radius r, will only represent a local shell of that corresponding metallicity at $r + dr$ in the final composite galaxy.

This simple exercise combines galaxy scaling relations to allow for a coarse estimate of local metallicity, but should not be over-interpreted, as it is essentially relying on dimensional analysis to produce a stochastic prediction for where *populations* of galaxies may lie in the $\nabla\Sigma_{dyn,*} - \nabla Z$ plane.

The middle panel of Figure 2.6 shows these representative mass density profiles for galaxies of different masses, and colour coded by local metallicity. The metallicity changes in these profiles are in qualitative agreement with the profiles in Figure 2.2. The predicted quantitative correlation between mass density gradient and metallicity gradient using only these empirical relations is shown in the right panel of Figure 2.6 as the contours. The scatter in the $M_* - n$, M_*-Re and mass-metallcity relations accounts for nearly all the observed intrinsic scatter in the ∇Z - $\nabla \Sigma_*$ relation. We suggest that the larger scatter in the ∇Z gradient versus total mass (Figure 2.3), is a consequence of the fact that the establishment of a metallicity gradient is a *local* phenomena in galaxies. Our empirical model also produces some galaxies with positive slopes, which are observed in high percentage for our late type galaxies. We will discuss the possible origin of these objects in Section 5.5.

It is rather surprising that such a simple dimensional analysis exercise based on galaxy structural and global chemical relations does a reasonable job in reproducing the average trend and scatter in ∇Z - $\nabla \Sigma_*$. It is unclear whether this is due to some fundamental simplicity which links local and global galaxy relations, for example a self-similar statistical form for how galaxies chemically enrich (e.g., Oey 2000; Leaman 2012; Hartwick 2015). However, it should be kept in mind that the empirical model may be reproducing the broad trends of this parameters space out of coincidence, and the ingredients are not necessarily causal in determining a galaxies structural and chemical gradients. This must surely be true in some sense for galaxies on an individual scale, given the significant number of mechanisms which are not incorporated into the model (e.g., AGN/star formation driven winds, radial migration, mergers). Nevertheless, this simple model can provide a starting point for continued and more detailed investigation of such chemodynamical relations.

2.5.3 Chemodynamic spatial signatures

Due to the wealth of kinematic information in CALIFA, and dynamical models for our galaxies (Zhu et al. 2017), we are able to investigate if any dynamical properties appear to be stronger causal factors in setting the stellar population gradients. This is motivated by some previous works on low mass galaxies, for example Schroyen et al., 2013a used simulations to investigate the metallicity gradients of dwarf galaxies. Their results suggested that metallicity gradients can be buildup efficiently during the evolution of non-rotating dispersion-dominated dwarf galaxies, as low angular momentum allows more gas to concentrate in a galaxy's central regions, leading to proportionally more star formation.

While this scenario is in agreement with some local group dwarf galaxies' observations (e.g., Leaman et al., 2013; Ho et al., 2015; Kacharov et al., 2017)), the gradient differences also span differences in mass SFH and environment as well as angular momentum, making a direct causal link between dynamics and the metallicity gradients unclear. More relevant for this study is the unknown dependence of this mechanism on host galaxy mass. Given the orbital decomposition that our Schwarzschild models provide, we can directly look for correlated behaviour of chemical and kinematic properties of our sample of higher mass galaxies.

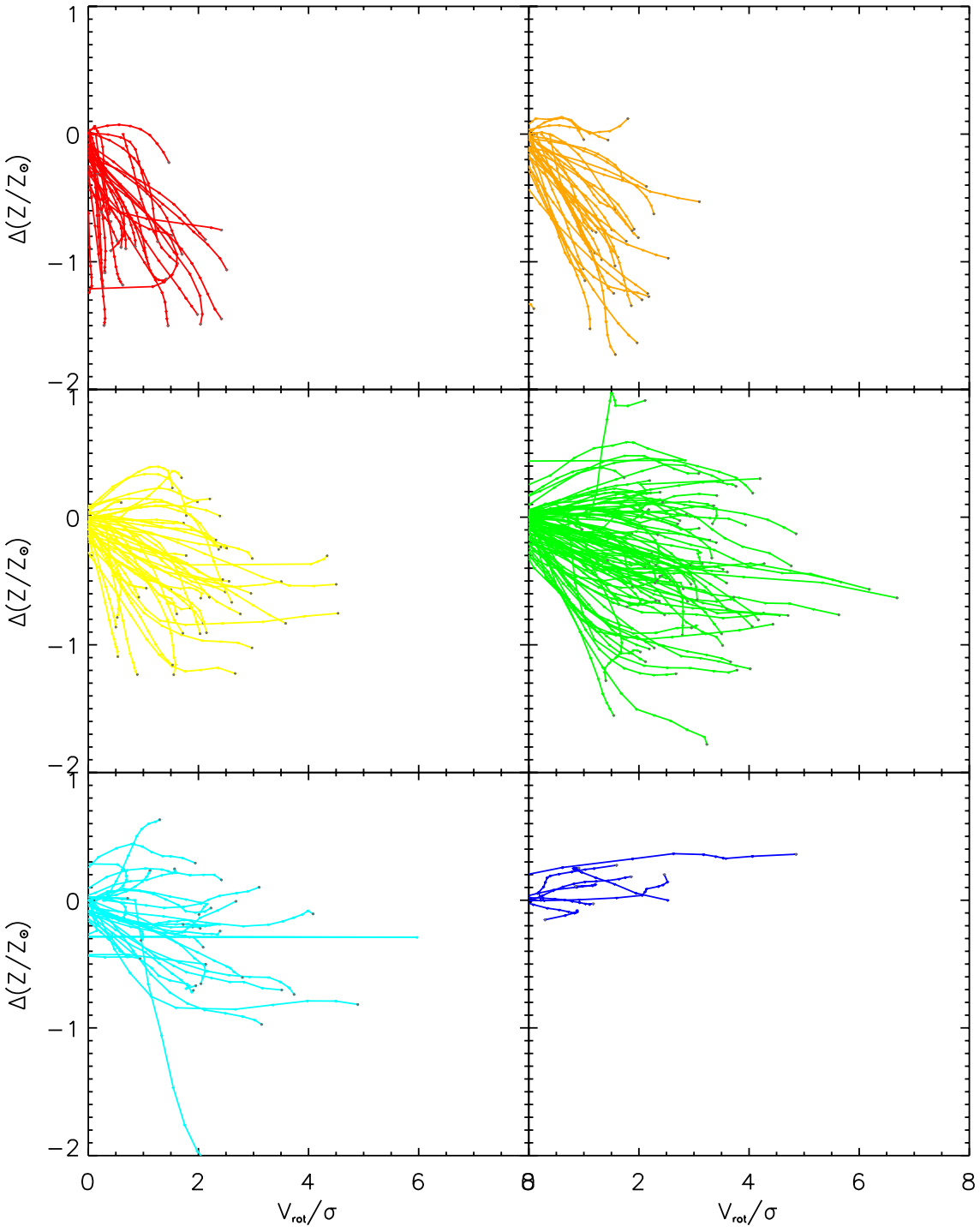

FIGURE 2.7: Metallicity Δ(Z) against V_{rot}/σ profiles for different galaxy types, each profile line represents one galaxy's Z and V_{rot}/σ values at different radii (from 0 to 1 Re). Color coding is by galaxy morphological type, same as in Figure 2.2.

Figure 2.7 shows a radial profile for each galaxy's V_{rot}/σ and ΔZ values, with

V_{rot}/σ increasing from inside to outside. Different galaxy types show some separation in the figure, as early type galaxies tend to have steeper gradients and low angular momentum, while later type galaxies show an increase in diversity of their tracks, but on average a flatter set of metallicity profiles extending to higher V_{rot}/σ. Unlike previous studies for dwarf galaxies, the higher mass galaxies likely have a greater number of factors influencing their evolution than the dwarf galaxies (bars, spiral arms, higher merger rates), and indeed a diverse set of tracks is evident.

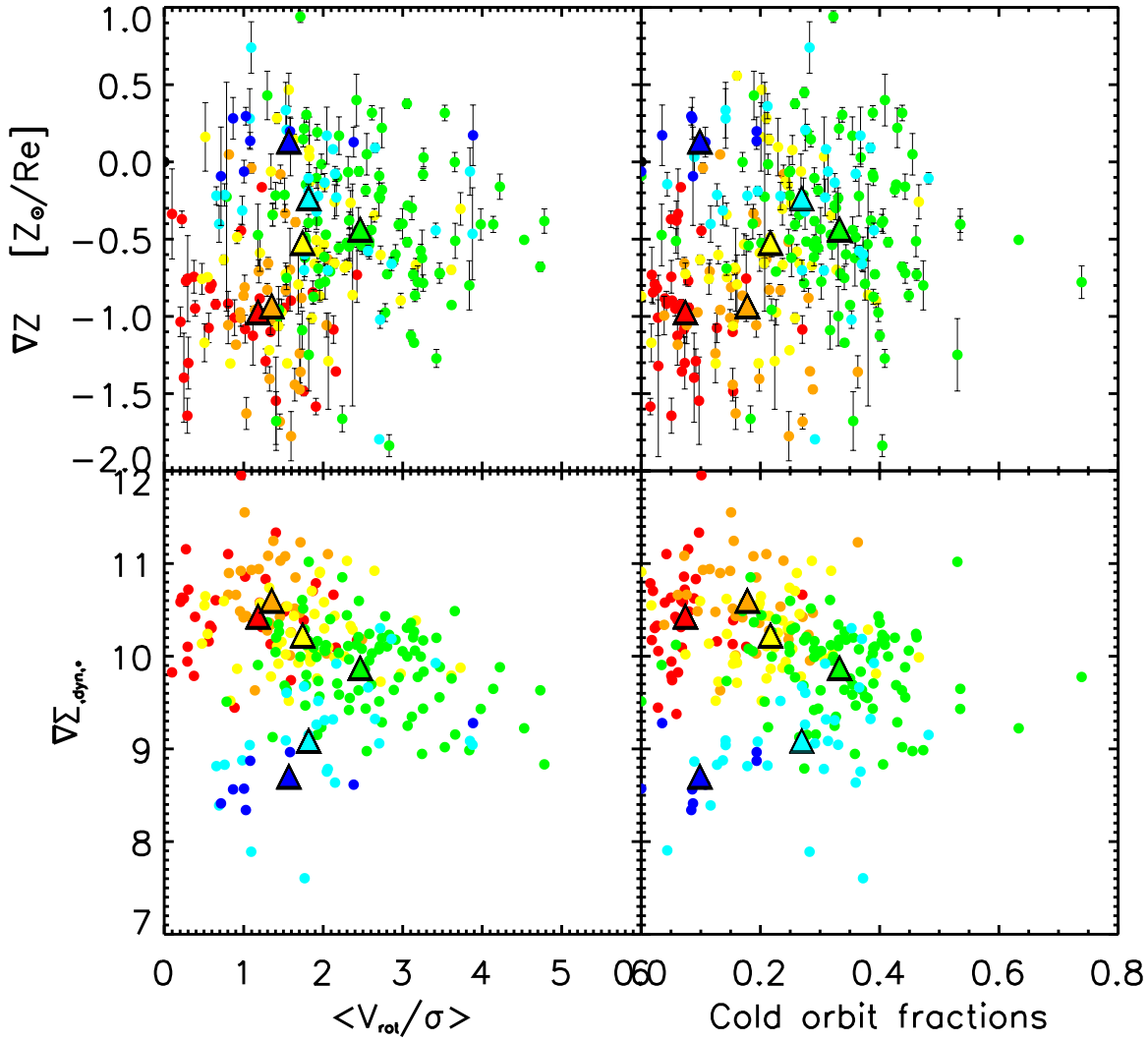

FIGURE 2.8: Top: Metallicity gradient against galaxies' angular momentum (average V_{rot}/σ between 0.5-1 Re) (left) and cold orbit mass fractions (right) of our 244 GALIFA galaxies. Bottom: Central mass concentration (stellar surface mass density gradient) against galaxies' angular momentum (left) and cold orbit mass fractions (right), triangles are the mean points of galaxies with each morphological types. Colour coded by galaxy morphological type, as in Figure 2.2.

To quantify correlations between angular momentum and metallicity gradients in our sample, we use the average V_{rot}/σ (between 0.5-1 Re) and the disky cold orbit mass fraction as two indicators of a galaxy's angular momentum. The top panels of

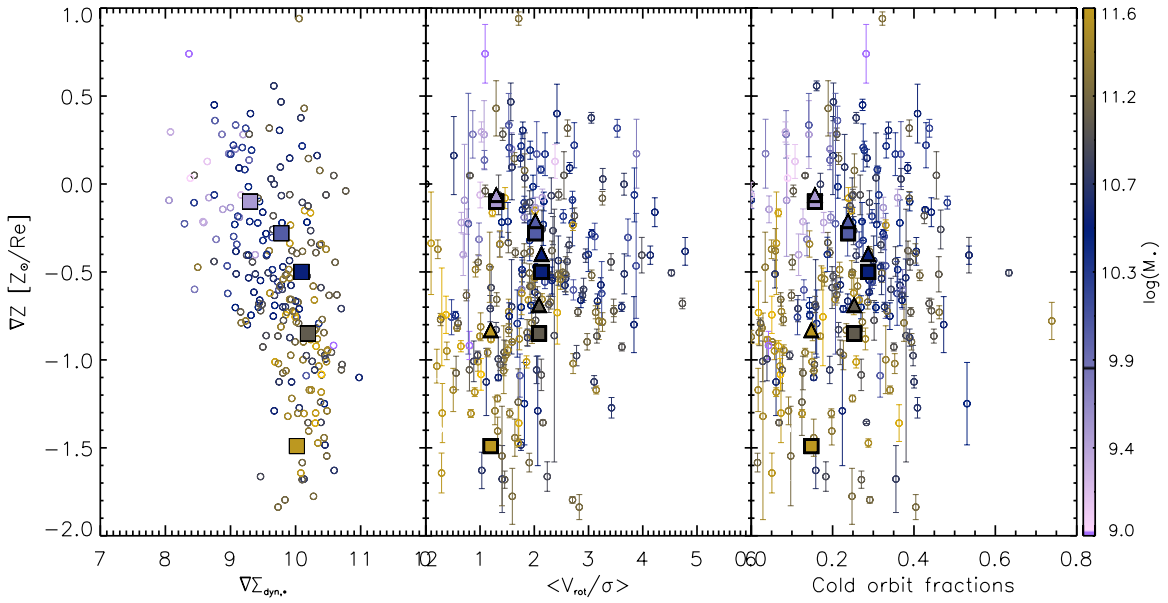

FIGURE 2.9: A repeat of Figure 2.6 right panel and the bottom panels of Figure 2.8. Left: shows the correlation between $\nabla\Sigma_{dyn,*}$ and ∇Z, Middle and right panels: the matallicity gradient against V_{rot}/σ and cold orbit fraction, but color coded by galaxies' stellar mass. Triangles are the mean points of galaxies within each mass bins, blocks are the predictions using the empirical model.

Figure 2.8 shows the metallicity gradients against these angular momentum proxies. It is evident that both early and very late type galaxies tend to have low angular momentum, but show different metallicity gradients. From type Sd to type Sb galaxies, as the metallicity gradient becomes steeper, the angular momentum increases, until a turning point at Sb. From type Sb to type E, the metallicity gradient steepens, while the angular momentum starts to decrease. Similar trends are seen in the bottom panels of Figure 2.8 when replacing metallicity gradients with stellar surface mass density gradients.

To better understand the role of mass concentration and angular momentum in setting metallicity gradients, we divide our galaxies into 5 groups according to their stellar mass $\log(M_*)$ from 9 to 11.5 with 0.5 dex wide bins. We then get mean locations of each mass bin in ∇Z and V_{rot}/σ or cold orbit fraction planes (shown as triangles in middle and right panels of Figure 2.9). With the empirical model we can compute the *average* $\nabla\Sigma_*$ and ∇Z of model galaxies in the corresponding mass bins, and we show these as squares in the left panel of Figure 2.9. In general the average mass bins for the model galaxies follow the average observed relation - however for the highest mass bins, the model galaxies show steeper Z gradients (at fixed density gradient) than what are observed in our CALIFA sample. This could speak to additional factors not included in our simple model (such as AGN driven outflows, or satellite galaxy mergers) altering the density and metallicity profiles of these galaxies. An interesting test with larger surveys would be to look at an environmental dependence of the $\nabla\Sigma_* - \nabla Z$ high mass regime to see if any systematic movement is apparent

The projections of the average model galaxies into the angular momenta parameter space is shown in the middle and right panels of Figure 2.9. As we don't explicitly compute an angular momentum observable for the model galaxies, we have associated the mass bins to the same angular momentum as is observed for galaxies of that mass. Compared to the observed mean chemo-dynamical values (triangles), the predicted points clearly show a similar mass dependence - suggesting that angular momentum is not a unique predictor of metallicity gradient, and that the primary factor in predicting the gradients should be the mass density profile. This is different from previous studies of low mass range ($M_* < 10^{10.5}M$) galaxies, where it was found that higher angular momentum galaxies tended to have steeper gradients. This suggests the role of angular momentum in preventing central gas build-up and the role of outer perturbations may not be a causal formation process for metallicity gradient in higher mass galaxies. The turning point around Sb galaxies in this parameter space is perhaps due to the correlation between angular momentum and mass - as beyond this mass, mergers likely alter the stellar angular momentum in galaxies. However, we must be careful as the current dynamical state is not necessarily representative of all epochs in the galaxies' evolution.

Thanks to our Schwarzschild models we are in the unique position to study any correlations between metallicity gradient and the surface mass density gradients of different dynamical components - which may give some insight into which epoch or assembly method imparted the present day metallicity profiles. We proceed by computing the stellar surface mass density profiles from *just* the cold, warm or hot orbital components. Differing behaviors might hint at a time dependence of gradient formation - as hot orbital populations may be composed of the earliest generations of stars, while cold orbital populations represent newly formed young stars. Figure 2.10 shows the stellar surface mass density gradients of cold $\nabla\Sigma_{dyn,*,(cold)}$, warm $\nabla\Sigma_{dyn,*,(warm)}$ and hot $\nabla\Sigma_{dyn,*,(hot)}$ orbit components against the metallicity gradients within Re.

In Figure 2.10, we see a progression where the ∇Z - $\nabla\Sigma_*$ correlation from Figure 2.6, becomes more evident as we look at hotter orbit densities. It appears that regardless of the final angular momentum of the galaxy, the density profile becomes established in conjunction with the formation or heating of the stars that make-up the hot orbits.

This could suggest that the density gradients of the coldest component may have large stochastic spatial variations due to young stars forming inhomogeneously out of a self-enriching ISM. Then over time a superposition of these radial distributions may statistically drive to a more regular ∇Z - $\nabla\Sigma_*$ correlation. However this again suggests that while there is a clear interconnection between: 1) the stellar mass build-up and dynamical state of a galaxy, and 2) the stellar mass build-up and the metallicity gradient, that it is not yet clear that present day dynamical structure has a causal link with the strength of metallicity gradients - at least within one Re and for galaxies in this mass regime. This link may be observationally difficult to untangle as the hot and warm orbits can simultaneously trace two different processes (e.g., stars born from a dynamically cooling ISM, and stars which were dynamically heated after their birth (Leaman et al., 2017).

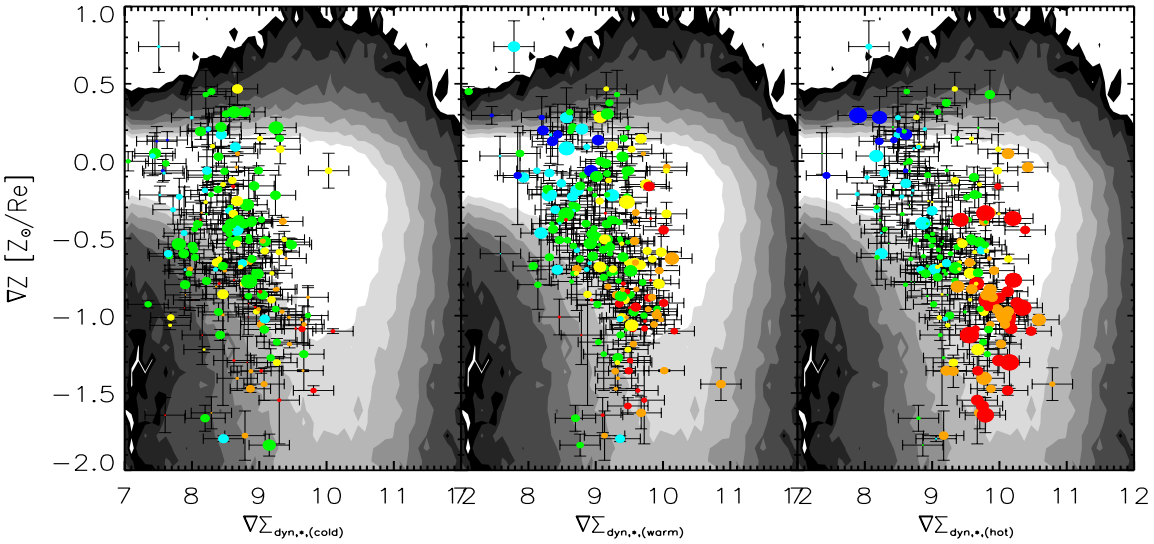

FIGURE 2.10: Metallicity gradient within 1 Re against stellar surface mass density gradients of different stellar orbit components: cold orbits $\nabla\Sigma_{dyn,*,(cold)}$ (left), warm orbits $\nabla\Sigma_{dyn,*,(warm)}$ (middle) and hot orbits $\nabla\Sigma_{dyn,*,(hot)}$ (right), . Symbol size represents the mass fraction of the respective components. Grey contours are the total ∇Z - $\nabla\Sigma_*$ relation from our model. Colour coded by galaxy morphological type, as in Figure 2.2.

2.5.4 Radial migration

Several theoretical works have demonstrated that radial migration of stars within a galaxy's disk could be a possible channel to flatten the radial stellar population gradient (e.g., Roškar et al., 2008; Loebman et al., 2016; El-Badry et al., 2016a). Clear observational signatures of radial migration remain hard to achieve however. Recently, Ruiz-Lara et al., 2017 studied profiles that extend to the very outer disk regions of a subset of the CALIFA sample presented here, and found that galaxies which have up-bending surface brightness profiles (e.g., disk surface density profiles which increase beyond some radius in the outer regions), show flatter stellar metallicity gradients in these regions - with very small statistical differences. While they focus on the outer regions of disks, given that spiral arms and bars should be found in high mass, cold disk galaxies, we can ask if our sample shows any second-order trends in the metallicity gradients that could be ascribed to radial migration.

To quantify this, in the top left panel of Figure 2.11 we show our stellar metallicity gradients against bar strength classifications of galaxies in our sample. There is a correlation between bar type and metallicity gradient in that galaxies with a clear bar feature show flatter Z gradients on average, but the correlation is quite weak compared to the scatter (see also Ruiz-Lara et al., 2017). The top middle and right panels explore the relationship between the metallicity gradient and the type of spiral pattern, and the number of spiral arms for the spiral galaxies in our sample. A signature might be expected here as grand design or two-armed spirals should have proportionally more mass in the arms, leading to a stronger scattering of stars in the disc. Just like the bar-stellar metallicity gradient relation in the left panel, we

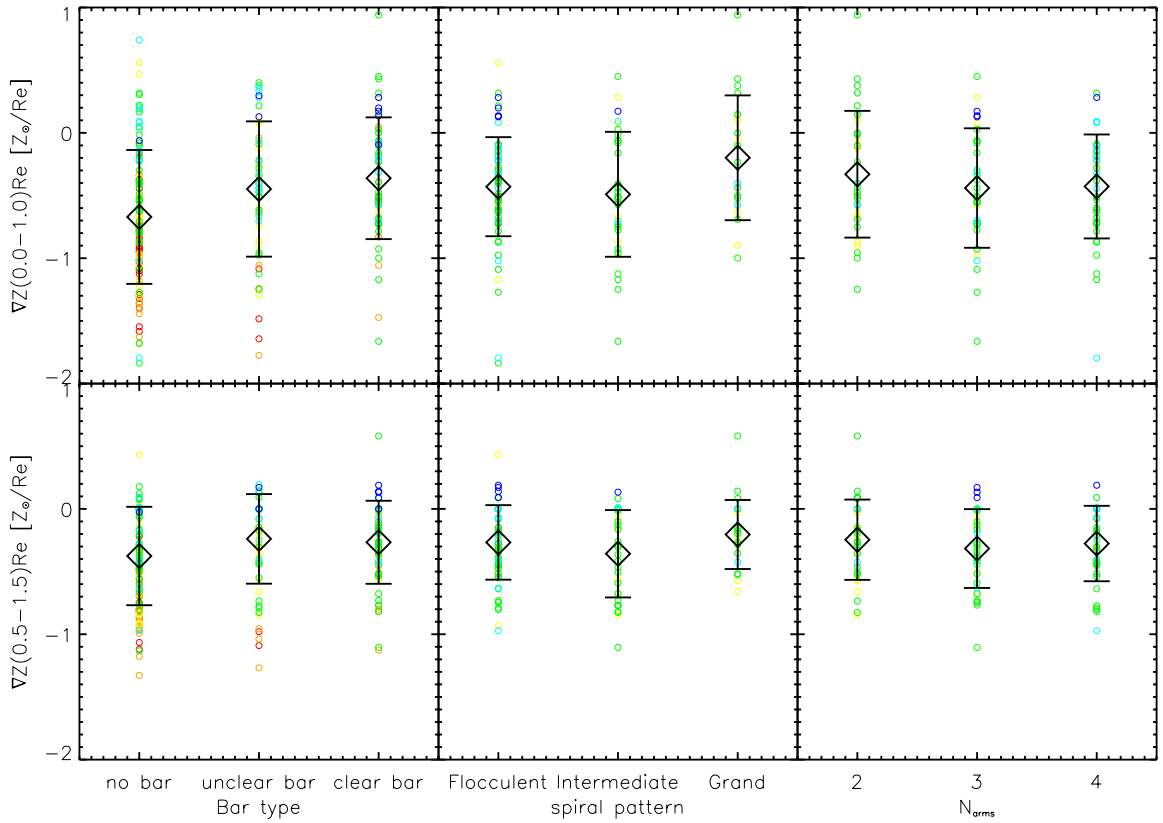

FIGURE 2.11: Metallicity gradient within 1 Re (top) and between 0.5 - 1.5 Re (bottom) against bar type (0: no bar, 1: unclear bar, 2: clear bar) of our 244 CALIFA galaxies (left), spiral pattern (1: flocculent, 2: intermediate, 3: grand designed) (middle) and the number of spiral arms (left) of all spiral galaxies. Color-coded by galaxy morphological type, as in Figure 2.2.

also see weak correlations between the spiral pattern and the diversity of metallicity gradients (grand design galaxies are averagely flatter in Z gradients).

As the radial migrations may have different impacts on the inner and outer regions of the disk, in the bottom three panels we also show the stellar metallicity gradient between 0.5-1.5 Re against bar strength, spiral pattern and spiral arm number. Excluding the very central region the trend does not change, but the correlations appear even weaker.

We note that we also do see a weak correlation between metallicity gradient and any of the higher order terms in our kinematic harmonic decomposition (which would have indicated radial non-circular motions).

Our sample shows that the most apparent observational metrics of radial migration (bars, thin disk orbits, spiral arms) do not strongly correlate with the stellar population gradients within 1 Re. This indicates that radial migration might be a secondary effect in the inner regions, but the best predictor of a galaxy gradient is still the present day mass density profile.

2.5.5 Positive metallicity gradients

Our sample shows a number of galaxies with positive metallicity gradients, with 12% of all of our galaxies having metallicity gradients with $\nabla Z > 0.1$. We find that late type galaxies are more likely to show positive metallicity gradients, as from type E to Sd the fraction of positive gradients rises from: 0%, 0%, 11.1%, 13.8%, 19.3% and 75.0%. In the context of our empirical model, these galaxies result from the scatter in metallicity at fixed local mass being large enough to allow for the formation of positive metallicity slopes. We show in Figure 2.12 the predicted fraction of galaxies in the simple model as a function of galaxy density gradient. The simple model of Figure 2.6 predicts the fraction of positive gradients rises as galaxies exhibit flatter density profiles, in excellent agreement with our data.

The underlying physics for the scatter in metallicity, or the shallowness of some density profiles is likely more complex than the simple model however. Some previous studies have explored the possible scenarios which may be relevant for these positive gradients galaxies. For example, El-Badry et al., 2016a used simulations to explore the stellar feedback processes in low-mass galaxies and suggested that strong feedback could effectively cause a radial migration by strongly perturbing the gravitational potential. In addition, by blowing out the central metal-rich gas, the intense feedback may lead to relatively low central metallicities (with respect to their 1 Re region) compared to other galaxies (see also Brooks et al., 2007a; Gibson et al., 2013b; Schönrich and McMillan, 2017).

Stellar feedback is expected to be proportionally more impactful in low mass galaxies. This could mean that more metals are lost due to feedback-driven outflows in low mass galaxies, due to their shallower potential wells. Concurrently, the star formation efficiency might be reduced in these low mass galaxies due to the impact of feedback on the ISM (Brooks et al., 2007c). Both effects will be enhanced if the intrisically lower angular momentum of lower mass, late type galaxies helps to funnel gas to their central regions. Together, these feedback effects would work to suppress metal build-up in the central regions, shallow the density profiles, and cause larger scatter in local metal enrichment - with increasing efficiency towards lower mass galaxies. This mechanism would be in qualitative agreement with our finding of more positive gradients as galaxy mass decreases (or moves to later types; Appendix).

2.6 Summary

In this Chapter, we discuss the radial stellar metallicity gradients of 244 CALIFA galaxies, spanning galaxy morphological type from E to Sd. We use a stellar kinematic based ellipse systems to extract flux-weighted stellar population profiles, and use a harmonic decomposition method to derive the kinematic profiles within 1 Re. As our sample covers a broad range of mass/morphological type galaxies, in order to avoid the effect of logarithmic suppression, we study their linear metallicity (metal mass fraction; Z) profiles and gradients.

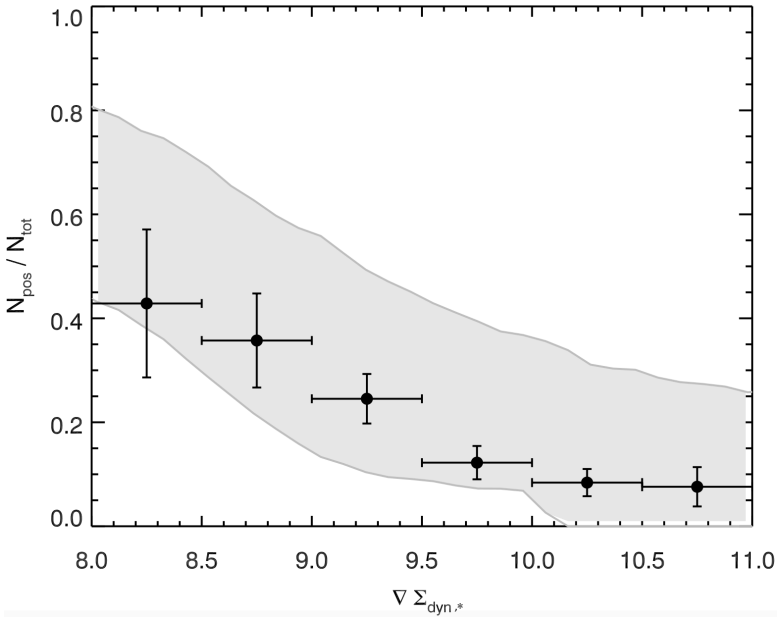

FIGURE 2.12: Fraction of galaxies with positive metallicity gradients as a function of the dynamically derived stellar mass density gradient. The grey band shows the predictions from the simple empirical model in Figure 2.6, black points show the fraction of positive metallicity gradients amoung the CALIFA galaxies.

• We find linear metallicity gradients ∇Z show clear galaxy morphological type dependence, with early-type galaxies tending to have steeper linear metallicity gradients ∇Z. The direct reason behind the Z gradient-G type correlation is the high central metallicity in earlier type galaxies.

• To further understand the origin of this correlation, we split our galaxies into three different groups according to their central Z, and test the local mass-metallicity relation at different radii in different groups of galaxy. The result not only shows a clear local mass-metallicity relation but also suggests a correlation between surface mass density gradient and ∇Z .

• We show that with empirical mass-dependent Sérsic index, size and metallicity scaling relations, the dependence and observed scatter of Z gradients and local stellar mass density can be reproduced.

• We also examine the role of angular momentum by studying V_{rot}/σ and cold disc fraction. For higher mass galaxies ($> 10^{10.5}\,M_{\odot}$) their V_{rot}/σ and thin disc fraction are correlated with both Z and stellar surface mass density gradients, but for galaxies with stellar mass below $10^{10.5}\,M_{\odot}$ their angular momentum is anti-correlated with the steepness of metallicity/surface mass density profiles. Analysis of the mass density in different orbital components further suggests that the angular momentum itself is not directly causal in setting the stellar metallicity gradient of the inner regions of galaxies.

• In order to explore the influence of radial migration, we use observable substructures (bar, spiral arm) as tracers of radial migrations. We find galaxies' radial migration features don't show strong correlations with stellar population gradients,

which suggests the radial migration may only provide secondary influence on the shape of gradients, at least within 1 Re.

• Finally, around 12% of our galaxies show positive metallicity gradients - however the fraction increases to as high as $\sim$ 80% as the galaxy mass decreases. We suggest stellar feedback could be one of the possible reasons behind this trend.

Though we found the local mass build-up is crucial to a galaxy's metallicity distribution, work still remains to be done to incorporate detailed knowledge about the local star formation history in different regions of a galaxy.

In this Chapter, our gradients are extracted from metallicity maps, in which the metallicity and mass of a single spaxel is the average metallicity and accumulated mass of all stellar populations it contains. Here we do not take age into our consideration. There may be interesting correlations between age and metallicity, given that the local mass buildup somewhat reflects the star formation history (e.g., light weighted age). This formation history may vary in different regions of a galaxy (e.g., bulge vs. disk), and further study will expand on the link between mass buildup and age. As our results show clear correlations between local mass and metallicity but with some scatter, the local SFH may contribute a possible source of this scatter.

Recently, Zibetti et al., 2017 studied the age distribution of CALIFA galaxies and found a bimodal local-age distribution, with an old and a young peak primarily due to regions in early-type galaxies and star-forming regions of spirals, respectively. In future works, we will test the ∇Z dependence on age using simulations to further explore how different mass build-up processes impart a signature on the present day stellar populations.

2.7 Appendix

Here we show in Figure 2.13 the total dynamical mass profiles plotted against the linear metallicity profiles. Progressing from earlier to later type galaxies we see a larger diversity in their density-metallicity tracks, with late type galaxies showing a larger fraction of positive metallicity profiles. This is consistent with the results in Figure 2.12, as these late type galaxies tend to have shallower density profiles on average. However it is clear that there are some objects in Figure 2.13, with positive gradients but which show significant negative density gradients - which may make these objects interesting test cases for further studies on the impact of feedback on the redistribution of gas and stars.

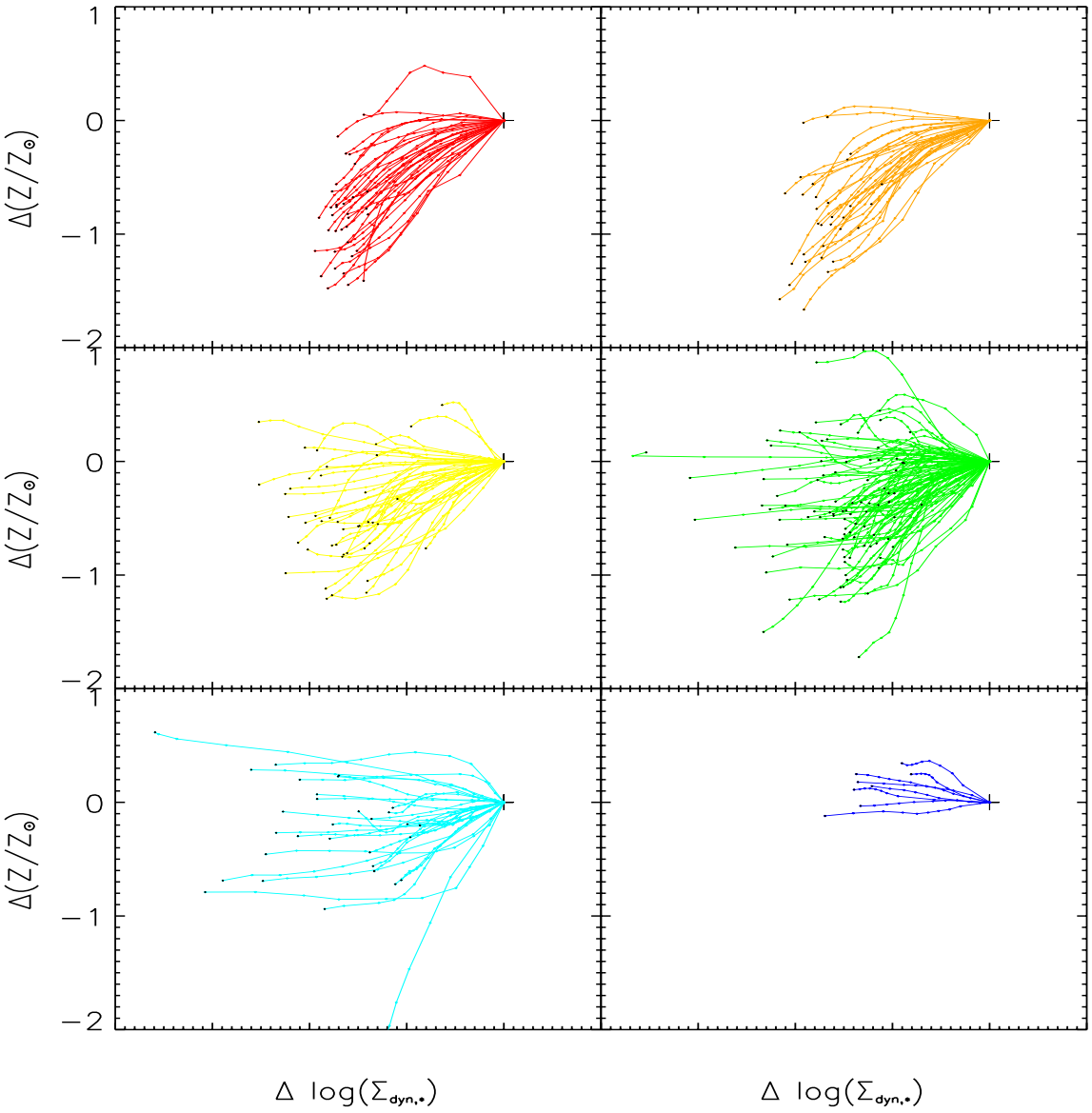

FIGURE 2.13: Metallicity Δ(Z) against logarithmic dynamically derived stellar surface mass density $\log(\Sigma_{dyn,*})$ profiles for different galaxy types, each profile represents one galaxy's Z and $\Sigma_{dyn,*}$ values at different radii (from 0 to 1 Re). Color coding is by galaxy morphological type, as in Figure 2.2.

Chapter 3

Tracing the origin of stellar metallicity gradients in simulations

This Chapter is based on an article in preparation "The in-situ origin of galaxies' stellar metallicity gradients". I am the lead author of the article, which was adapted for this thesis.

Overview:

In this chapter, We study the radial stellar metallicity profiles of simulated central galaxies (in the centre of their host dark matter haloes) at redshift z=0 within the total stellar mass range $10^{9.5} - 10^{12.5} M_{\odot}$ from the IllustrisTNG simulations. We find that the radial stellar metallicity profiles within an effective radius closely follows the stellar surface mass density distribution (a local mass-metallicity relation). Just like stellar surface mass density profiles, the stellar metallicity profiles can also be characterized by a Sérsic function, and we demonstrate how the resulting tight correlation between the stellar surface mass density and metallicity Sersic indices (n_S and n_Z respectively) can be used to estimate the radial variations in stellar populations in galaxies where direct metallicity estimates are lacking. We find that this relation is relatively insensitive to differences in star formation history, present day kinematics, accretion history and environment. Which confirms that the stellar metallicity gradients in the inner part of galaxies are primarily driven by the time integrated in-situ stellar mass buildup maintaining a local mass-metallicity relation.

3.1 Introduction

In Chapter 2, we analyzed the radial stellar metallicity ($Z/Z_{\odot}$) gradients out to 1 Re for 244 CALIFA galaxies to study the driving mechanisms behind stellar metallicity gradients. Our results suggested that the linear $Z/Z_{\odot}$ gradients simply reflect the local mass-metallicity relation within a galaxy. Where there is more concentrated stellar mass accumulation - the stellar populations are locally more enriched. This suggests that the radial stellar population distribution is primarily a result of the in-situ local star mass buildup. In this simple picture, the stellar surface mass density gradient ($\nabla\Sigma_*$) is well correlated with the stellar metallicity gradient ($\nabla Z/Z_{\odot}$) of a galaxy. The correlation implied that the structure of a galaxy at redshift zero was a simple predictor of the type of stellar population gradients present. We were able to exploit galaxy scaling relations to show that the observed global galaxy stellar mass - size, metallicity and concentration relations indeed predicted a correlation between the stellar surface mass density and the stellar population gradient.

To further understand the role of secular evolutionary processes in changing the stellar population gradients, we explored links between a galaxy's local stellar populations and its orbital distributions, by using Schwarzschild dynamical models. These models were constrained by the observed kinematics of each galaxy, and the best model for each galaxy produced a distribution of orbital circularities which best represented each galaxy. As different orbital components link to their dynamical heating history, by looking jointly at the metallicity gradient and mass density of each dynamical orbit family, we could get an understanding on the timescale of the buildup of $\nabla\Sigma_*$ - $\nabla Z/Z_\odot$ relations.

We found that the $\nabla\Sigma_*$ - $\nabla Z/Z_\odot$ relation seemed to be tighter for hot orbit components, while the correlation was much weaker for cold orbital components within a galaxy. However, we couldn't find any persuasive evidence that could link the present day dynamical structure of a galaxy with the causal formation of its stellar metallicity gradients. Also, we found that gradients in the inner disk did not appear to be strongly shaped by radial migration, which was evident from the lack of correlation between the metallicity gradients and observable probes of radial migration in the galaxies, such as bars and spiral arms.

While the observations provided a good starting framework - they do not allow us to isolate individual factors as well as numerical simulations. In addition simulations will be able to study the evolution of the key relation in our previous chapter: the local mass metallicity relation observed in a wide range of galaxy masses and morphological types. The simulations from the IllustrisTNG project (Springel et al., 2018; Pillepich et al., 2018; Nelson et al., 2018; Naiman et al., 2018; Marinacci et al., 2018) provides an ideal opportunity to better understand and interpret our previous findings. Since IllustrisTNG also contains stellar age information, we are able to further explore the evolution of metallicity gradients, and in addition the impact of environment and accretion history.

In this Chapter we will discuss the diversity of stellar metallicity gradients from numerical simulations, by analysing galaxies at redshift z=0 within the IllustrisTNG100 simulation. While there are many astrophysical processes that we could study or isolate with this rich numerical data set - we will focus on understanding the correlated build up of stellar population and surface mass density gradients seen in our observational study.

3.2 Data & Methods

3.2.1 Illustris TNG-100 simulation data

To study the evolution of stellar population gradients in galaxies of different masses and environments, we make use of the IllustrisTNG simulation (Springel et al., 2018; Pillepich et al., 2018; Nelson et al., 2018; Naiman et al., 2018; Marinacci et al., 2018), which is a new generation of the original Illustris simulation project (Vogelsberger et al., 2014b; Vogelsberger et al., 2014a; Sijacki et al., 2015) with the updated physical model and cosmology consistent with the 2015 Plank collaboration results (Planck Collaboration et al., 2016a). It traces multiple processes in galaxy evolution, e.g. star formation, feedback from both stars and active galactic nuclei, gas motions, chemical enrichment and magnetic fields (Pakmor, Bauer, and Springel, 2011; Pillepich

et al., 2018; Weinberger et al., 2018). The TNG project consists of three simulation volumes: TNG50, TNG100, and TNG300.

In this paper we use the TNG100 data, which has a cosmological box size of 100 Mpc, and contains three different resolution subset simulations (TNG100(-1), TNG100-2 and TNG100-3). Throughout this work, we present results mainly from the simulation with the highest resolution: TGN100(-1). The TNG100 simulation has a stellar particle resolution of $10^6 M_\odot$, and the minimum softening factor of gas cells is ~ 0.19 kpc (Dylan Nelson et. al. 2019), but we also compare our results with lower resolution simulations (TNG100-2 and 3) in the discussion.

TNG simulation keeps each particle's stellar mass $m_{*,p}$ and metal mass fractions Z, age, velocity and other properties. To get the metallicity $Z/Z_\odot$ we simply divide Z by the solar metal mass fraction (in this work we use $Z_\odot = 0.0127$). Some previous works used different solar metallicity $Z_\odot = 0.02$ which might cause slightly higher metallicity values compared to other studies.

We selected 7109 central galaxies from the IllustrisTNG100 simulation at redshift z=0. The term 'central galaxies' refers to galaxies located at the centre of their dark matter halo (as opposed to satellite galaxies). The selected galaxies have total stellar mass $M_{*,all}$ ranging from $10^{9.5}$ to $10^{12.6}$ $M_\odot$ and 3D half mass radii $R_{e,3d} > 0.5$ kpc. These choices were motivated in order to allow us to have enough stellar particles in each galaxy to extract robust radial profiles of quantities of interest.

We define an enclosed stellar mass M_* to be the total mass of all stellar particles within 2 times $R_{e,3d}$, and use this as a comparable to the observable stellar mass of real galaxies. The ratio between the total stellar mass and this observable stellar mass $M_*/M_{*,\mathrm{all}}$ is between 0.584 and 0.932 for our whole sample. The full range of M_* in our sample of galaxies then ranges from $10^{9.3}$ to $10^{12.5}$ $M_\odot$. Figure 3.1 shows the TNG galaxies in our sample distributed in photometric colour-mass (left) and size-mass planes (right), In both panels the color coding is by the logarithmic specific star formation rate (log(sSFR)). Here the specific star formation rate (sSFR) is defined as the sum of the individual star formation rates of all gas cells in one galaxy divided by its total stellar mass. The final sample covers a large enough range in mass and sSFR such that it will make a good comparable to the morphological diversity and mass diversity in the CALIFA sample from Chapter 2.

3.2.2 Radial profile extraction

For each galaxy, we define its main rotation plane by calculating the average angular momentum of all stellar particles between 0.5-1.5 $R_{e,3d}$. We then project all the particles onto this 2D plane to get the 2D particle maps. This exercise explicitly assumes a face-on orientation for all galaxies. While real galaxies may be observed at arbitrary orientation, CALIFA is biased towards high filling factor galaxies and is perhaps slightly biased towards face-on galaxies as well.

We divide the galaxy's 2D particle map with a series of concentric rings with radial width (resolution) r_{bin}=0.1 kpc, and are centred on the main rotation centre. Next we extract the radial profiles by calculating the mass and r-band flux weighted metallicity ($Z/Z_\odot$) and age, as well as average surface stellar mass density (Σ_*), which is computed by the total stellar mass of each annuli divided by its surface

area, stellar velocity dispersion (σ) is defined as the standard deviation of the line-of-sight (vertical to the main rotation plane direction) velocity component within each annulli and rotation velocity (V_{rot} which is defined as the velocity component that is rotating the main axis of the main rotation plane) for stellar particles within each annulli.

As our radial resolution of 0.1 kpc is higher compared to CALIFA data ($\sim$ 0.4 kpc), we are able to trace the metallicity gradient in the central region in a way that will be more informative but also comparable with observational data. In order to compare with observations, we also create 2D stellar population spaxel maps for each galaxy by binning the projected 2D particle map into $0.2 \times 0.2\,\mathrm{kpc}^2$ pixel sized 2D maps, with each quantity weighted by the mass of the particles in that spaxel..

Though we will compare some of our results with the observations, all our sample galaxies will be studied from the face-on direction. Because our primary goal is to study the intrinsic properties and possible origins of galactic stellar metallicity gradients. We would avoid any effect from observational uncertainties e.g. position angle, dust extinction, amongst others.

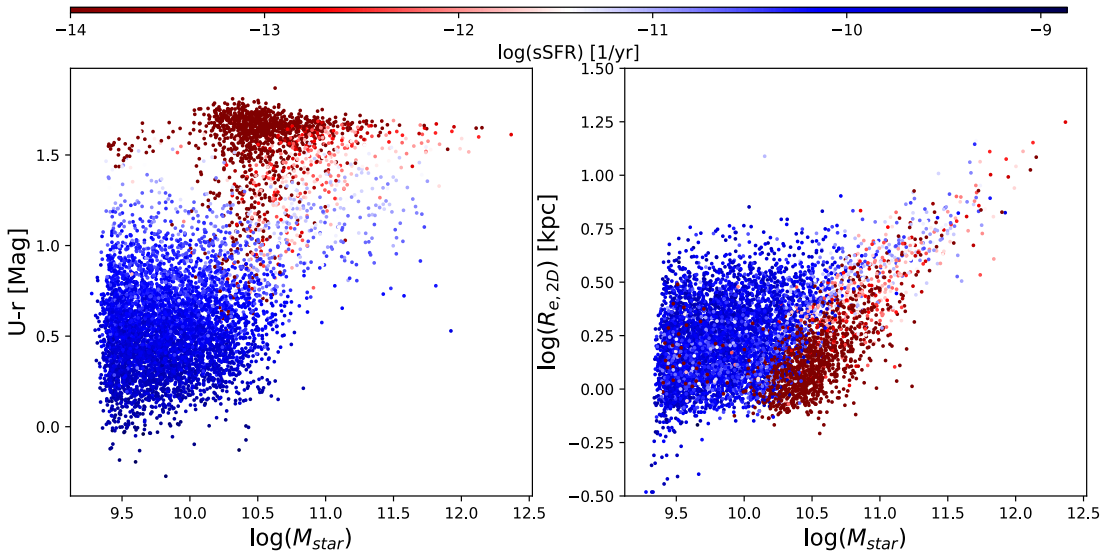

FIGURE 3.1: Left: The sample of TNG galaxies plotted in U-r - M_* space, right: The M_* - $R_{e,2d}$ relation of our sample galaxies. Both panels are color coded by the specific star formation rate.

3.2.3 Half mass radius and mass concentration

In this work we are interested in the stellar metallicity gradients relative to the projected 2D half mass radius ($R_{e,2d}$). We define $R_{e,2d}$ as the radius which encloses half of a galaxy's M_* from the projected 2D particle maps. The bottom panel of figure 3.1 shows the $R_{e,2d}$ as a function of M_*. As the main goal of our work is to explore the buildup of stellar populations in the inner regions of galaxies, in the rest of the paper we will mostly focus on the particle or spaxel distributions within $1R_{e,2d}$, for the sake of simplicity, we will use Re to indicate $R_{e,2d}$ in the rest of the paper.

In addition, we use a galaxy's stellar mass concentration R_{1050} as an estimator of its morphological type. R_{1050} is defined as $R_{1050} = R_{10\%,2d}/R_{50\%,2d}$, which is the ratio between a galaxy's projected 2D radius enclosing 10% stellar $R_{10\%,2d}$ and the radius enclosing 50% stellar mass $R_{50\%,2d}$. The lower the R_{1050} the higher the central mass concentration.

3.3 Results

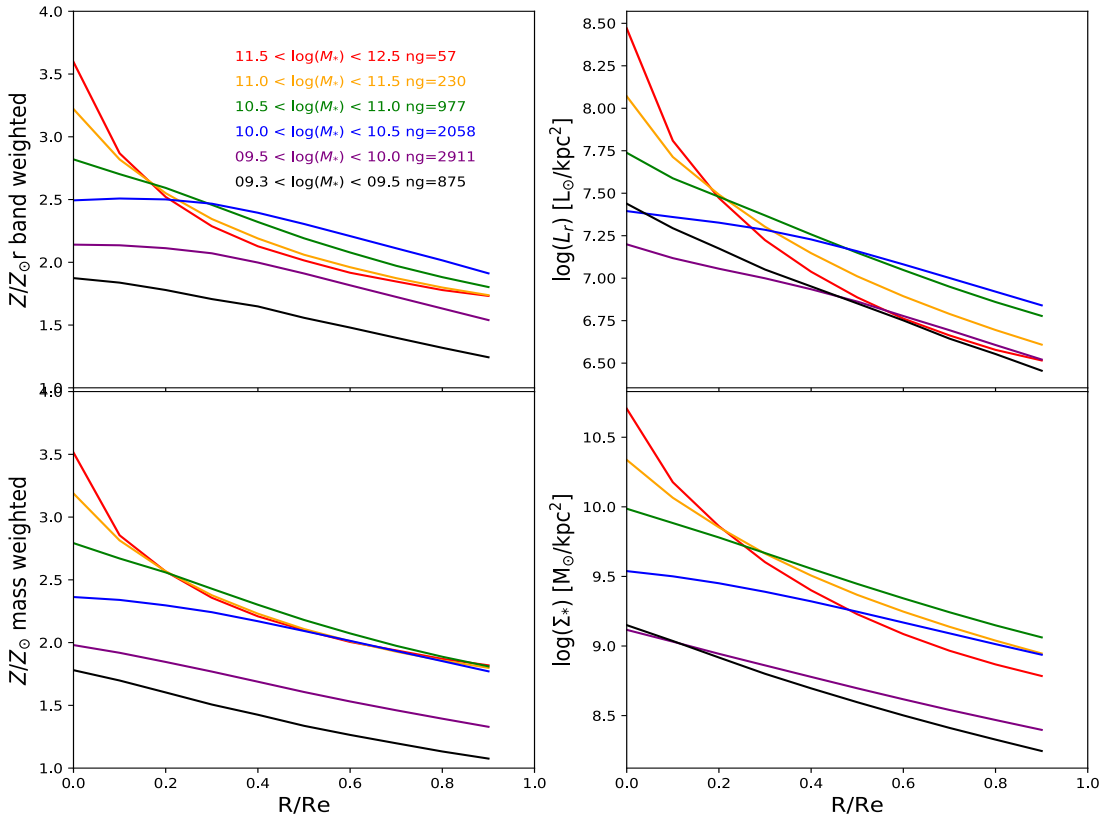

FIGURE 3.2: Average *r*-band light weighted stellar metallicity profiles (top left), stellar mass weighted stellar metallicity profiles (bottom left), stellar luminosity profiles (top right) and surface mass density (bottom right) profiles of galaxies within 6 different stellar mass bins (from red to black are the bins from high mass to low mass) for our selected galaxies from TNG100. *ng* are the number of galaxies within each bin.

In this section we explore the diverse behaviour of stellar metallicity gradients of 7109 central galaxies in the TNG100 simulation.

Figure 3.2 shows the average profiles of both *r*-band light weighted and mass weighted stellar metallicity as well as surface mass density and surface brightness, for galaxies of different stellar masses. A global mass-metallicity relation is evident, with high-mass galaxies showing higher average metallicity. We can see that except for the lowest mass bin (black lines), all other groups show similar metallicity at 1 Re. In contrast, the central regions show noticeable differences as a function of

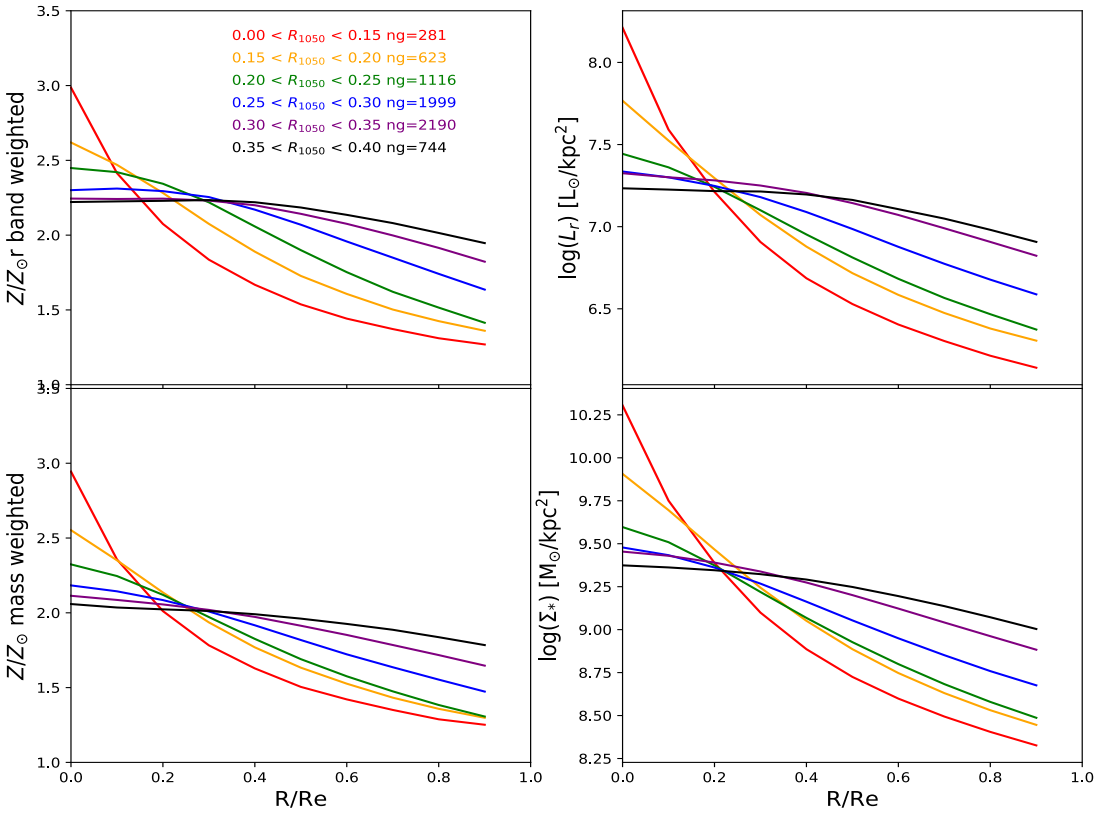

FIGURE 3.3: Average *r*-band light weighted stellar metallicity profiles (top left), stellar mass weighted stellar metallicity profiles (bottom left), stellar luminosity profiles (top right) and surface mass density (bottom right) profiles of galaxies within 6 different R_{1050} bins (from red to black are the bins from high concentration to low concentration). *ng* are the number of galaxies within each bin.

stellar mass, with the highest mass galaxies showing the most steeply rising metallicity profiles in the inner regions. Additionally, the shapes and relative positions of Z profiles and surface mass density profiles of different mass bins show similarities.

Figure 3.3 shows the average profiles of both *r*-band light weighted and mass weighted stellar metallicity and surface mass density of galaxies within bins of different mass concentration R_{1050}. Here we see that the galaxies with the highest structural concentrations (low values of R_{1050}) show steeply rising stellar metallicity profiles. However unlike Figure 3.2, the profiles show a larger spread in the outer regions. The radial metallicity profiles not only show similar shapes as the stellar surface mass density profiles but also show a clear correlation with R_{1050}.

In Figure 3.4 we further decompose the galaxies into two different mass bins ($10^{9.3}$-10^{10} and $10^{10.5}$-$10^{11.5}$ $M_\odot$). Within each mass range the correlation between metallicity profile shape and R_{1050} can clearly be seen, as galaxies with smaller R_{1050} tend to show steeper metallicity profiles. Compared to the total stellar mass, the simulated galaxies' radial stellar metallicity distributions are more correlated with the central stellar mass concentration, this in agreement with what we have found in CALIFA galaxies (Zhuang et al., 2019). As there is no obvious difference between

r-band light weighted and mass weighted profiles, for the sake of simplicity, in what follows we will describe the results from the mass-weighted profiles.

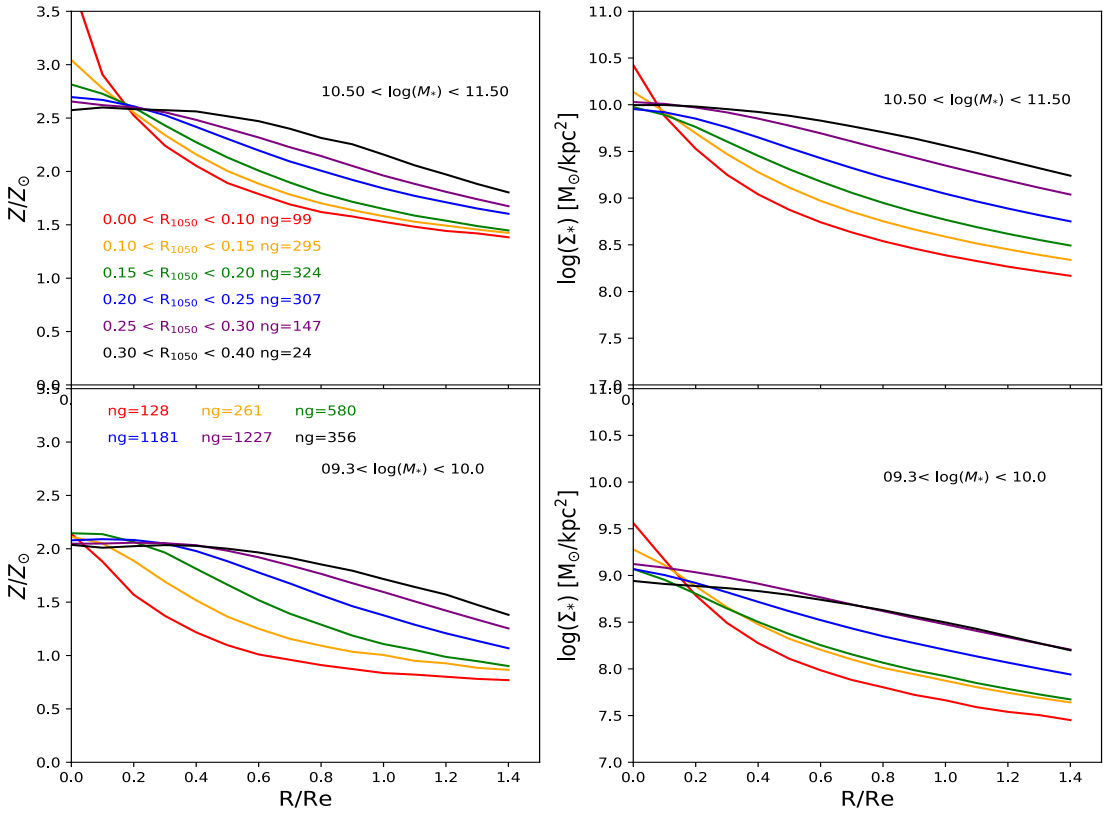

FIGURE 3.4: Stellar metallicity (left) and surface mass density profiles (right) of all galaxies within 6 different bins of R_{1050} (From red to black are the bins from high concentration to low concentration). Top panels are for galaxies with higher stellar masses ($10^{10.5} < 10^{11.5}$ $M_\odot$), while, bottom panels show results for only low mass galaxies ($10^{9.3} < 10^{10}$ $M_\odot$). *ng* are the number of galaxies within each bin.

3.3.1 Stellar mass density and metallicity gradients

The shape of stellar metallicity profiles show a clear correlation with the stellar mass radial distribution in our TNG sample. To help in quantifying the role of various processes in shaping the metallicity distributions we characterize the metallicity gradients (∇Z) from those profiles. Figures 3.2, 3.3 and 3.4 illustrate that most of the profiles are more complicated than a simple linear relation between Z vs. radius, or surface mass density vs. radius. In order to provide a more flexible and informative characterization of the Z distributions in this work we introduce a new way to represent the radial metallicity gradient. As the metallicity profiles show similar shapes and trends as the logarithmic surface mass density profiles, we should be able to fit them with an analogous functional form. The surface mass density can be approximately described as a Sérsic profile:

$$\log(\Sigma) = \log(\Sigma_0) - b(n_S)\,((r/R_{\rm e})^{1/n_S} - 1) \tag{3.1}$$

As we have mentioned in Section 1.1.2, n_S is the Sérsic index, the higher the n_S the higher the central stellar mass concentration. $b(n_S)$ follows from the relation $\Gamma[2b(n_S)] = 2\,\gamma[2b(n_S), b(n_S)]$, where Γ and γ are respectively the Gamma function and lower incomplete Gamma function (Ciotti and Bertin, 1999). To high precision, those can be approximated by:

$$b = 2\,n_S - \frac{1}{3} + \frac{4}{405}\,\frac{1}{n_S} + \frac{46}{25515}\,\frac{1}{n_S^2} \approx 2\,n_S - \frac{1}{3}. \tag{3.2}$$

We define the metallicity profiles to have a metallicity 'Sérsic' profile:

$$Z = Z_0 - (2\,n_Z - \frac{1}{3}) * ((r/R_{\rm e})^{1/n_Z} - 1) \tag{3.3}$$

Where we define the 'metallicity Sérsic index' n_Z, and just like a classical Sérsic index, it is proportional to more centrally concentrated distributions. In general, the higher n_Z means 'steeper' gradients, or in other words, the more quickly rising the central metallicity will be in the inner regions of the galaxy. Z_0 is the stellar metallicity at Re, and as another advantage of n_Z is that it is independent from the choice of Re.

In Figure 3.5 we linearly fit the n_S - n_Z relation ($n_Z = b_{Z,S} + a_{Z,S} * n_S$)for all our sample TNG galaxies with the slope $a_{Z,S}$=1.51 with standard deviation $\sigma_{Z,S}$ = 0.25. We also fit the relations at three different stellar mass ranges as shown in the top right, bottom left and right panels. In all mass ranges the n_S - n_Z relations show similar slopes ($a_{Z,S}$=1.52, 1.48 and 1.56 for low, intermediate and high mass galaxies respectively); while the standard deviation is higher for high mass galaxies ($\sigma_{Z,S}$ = 0.24, 0.19 and 1.02 for low, intermediate and high mass galaxies respectively). Figure 3.5 shows that there exists a tight relation between the Sérsic index of stellar surface mass density (n_S) and the metallicity 'Sérsic index' of the stellar metallicity profile (n_Z); for galaxies with high n_S also show high n_Z, and this relation is independent of the host galaxy stellar mass, $\log(M_*)$.

In order to be comparable with previous studies, in this paper we use three different values to represent radial stellar metallicity gradients:

- We linearly fit the stellar metallicity profile within 1 Re and take the slope of that fit (Z slope).
- We compute the difference between the central stellar metallicity and the stellar metallicity at 1 Re ($Z_{\rm Re} - Z_{\rm centre}$).
- We compute the metallicity 'Sérsic index' of the stellar metallicity profile (n_Z).

Figure 3.6 shows the 3 different stellar metallicity gradients estimators against galaxy's stellar mass M_*, and mass concentration R_{1050}. As expected given Figure 3.5, one can easily notice that R_{1050} correlates with all three metallicity gradient estimates - with galaxies that have a higher stellar mass concentration showing steeper the stellar metallicity gradients. This tight link exists in all $\log(M_*)$ ranges (shown

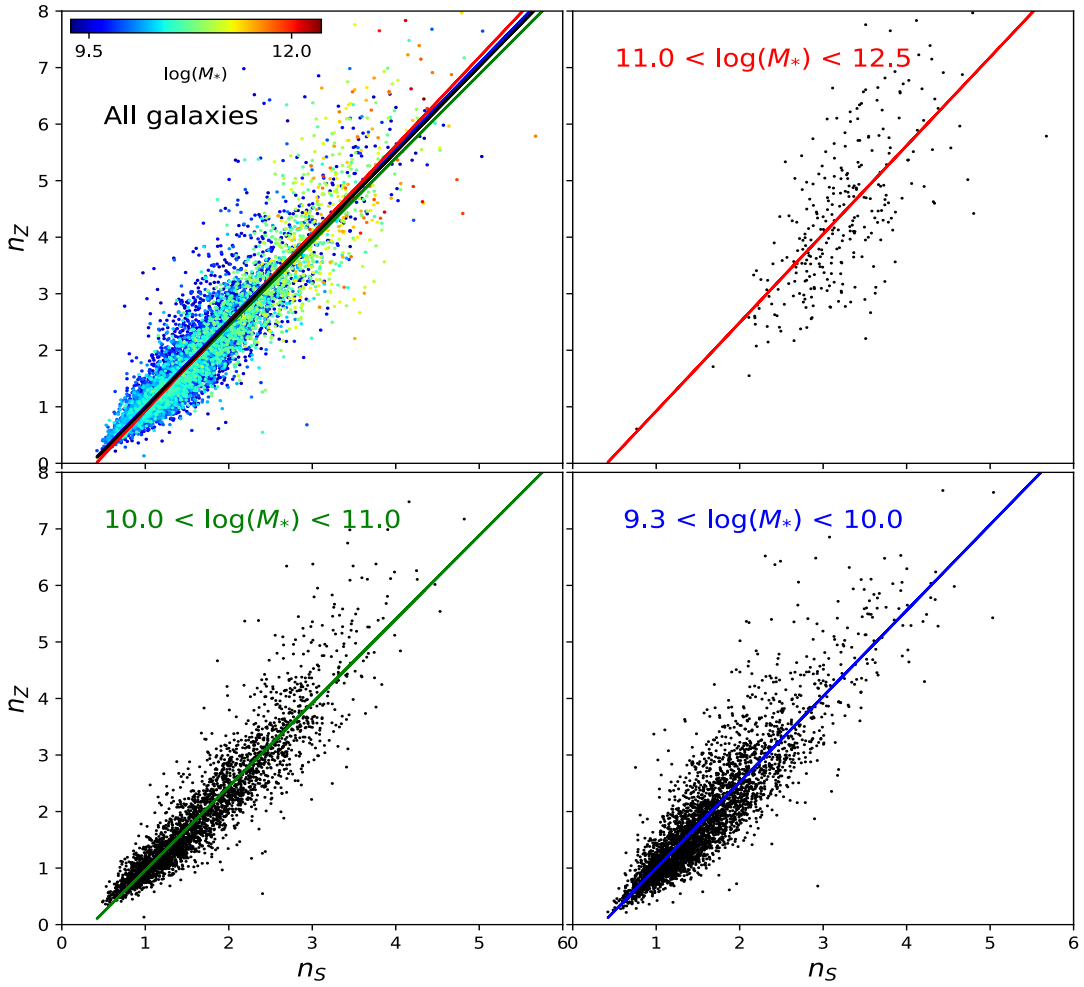

FIGURE 3.5: The correlation between the Sérsic index of stellar surface mass density (n_S) and the metallicity 'Sérsic index' of stellar metallicity profile (n_Z) for galaxies within different $\log(M_*)$ ranges, lines are the linear fit relations. Top left: the relation for all galaxies in our sample and color coded by $\log(M_*)$, top right, bottom left and right are the relation for galaxies with $\log(M_*) > 11.0$, $10.0 < \log(M_*) < 11.0$ and $9.3 < \log(M_*) < 10.0$ separately.

by the color coding in left panels). This suggests the radial stellar metallicity distribution is tightly linked to the present day radial stellar mass distribution.

The black circles in the top left panel are the results from the CALIFA galaxies, which agrees with the TNG results quite well, except for the very low mass regions. As we will discuss later this is likely because in the CALIFA sample we do not have early type (high concentration) galaxies. In addition the TNG galaxies do not seem to produce galaxies at any mass with significant positive metallicity gradients, at odds with the CALIFA sample which shows approximately 12% of galaxies exhibit positive gradients.

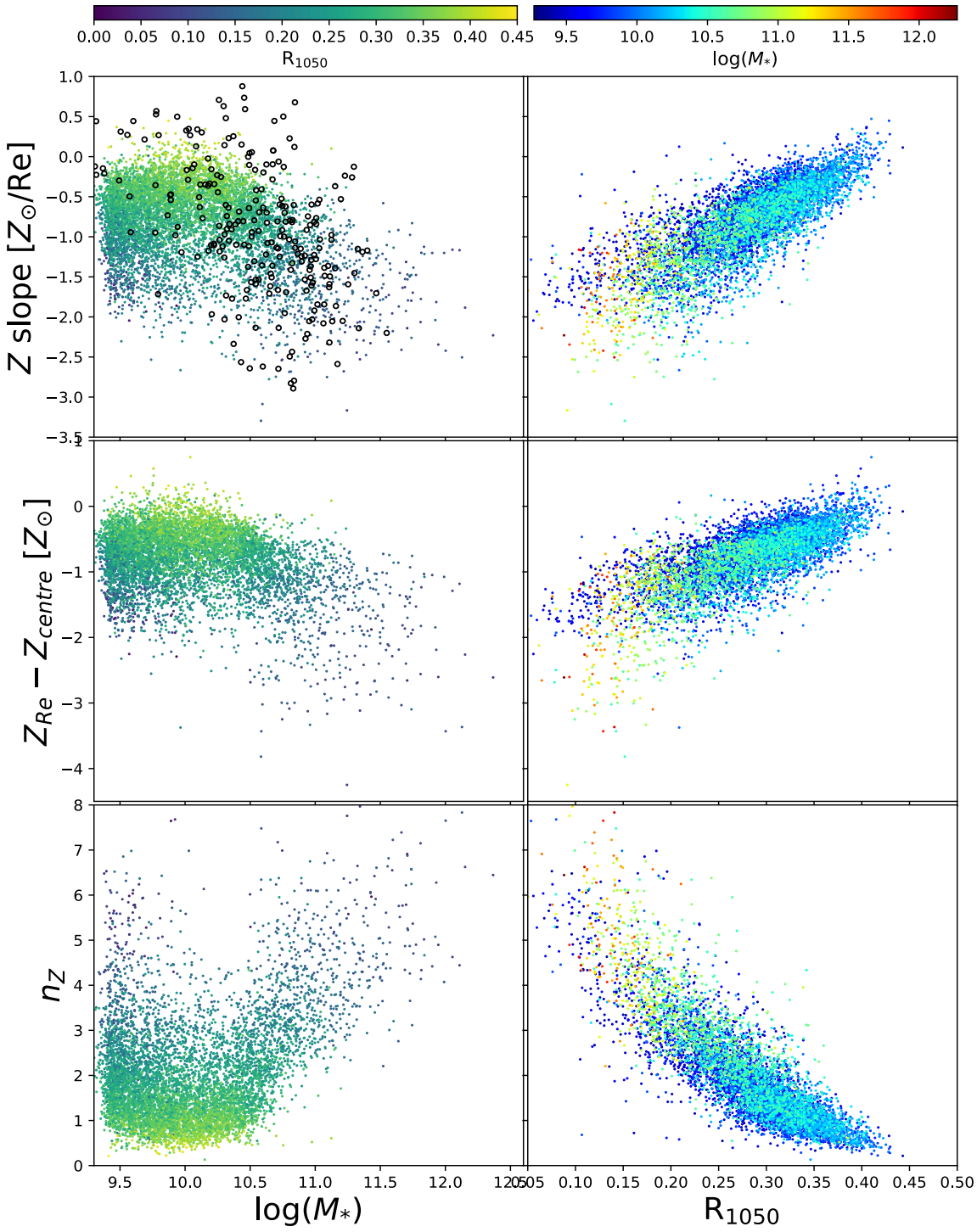

FIGURE 3.6: Three different metallicity gradient estimators (top: linear fitted Z slope; middle: difference between central Z and Z at 1Re: $Z_{\rm Re} - Z_{\rm centre}$; bottom: metallicity 'Sérsic' index: n_Z) against total stellar mass and stellar mass ($\log(M_*)$) concentration R_{1050}. The black diamonds in top left panel are the observed gradients from CALIFA galaxies.

3.3.2 Local mass-metallicity relation

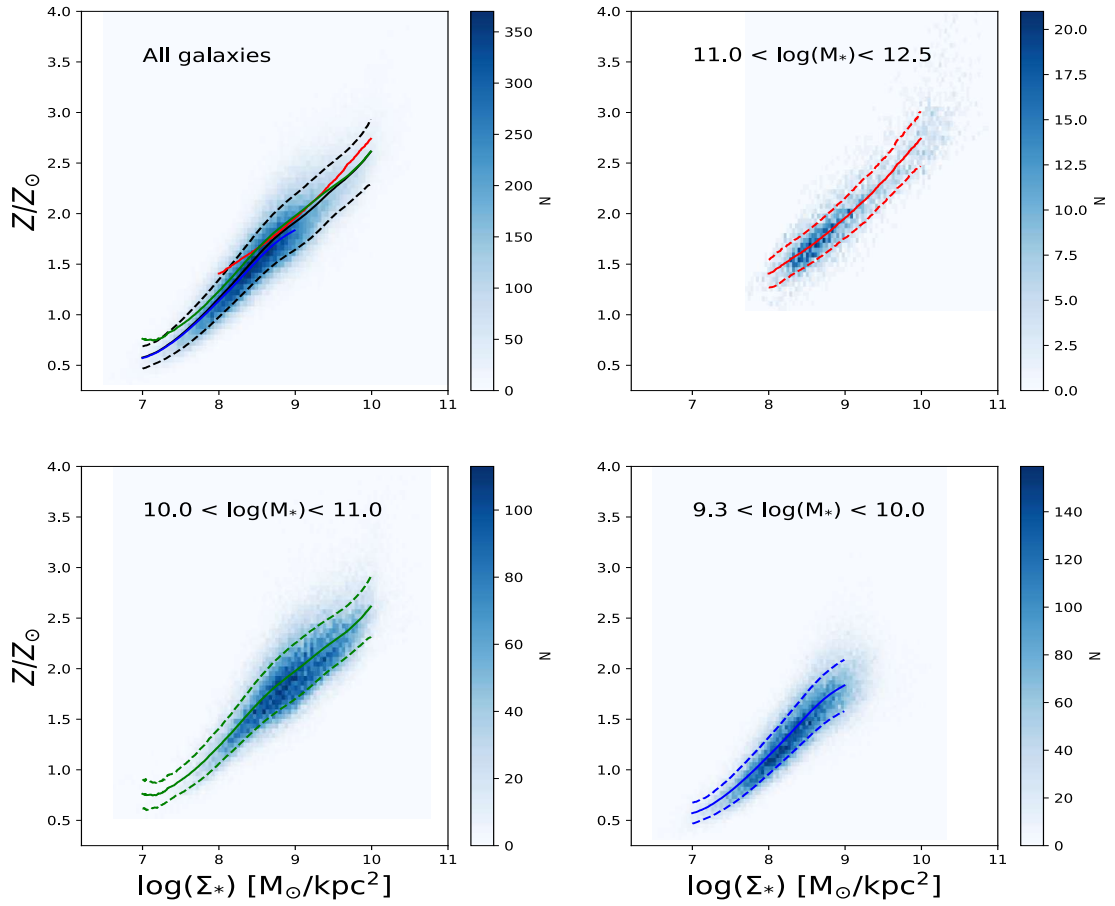

FIGURE 3.7: Density histograms of the stellar surface density versus the local metallicity for all annuli within 1 Re for: all our galaxies (top left), only high mass galaxies (top right); intermediate mass galaxies (bottom left) and low mass galaxies (bottom right). Solid and dashed lines are the mean trends and standard deviations of each mass range (Black: all galaxies, red: high mass galaxies, green: intermediate mass galaxies, blue: low mass galaxies).

The clear correlation between stellar mass gradient and stellar metallicity gradients in IllustrisTNG galaxies as well as what we have found in CALIFA galaxies before (Zhuang et al., 2019) indicates that in the inner region of galaxies, the local stellar metallicity mainly depends on the local stellar mass buildup. Figure 3.7 shows the local stellar mass-metallicity realtion (MMR) of all annuli within 1 Re of all our galaxies, and galaxies within different mass ranges. All four panels show clear correlations between local stellar metallicity and surface mass density, with higher local stellar surface mass density corresponding to higher local stellar metallicity. There is very little difference in the slopes or intercepts of the relations for different mass galaxies; however the highest surface mass densities and metallicities occur preferentially in the highest mass galaxies.

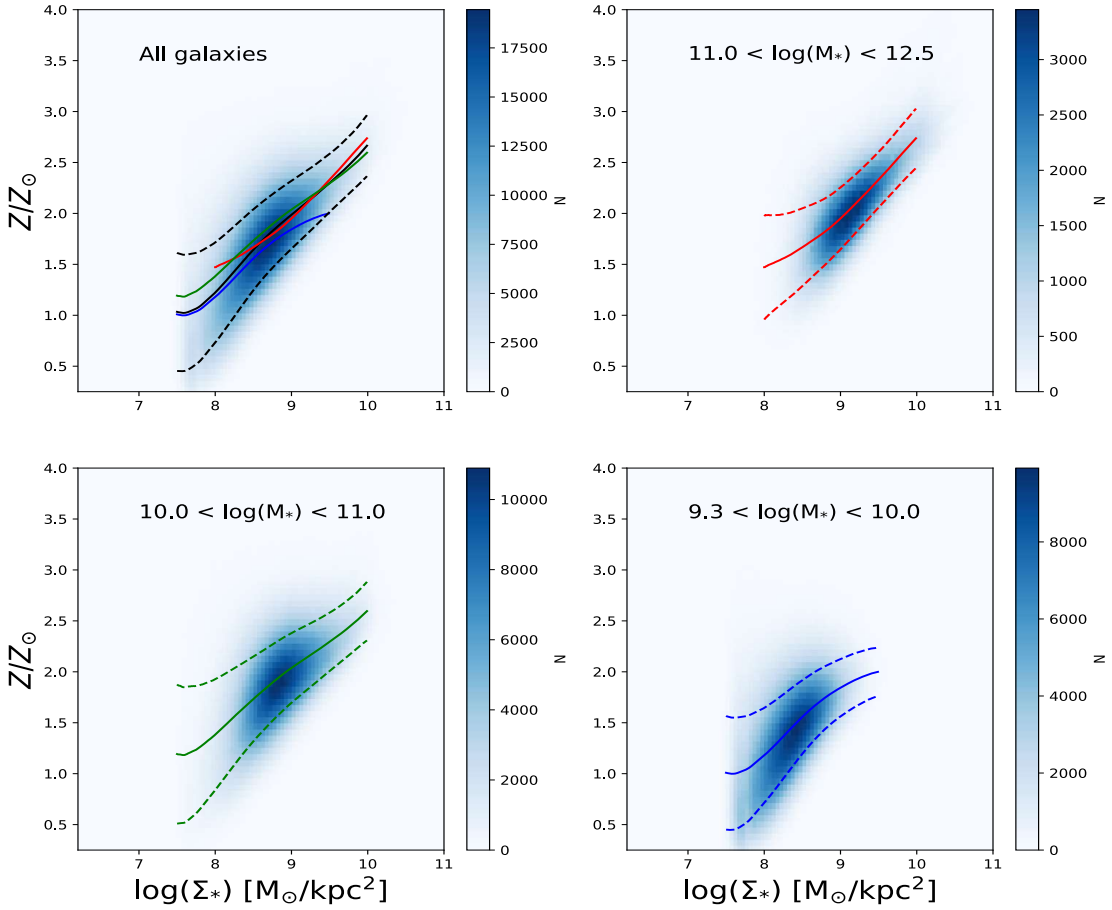

FIGURE 3.8: Density histograms of the stellar surface density versus the local metallicity for all pixels within 1 Re for: all galaxies (top left), only high mass galaxies (top right); intermediate mass galaxies (bottom left) and low mass galaxies (bottom right). Solid and dashed lines are the mean trends and standard deviations of each mass ranges (Black: all galaxies, red: high mass galaxies, green: intermediate mass galaxies, blue: low mass galaxies).

The local MMR in Figure 3.7 is based on an axis symmetric annuli systems (the Σ against Z of each annuli). In order to understand a more detailed link between local mass and metallicity of galaxies, we test the impact of non-axis symmetric azimuthal variations on the derived radial profiles. To do thiswe use the 2D pixel (mock IFU) maps. With these, we are able to trace the local MMR relations and understand how azimuthal variations may introduce scatter in the local surface mass density - metallicity relation.

The top left panel of figure 3.8 shows the local MMR of all pixels within 1 Re for all our galaxies. Compared with Figure 3.7, the pixel version shows a similar MMR trend but with larger scatter - likely because of the non-axis symmetric azimuthal variation which could be caused by non-axissymmetric perturbations/overdensities (e.g., spiral arms, bars.).

The top right, bottom left and bottom right panels of figure 3.8 shows the pixel MMR for galaxies within different mass ranges. For higher mass galaxies the local

MMR shows smaller intrinsic scatter than the low mass galaxies. This suggests the local MMR relation is statistically strengthened when an increased number of star formation generations can occur. The scatter decreases as more stars are formed and the stellar mass density and metallicity tend towards a common relation.

3.3.3 A joint look at age and metallicity distributions

Galaxies of different morphological types and different substructures likely have different star formation histories. Disk galaxies (as for example the MW) can have a central region that is quite different in terms of chemical evolution, because it is dominated by an old population, whereas the outskirts of a disk may be dominated by a young population. A combined study of both age and metallicity spatial distributions might reveal more clues about how stellar population gradients were built up.

IllustrisTNG data provides the age when each stellar particle was born, and to further understand the stellar metallicity and local stellar mass buildup, we separate the stellar particles into three age groups (old: older than 6 Gyr, intermediate: between 2-6 Gyr and young: younger than 2 Gyr). Next we extract the radial stellar metallicity and surface mass density profiles of each age population as shown in Figure 3.9.

The right panels of Figure 3.9 show that in all age groups, the shape of the surface mass profiles of the high mass galaxies is consistently more concentrated and steeply rising in the inner regions, compared to the low mass galaxies. On top of this we can see that the absolute value of the surface mass density decreases strongly for the highest mass galaxies as one looks at younger stars. This reflects the fact that these high mass galaxies form most of their stars rapidly and are quenched in late times, with minimal star formation. A similar trend is seen in the left panels: the absolute value of metallicity for the high mass galaxies decreases relative to the low mass galaxies as one considers younger stars. Here this effect is likely due to the small levels of latent star formation in high mass galaxies being driven by re-accreted lower metallicity gas from the circumgalactic medium (CGM). The shape of the stellar metallicity profiles of the old stars are most centrally concentrated and steeply rising in the highest mass galaxies. In intermediate and young aged stars, the shape of the metallicity profiles becomes more similar for all galaxy masses - with a noticeable central 'core' in the youngest stars. This is likely a numerical effect due to the small number of young star particles in these high mass galaxies.

As seen in Figure 3.8, the correspondance between the surface mass density and metallicity becomes weaker as one considers younger stars (or lower mass galaxies). This again suggests the correlation between surface mass density and metallicity becomes tighter as more star formation and enrichment episodes occur locally within a system. It suggests that for galaxies within all mass bins, the Z profile of young population stars does not correlate with either newly formed stellar density or the total accumulated stellar density (shown in figure 3.2).

This indicates that the correlation between local stellar metallicity and mass was built up during the earlier stages of galaxy evolution, and most likely in periods with efficient/fast star formation. Later the star formation was limited by the amount of 'new' gas that is randomly distributed and mixed due to infall, feedback

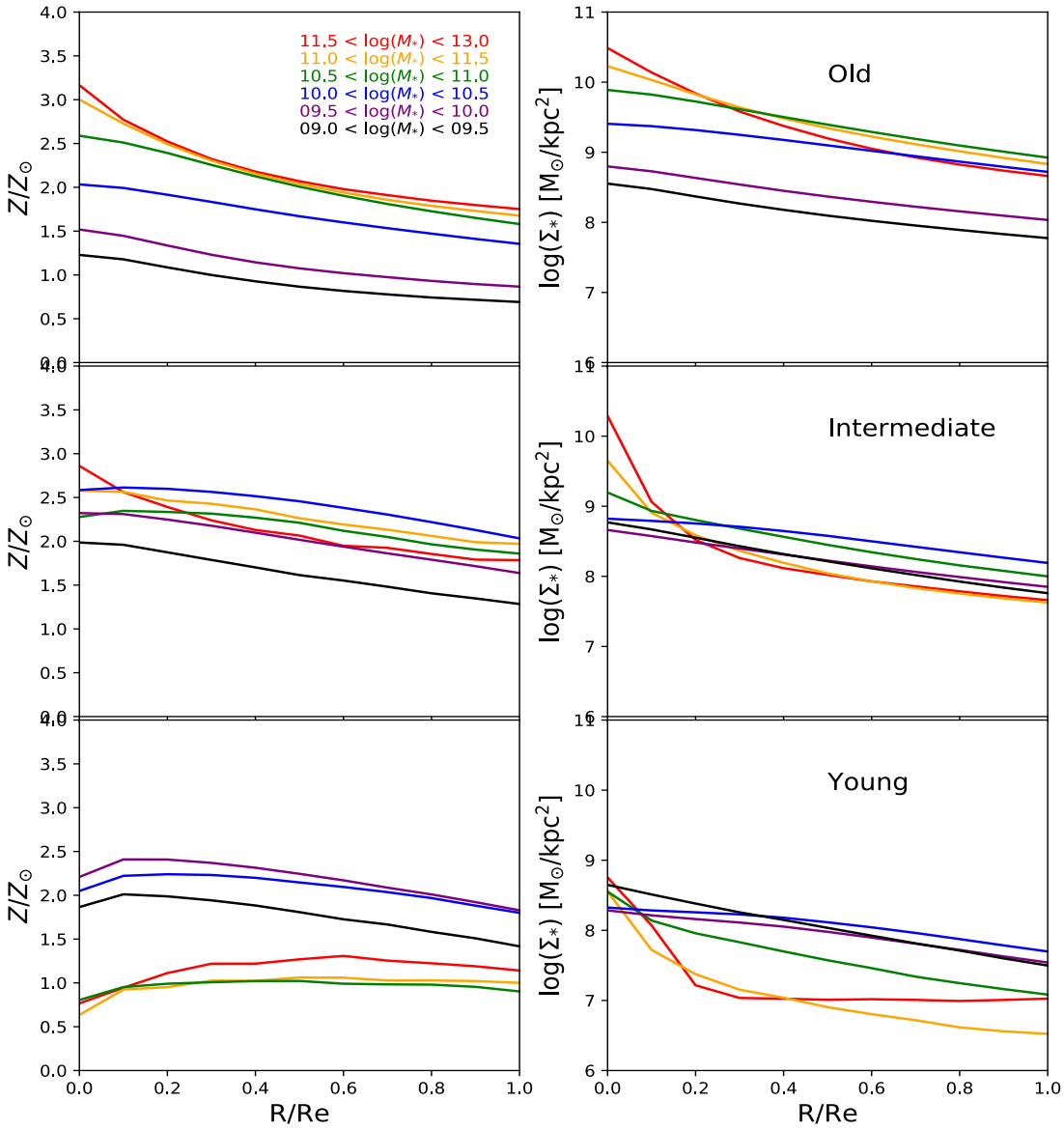

FIGURE 3.9: Average radial stellar metallicity (left) and surface mass density (right) profiles of galaxies of each age populations within six mass bins, old population: older than 6 Gyr (top right); intermediate population: between 2-6 Gyr (bottom left) and young population: younger than 2 Gyr (bottom right), different colours represent different present-day mass bins from red to black are the bins from high mass to low mass.

and migration processes. This also confirms what we have found in figure 3.8 that the local MMR were buildup statistically through a large number of star forming events, while for small numbers of events it may show more 'stochastic' behavior.

We caution that, the mass of galaxies can be very different at different periods, so the present-day high mass galaxies did not necessarily have the highest masses in their early evolutionary stages.

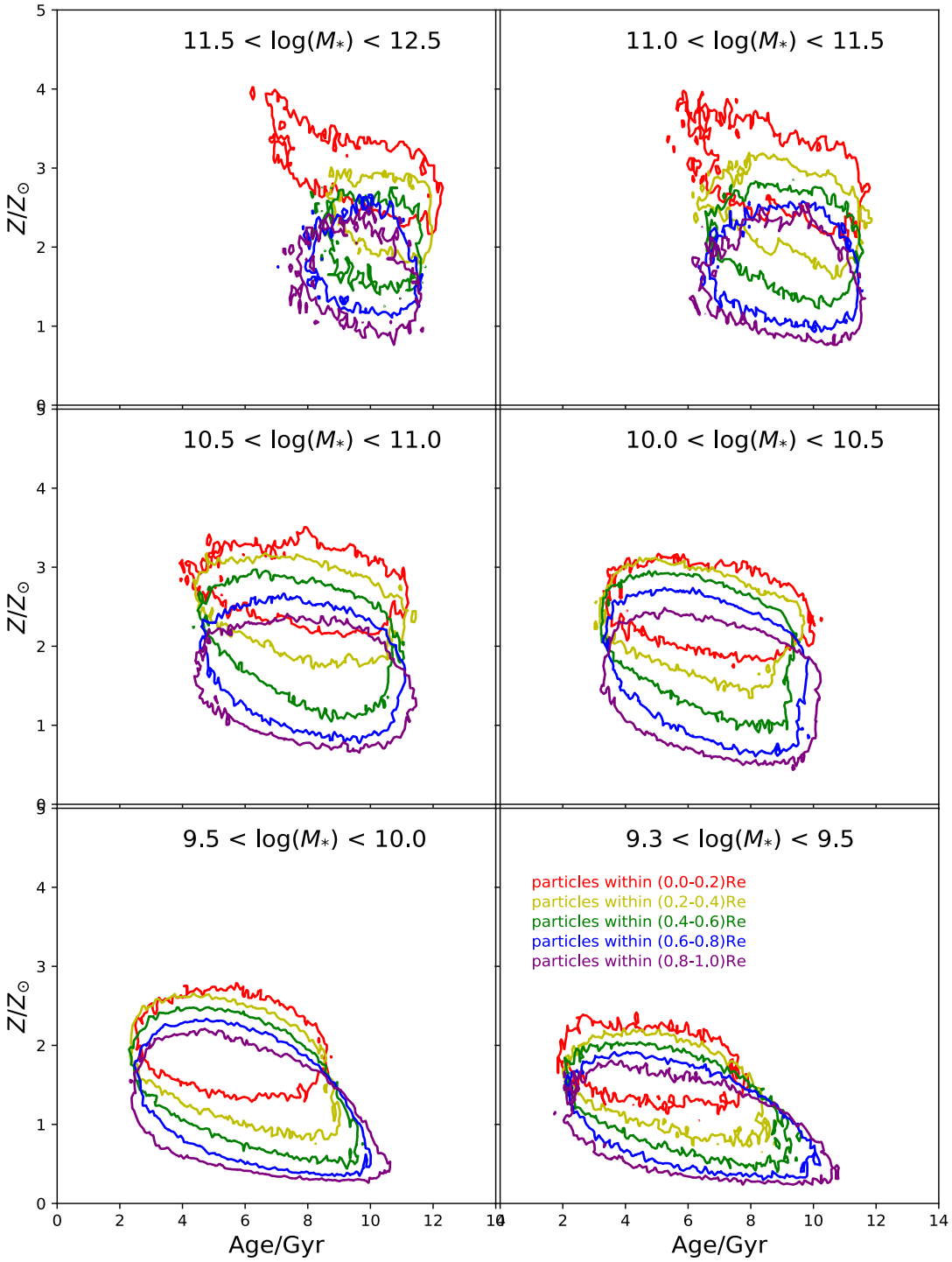

FIGURE 3.10: The contours at average values of the stellar age and metallicity distributions for pixels (from our 2D pixels maps) at different radials (Red: within 0.2Re; yellow: between 0.2-0.4Re; green: between 0.4-0.6Re; blue: between 0.6-0.8Re; purple: 0.8-1.0Re.) of different M_* subgroups. Dots are the average age and metallicity for pixels within certain radial ranges.

To jointly look at the age and metallicity distributions, we study the spatial distribution of all 2D pixels (from 2D binned maps we derived in Section 3.2) in age and metallicity space. We divide the disk into 5 different galactocentric distance bins. For galaxies of each mass range, we get the age metallicity space distributions of pixels within each radial regions, from inside to outside, as shown in Figure 3.10.

In a given radial region, low mass galaxies show broader age ranges and narrower metallicity ranges than the corresponding regions in high mass galaxies. In all galaxies there is a progression to have the most central regions at higher metallicity (e.g., negative gradients). However at low masses we see that the average age *increases* towards the outer regions, while for MW mass galaxies the age is approximately equal at all masses, and for thigh mass ellpticals the age *decreases* as you go to the outer regions, e.g., the existence of 'younger' intermediate ages and very metal-rich populations in the very central regions of massive galaxies. The different age gradients in the different mass galaxies may not only suggest different star formation or assembly histories (e.g. inside-out vs. outside-in) in these different galaxies, but also between different parts of a galaxy.

Though different galaxies or regions may show different star formation histories, the most important factor that shapes the Z gradient may still be the accumulated local stellar mass buildup at the inner part of a galaxy. The age dependency of stellar population distribution here may not exactly map to spatial evolution of stellar population distribution, because of the dynamical evolution (secular migration) of stars. We plan to study the signatures of such effects in TNG on metallicity gradients in future works.

3.3.4 In-situ and ex-situ populations

Our results show that the local accumulated in-situ stellar mass distribution is the main factor that sets the shape of the radial stellar metallicity profiles. However, galaxy merging and accretion are important and almost inevitable process in the evolution of stellar populatoion gradients, as a galaxy can accrete stars that were formed in other galaxies (ex-situ stars) through mergers. Previous studies have shown that the outer region (halo) metallicity gradients of galaxies are correlated with accretion histories (Cooper et al., 2013b; Oogi and Habe, 2013b; Pillepich et al., 2014b; Cook et al., 2016). Therefore, it is necessary to also check the role of those ex-situ stars in the *inner* regions of the galaxy.

The IllustrisTNG simulation allows us to trace the origin of each stellar particle, and when they were formed or brought into the primary halo. Rodriguez-Gomez et al., 2016 investigated several aspects of the stellar mass assembly of TNG galaxies, by employing merger trees and a classification scheme for individual stellar particles. They separated the stellar particles into two groups: 1) in-situ stellar particles, stellar particle were formed along the main progenitor branch of a given galaxy; 2) ex-situ stellar particles, accreted stars that formed within another galaxy and were subsequently accreted.

Using this classification, we calculate the in-situ stellar mass fraction within 1 Re and the associated stellar metallicity gradients of both in-situ and ex-situ populations. As shown in the left panel of Figure 3.11, within 1Re, low mas galaxies ($< 10^{11}$

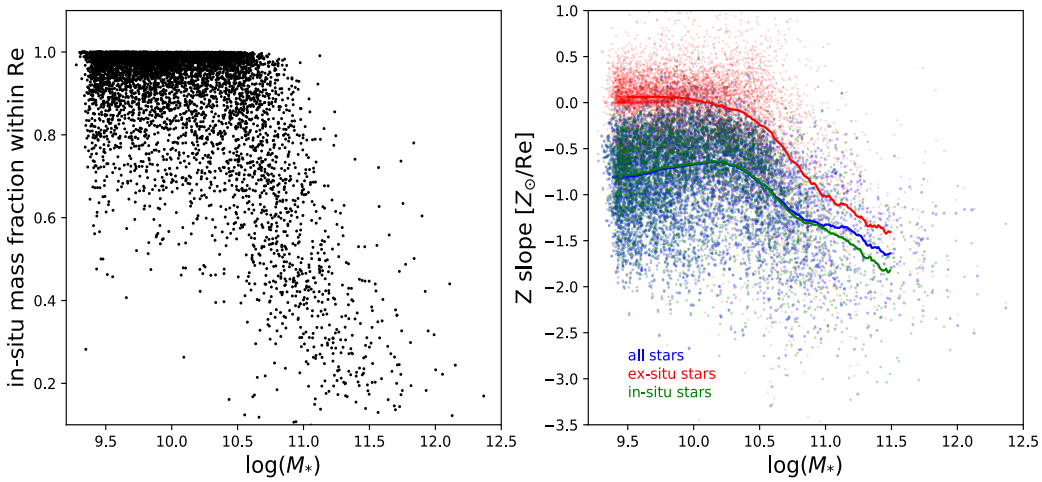

FIGURE 3.11: Left: the in-situ stellar mass fraction within 1 Re as a function of galaxies' stellar mass, colour coded by Z slopes.; right: Z slope within 1 Re for ex-situ stellar particles (red), in-situ stellar particles (green) and all stellar particles (blue).

M_*) are dominated by in-situ stellar particles, while at higher mass ($> 10^{11}$ M_*) the ex-situ components quickly increase with the total stellar mass of the galaxy.

The right panel of Figure 3.11 shows metallicity gradients (Z slope) of both in and ex-situ components, as well as the total stellar particles within 1Re. At all masses the shape of the metallicity gradient (Z slope) vs. stellar mass trend follows is the same for the ex-situ and in-situ stars. The total slope computed over all stars begins to track the ex-situ populations more closely above 10^{11}, as the ex-situ fraction increases.

While the trend with mass of the Z slope is the same for the in-situ and ex-situ populations across the TNG sample, the metallicity gradients of the ex-situ stars are consistently flatter than of the in-situ stars. This is expected as the ex-situ stars are by-nature collisionless and during the merger will be distributed into a more spatially extended configuration than the in-situ stars which retain some spatial coherence with the collisional gas distribution out of which they formed (barring their significant redistribution during the merger itself).

Our result shows the existence of ex-situ stellar particles does not strongly influence a galaxy's radial stellar metallicity gradients within 1Re.

3.3.5 Kinematics

Some previous works have suggested that kinematic properties could play a strong role in shaping the metallicity gradients. For example, Schroyen et al., 2013b used simulations to investigate the metallicity gradients of dwarf galaxies and found that steeper stellar metallicity gradients can form efficiently during the evolution of low angular momentum dwarf galaxies, because the low angular momentum allows more gas to concentrate in the galaxy's central regions, enhancing the star formation in the inner regions.

In our previous work, due to the abundance of kinematic information in CALIFA and available Schwarzschild dynamical models (Zhu et al., 2018d; Zhu et al., 2018b; Zhu et al., 2018a), we investigated if any dynamical properties appear to be strong causal factors in setting the stellar metallicity gradients (though with galaxies at higher mass range). The galaxies in the CALIFA sample are several orders of magnitude more massive than the dwarfs studied by Schroyen et al., 2013b, and in these higher mass galaxies we did not find any obvious correlations between the kinematic features and stellar metallicity gradient.

To compare the TNG galaxies to our previous study, we extract the radial rotation velocities (V_{rot}) and velocity dispersion (Σ_*) profiles of all our IllustrisTNG galaxies following the method described in Section 1.2.2. Figure 3.12 shows the V_{rot}/σ against radial stellar metallicity gradients (defined as: $\Delta Z(r)=Z(r)-Z_{centre}$), in galaxies of different mass concentration (R_{1050}) bins.

We can see that for highly concentrated galaxies (low R_{1050} value) the galaxies show steeper Z gradients and bimodal distributions in angular momenta. When moving to low concentration galaxies, distribution is dominated by relatively high angular momenta points due to the lack of massive galaxies with low mass concentrations. This suggests that the present-day stellar V_{rot}/σ does not appear to correlate with final Z gradient, while mass concentration is always the stronger factor that predicts to the Z gradient. In addition, massive galaxies always have low V_{rot}/σ and high concentration, while lower mass galaxies show large diversity in both V_{rot}/σ and mass concentration.

In the left panel of figure 3.13, we show the V_{rot}/σ against Z gradient for all our galaxies, and this similarly shows a separation between high mass galaxies and other galaxies, with a 'red tail' and a 'blue triangle'. High mass galaxies generally have lower V_{rot}/σ and steeper Z gradients (the red tail). For lower mass galaxies, the correlation is more complicated, with low V_{rot}/σ, Z gradients are mostly flatter, while with higher V_{rot}/σ galaxies show larger diversity in Z gradients and can have steeper Z gradients (blue triangle).

In the right panel, we plot the relation between $\log(M_*)$ and V_{rot}/σ at 1 Re of all our galaxies. This also shows a clear separation between the high mass galaxies and other galaxies: galaxies show an increase in angular momenta as their mass increases, until reaching $\log(M_*) \sim 10.5$. Above that, their angular momentum quickly drops to a very low value. This bimodality we see from the left panel of figure 3.13 is a manifestation of the trends between the high mass galaxies and low mass galaxies shown in the bottom panel.

The left panel of Figure 3.11 suggests the ex-situ stellar mass fraction within 1 Re quickly increases with total stellar mass for massive galaxies ($\log(M_*) > 10^{10.5}$). The V_{rot}/σ drops quickly at this mass range likely due to the onset of mergers (as evident in the ex-situ fraction in Figure 3.11. The angular momentum content may therefore be diluted by mergers, without significant modulation to the metallciity gradients of the inner regions (see e.g., the right panel of Figure 3.11).

In Figure 3.14 we reproduce figure 3.13 again but color coded by the in-situ stellar mass fraction within 1Re. This clearly shows the bimodality in $\log(M_*)$ and V_{rot}/σ space is mostly due to the accretion of ex-situ stars, while the bimodality in $V_{rot}/\sigma_{(Re)}$ and Z slope space is just because both V_{rot}/σ and Z slope have correlations with $\log(M_*)$. This suggests that V_{rot}/σ *as measured at present day*, does not

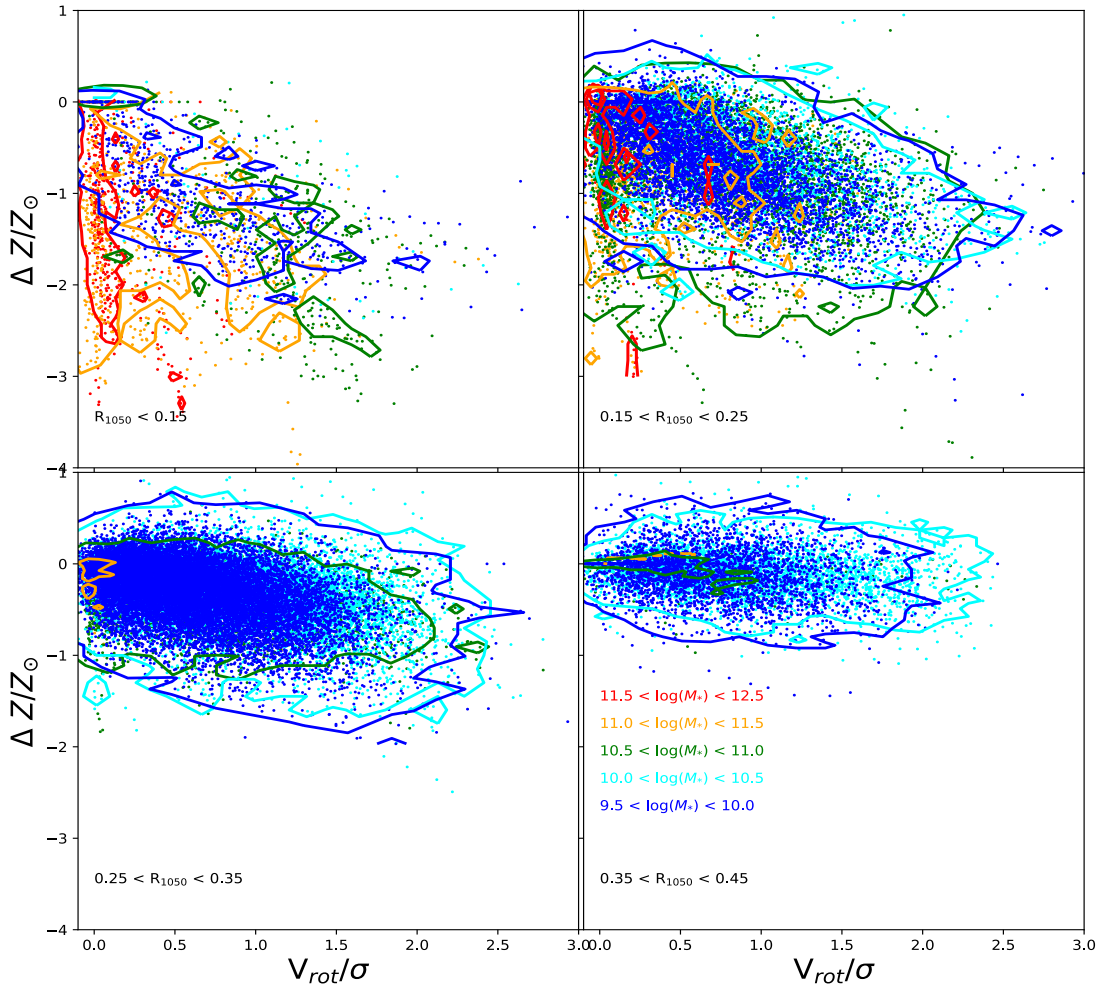

FIGURE 3.12: The V_{rot}/σ against radial stellar metallicity gradient ΔZ of each annuli of galaxies within different $\log(M_*)$ ranges. color coded by different mass ranges.

directly influence the stellar metallicity gradient. It is possible however that the instantaneous V/sigma at the time gas was settling into the disk may have dictated the local star formation distribution in the galaxy disk, and hence played a role in setting the close correlation between mass density and local metallicity.

3.3.6 Environment

Satellite galaxies can show very different features compared to field (central) galaxies. The satellite galaxies in different environments are involved in different levels of environmental processing (tidal stripping, ram-pressure, mergers.).

As the tidal field, ambient gas density and encounter rate may all be a function of the environmental density, we might expect different stellar population gradient for satellite galaxies in different environments. To explore this effect, we also extract the metallicity profiles of satellite galaxies in different environmental densities. We separate our satellite galaxies into two different groups: Inner satellite galaxies that

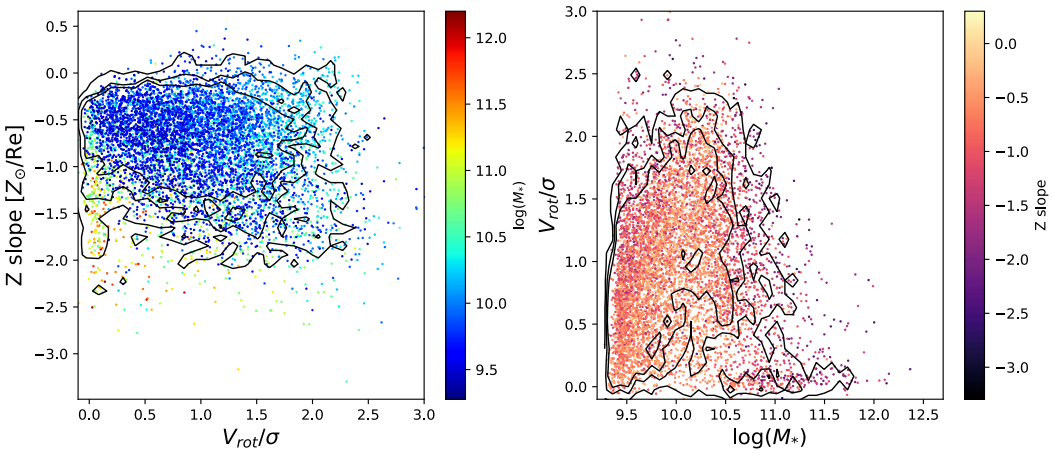

FIGURE 3.13: Left: The relation between $V_{rot}/\sigma_{(Re)}$ and Z slope of all our galaxies, color coded by stellar mass. Right: The relation between $\log(M_*)$ and $V_{rot}/\sigma_{(Re)}$ of all our galaxies, Color coded by their Z slopes.

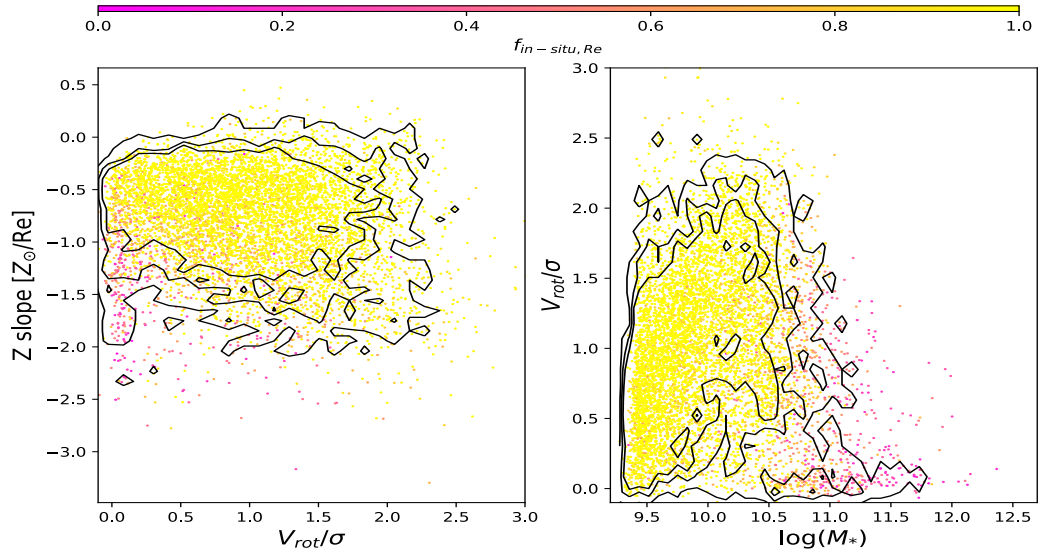

FIGURE 3.14: Similar to figure 3.13. Left: The relation between $V_{rot}/\sigma_{(Re)}$ and Z slope of all our galaxies. Right: The relation between $\log(M_*)$ and $V_{rot}/\sigma_{(Re)}$ of all our galaxies. In both panels the dots are color coded by the in-situ stellar mass fraction within 1Re.

located at present day inside 0.25 of the viral radius (R_{vir}) of the cluster; and outer satellite galaxies located between 0.25 and 1 R_{vir} of the cluster.

Figure 3.15 shows the comparison of central (field) galaxies, inner (r < 0.25 R_{vir}) and outer (r > 0.25R_{vir}) satellite galaxies. We can see the three type of galaxies do show different stellar mass functions, as more massive galaxies tend to be centrals, while inner satellite galaxies show the smallest stellar mass amount the three groups. The sizes of the inner satellites tend to be smaller on average at fixed mass compared to the outer or central galaxies. However the correlation between the metallicity and mass density Sersic indices (ns - nz) does not show a difference in slope or scatter.

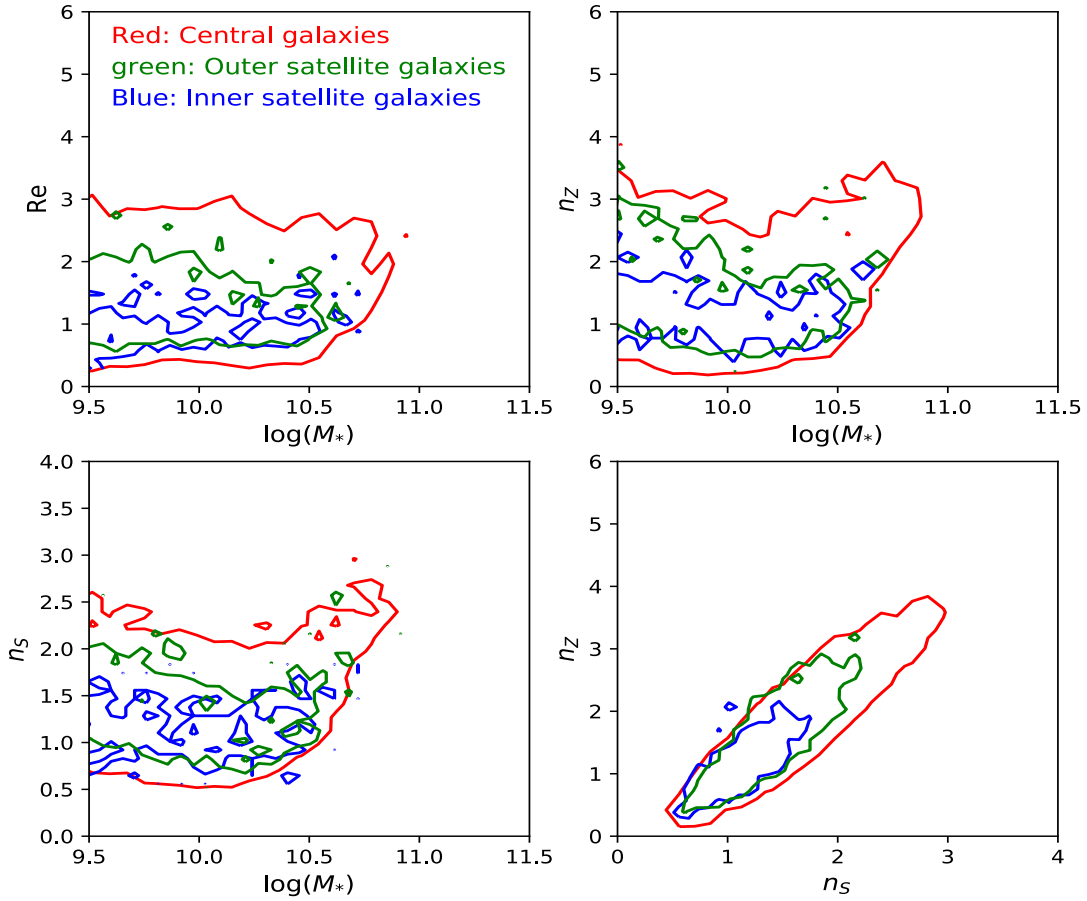

FIGURE 3.15: Comparison between central (red), inner satellite (r < 0.25R_{vir}, blue) and outer satellite (r > 0.25R_{vir}, green) galaxies' distributions in different parameter spaces with contours at average values. Top left: stellar mass against Re; top right: stellar mass against n_Z; bottom left: stellar mass against n_S; bottom right: n_S against n_Z.

3.4 Discussion

Our results using the IllustrisTNG simulation have shown that the stellar metallicity gradient of the inner part of a galaxy is mostly determined by the local stellar mass

buildup.

3.4.1 Comparison to observations

In Chapter 2, we studied the metallicity gradients from CALIFA galaxies, due to their large range in galaxy mass and morphology, provide an excellent sample with which to compare the Illustris results.

When comparing gradients, it is important to keep in mind that the CALIFA galaxies have a lower average spatial resolution (~ 0.4 kpc) compared to the TNG galaxies (profiles for TNG galaxies have 0.1 kpc resolution). This means, for CALIFA galaxies the central peak of both stellar metallicity and Σ_* profiles will be smoothed out. This prevented us from quickly extracting reliable Sérsic indices n_S and n_S. Therefore to compare the link between stellar metallicity gradients and stellar mass concentrations, we have to use different estimators: for stellar metallicity profiles, we use the linearly fit metallicity gradient Z slope. While for the mass concentrations, as we can't get either 'n_S' or 'R_{1050}', we defined a 'stellar surface mass density gradient' ($\nabla\log(\Sigma_*)$) to indicate the gradient of stellar mass:

$$\nabla\log(\Sigma_*) \equiv \log(\Sigma_{*(r=0)}) - \log(\Sigma_{*(r=Re)}) \tag{3.4}$$

Note, the surface stellar mass density Σ_* of CALIFA galaxies is written as $\Sigma_{dyn,*}$ in Chapter 2 to emphasize that the stellar surface mass density in CALIFA galaxies was derived from the dynamical Schwarzschild models (Zhu et al., 2018c).

As shown in the top left panel of Figure 3.16, we compare the Z slope and $\nabla\log(\Sigma)$ correlation of TNG and CALIFA galaxies. Despite of the large scatter of the CALIFA galaxies, they show the same trend as TNG galaxies, in the sense that the Z slope steepens with increasing $\log(\Sigma_*)$ gradient. The large scatter in CALIFA galaxies is most likely due to the lower spatial resolution of CALIFA, as well as the uncertainties in the stellar population (SP) models used to derive the metallicity.

In addition to the global gradients, CALIFA galaxies show a similar local MMR as found in the TNG galaxies. The top right panel of figure 3.16 shows a good agreement in the comparison between the two local mass metallicity relation when plotting the values in each annulli for all the galaxies in both TNG and CALIFA. For the local MMR per pixel, both data show similar correlations in the bottom two panels of figure 3.16. However, the slope of the CALIFA pixel MMR is noticeably steeper, and the scatter larger. This could be due to the difference in pixel numbers and sizes, a larger diversity of inclination angles of the observed galaxies and/or the uncertainties of the measured stellar population values, as most of those tend to smooth the stellar gradients. At first glance, it appears the effects have effected the surface mass density more than the metallicity gradients. The net effect is then to steepen the relation.

3.4.2 Comparison to lower resolution TNG models

As all our analysis is based on the distribution of matter and metals within an effective radius. It is very important to check the effect of the finite numerical resolution of the simulation. As mentioned above, TNG100 has three different resolution sets - our result described in the preceding sections are based on the highest resolution

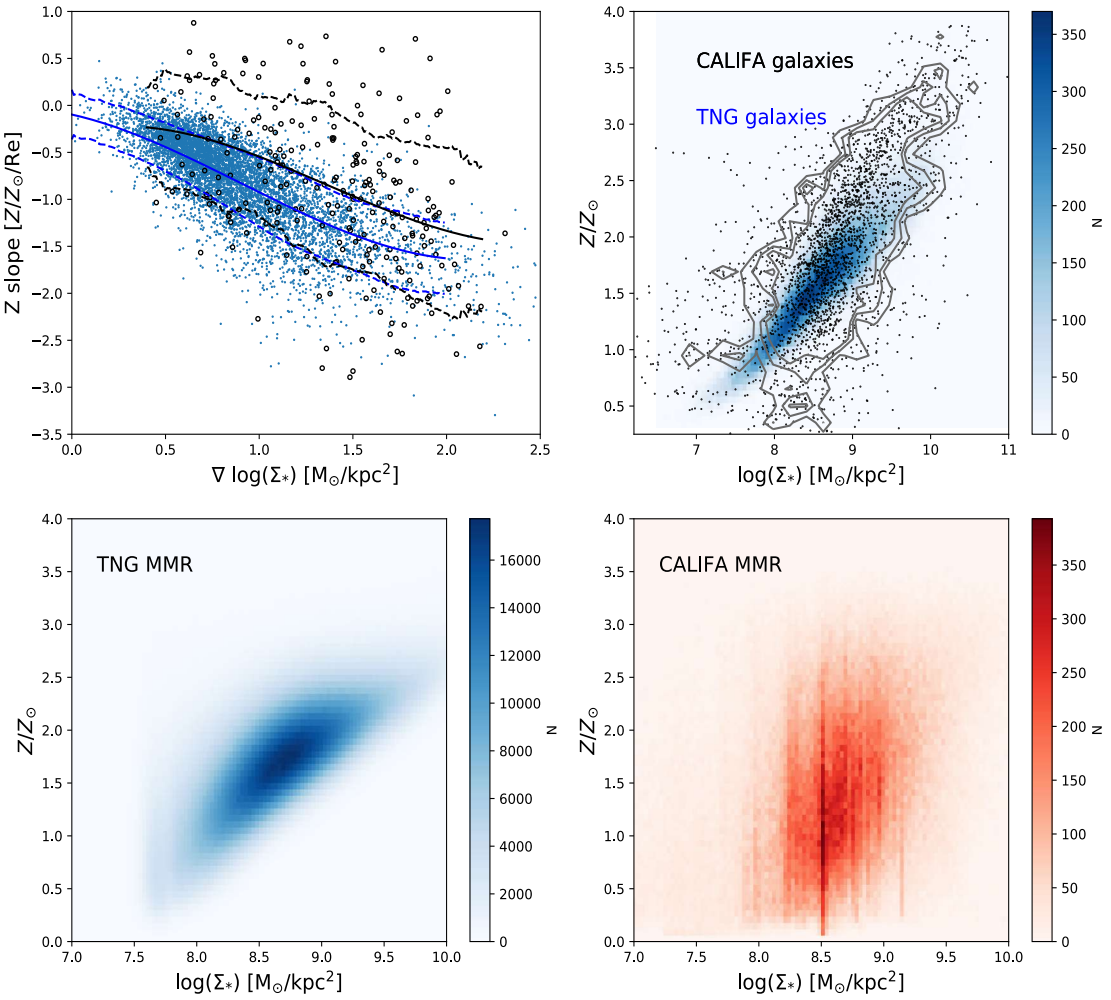

FIGURE 3.16: Top left: Comparison between TNG (black circles) and CALIFA (blue dots) galaxies in $\nabla\log(\Sigma_*)$-Z slope space. Solid and dashed lines are mean and standard deviations. Top right: the comparison between the local mass-metallicity relation per annuli of TNG (blue 2D histogram) and CALIFA (black dots with contours) galaxies. Bottom: the local mass-metallicity relation for all pixels from TNG (left) and CALIFA (right) galaxies.

TNG100(-1) simulation which has a minimum gas gravitational softening (spatial resolution) ~ 0.19 kpc and stellar particle mass $\sim 7.5 \times 10^6 M_\odot$ at z=0. To understand any numerical effects we are able to check our conclusions by analyzing two lower resolution simulations (TNG100-2 with minimum gas gravitational softening ~ 0.38 kpc and stellar particle mass $\sim 59.7 \times 10^6 M_\odot$; and TNG100-3 with typical spatial resolution ~ 0.76 kpc and stellar particle mass $\sim 477.7 \times 10^6 M_\odot$ at z=0).

Figure 3.17 shows the comparison of $\log(M_*)$, Re relation between the three different resolution simulations. The trends are similar however for the absolute value, the lower resolution simulations show larger $R_{(e,2D)}$. This is expected as the low resolution may effectively smooth the central peak of stellar surface mass density profiles. We also notice that the difference between TNG100-2 and TNG100-3 is larger than the difference between TNG100-1 and TNG100-2. This suggests the influence

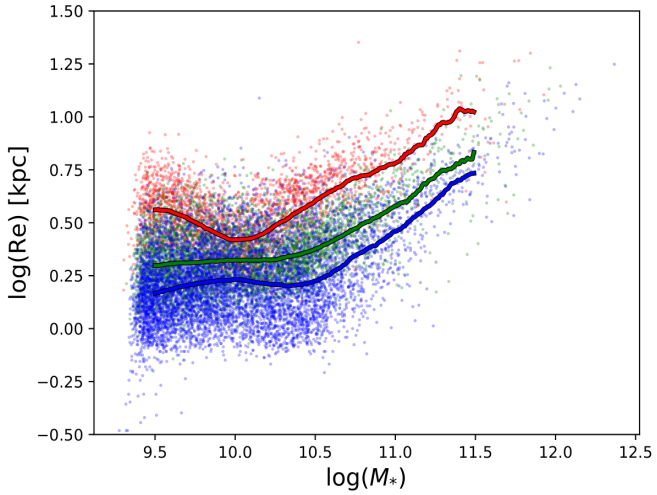

FIGURE 3.17: The $\log(M_*)$, $R_{(e,2D)}$ relations of three resolution TNG100 simulations, blue: TNG100(-1), green: TNG100-2 and red: TNG100-3.

of the limited numerical resolution is becoming less important as the resolution increases.

Figure 3.18 shows average stellar metallicity and surface mass density profiles of different stellar mass bins for different resolution simulations. In general, TNG100(-1) and TNG100-2 show quite good agreements in terms of the shapes and relative positions of average profiles of different mass bins. However, the TNG100-3 data show large difference from the other two with stochastic behaviour evident in the profiles of the lowest mass galaxies. All three resolution simulations show similar profile shapes at high mass bins. But for lower mass galaxies, the $\log(\Sigma_*)$ profiles start to show very high central concentrations when moving towards low resolutions, due to stochastically sampling the small stellar particle numbers. For TNG100-3 we see clear "unnatural" central concentrations (unlikely due to real physical reasons) for galaxies with $\log(M_*) < 11$. For TNG100-2 the average profiles show similar trends and relative positions compared to TNG100(-1). Galaxies with $\log(M_*) < 10$ still start to show averagely "unnatural" central concentrations. For TNG100(-1) we don't see any clear "unnatural" central concentrations in average profiles. This suggests, for higher stellar mass galaxies, different resolutions do not show large discrepancies. While, lower mass galaxies are more sensitive to the resolutions, and start to show averagely "unnatural" central concentrations when resolution reduces.

One possible way to separate these "unnatural" galaxies is to check their local stellar mass-metallicity relations. As shown in the bottom panels of figure 3.18, when the $\log\Sigma_*$ profile shows "unnatural" central concentrations the stellar metallicity profiles may not follow, and actually they appear to show very low stellar metallicity in the central regions. This suggests that the local MMR may show large scatter in low resolution simulated galaxies.

Figure 3.19 shows the comparison of local stellar mass-metallicity relations between the three different resolved simulations. Though the absolute value varies

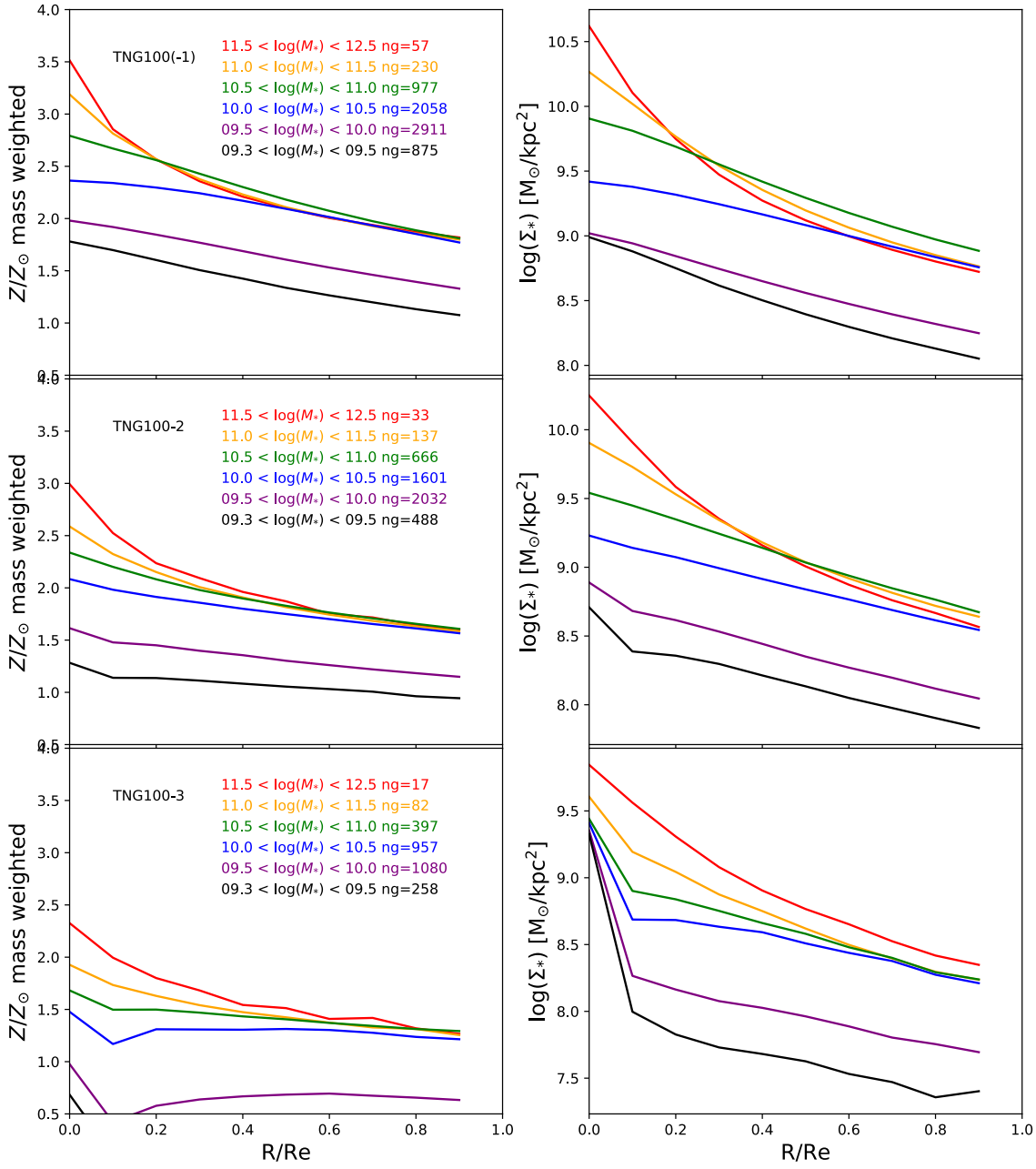

FIGURE 3.18: Average mass weighted stellar metallicity (right) and surface mass density (left) profiles of galaxies within 6 different stellar mass bins. *ng* are the number of galaxies within each bin.

from each other, all three resolutions show clear local stellar MMR. IN the TNG100-3 galaxies, at high $\log\Sigma_*$ regions ($\log\Sigma_* \sim 9.5$) the stellar metallicity shows a drop that is likely reflecting the large discrepancies in the bottom panels of figure 3.18. This lack of correspondance in the local MMR may help us identify the potential "unnatural" galaxies from the majority of TNG100(-1) galaxies.

Figure 3.20 shows the comparison of six basic relations in our result between the three different resolution simulations. Like in figure 3.17 the trend between three different simulations are similar except for the absolute values, and n all cases the

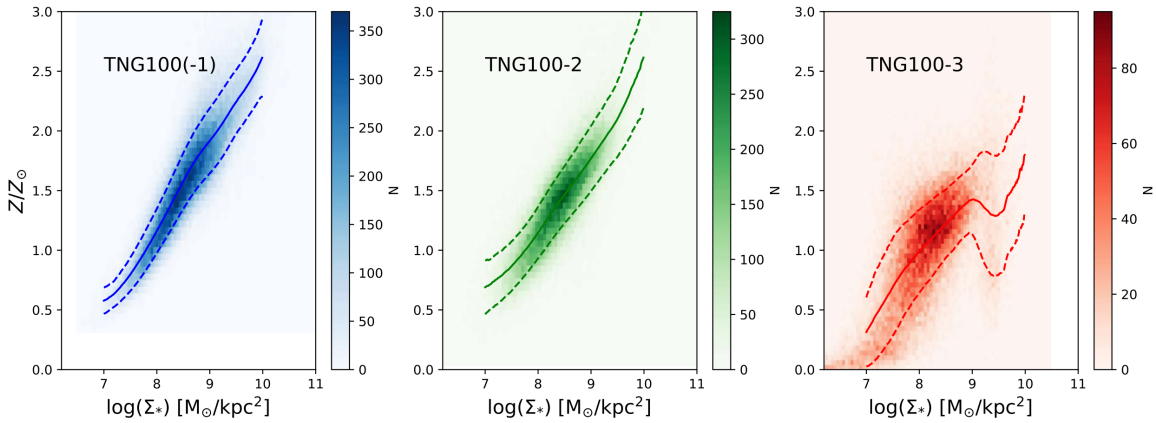

FIGURE 3.19: The local stellar mass-metallicity relations of three resolution TNG100 simulations, blue: TNG100(-1), green: TNG100-2 and red: TNG100-3.

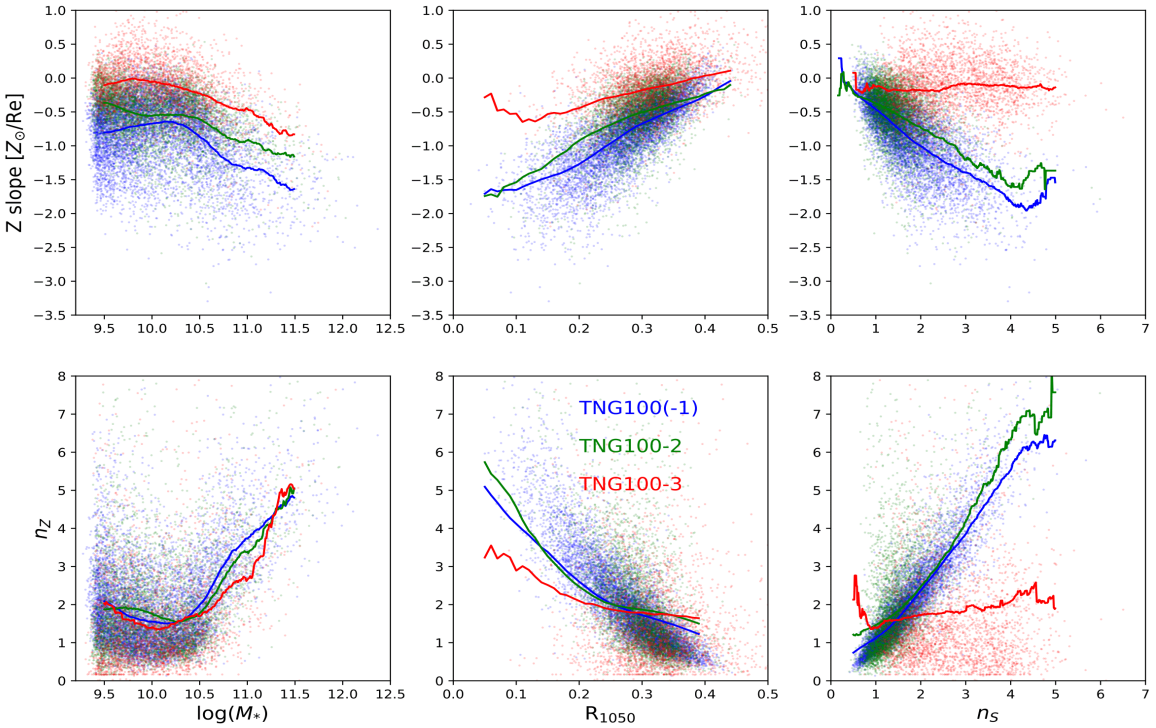

FIGURE 3.20: Top: the relations between Z slope and $\log(M_*)$ (left), R_{1050} (middle), n_S (right); bottom: the relations between n_Z and $\log(M_*)$ (left), R_{1050} (middle), n_S (right) of three different resolution TNG100 simulations, blue: TNG100(-1), green: TNG100-2 and red: TNG100-3.

difference between TNG100-2 and TNG100-3 is larger than the difference between TNG100-1 and TNG100-2. The Z slope and n_Z show a convincing agreement with their relation against $\log(M_*)$; while for the mass concentration R_{1050} and Sérsic indices, the two higher resolved simulations show much better agreement compared

to the lowest resolved one (TNG100-3). This might due to the fact that for low resolution galaxies, the central peak of the surface mass density are too diffuse to extract the reliable $R_{10\%}$ or Sérsic indices (similar to what we find when comparing CALIFA data in Section 3.4.1).

The comparison between three different resolution TNG100 simulations gives confidence that our main conclusions are independent of the limited numerical resolution of the simulation.

3.5 Summary

In this work we study the diversity of stellar metallicity gradients within 1 Re of galaxies by analyzing data from IllustrisTNG100 simulations. We jointly look at galaxies' radial stellar population distributions in relation to their total stellar mass, stellar surface mass density distribution, stellar dynamical properties, stellar in-situ and ex-situ fractions as well as their environments. As we are studying a broad range of mass/morphological type galaxies, in order to avoid the effect of logarithmic suppression, we study their linear metallicity (metal mass fraction; Z) profiles and gradients.

• We find that the shape of the stellar surface mass density profiles and the metallicity profiles in the TNG galaxies are tightly correlated.

• This results in a tight local mass metallicity relation, whereby the regions with higher surface mass density have higher stellar metallicity.

• We show that the radaial metallicity profiles are significantly non-linear and can be described well by a metallicity sersic index. The metallicity and mass Sérsic indices are tightly correlated, and this provides a helpful way to estimate the likely in-situ stellar population gradients when the structural properties of a galaxy are known.

• By jointly looking at the spatial distribution of stellar metallicity and age, we find that the star formation histories may vary in different regions of the galaxy, but that this does not effect the correlation between mass density and stellar metallicity profiles.

• We find that galaxies below log(M*) $\sim$ 10. show positive age gradients, while above that mass they tend to show negative age gradients. In most cases the metallicity gradients are typically negative in the simulated galaxies however.

• We find that, for high mass galaxies ($\log(M_*) > 11$) the existence of ex-situ stars do slightly flattens the total stellar metallicity gradients, but this depends on the ex-situ stellar mass fraction within 1 Re.

• We also examine the role of angular momentum by studying stellar V_{rot}/Σ_* in figure 3.14. Our results show no causal relation between stellar metallicity gradients and present day stellar angular momentum (as traced by V_{rot}/σ). However it is likely that the angular momentum of the gas at the formation epoch of the stellar population was important in stetting the stellar population and mass gradients at that time.

• We do not find significant differences in the correlated behaviour of stellar metallicity and surface mass density gradients if we consider satellite galaxies relative to central galaxies.

In this work we found the local in-situ stellar mass buildup is crucial to a galaxy's stellar metallicity distribution, which agrees with the result of our previous study with CALIFA galaxies (as shown in figure 3.16). Work still remains to incorporate detailed knowledge about the nature of low mass high concentration galaxies, as well as the role of ex-situ stars in flatterning the stellar metallicity gradients of massive galaxies.

Chapter 4

Semi-analytical approaches to model stellar population gradients

This Chapter is based on one of my current project which is still in progress.

Overview:

In this chapter, we aim to use a semi-analytical galactic chemical evolution model to understand the chemical and structural trends we have found from both simulation and observations. We follow this approach in order to check our scenario from a more theoretical prospect of view, where we can isolate particular physical parameters. Based on an analytic chemical evolution model, we create a 1D galactic chemical evolution model which implements two phases of gas inflow in order to create galaxies with different morphological types. We show how this approach successfully reproduces most of the empirical relations we have found in observation and simulations. This will be helpful in illustrating our scenario that galaxies' stellar metallicity distributions are primarily determined by the local accumulated stellar mass.

4.1 Introduction

In previous Chapters we have demonstrated with observations and simulations that there is a link between a galaxy's stellar metallicity gradient and surface mass density gradient. The consequence of this finding, is that for the inner part of the galaxy, a scenario arises where the present-day local stellar metallicity is mainly determined by the local star formation history and in-situ stellar mass buildup. A consequence of this is that radial migratory processes may be minimal, and that how the density of gas that forms stars changes in different regions over different times, will be an important factor.

To test how the local stellar mass buildup contributes to the final metallicity gradient, it would be helpful to have a simple window to isolate this effect. While the simulations described in Chapter 3 are extremely useful for understanding how gradients form, they are difficult to uniquely separate one effect (e.g., inflow, feedback, mergers). A simpler approach is to use analytic chemical evolution models. These can provide a direct way to control variables responsible for the creation of stars and metals. For example, we can study how different outflow or inflow, or chemical yields will impact the final stellar population distributions.

This approach has been successful in past studies of chemical evolution and metallicity gradients (Matteucci and Francois, 1989; Carigi, 1994; Timmes, Lauroesch, and Truran, 1995; Portinari and Chiosi, 1999), but most of them have dealt with the evolution of the Milky Way disk only. In this Chapter, we implement a simple 1D semi-analytic model to test if this simple scenario can reproduce many of the structural and chemical scaling relations we identified in the CALIFA and TNG samples. The novelty of our approach is that we simultaneously focus on the co-evolution of the stellar density and metallicity in the analytic model. In addition, we make the chemical evolution models applicable to galaxies of a wide variety of masses and morphologies. This will allow a more insightful comparison to our previous results. The main purpose of this approach is: 1) to provide a simple physical framework to understand this scenario via a flexible theoretical analytic model for chemical evolution; 2) to study the possible time evolution of Σ_* - Z correlations, and 3) to gain a conceptual understanding of the role of *instantaneous* angular momentum of the gas and its effect on the evolving stellar population gradients.

In Section 1.2.3 we introduced the basic principles of chemical evolution models by using the classic close-box model as an example. To trace the evolution of galactic stellar metallicity gradient, we have to extend the model with spatial factors.

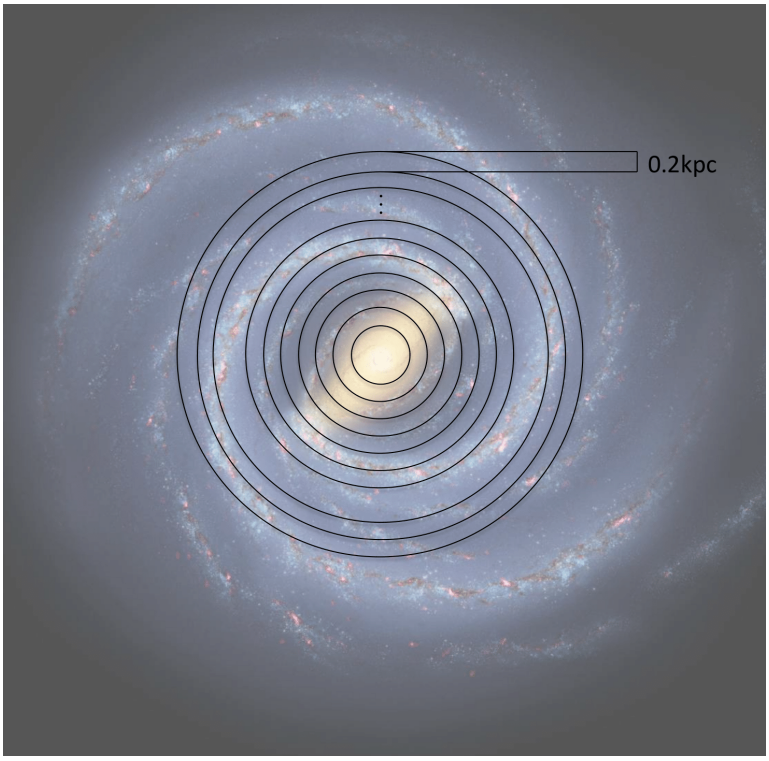

FIGURE 4.1: Illustration showing how we divide a galaxy into a serious of concentric annuli with resolution of 0.2 kpc in order to track the baryon and metal evolution in each region.

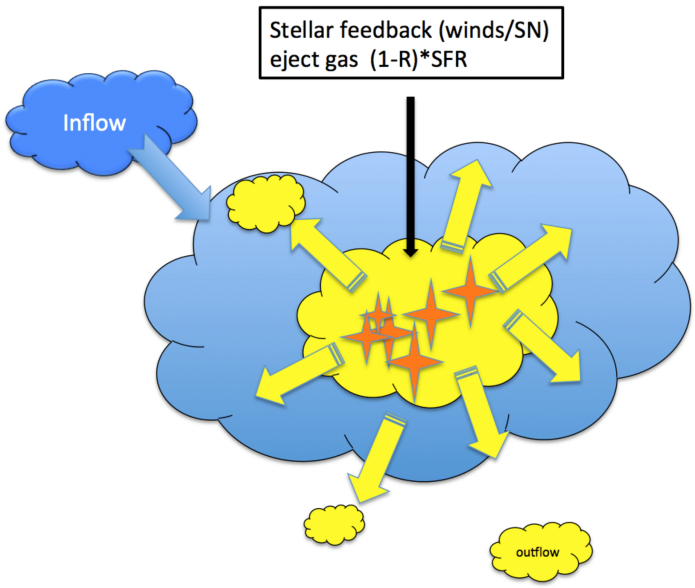

FIGURE 4.2: The cartoon shows the basic processes in the open-box model, which contains the inflow of metal poor gas, local star formation, and the production of metal rich gas which will mix with local ISM, as well as the gas outflows through stellar feedback.

4.2 One dimensional chemical evolution model

In this approach, we assume a model galaxy is a non-interacting galaxy and it evolves in isolation. This is analogous to our definition of central galaxies in the TNG sample, and means the galaxy is located in the centre of its own DM halo. Its growth purely due to the inflow of pristine gas from the circum-galactic medium, without galaxy-galaxy mergers or other environmental interactions.

In order to model the radial profiles of the baryons and metals in the galaxy, we begin by creating a one-dimensional radial grid where we divide the galaxy's disk plane into a set of annuli. We set the width of the annuli to mimic the radial resolution 0.2 kpc, which is comparable to the TNG-100 and CALIFA spatial resolutions. We show a conceptual example of this in Figure 4.1. In order to model the spatial evolution of the galaxy's stellar populations, we model each annuli and let it evolve independently as an open-box. This means that in each radius there can be pristine gas inflow and partially enriched ISM outflows of the gas - but no radial mixing of the gas. Figure 4.2 shows a cartoon that illustrates the basic processes that is considered in our open-box model for each annuli, which we describe below in more detail. In what follows we assume time $t = 0$ is the formation of the galaxy, while $t = t_H = 13.8$ Gyr is the galaxy at present day.

Star formation

For each annuli, we model the evolution of several relevant baryonic components as follows. Stars are formed following an empirical Schmidt Law (see Section 1.2.1):

$$\Sigma_{\rm SFR}(r,t) = v \times (\Sigma_{\rm gas}(r,t)^k) \tag{4.1}$$

here, $\Sigma_{\rm SFR}(r,t)$ is the surface stellar formation rate density at radius r and time t with a unit of $\mathrm{M}_\odot * \mathrm{kpc}^{-2} * yr^{-1}$. While $\Sigma_{\rm gas}(r,t)$ is the gas surface mass density at radius r and time t with a unit of $\mathrm{M}_\odot * \mathrm{pc}^{-2}$, v is the absolute SFR efficiency.

Recent studies show that the SFR is proportional to the local molecular H_2 density (Bigiel et al., 2008). However as we do not trace the ratio between HI and H_2 gas in our model, we instead choose k=1.3 and v=0.0001, which reproduced the trends seen in both our observation and simulation.

Evolution of gas

After stars are formed, they evolve and via feedback (winds, SNe) return the enriched gas to the ISM and blow a fraction of gas away from the galaxy as outflows. We use the instantaneous recycling approximation (IRA) in our model (also seen in Section 1.2.4), which means we assume the metals released from dying stars which stay in the galaxy will mix with the ISM perfectly and instantaneously. Thus, for each step the evolution of the gas $\Sigma_{\rm gas}(r,t)$ is shown as follows:

$$\begin{aligned}\Sigma_{\rm gas}(r,t) =& \Sigma_{\rm gas}(r,t-1) + \Sigma_{\rm SFR}(r,t) \times (1-R_m) \\ &+ \Sigma_{\rm gas,in}(r,t) - \Sigma_{\rm gas,out}(r,t)\end{aligned} \tag{4.2}$$

Where $\Sigma_{\rm gas,in}(r,t)$ is the inflow of gas density (see Section 4.2.1) at certain radius r at certain time t, R_m is the mass fraction of stellar remnants for a stellar population, according to the stellar evolution theory R_m mostly depends on the IMF and stellar metallicity of the stellar population. Thus, $\Sigma_{\rm SFR}(r,t) \times (1-R_m)$ is the gas that is returned from stars through feedback, in addition part of the gas from ISM is lost due to the outflow $\Sigma_{\rm gas,out}(r,t)$.

In reality, there are multiple factors that play roles in regulating the gas outflow rate, e.g. star formation rate, gravitational potential, AGN feedback, ISM distribution (Zschaechner et al., 2018; Koudmani et al., 2019). In this model, for the sake of simplicity, we set the gas outflow rate relative to the local star formation rate, and include a regulator that is a function of the total baryonic (star and gas) mass M_{baryon}. which slightly reduces the gas outflow rate in the central but increases it in the outer part of the galaxy (e.g., https://academic.oup.com/mnras/article/432/3/1894/1078965).

$$\Sigma_{\rm gas,out}(r,t) = 0.3 \times \Sigma_{\rm SFR}(r,t) \times (12 - \log(M_{\rm baryon}(t-1) + 10))/10 \tag{4.3}$$

Evolution of metallicity

To trace the evolution of metallicity, we define the gas metallicity $Z_{\rm gas}$.

$$Z_{\rm gas}(r,t) = \Sigma_Z(r,t)/\Sigma_{\rm gas}(r,t) \tag{4.4}$$

The metallicity here we trace is the abundance of all heavy elements, e.g. total metallicity Z. The subsequent evolution of metals in the gas is described by the following balance equation:

$$\begin{aligned}\Sigma_Z(r,t) =& \Sigma_Z(r,t-1) + y \times (\Sigma_{\rm SFR}(r,t) \times (1-R_m)) \\ & - \Sigma_{\rm Z,out}(r,t)\end{aligned} \tag{4.5}$$

Where $\Sigma_Z(r,t) = Z_{\rm gas}(r,t) \times \Sigma_{\rm gas}(r,t)$ is the metal surface mass density in the gas, $\Sigma_{\rm Z,out}(r,t) = Z_{\rm gas}(r,t) \times \Sigma_{\rm gas,out}(r,t)$ is the metals which are lost in the outflow of gas, y is the total nucleosynthetic yield which is described in Section 1.2.3, R_m is the stellar remnant fraction represents the ratio of mass that is locked in the stellar remnants. To explore the impact of gas inflow in our model, we adopt a constant nucleosynthetic yield $y = 0.01$ and a constant remnant fraction $R_m = 0.35$.

In our model, the metallicity of stars at a certain time t is equal to the gas metallicity at the time when the star was born. The total stellar metallicity at this time and radius $Z(r,t)$, is then the stellar mass weighted average metallicity of all stellar populations contained in that annulus.

$$Z(r,t) = \frac{\int_0^t R_m \times \Sigma_{\rm SFR}(r,T) \times Z_{\rm gas}(r,T) dT}{\int_0^t R_m \times \Sigma_{\rm SFR}(r,T) dT} \tag{4.6}$$

Where, $R_m \times \Sigma_{\rm SFR}(r,T)$ is the surface mass density of each stellar population with its stellar metallicity equals to the gas metallicity at its birth position and time $Z_{\rm gas}(r,T)$. This is the main recipe of our model, as our main purpose is to trace the link between local stellar mass and stellar metallicity, in this work we fix all the parameters (v, k, R_m and y) so they will not change in the rest of the work.

4.2.1 Two-phase gas inflow

In our model, the primary input will be the functional form of the gas inflow (e.g., the shape, scale lengths, masses and time dependence). There are many different methods to address the gas infall to a galaxy, and its impact on chemical evolution. For example, Chiosi, 1980 demonstrated a good agreement between observed chemical properties of the Milky Way Galaxy and their model, by assuming that the disk was formed by infall of pristine gas. Subsequent works introduced different propertis of the infalling as, modifying time or spatial dependence of the gas accretion rates (Lacey and Fall, 1985; Matteucci and Francois, 1989; Malinie et al., 1993; Samland, Hensler, and Theis, 1997).

In particular Chiappini, Matteucci, and Gratton, 1997; Chiappini, Matteucci, and Romano, 2001 presented a model that assumes the Milky Way galaxy experienced two main modes of gas infall. These were intended to represent the formation of the bulge and thin disk, respectively. The first infall mode is responsible for the formation of the bulge and thick-disk stars. The second infall mode forms the thin-disk component, with a timescale much longer than that of the thick disk formation. This model implies that most of the galaxy's initial disk structure, was formed via

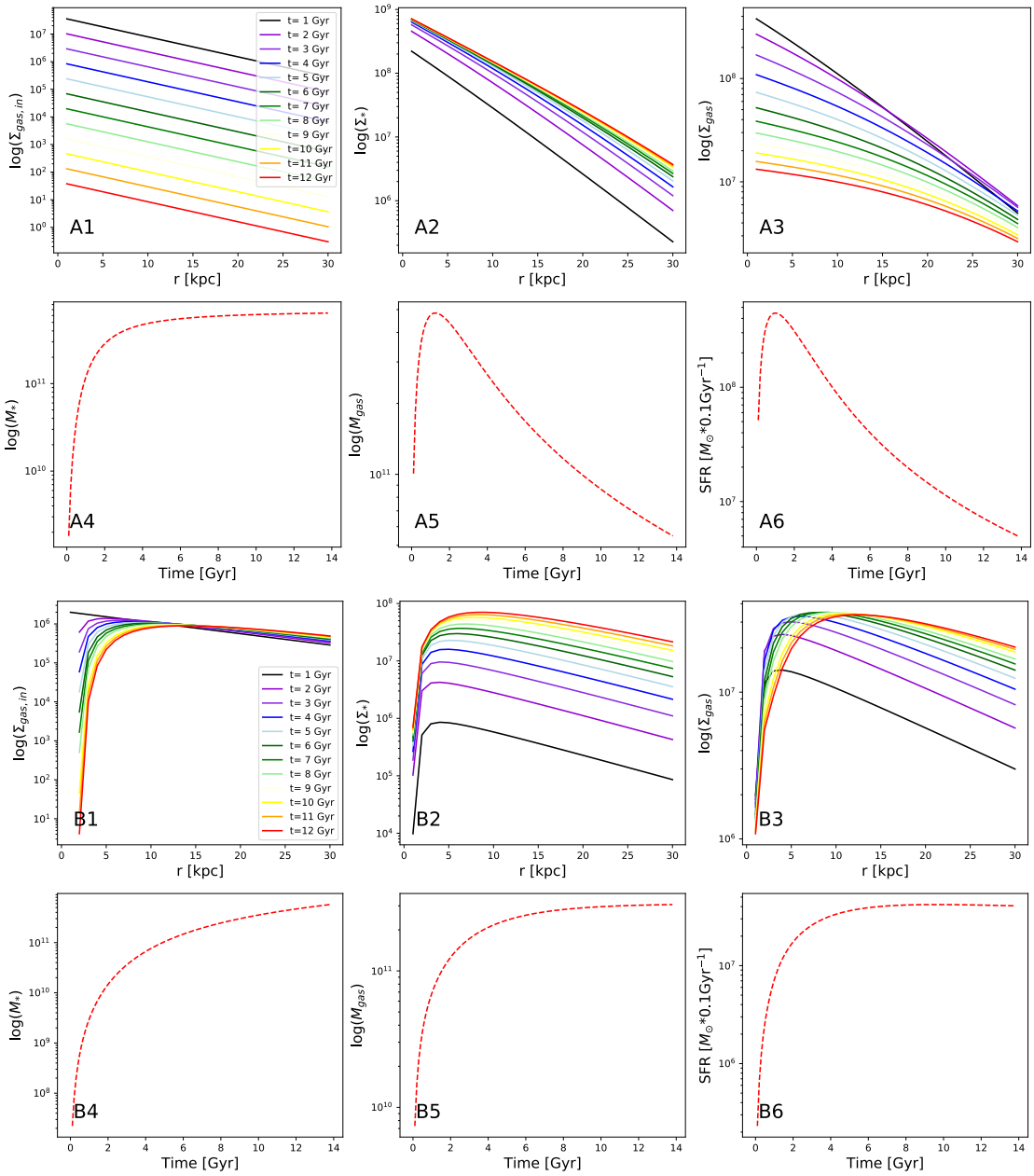

FIGURE 4.3: Comparison of the two modes of gas inflow in our model. Upper six panels (A1-6) show the evolution of a galaxy only with A mode inflow, while lower six panels (B1-6) are the results only with B mode gas inflow. The six panels of each mode show from 1-6, top three panels are the radial distribution of infall gas (right A1,B1), stellar surface mass density profiles (middle A2,B2) and gas surface mass density profiles (right A3,B3) at different ages (color coding is shown in the legend). The bottom three panels are the time evolution of total stellar mass (left A4,B4), gas mass (middle A5,B5) and star formation rate (right A6,B6).

accreting gas from the IGM, though later dynamical processes can reconfigure the orbits of stars.

As we want to study gradients in a wide variety of galaxy types, we need to be able to distribute baryons in many different configurations. In this work we adapt a similar two mode gas inflow prescription into our model, in order to flexibly reproduce galaxies of different morphological types. Here we name the two modes mode A (low angular momentum) and mode B (high angular momentum). We use mode A to represent the infalling gas that carries low angular momentum. This may represent gas from the fast collapse of initial clouds in the early stages of the galaxy. Such inflow may be responsible for the formation of a galaxy's bulge. Mode B is meant to represent higher angular momentum infalling pristine gas from the IGM, mostlyin the later stages of the galaxy's evolution. This form of accretion is likely responsible for the formation of disk components in galaxies. By varying the amount of inflow in each mode, we thus will be able to test how galaxies of different morphologies can form in this simple picture. The two phase infall model is theoretically motivated, as simulation studies suggest a dichotomty in gas accretion modes is an important aspect of galaxy assembly, and maybe a function of galaxy mass and redshift (Brooks et al. 2007, Keres et al. 2005).

In our model, Mode A inflow distribute gas in the galaxy with a Sérsic radial surface density profile, and the infall rate decreases with time exponentially with respect to the Hubble time (t_H). This is in agreement with the decline of low-angular momentum cold-flow accretion with decreasing redshift (Brooks et al. 2007). As this mode is representing gas which later may go on to form stars within a centrally concentrated bulge component, it is described as a function of radius and time in terms of an amplitude D_A, a Sérsic index n_{Srsic}, and a scale length Rd_A.:

$$\Sigma_{\mathrm{gas,in,\ A}}(r,t) = D_A \times e^{-(2n_{Srsic}-0.331)\times(-r/Rd_A)} \times e^{-t/t_H} \tag{4.7}$$

Mode B gas inflow distributes gas in the galaxy with an exponential radial surface density profile and has its peak gas infall at time t_{max}, and is spread out over a characteristic timescale $t_D(r)$. Together these parameters introduce a time-lag to the inflow as radius increases, in order to mimic the inside-out formation of the disc component:

$$\Sigma_{\mathrm{gas,in,\ B}}(r,t) = D_B \times e^{-r/Rd_B} \times e^{(t-t_{max})/t_D(r)} \tag{4.8}$$

where D_B is the amplitude of the infalling gas, t_{max} is the peak inflow time, Rd_B is the scale length, and t_D is a radius dependent time delay term given by:

$$t_D(r) = \min[]0.01, (1.03r - 1.27) \times 10] \tag{4.9}$$

We note that D_A and D_B are the initial mass weight of each mode are defined a single time for each galaxy. Thus even though this is a 1D description of the gas density profile, the ratio will give some inidication to how spherical and pressure supported a galaxy is relative to a pure disk.

Figure 4.3 shows a comparison of those two modes of gas inflow in our model, by evolving an example galaxy which only has mode A gas inflow (upper six panels) or mode B gas inflow (lower six panels). The difference between the two modes is evident in the time evolution of the infalling gas ($\Sigma_{gas,in}$) radial surface density profiles (panels A1 and B1).

The A mode shows similar $\Sigma_{gas,in}$ radial profiles at all times, and at every radii $\Sigma_{gas,in}$ decreases with time. In this mode, gas distributions are very centrally concentrated, due to the non linear correlation between star formation rate and gas density (equation 4.1). Because of this, large amounts of gas in the central region will be transformed into stars in the early periods. This leads to a steeper stellar surface mass density profile (panel A2) and a fast exhaustion of gas in the central region (panel A3). From the time evolution tracks (panels A4,5,6) we see the galaxy experiences an intense star formation activity in the early period that forms most of its stellar mass and uses up most of the gas.

Conversely, B mode shows an evolving shape of the $\Sigma_{gas,in}$ radial profiles with time. At each radius $\Sigma_{gas,in}$ increases first to the peak time for that radius, then decreases with time. In this mode, gas is very smoothly distributed along the disk. Compared with mode A, mode B shows flatter final stellar surface mass density profiles (panel B2) and with large amount of gas in the disk regions (panel B3). From the time evolution tracks (panels B 4, 5, 6) we see the galaxy experiences a weaker but much more extended star formation history during its life time, forming stars almost constnatly over its lifetime.

In reality, a galaxy will undergo accretion following both modes. By combining the two modes with different ratios (D_A, D_B), we can mimic the evolution of galaxies with different morphological types (characterized to first order by different surface mass densities or concentrations). For example, for bulge dominated early type galaxies we would have a higher ratio of mode A gas inflow; for more disk dominant late type galaxies, a higher proportion of mode B gas inflow. In summary, the only five parameters that define our inflow gas D_A, Rd_A, D_B, Rd_B and n_{Srsic}, can be used to model the evolution of a wide range of galaxy morphologies. We note that our model can only be used to describe isolated in-situ formed galaxies. For massive ellipticals with high accretion fractions (Vincente-Gomez et al. 2015), their morphology is most likely due to the external dynamical processes (mergers, interactions), and these may impart different chemical evolution features.

Figure 4.4 shows the evolution of a model galaxy, with present-day $\log(M_*) \sim$ 10.22 and has a total A mode gas infall $\sim$ 10.06 and a total B mode gas infall $\sim$ 10.07. From the profiles we can see a clear difference between a central bulge with steeper metallicity and mass profiles, and outer disk regions dominated by flatter profiles. Both $\log(\Sigma_*)$ and Z_* profiles show similar shape at present time (red), but can be quite different in the earlier stages. This is what we might expect as the Σ - Z correlation is based on local in-situ star formation in this model, and the relation becomes more prominent when a larger amount of stellar mass is built-up. From the time evolution plots (right) we can see the galaxy experienced an intense star formation period at early epochs. After the quick exhaustion of gas and rapid assembly of stellar mass (especially in the central region), after 2 Gyrs the star formation rate starts to decrease.

4.3 Results

With all the prescriptions for gas inflow and chemical evolution specified, we can now assess how well the model reproduces the results of stellar population and mass density gradients seen in observations and simulations.

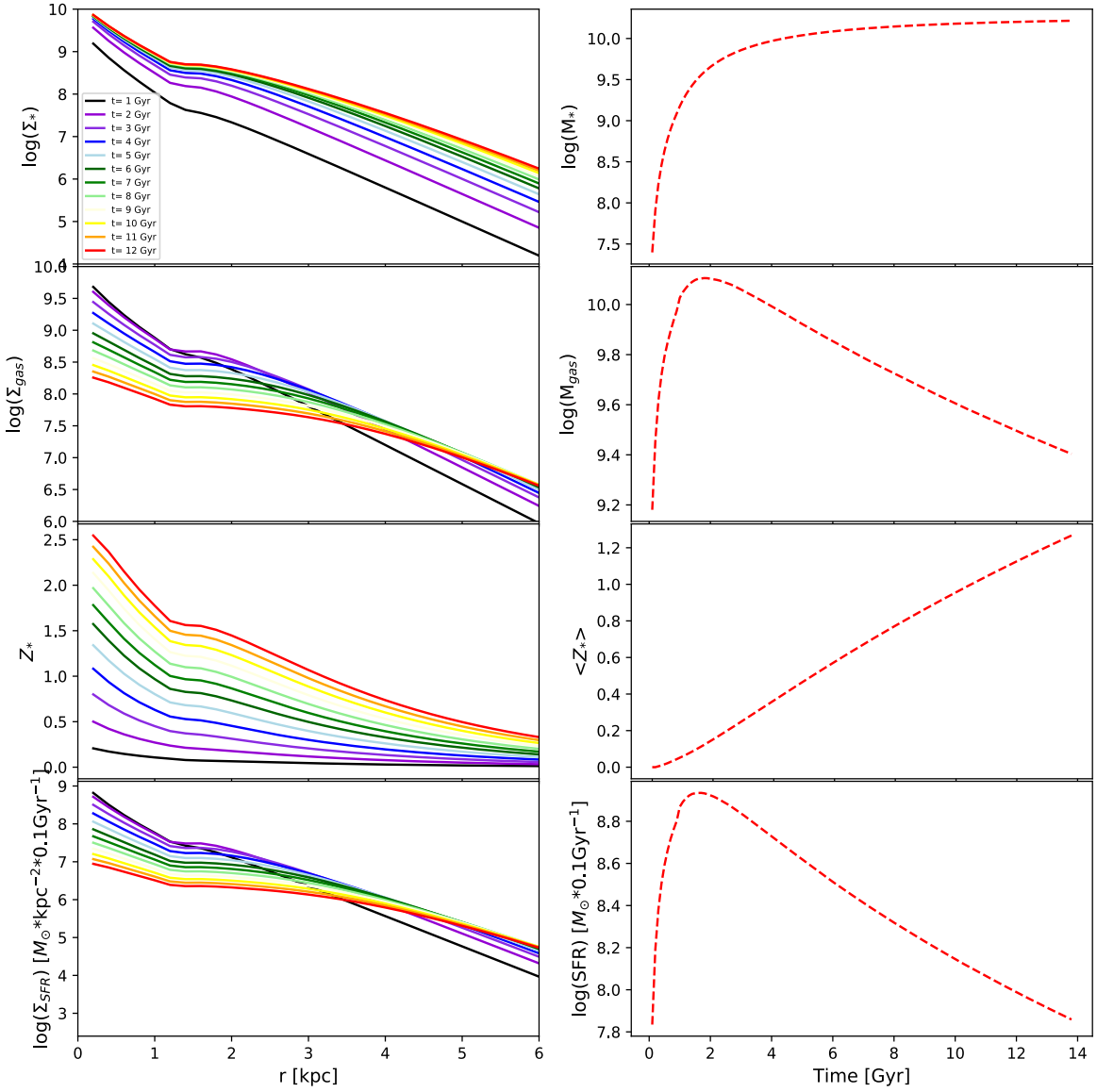

FIGURE 4.4: Left: radial profiles of $\log(\Sigma_*)$, $\log(\Sigma_{\rm gas})$, stellar metallicity and $\log(\Sigma_*)$ at different ages. Right: time evolution of the integrated $\log(M_*)$, $\log(\rm M_{gas})$, stellar metallicity and log(SFR).

4.3.1 Structural calibration

As we have mentioned before, the primary input in our model is the inflow gas distribution. Unfortunately, how the gas inflow occurs in different periods of a galaxy's assembly is a topic that is more or less unconstrained from present day observations. We therefore decide to use the present-day structural scaling relations to calibrate the inflow parameters of our model. With those specified we can then ask what the stellar population predictions are that result from the structurally calibrated galaxy chemical evolution model. Below we describe how we calibrate our models by first asking what inflow parameters make galaxies of the correct *structure* - in particular the galaxy mass-concentration relation.

For the first step, we run 20000 models with different gas inflow patterns, by randomly setting the five input parameters within certain ranges. Each parameter is drawn from a uniform distribution independently (with $\log(D_A)$ and $\log(D_B) \in$ (8.75,11.25), $Rd_A \in$ (0.5,10), $Rd_B \in$ (1,20), and $n_{Srsic} \in$ (0.25,10)). Figure 4.5 show the result of the 20000 models in the present-day $\log(M_*)$ - n_S space. Pink dots shows the model galaxies that are created through these random parameter draws, while the blue dots are structural parameters of the TNG galaxies.

The pink dots in Figure 4.6 show the input parameter spaces for all our models. As the input parameters for the inflow model are chosen uniformally over a wide range of values, they are not anticipated to make solely galaxies which follow the physical scaling relations observed in galaxies. Therefore, in the second step we isolate galaxies which have present day structures which match the TNG galaxies. To do this we select all of our model galaxies which follow the $1-\sigma$ TNG stellar mass-morphological relations ($\log(M_*)$ - n_S and $\log(M_*)$ - $R_{\rm eff,2D}$ relations). These more physical SAM galaxies are shown in Figure 4.5 as the red dots.

In Figure 4.6 we show the distributions between our five different input parameters for all our model galaxies (pink dots) and with our calibrated physical SAM galaxies in red. One can see, in general the shape and size of mode A inflow profiles are better constrained by the present-day physical relations, as the mode B always follows an exponential profile. In general, there are some weak correlations between the input parameters, but it is apparrent that there is no one parameter that is the most dominant predictor of whether the SAM model will make a structurally appropriate galaxy. We also note that the model parameters are held constant over all times.

The results of Figure 4.5 show that our model can be calibrated in order to reproduce the structural correlations seen across a wide range of galaxies in the Illustris TNG simulations. Figure 4.6 shows that there is no one or two key parameters which allow for physical galaxies, but rather a combination of all five inflow parameters is important in making galaxies with the appropriate size and concentration. We can now ask what are the predicted stellar population distributions for these structurally calibrated SAM model galaxies.

4.3.2 Metallicity gradients

With the gas inflow parameters calibrated to reproduce the correct galaxy physical structures, we next check the resulting relations between the galaxies' stellar mass distribution and metallicity predicted in our analytic chemical evolution model. The simplicity and clarity of the models means that we can easily understand and test our scenario for whether stellar metallicity gradient in the inner part of a galaxy is mainly depending on its local in-situ stellar mass buildup. For each galaxy, with a gas inflow set from the physical parameter draws, the 1-D chemical SAM model produces the stellar metallicity in each annuli at each time. From this we can directly measure the radial profiles of stellar metallicity, surface mass density, age, and compare these for ensembles of SAM model galaxies, to the galaxy distributions in simulations and observations. In addition to the radial profiles, we also calculate the metallicity gradient estimators: Z slope and metallicity Sèrsic index n_Z as well

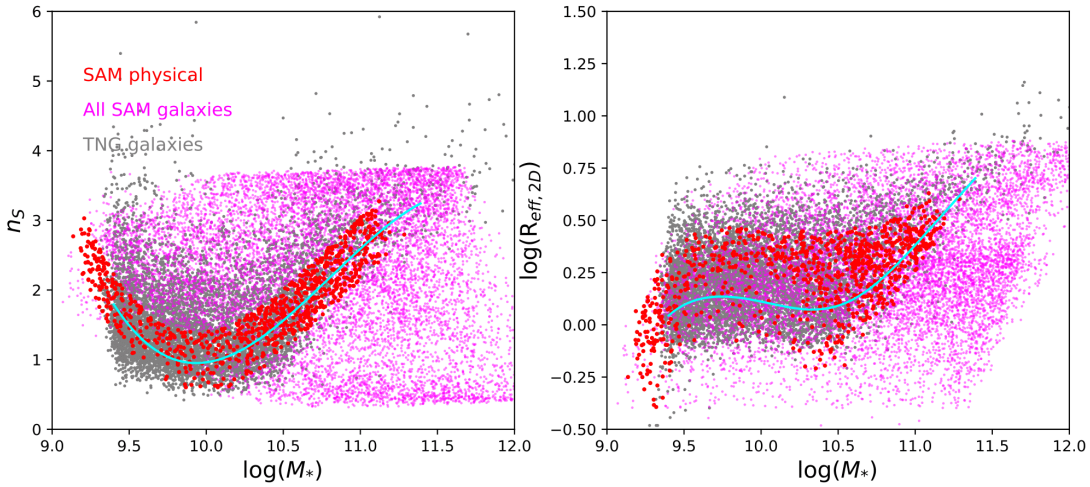

FIGURE 4.5: Comparison between TNG results (Blue) and our SAM model results (pink) in log(M_*) - n_S space (left) as well as log(M_*) - $R_{eff,2D}$ space (right). Cyan lines are the mode lines of TNG galaxies distributions. Red dots are the picked SAM model galaxies we picked according to the physical stellar mass-morphological relation of TNG galaxies.

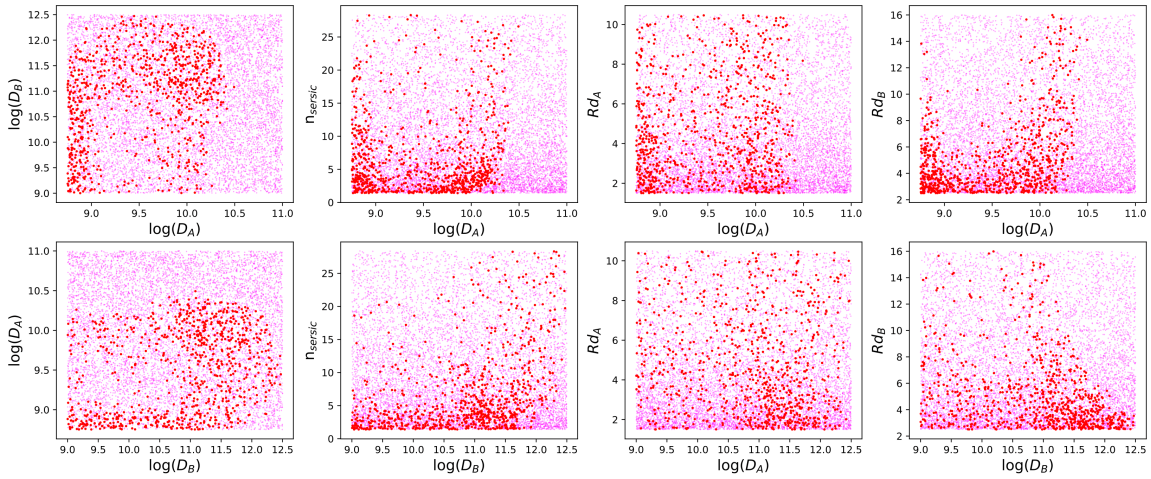

FIGURE 4.6: The input parameter space of all our 20000 models (pink dots) and the physical galaxies (red dots): Top 4 panels are the log(D_A) against log(D_B), n_{Srsic}, Rd_A and Rd_B. Bottom 4 panels are the log(D_B) against log(D_B), n_{Srsic}, Rd_A and Rd_B. (in kpc).

as the mass Sèrsic index n_S, which is also an indicator of the galactic morphology and mass concentration.

In Figure 4.7 we plot the distributions of the two stellar metallicity estimators: Sérsic metallicity index n_Z and the linear Z slope as a function of the model galaxy present day stellar mass. For galaxies of all masses our SAM model shows steeper metallicity gradients compared with the TNG galaxies, at least in an absolute sense. This is likely due to a combination of numerical and astrophysical effects (resolution

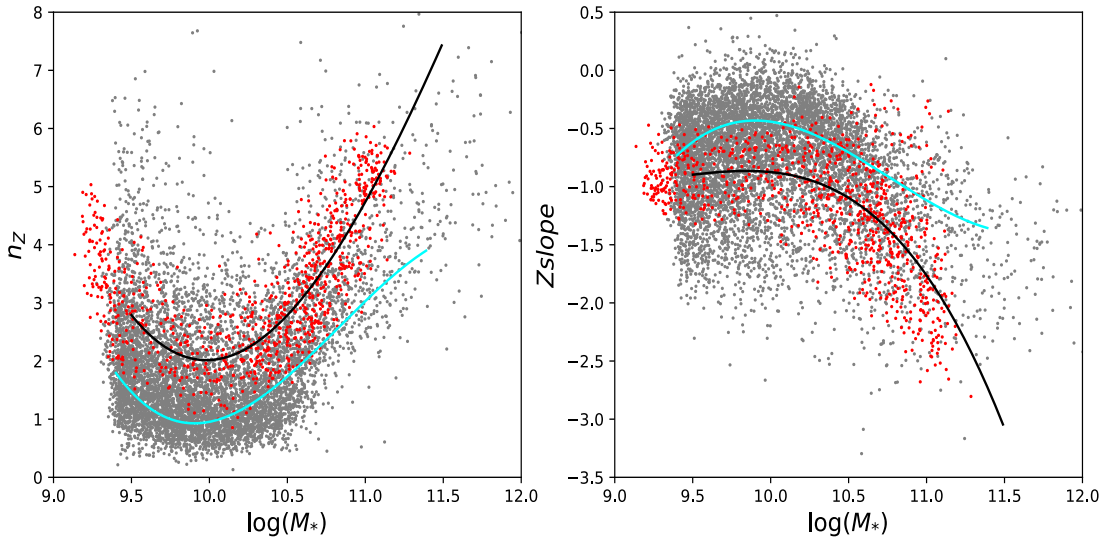

FIGURE 4.7: Comparison between TNG results (gray) and our calibrated model prediction (red) in different present-day stellar metallicity gradient parameter spaces. Left: Stellar mass against n_Z; right: Stellar mass vs Z slope. Cyan lines are the mode lines of TNG galaxies, while black lines are the best fit from SAM physical galaxies.

smearing out the central metal rich regions, absence of mergers or migration effects) as we have discussed in the previous Section 3.3.4. However the differential trend of metallicity gradient strength with stellar mass is very similar.

In Figure 4.8 we show the correlation between stellar mass and metallicity Sérsic indices for our selected SAM physical galaxies, within different stellar mass bins. The plot of $n_Z - n_S$ shows nearly identical slope as the TNG simulated galaxies. The tightness and similar slope of this correlation is a success of our model. As our models does not include migration or other effects, the reproduction of this slope is a strong indicator that the correlation between $n_Z - n_S$ arises due to in-situ star formation processes.

We note there is a systematic shift between the TNG galaxies and our SAM physical galaxies, with our SAM model galaxies showing steeper Z gradients compared to the simulation. As the TNG simulated galaxies have finite spatial and mass resolution, and include effects such as feedback driven gas mixing, migratory processes and merging of satellite galaxies, we naively would expect some offset to this relation.

In Figure 4.9 we show the local stellar mass metallicity relation in our SAM physical galaxies, within different galaxy stellar mass bins. Here we show the surface mass density of stars and average metallicity within each annuli of the ensemble of SAM model galaxies. Our SAM model produces a very clear local mass metallicity relation and the slope of the relation agrees well with TNG galaxies at low stellar mass bins. At higher stellar mass bin, our local mass metallicity relation shows steeper slopes. As we have mentioned above, this is probably due to our simple model not incorporating other factors (radial migration, AGN feedback, interactions) which mostly contribute to the flattening of gradients. Most of these

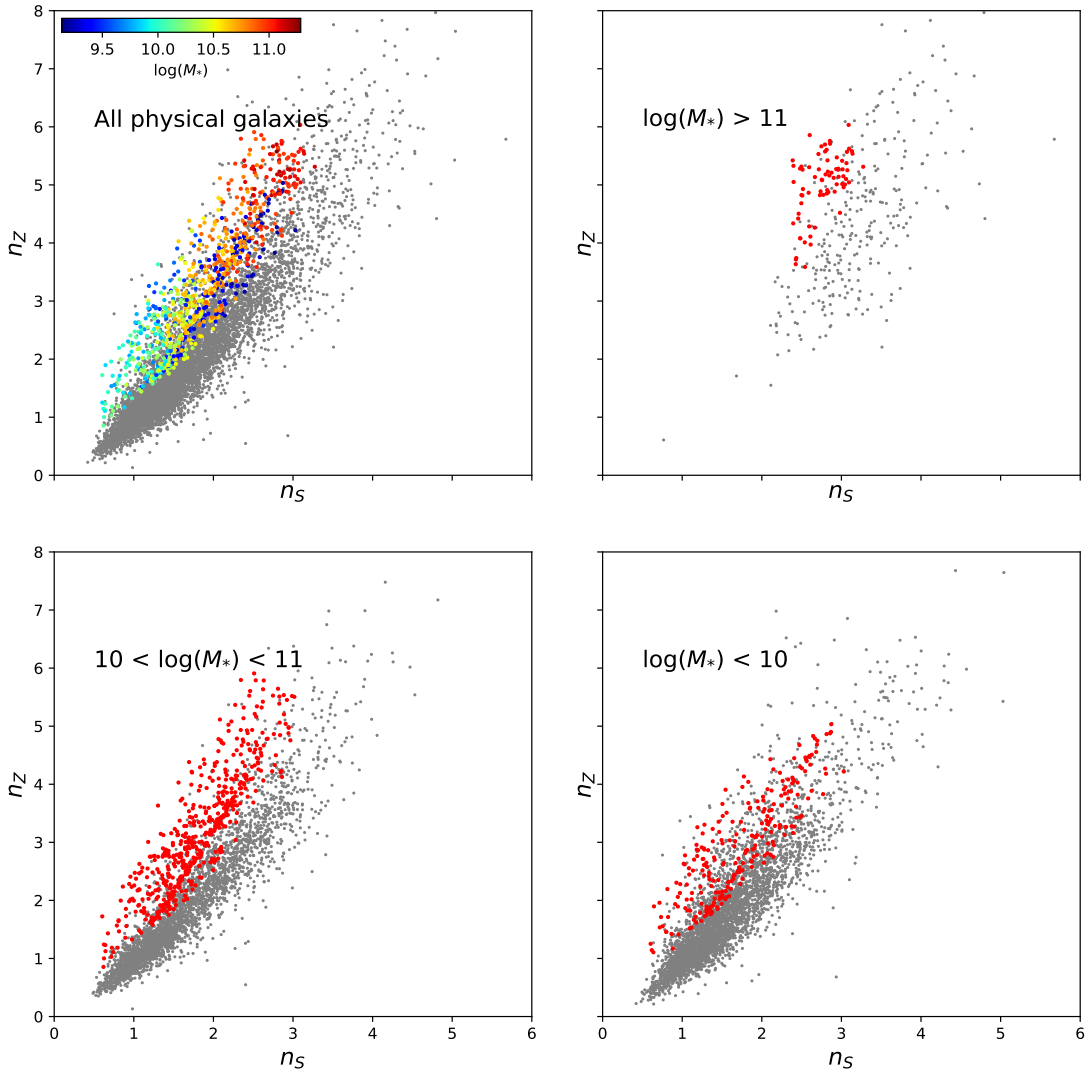

FIGURE 4.8: Comparison of n_S - n_Z relations of our selected SAM physical galaxies within different mass bins. Top left: all our SAM physical galaxies with color coding by their stellar mass. Top right, bottom left and right are the high ($\log(M_*) > 11$), intermediate ($10 < \log(M_*) < 11$) and low ($\log(M_*) < 10$) mass SAM physical galaxies respectively. Background gray dots are the n_S - n_Z relations for TNG galaxies within certain mass bins as a comparison.

processes would begin to dominate in the high mass galaxies, and so the effect is expected to be largest when we look at the high mass galaxies. Unlike Figure 4.8, we do not see an offset in this relation, but rather a tilt. This is still consistent as an offset in the Sersic index would correspond to a tilt in the local mass metallicity relation. This Figure then gives a more intuitive understanding to how the MMR is tracing the local mass metallicity relation, and the reproduction of it by our simple SAM model, hints to its importance and result of the local stellar mass buildup in setting galaxy stellar population distributions.

The main result from seen in the structural and metallicity correlations in our

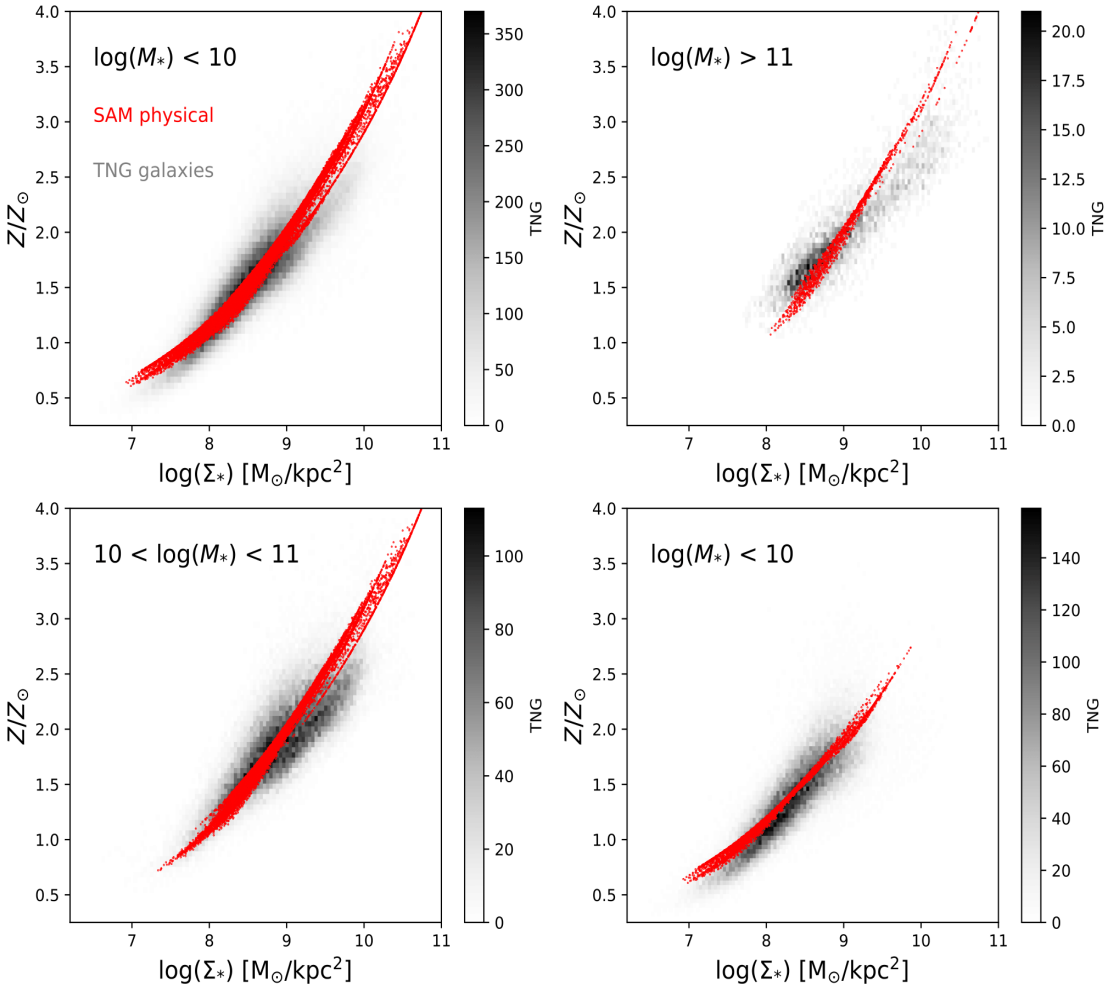

FIGURE 4.9: Local MMR per each annuli of our selected SAM physical galaxies within different mass bins. Top left: all our SAM physical galaxies with color coding by their stellar mass. Top right, bottom left and right are the high ($\log(M_*) > 11$), intermediate ($10 < \log(M_*) < 11$) and low ($\log(M_*) < 10$) mass SAM physical galaxies respectively. Background gray scale maps are the local MMR per annuli for TNG galaxies within certain mass bins as a comparison. Surface mass densities are in units of $M_\odot$ kpc^{-2}.

SAM model is that there is a clear causal link between the type of gas inflow, subsequent star formation integrated over time, and the final stellar metallicity profiles. Future analytic models that can study how much additional factors (feedback, mixing) can be added without deviating strongly from the observed or simulated relations would be of interest.

4.4 Discussion

The simple SAM model results have shown that by modulating what type of gas inflow a galaxy undergoes, a variety of stellar metallicity and mass structural relations

can be reproduced. Given the limited physical processes contained in the analytic chemical evolution model, this exercise suggests that the that the present-day stellar metallicity gradient of a galaxy's inner region is mostly determined by the in-situ star formation history. Below we look at how the models can illuminate aspects of the stellar population gradients' time evolution and correlation with kinematics.

4.4.1 Time evolution of model metallicity gradients

A novel aspect of our model is that we can follow the buildup of the stellar and metallicity profiles as they evolve 4.4. This can allow us to predict what metallicity profiles might look like at different redshifts, or the diversity of paths that a galaxy can take to get the same redshift zero structural and stellar population gradients.

To study the evolution of both stellar surface mass density and metallicity gradients, for each time step we calculate their estimators (n_Z, n_S, Z slope and $\log(\Sigma_{\rm Re})$-$\log(\Sigma_{\rm centre})$) in the model galaxies. The top two panels of Figure 4.10 show the mass evolution of stellar and gas components for our SAM physical galaxies. Most of model galaxies share the same time evolution trend, with a rapid increase in stellar mass in the early stages of the galaxy (before 2 Gyrs), accompanied by a slow decrease in the total gas mass.

The middle two panels of Figure 4.10 are the time evolution of Sérsic indices of stellar surface mass density and metallicity profiles. Both n_S and n_Z share similar evolution tracks (middle two panels of Figure 4.10), starting with a rapid increase in the Sérsic index values, then become stable or slowly decreasing after the first 1 Gyr. This suggests the present-day Sérsic indices which trace the metallicity and mass profiles, were primarily shaped during the very early starburst periods of the model galaxies, and their values remain unchanged for most of a galaxy's lifetime.

An interesting aspect is that there is a range of roughly 2 Gyrs in the exact time when a galaxy achieves a peak value of the index. In addition we can see that the difference between the peak value and present day value is larger for the high mass galaxies - a reduction of roughly 35% compared to 10% for the lowest mass galaxies. There is also an apparent inflection in the mass dependence of the mean indices - with the lowest mass galaxies showing slightly higher present day Sersic indices than the MW mass galaxies. However behaviour is present in both the metallicity and structural indices, suggesting that the galaxies still fall on the local mass metallicity relations as seen in the previous chapter.

The bottom two panels of Figure 4.10 show the evolution of Z slope and $\log(\Sigma_{\rm Re})$-$\log(\Sigma_{\rm centre})$, as these two estimators are more representative of the absolute value of the gradient. The Z slope values show quite different evolutionary curves compared with the other top four panels. In particular it grows steeper gradually with time, which means its correlation with the n_Z index is changing through time. An interesting aspect of the n_Z and Z slope evolution is that even in this physically limited model, there may be epochs when high mass galaxies show even more extreme central mass and metallicity concentrations. While, $\log(\Sigma_{\rm Re})$-$\log(\Sigma_{\rm centre})$ show similar evolution tracks with n_S, with the same fast early stage increasing but then tends to slowly increase.

Similar to the top four panels, we see there is some diversity at fixed stellar mass in the metallicity slope evolution. However here the present day gradient strength

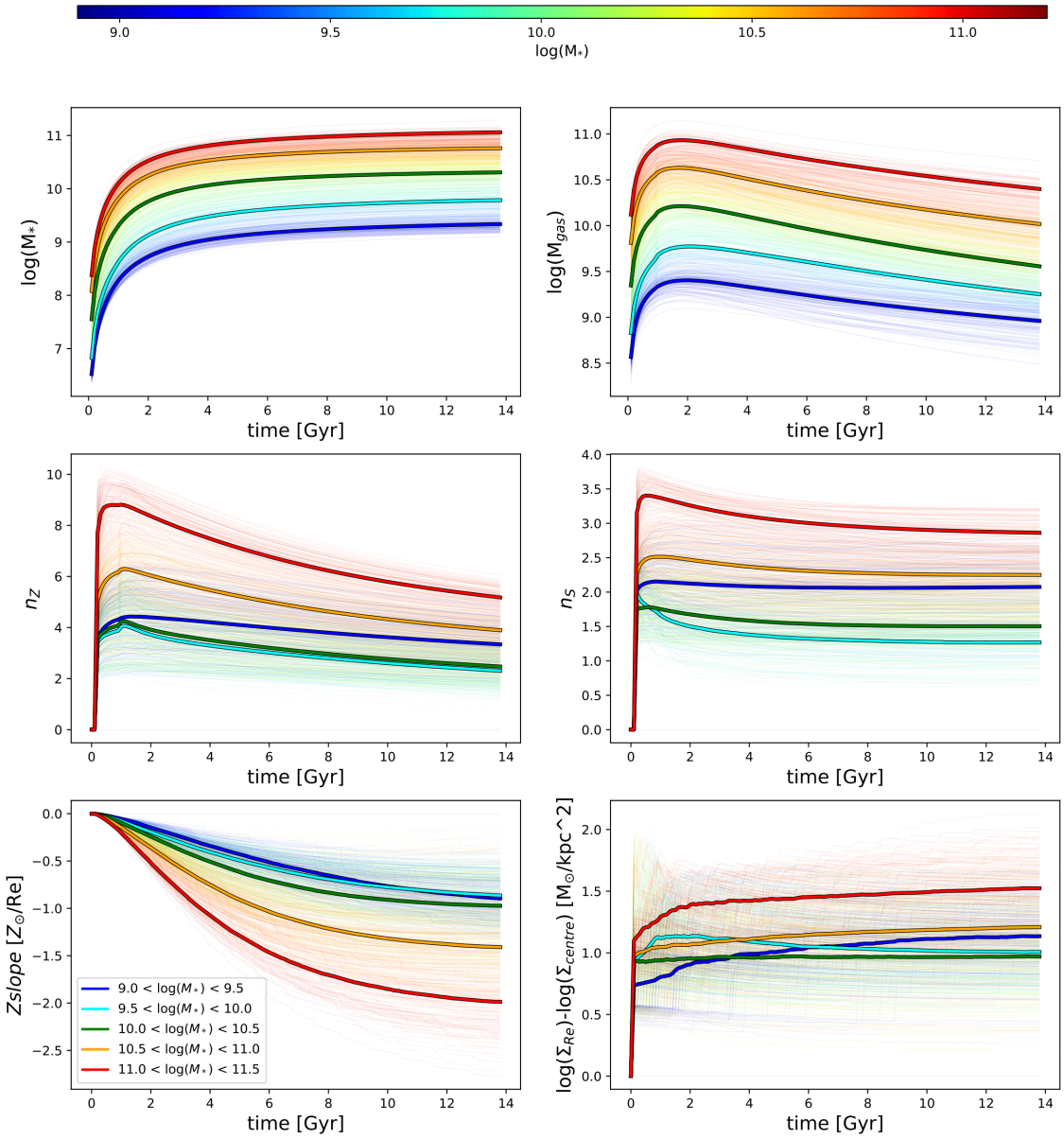

FIGURE 4.10: The time evolution of total stellar mass (top left), gas mass (top right) and different stellar metallicity/mass gradient estimators for our SAM physical models. Middle left: n_Z, Middle right: n_S, bottom left: Z slope, bottom right: $\log(\Sigma_{\rm Re})$-$\log(\Sigma_{\rm centre})$, color coded by their present-day stellar mass. Thick lines are the average profiles in different present-day stellar mass bins: blue: $(8.5 < \log(M_*) < 9.5)$; cyan: $(9.5 < \log(M_*) < 10.0)$; green: $(10.0 < \log(M_*) < 10.5)$; orange: $(10.5 < \log(M_*) < 11.0)$; red: $(11.0 < \log(M_*) < 11.5)$. The present day is located at 13.8 Gyr on these plots.

shows a monotonic decrease (steepening) with present day stellar mass. The structural evolution shown in the bottom right panel suggests that there is a large diversity in density gradient evolutionary pathways. However at present day there

always seems to be a close correspondance with the stellar population spatial distributions. This again may suggest that the correlation is imparted at early times during the epochs of the most significant in-situ star formation. This would be consistent with our results in Chapter 2 which showed that the stellar metallicity gradients were most closely correlated with the density profiles of the dynamically hot (older) components of the stellar mass distributions in observed galaxies.

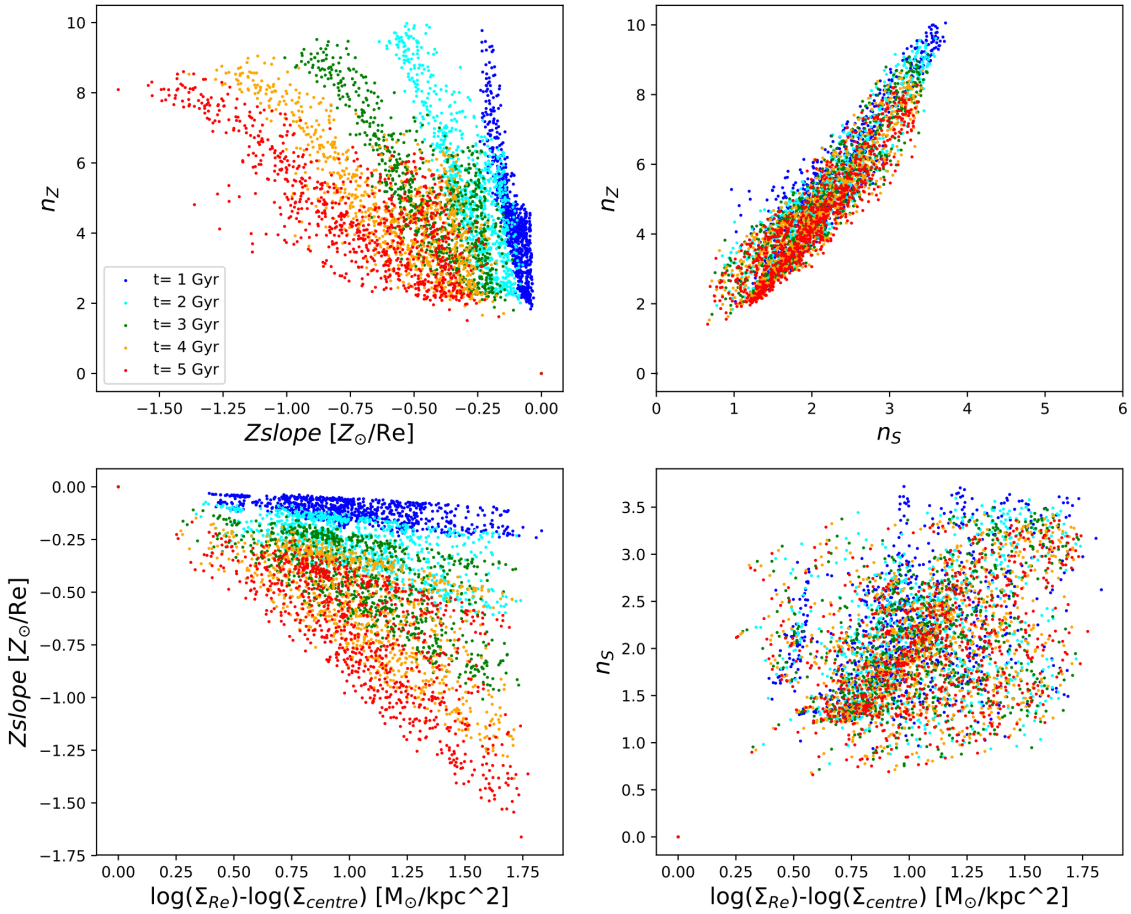

FIGURE 4.11: The relation between different stellar mass/metallicity gradient estimators at different ages. Top left: the relation between Z slope and n_Z; top right: the relation between n_S and n_Z; bottom left: the relation between log($\Sigma_{\rm Re}$)-log($\Sigma_{\rm centre}$) and Z slope; bottom right: the relation between log($\Sigma_{\rm Re}$)-log($\Sigma_{\rm centre}$) and n_S. Color coding is by time after formation of the model galaxy.

The evolution tracks in the above Figures suggest a time variation on the relations between Z slope and other stellar mass/metallicity gradient estimators. To better visualize this mass-metallicity co-evolution, in Figure 4.11 we plot the relations between the 4 different stellar mass/metallicity gradient estimators at 5 different ages.

We can take away a few different aspects of the co-evolution from these plots. Firstly, the anti-correlation between the Z slope and the density gradient is not immediately in place, and takes some time to become stronger (bottom left panel). This

again suggests that the local mass-metallicity is a result of time integrated in-situ star formation, and the correlation becomes more prominent as more stellar generations are assembled. The metallcity Sersic index is similarly uncorrelated at early times with the slope of the metallicity gradient (top left panel), but over time the anti-correlation develops. Similarly the mass Sersic index shows a tighter correlation with the mass density gradient as time goes on.

Together, the time evolution of the bottom two panels combines to result in almost no time evolution of the scatter in the $n_Z - n_S$ indices in the top right panel. However there is some indication that the relation becomes offset to lower values of n_Z at fixed mass Sersic index. This could suggest that the offset in Figure 4.8 is representative of differences in the length of time (or average SFR) between the SAM model galaxies and those from TNG. However more work is needed to isolate that effect from other physical processes contained in the TNG simulations.

In summary, studying the evolution between the two Sérsic indices and two absolute value mass and metallicity gradients, we can conclude that under our scenario, though the absolute value of stellar metallicity and surface mass density gradients may change with time, the shape of their profiles are always correlated with each other. However we should keep in mind, in observed galaxies the stellar mass buildup isn't as smooth and regular as in our model, and there are many other stochastic effects (intense star burst, mergers) that can modify the processes. This may especially be true in early times as the absolute value of stellar mass and metallicity are low, and the proportional influence of for example a merger, would be stronger. Future work may be able to isolate how the co-evolution would respond to such processes, but this is out of the scope of our model capabilities.

4.4.2 Angular momentum

From both observations and numerical simulations we have found a correlation between present day angular momentum $<V_{\rm rot}/\sigma>$ and stellar mass $\log(M_*)$ of the galaxies. For high mass galaxies ($\log(M_*) >= 11$) the CALIFA results showed that above this mass $<V_{\rm rot}/\sigma>$ drops quickly. The TNG simulations confirmed this behaviour, and analysis of the ex-situ fractions in the simulated galaxies showed that it is most likely due to the increased prominence of merger and accretion (see Chapter 2 and 3). Below that mass range ($\log(M_*) < 11$) we saw that with increasing $\log(M_*)$ $<V_{\rm rot}/\sigma>$ also increases, due to the inside-out growth of the disk.

In an isolated case one might then expect a correlation between kinematic features and the stellar population distributions in low mass galaxies (with $\log(M_*) < 11$). This is largely evident in the observed and simulated galaxies, however even for those galaxies, their kinematic properties may also be influenced by many other factors. For example, stellar feedback may eject energy to the ISM, which could consequently alter the gravitational potential well (El-Badry et al., 2016b); or disc instabilities may dynamically heat up the disk stars. (Binney and Tremaine, 1987), potentially altering the angular momentum or spatial distributions of the stars. Therefore the *present* day stellar kinematics may not always show correlations with the metallicity gradients, and may not be causally connected. However, it remains to be seen what role the *intial* angular momentum of the gas which stars formed from plays in the formation of the metallicity gradients in galaxies.

The parameterized gas inflow modes in our chemical evolution model may provide us a potential way to study the relation between the initial kinematic properties and stellar populations gradients of galaxies that evolve in isolation. While the SAM model is simplistic and by no means captures the full physics or geometry of the star formation and subsequent dynamical settling processes, we here simply ask how the spatial distributions of the two modes of gas infall might map into angular momentum proxies. This is most useful in a differential sense, and may let us explore if the relative weight between the two modes of infall correlate with some of the metallicity properties at present day. This would give some indication of whether the angular momentum of the gas at the time the stars formed is an important factor in setting the metallicity gradients in galaxies.

As mentioned previously, we assume the A mode gas carries minimal angular momentum, and its spatial distribution is centrally concentrated, mimicking that of a galaxy's bulge. Therefore it is reasonable to assume that the stars which form out of it will be supported by random motion (velocity dispersion) either initially, or after some heating process which our model doesn't include. On the contrary, B mode gas is supported by rotation and extended in a disk distribution, so the stars which form out of it will likely be rotationally supported. Therefore, by simply adjusting the ratio between mode A and B we should be able to crudely mimic galaxies with different dynamical properties.

In order to quantify the angular momentum in our SAM model, we need to know the gravitational potential of the galaxy at each timestep. The potential of a galaxies is determined by the mass distribution of both baryonic and dark matter. Though we do not have DM in our chemical evolution recipe, we can quickly calculate the dark matter mass profiles through empirical stellar mass - DM halo profile relations constructed from the TNG galaxies.

Empirical stellar mass - DM halo profile relation

To characterize the typical DM profile of galaxies of different stellar masses, We pick a small sample of 275 galaxies from TNG100(-1) simulation with mass range from 10^9 to 10^{13} M_*. For each of these galaxies we compute the DM mass in a 3D spherical shell and fit the DM mass density profiles with a Sérsic function, as shown in the top left panel of Figure 4.12. In otherwords, for galaxies of a given stellar mass, we characterize their DM mass distribution with three parameters: a normalization (I_0), a scale length (R_0) and a Sérsic index (n).

We next plot the typical variation of those parameters as a function of galaxy stellar mass for the subset of TNG galxies. This is shown in the three other panels of Figure 4.12. For each of these relations we fit a functional form to the parameter versus stellar mass of the galaxy.

The top left panel of Figure 4.12 shows the correlation between $\log(M_*)$ and the dark matter profile normalization, I_0. With increasing stellar mass, galaxies tend to show higher I_0. As I_0 represents the intensity of the profiles, this correlation indicates galaxies with high stellar mass tend to have higher DM mass.

The bottom right panel of Figure 4.12 shows the correlation between $\log(M_*)$ and the scale length of 3-D DM mass profiles R_0. For galaxies with stellar mass below 10^{11} R0 does not vary strongly with stellar mass, while for galaxies with stellar mass

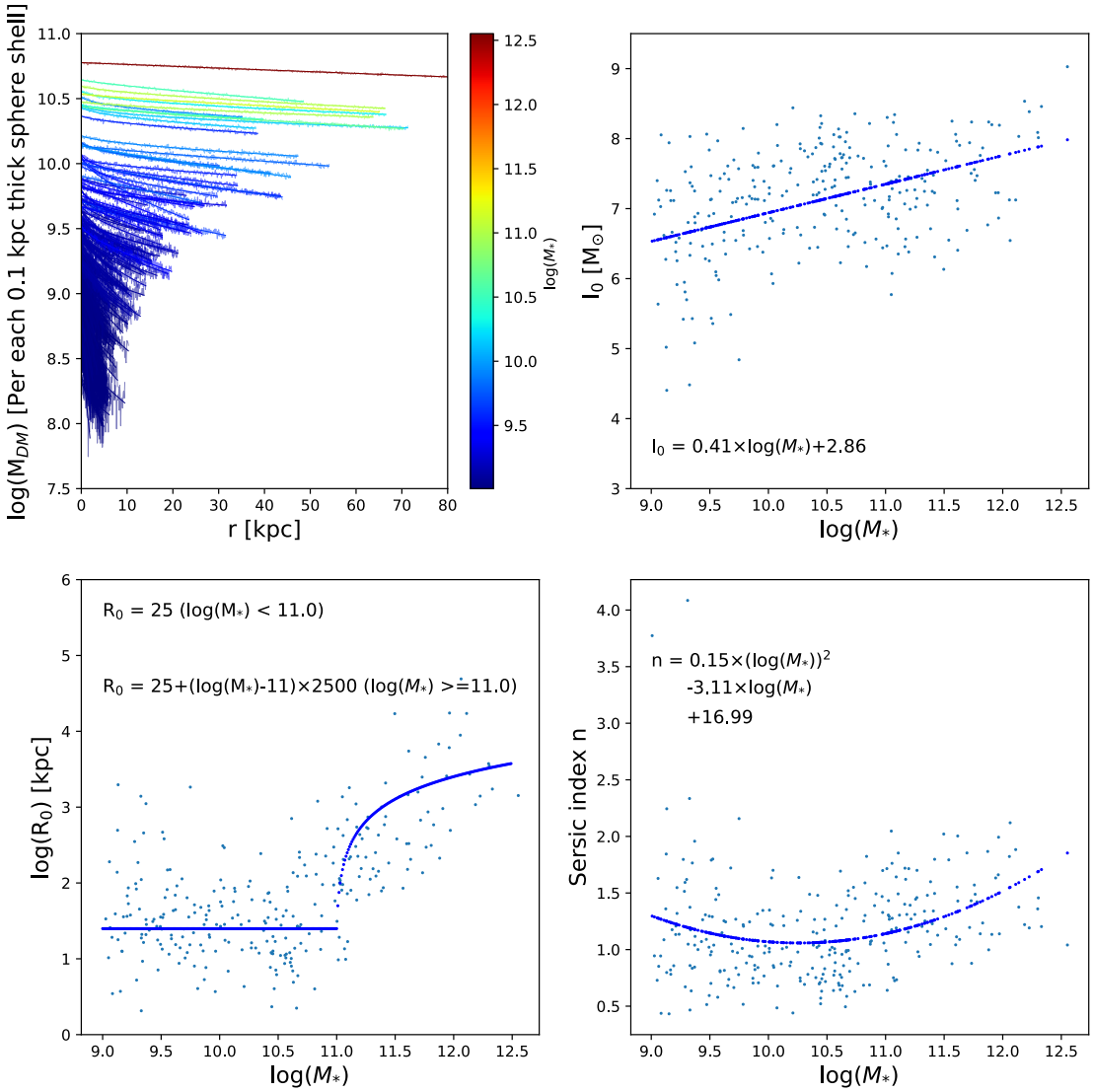

FIGURE 4.12: Top left: the 3-D DM radial mass profiles (color coded by $\log(M_*)$ and the fitted Sérsic profiles (black). Top right, bottom left and right panels are the correlation between $\log(M_*$ and three Sérsic profile parameters (intensity: I0, scale: R0, and Sérsic index: n).

beyond 10^{11}, R0 increases with stellar mass. This is likely due to those galaxies having experienced more merger events, which may increase and flatten their DM halos. The functional form of the fit to this distribution is indicated in the panel.

Finally, the bottom left panel of Figure 4.12 shows the correlation between $\log(M_*)$ and DM profile Sérsic index n. Galaxies with very low stellar mass and very high stellar mass tend to have larger n. This correlation is similar to the stellar surface mass density (Σ) profiles we derived from TNG100(-1) galaxies (in Section 3.3.1).

With these correlations defined from the TNG galaxies, we are able to create an approximate DM halo for our each of our SAM model galaxies of stellar mass M_*. With this profile, we can compute the gravitational potential at each time step (baryons plus dark matter) for the SAM model galaxies. Using this information

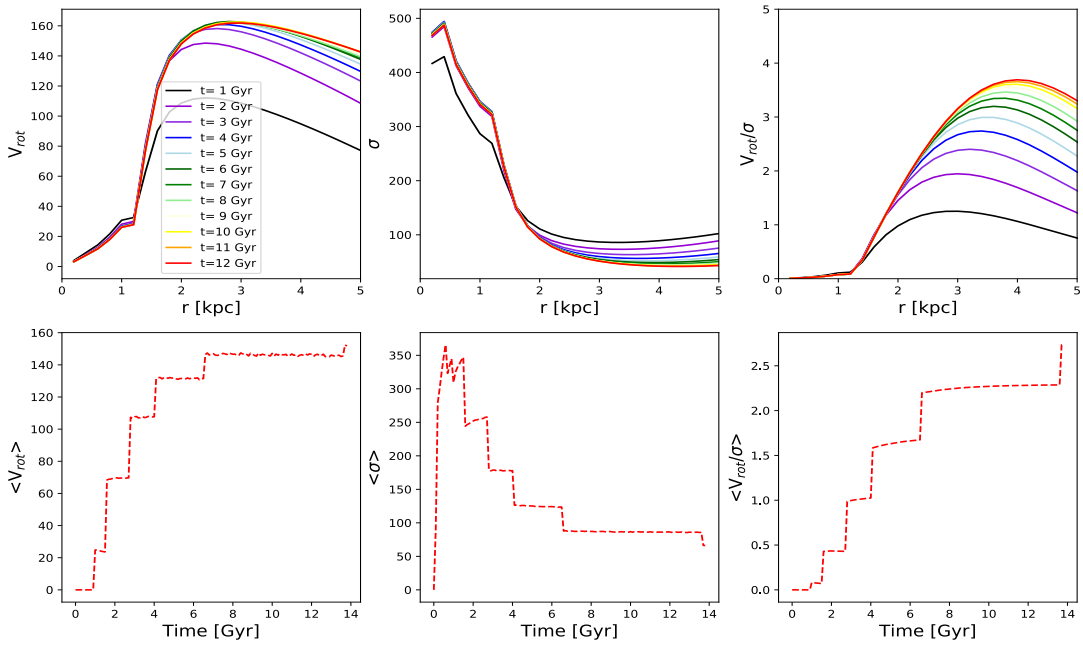

FIGURE 4.13: The radial profiles of V_{rot} (top right), σ (top middle) and V_{rot}/σ (top right). Bottom three panels are the time evolution of their average (for V_{rot} and σ) or total V_{rot}/σ values.

we assign the rotation velocity and velocity dispersion at each radii to mode B and mode A gas separately, as follows:

$$V_{\rm rot}(r) = ((G \times M_{\rm tot\ (<r)})/r)^{0.5} \times F_{\rm total\ gas,\ B} \tag{4.10}$$

Where $F_{\rm total\ gas,\ B}$ is the time accumulated B mode gas fraction:

$$F_{\rm total\ gas,\ B} = M_{\rm total\ gas,\ B}(r)/(M_{\rm total\ gas,\ B}(r) + M_{\rm total\ gas,\ A}(r)) \tag{4.11}$$

$$\sigma(r) = ((1/3 \times G \times M_{\rm tot\ (<r)})/r)^{0.5} \times F_{\rm total\ gas,\ A} \tag{4.12}$$

Where $F_{\rm total\ gas,\ A}$ is the time accumulated A mode gas fraction:

$$F_{\rm total\ gas,\ A} = M_{\rm total\ gas,\ A}(r)/(M_{\rm total\ gas,\ A}(r) + M_{\rm total\ gas,\ B}(r)) \tag{4.13}$$

Here, $M_{\rm tot\ (<r)}$ is the enclosed total mass (DM, star and gas) within radius r. While simple, this prescription may provide an approximate way to understand the kinematic properties the newly formed stars may likely have in the SAM model galaxies.

Similar to our previous Chapters on CALIFA and TNG galaxies we use the $V_{\rm rot}/\sigma$ as the indicator of angular momentum. In this work, as our model contains no dynamical processes, the disk part (mode B) cannot be dynamically heated up through galaxy's evolution. Thus this is best studied as a differential estimator of the instantaneous angular momentum of stars which are newly formed at that model timestep.

To isolate and clarify the role of angular momentum in the creation of metallicity gradients, we hold the inflow parameters fixed (while still reproducing the structural calibration relation of $n_S - M_*$. This allows us to focus on the evolution and present day kinematic and stellar population properties for a fixed, realistic inflow model.

Figure 4.13 shows an example of the evolution of V_{rot} profiles and σ profiles, and the time evolution of their mean values within ($3R_e$) in an example galaxy with present-day $\log(M_*) \sim 10.22$ and has a total A mode gas infall ~ 10.06 and a total B mode gas infall ~ 10.07. Though our method can only provide the original angular momentum distribution in absence of internal and external dynamical processes (e.g., feedback, mergers), the time evolution tracks are comparable to observations (as shown in Figure 2.1), though with potentially lower angular momentum in the inner 1kpc than seen for observations of MW mass galaxies.

Predicted chemo-dynamical features

As our default input gas flow profiles cover a very large parameter space (see Figure 4.6), here we wish to focus on the predicted kinematic evolution for approximate fixed inflow models. Thus, to clearly show the relation between stellar population features and dynamical properties, we create a set of canonical gas inflow profiles by manually tuning the shape of the gas inflow parameters (Rd_A, Rd_B, n_{Srsic}) to reproduce a "best fit" present-day $\log(M_*)$ and stellar Sérsic index S_n relation of TNG galaxies. These SAM model galaxies are shown as the red dots in the top left panel of Figure 4.14) in comparison to the TNG galaxies (the cyan line).

With this calibration, we can check that the differential trends of n_S, n_Z and Z slope with respect to galaxy stellar mass can be reproduced, and with similar forms as the TNG galaxies - as shown in the top right and bottom panels of Figure 4.14. In what follows, we utilize this set of canonical SAM galaxies to study the chemo-dynamical features predicted in these models.

The top left panel of Figure 4.15 shows the comparison between our canonical SAM galaxies and TNG galaxies in the $\log(M_*)$ and V_{rot}/σ parameter space. Despite the simplicity of the model, we see similar trends between the SAM and TNG galaxies, with V_{rot}/σ increasing with stellar mass up to a mass of ($\log(M_*) < 10$), above which V_{rot}/σ quickly drop with further increase of stellar mass. A similar trend can also be found in CALIFA galaxies (see Section 2.5.3). Top left, Bottom left and right panels show the correlation between V_{rot}/σ and n_S, Z slope and n_Z respectively. We see though the scatter of TNG and our SAM canonical models are different, (due to the restricted nature of the inflow parameters we consider in this exercise) they do show similar trends. In general, the low angular momentum galaxies show steeper mass and metallicity profiles. The Z slope values show an inflected behaviour, which while not apparent in the TNG galaxies, is seen clearly in the CALIFA sample: low mass galaxies increase in V/sigma while only marginally changing gradient, until a galaxy mass (or morphology) when a decrease in V/σ and steepening of the gradient is seen (e.g., Figures 2.8 and 2.9).

Figure 4.16 shows the time evolution of V_{rot}/σ and Z slope for the SAM model galaxies. Here we see that the V_{rot}/σ increases with time, likely due to the dominance of A mode gas inflow in the early epochs. However their relative positions at

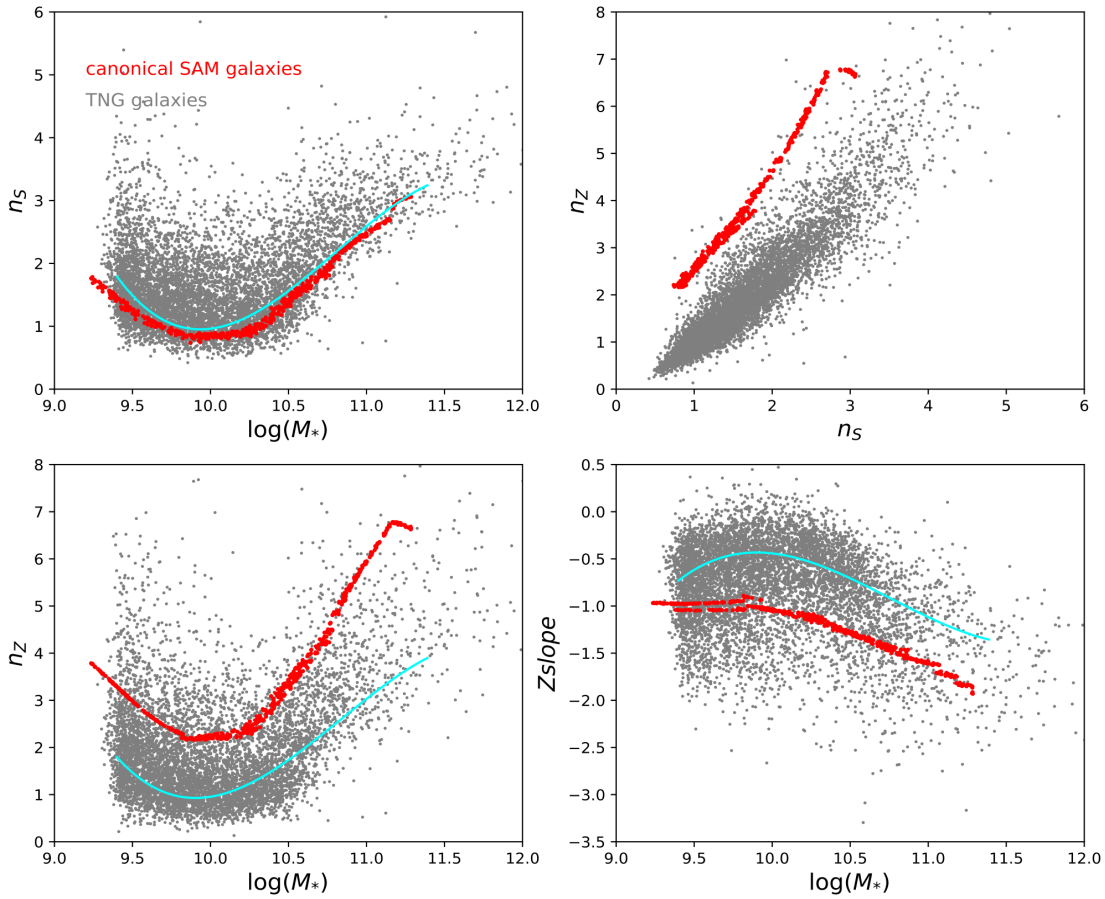

FIGURE 4.14: Comparison between TNG and our canonical SAM galaxies in log(M_*) - n_S (top left), n_S - n_Z (top right), log(M_*) - n_S (bottom left) and log(M_*) - Z slope (bottom right). Cyan lines are the mode lines of TNG galaxies.

different ages do not show a large correlation with present-day present-day galaxy mass. Conversely the model Z slope evolution of this restricted set of SAM galaxies is similar to the time evolution of the larger subset of SAM model galaxies (Bottom left panel of Figure 4.10), and shows a clearer correlation with galaxy mass. This might suggest that their is a strong diversity of evolutionary pathways of the gas kinematics (or alternatively the ratio of A and B mode gas inflow) which can still produce metallicity and mass gradients consistent with the observations.

In the left panel of Figure 4.17 we see the combined version of Figure 4.16. Here we plot evolutionary tracks in $V/sigma$ and metallicity slope or Sersic index planes, for galaxies of different stellar mass. As time increases, both V_{rot}/σ and the steepness of stellar metallicity gradients increase. While in the right panel, the relation with time becomes slightly more complicated, as the present-day metallicity Sérsic index is predominantly set in the very early stages of our model galaxies' evolution (see Section 1.4.1), and so there is less evolution in n_Z over the lifetime of the model galaxies.

The left panel of Figure Figure 4.17 is partiuclarly instructive to understand the role of initial angular momentum in the evolution of the galaxy's stellar population

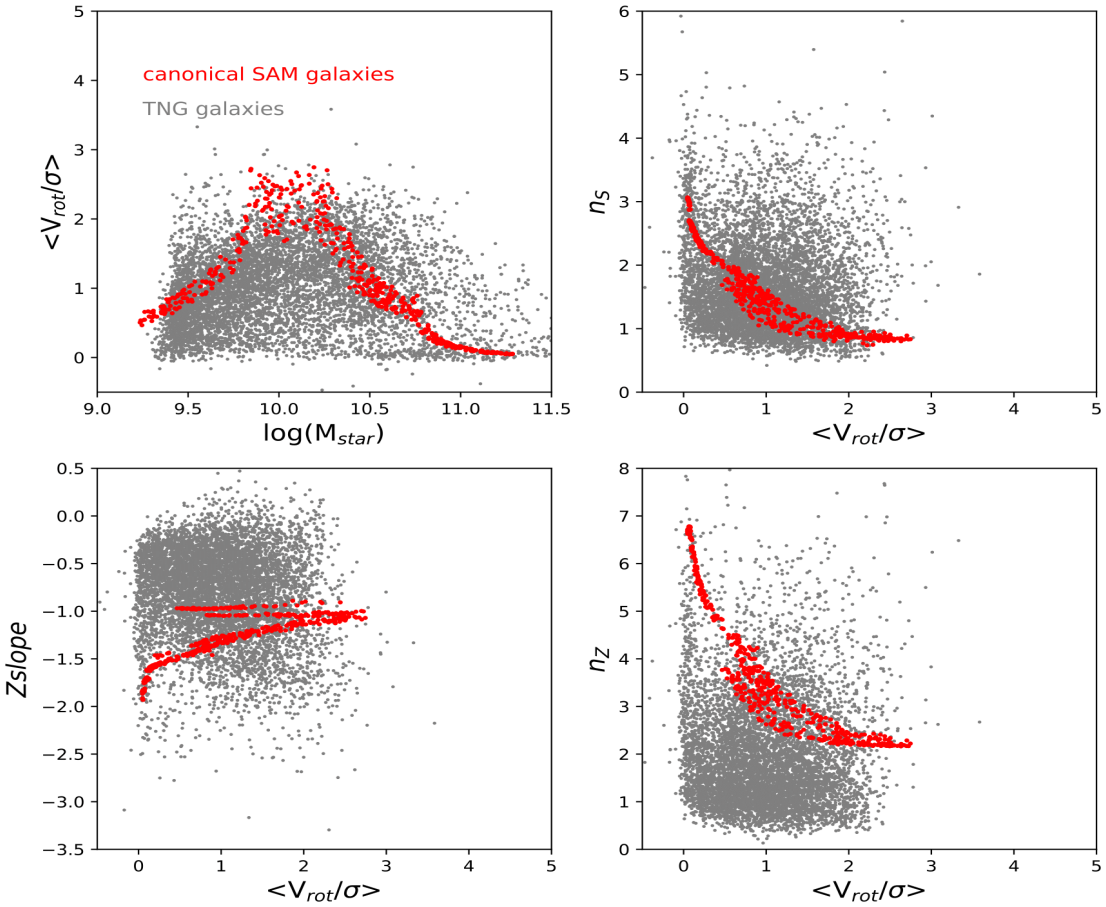

FIGURE 4.15: Comparison between TNG and SAM galaxies in $\log(M_*)$ - V_{rot}/σ (top left), and V_{rot}/σ against n_S (top right), Z slope (bottom left) and n_Z (bottom right) spaces, blue dots are TNG galaxies, red dots are SAM galaxies.

gradients. Here we can see that as the galaxy mass increases, the final day angular momentum content increases, up to MW mass galaxies. These have intermediate strength metallicity gradients (Z slope approximately -1.0), while higher mass galaxies show final positions with lower angular momentum and steeper gradients. This differential trend is remarkably close to what is seen in the observations of CALIFA galaxies (e.g., Figures 2.8 and 2.9). Given that the SAM model tracks only have a variation in V/σ due to changes in the gas accretion history (not dynamical heating of the stellar orbits), it would be interesting to better understand how much of the inflection in the galaxy mass sequences can be explained without needing to invoke galaxy mergers. Figure Figure 4.17 suggests at very least that the instantaneous angular momentum important in the final spatial distribution of the stellar metallicity profiles. Further work will be crucial to separate how much the inner regions of galaxies may uniquely result from the galaxies gas inflow history.

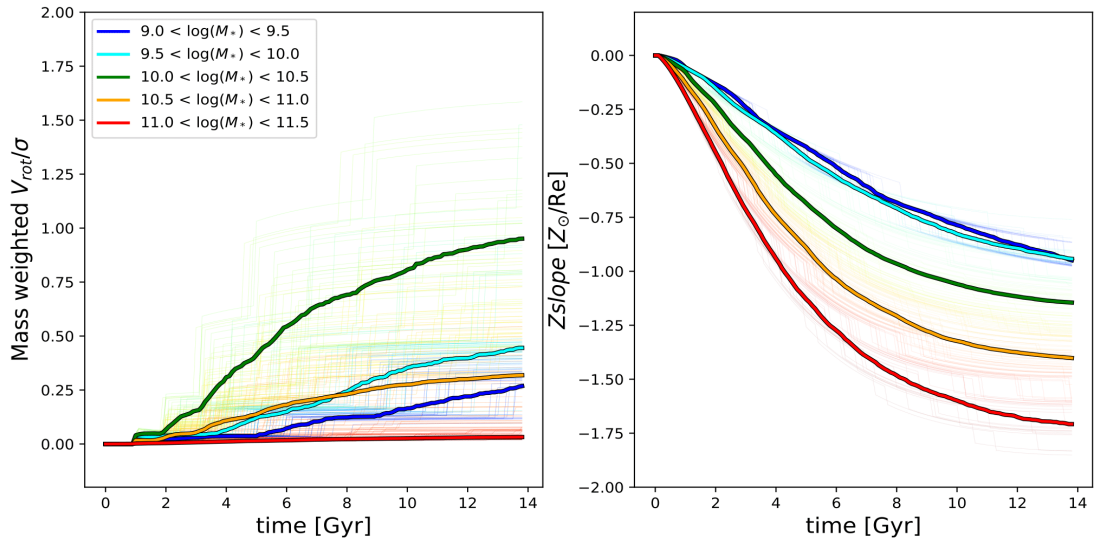

FIGURE 4.16: The time evolution of V_{rot}/σ (left) and Z slope (right) for each of our canonical SAM galaxies (thin lines color coded by their present-day stellar mass), thick lines are the average evolution of each mass bins.

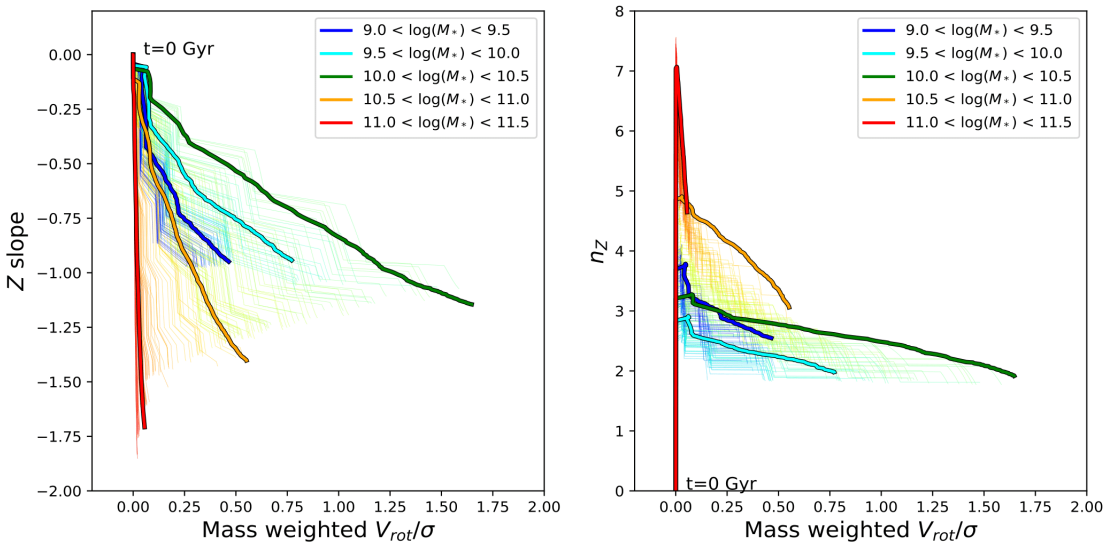

FIGURE 4.17: The time evolution tracks of V_{rot}/σ - Z slope (left) and V_{rot}/σ - n_Z (right) for each of our canonical SAM galaxies (thin lines color coded by their present-day stellar mass), thick lines are the average evolution of each mass bins.

4.5 Summary

In this work, we study the formation and evolution of galactic stellar metallicity gradients via a one dimension semi-analytic chemical evolution model. The model allows for two modes of gas inflow in order to flexibly model galaxies of a variety of mass and morphological type. The chemical model primarily relies on a spatially

evolving gas inflow rate in order to mimic the mass evolution of bulge and disc-like components in galaxies. This allows us to directly test our scenario whereby the local in-situ stellar mass buildup plays a prominent role in shaping the stellar metallicity radial profiles in the inner part of a galaxy (within 1 Re).

Our results show that the structural and chemical properties of the analytic model galaxies reproduce the differential trends seen in both the CALIFA observed galaxies and the TNG simulated galaxies. In particular the slope of the local mass metallicity relation is well reproduced in our model, but also the correlations between galaxy stellar mass and metallicity profile shape.

We also discuss the time evolution of different stellar mass/metallicity properties and their scaling relations. We find that in our model, the link between local stellar mass-metallicity gradients exists from the very early stages of the galaxy, as much of the mass is assembled then. However the tightness of the relations may increase as further stars are formed. We find that while estimators of the stellar population distributions (e.g. Z slope) can show a variation in their absolute value over time, their relative relation to the stellar mass gradients remains tightly correlated through time.

We further exploit the two phase gas inflow parameterization of our chemical evolution model to approximate the instantaneous kinematic properties of the stars formed out of the newly accreted gas. By introducing an empirical stellar mass - dark matter halo mass profile relation from IllustrisTNG galaxies, we are able to calculate coarse dynamical features of our model galaxies and study their evolution over time.

We find that the predicted angular momentum content, and the correlations between stellar kinematics and metallicity gradients show comparable trends to the TNG galaxies and observed CALIFA galaxies. This may suggest that correlations between the metallicity and kinematic or mass density profiles in the inner regions of the galaxies may be a result of the type of gas accretion the galaxy has undergone. Together the results of our analytic chemical evolution models further strengthen the idea that the local gas inflow and star formation history and their variation over time and radius is a crucial factor in setting the observed galaxy metallicity gradient scaling relations.

Chapter 5

Conclusions and open questions

5.1 Summary

Stars are the basic observable component of galaxies, and they are fundamental in regulating subsequent star formation, and defining and tracing the morphology and evolutionary processes of galaxies. Measuring their spatial distribution and those of the metals they produce, helps us understand the the driving forces behind star formation and galactic evolution.

In this thesis we have focused on understanding the radial stellar metallicity distribution of a galaxy. This is an important tracer of a galaxy's evolutionary history, as the long-lived stars can preserve a record of how efficiently the galaxy was enriched, or structurally and dynamically reconfigured. The main goal of the thesis is to study the diversity and possible origins of stellar population gradients in the inner part of galaxies (within 1 R_e). To accomplish this goal, we use three different methodologies: observations and analysis of stellar populations and kinematics in a diverse sample of galaxies, analysis of kinematic and chemical properties of galaxies in a state-of-the-art cosmological simulation, and flexible analytic models of galaxy chemical evolution.

Stellar metallicity from observations

In Chapter 2, we analyzed the radial stellar metallicity gradients out to 1 R_e for 244 CALIFA galaxies which range from morphological type E to Sd, to study the driving mechanisms of stellar metallicity gradients. Different from previous studies, we not only measured the logarithmic stellar metallicity gradients $\nabla \log(Z/Z_\odot)$ but also measured the linear metallicity gradients $\nabla Z/Z_\odot$, as these may be less impacted by the mass-metallicity relation in large galaxy samples. Our results show that logarithmic $\log(Z/Z_\odot)$ gradients show large scatter similar to other studies, while linear $Z/Z_\odot$ gradients offer a clearer correlation with galaxy morphological type - with early type galaxies showing the steepest gradients.

A primary finding of this analysis is that the linear $Z/Z_\odot$ gradients simply reflects the local stellar mass distribution of the galaxy. This suggests that the radial stellar population distribution is primarily a result of the local stellar mass buildup and that there should be a tighter correlation between metallicity gradient and local properties of its structure, than with total galaxy mass. In particular, we showed using dynamical models that the stellar surface mass density gradient $\nabla \Sigma_*$, directly correlates with the metallicity gradient $\nabla Z/Z_\odot$ of a galaxy. We showed that this

correlation and its scatter can be reproduced entirely by using *independent empirical* galaxy structural and chemical scaling relations.

By using Schwarzschild dynamical models we explored links between a galaxy's local stellar populations and its kinematic features. By jointly looking at galaxies' stellar population gradients and their stellar orbital compositions, we got the constraint on the timescale of the build-up of $\nabla\Sigma_*$ - $\nabla Z/Z_\odot$ relations. In particular we found that the mass density-metallicity gradient correlations are most prominent in the dynamically hotter (potentially older) components of the galaxy. The strength of the metallicity and mass density gradient correlation becomes stronger as more star formation occurs, suggesting that the local mass-metallicity relation scatter may reflect differences in the dynamical and star formation history of a galaxy.

Our results indicate no causal correlation between the metallicity gradients and observable probes of radial migration in the galaxies, such as the presence or strength of bars and spiral arms. This suggests that stellar metallicity gradients in the inner part of galaxies are not strongly shaped by radial migration.

Stellar metallicity from simulation

To further understand the in-situ origin of stellar metallicity gradients and understand the metallicity gradient correlations seen in our CALIFA results, we analyzed galaxies from the IllustrisTNG100 simulations in Chapter 3. As a cosmological simulation, TNG100 allows us to derive galaxies' radial stellar population distributions in relation to their total stellar mass, stellar surface mass density distribution, stellar dynamical properties, stellar in-situ and ex-situ fractions as well as their environments.

Like CALIFA galaxies, TNG100 galaxies show similar trends between surface mass density (Σ_*) and metallicity profiles, with the steeper Σ_* gradients indicating steeper Z gradients. We confirm that the simulation galaxies show a clear local stellar surface mass density and metallicity relation (local MMR) at all stellar mass ranges - with regions within a galaxy that have higher Σ_* tending to have higher stellar metallicity. This relation indicates the stellar population gradients in the inner galaxy are dominanted by the local in-situ stellar mass buildup.

We show that similar to the surface mass density profiles, a galaxy's linear metallicity profiles can be described extremely well by a Sérsic profile. We show that the mass density Sérsic index and the metallicity profile Sérsic index are extremely tightly correlated over all ranges of galaxy mass. This offers a useful way to predict the distribution of metallicities at present day in more distant galaxies where only light profiles are available. This may be helpful for putting priors on M/L ratios or deriving further stellar population profiles.

Combining the metallicity with stellar age information in the simulated galaxies, we found the relation between Σ_* and stellar metallicity gradients is independent of the local star formation history. This means, the local stellar metallicity is always proportional to the local accumulated stellar mass, despite when those stars formed. We do see some indication for a host galaxy mass dependence to the type of assembly history (inside out to outside-in) in the TNG100 simulated galaxies.

By tracing the origin of each stellar particles, we found that the existence of ex-situ stars can slightly flatten the total stellar metallicity gradients for high mass galaxies ($\log(M_*) > 11$) in the inner regions. This is anticipated as high mass galaxies

are expected to experience more merger events, however the change to the stellar metallicity gradient strength in the inner regions is less than 10% for these galaxies. In addition, we show that galaxies' environment does not show show any role in shaping the relation between Σ_* and stellar metallicity gradients, as satellites show comparable trends regardless of their host mass or location to their host. Finally, the trends between galaxy metallicity distributions and the present day kinematic features are present in the simulated galaxies as well, however by considering the ex-situ fraction of stars in those galaxies we demonstrate how the chemo-dynamic distributions are mostly tracing mergers after the metallicity gradients were put in place.

In this way we further clarified that the local, in-situ mass buildup is crucial to a galaxy's stellar metallicity spatial distributions, while subsequent morphological or dynamical evolution may introduce small amounts of scatter in the scaling relations we present.

From empirical to theoretical

With both observation and simulation results indicating a link between stellar metallicity gradients and surface mass density gradients, in Chapter 4, we implement this scenario into a simple 1D semi-analytic model designed to test the empirical present-day relations we found in CALIFA and IllustrisTNG galaxies.

We model a galaxy as a 1D set of concentric annuli and evolve each of region with a $open - box$ chemical evolution model, which includes gas inflow outflow, star formation and feedback. In order to mimic galaxies with different morphological types (central concentrations), we implemented a two phase gas infall model, which not only can help us to create galaxies with different concentrations but also provides us with a way to understand the impact of the instantaneous gas inflow properties (spatial dependence, angular momentum) on the final stellar metallicity gradients.

Similar to both CALIFA and TNG galaxies, our model shows a clear local stellar surface mass density - stellar metallicity relation in galaxies of all masses. By constraining our model with present-day galaxies' stellar mass ($log(M_*)$) - morphology (n_S) and size (Re) relations from TNG galaxies, we successfully reproduce the present-day empirical $log(M_*)$ - stellar metallicity gradient relations as well as the newly developed, tight correlation between mass and metallicity Sérsic indices.

By checking the time evolution of different stellar mass and metallicity gradient estimators, we find the correlation between the two exists throughout most of the lifetime of our model galaxies - and though the absolute value of some metallicity and mass gradients can evolve through time, the relative trends between the shape of mass and metallicity profiles remain tightly correlated regardless of mass or assembly history.

We further use our two phase gas infall model to provide an approximate window into the evolution of galaxies' angular momenta. By using the stellar mass - DM halo radial profile relations from TNG galaxies, we calculated the stellar V_{rot}/σ at each time for each analytic model galaxy, and demonstrate that the evolution of the present-day stellar mass - V_{rot}/σ can also be reproduced with this simple model. The analytic chemical evolution model contains no migratory processes and so the

reproduction of the metallicity gradients solely due to gas inflow variations, suggests that the local stellar mass buildup is a dominant driver of the present day gradients in the inner regions.

5.1.1 Conclusions

Our result from different approaches reveals the diversity and origins of galactic stellar metallicity gradients, ∇Z. We find that ∇Z is most strongly a function of galactic morphological types, with early type galaxies tending to show steeper gradients. This is physically due to the early type galaxies showing higher mass concentrations, and using observations, simulations and analytic models demonstrate that a galaxy's stellar metallicity gradient ∇Z is directly and tightly correlated with its stellar mass concentration. We find that this correlation exists independent of galaxy mass, and is a manifestation of a tight, local stellar mass-metallicity relation which is evident in our observations, and numerical and analytic models. Our primary finding is then that the local stellar metallicity in the inner regions of a galaxy is determined by its integrated past in-situ stellar mass buildup. The analysis of our models and simulations suggests that the role of gas inflow and star formation in the early history of the galaxy will be a strong factor in setting the stellar metallicity gradients. Conversly we find no strong or causal relation between galaxies' kinematics or indicators of radial migration (e.g., bar strength, sprial features) and their metallicity gradients. This suggests for the inner part of the galaxies, radial migration, age distribution may not play any important roles in shaping the local stellar metallicity. Similarly accretion of ex-situ stars can introduce some changes to the gradients in the inner regions of galaxies, but at a small level of 10%.

Together the observational, numerical and analytic modelling approaches have offered a holistic window into how stellar population spatial distributions can be quantitatively used to understand the importance of in-situ and ex-situ processes in galaxy evolution.

5.2 Future perspectives

The chemical evolution of galaxies is an amazing and important topic in modern astronomy, which can help us to understand how/why our planet, and us come to exist. Our work in exploring the stellar metallicity gradients in the CALIFA and Illustris galaxies has found new ways of looking at the build-up of metals in galaxies, but there are still many questions to explore.

5.2.1 Low mass galaxies

One area where further numerical and observational work can focus is in the regime of dwarf galaxies. These objects are interesting probes of galaxy evolution, as they are some of the most dark matter dominated objects, and have not been subject to significant mergers. However at the moment, for example, the CALIFA and IllustrisTNG simulation can not provide the detailed and data for low mass galaxies ($\log(M_*) < 10^{9.0}$).

Far more than MW mass galaxies, the formation and evolution of low mass galaxies are perhaps very unclear to us. They show many different morphological types and metallicity gradient properties, and they can show very compact or very diffuse structures. With respect to the correlations between galaxy mass concentration and metallicity outlined in this thesis, these objects then provide a very interesting comparable. Under our scenario what kind of stellar metallicity gradients could they have?

As the local MMR relation needs to have enough stellar mass to generate the correlation, for very diffuse low mass galaxies, this relation many not be able to play a very strong role in shaping the present day stellar metallicity gradient. This may provide us a chance to study the impact of several second order processes (radial migration, star formation history, or angular momentum). Leaman, 2012 show the strong correlation between stellar metallicity gradients and angular momentum for dwarf galaxies, this is not clearly shown in our galaxy samples - however it is not singularly correlated, as those galaxies also show correlations between gradient strength and: total mass, environment, gas fraction, star formation history and distance from the MW. Further study of gradients in low mass galaxies would be extremely helpful to understand the timescale or number of star formation events needed to buildup the tight correlations between stellar metallicity gradients and mass concentration seen in our studies.

5.2.2 High mass galaxies

On the other side of the galaxy mass function, massive galaxies may also be expected to show deviations from the local MMR scenario. For galaxies $M_* > 10^{11}$, we see that the central stellar mass density stops increasing and the $\nabla\Sigma_*$ correlates only weakly with $\nabla Z/Z_\odot$, while their metallicity gradients may keep growing. This may indicate there are other processes that strongly influence the metallicity distributions for high mass galaxies. A possible reason could be the central region preferentially runs out of gas (possibly due to strong feedback from an AGN in the central region), which restricts the stellar mass buildup (Hopkins et al., 2009). Another possible explanation may be strong radial redistribution due to the internal (disc instability) or external (e.g., mergers) processes moving the older stars outward and flatten the inner density cusp.

These effects may be enhanced, as for many massive galaxies their star formation processes have been halted for a long time. Therefore the dynamical redistribution of stars should play a more crucial role, as the correlation was set early and only effects which can erase the MMR correlation will take place afterwords. This is different than galaxies which constantly form stars, and thus continually add to the mass concentration-metallicity correlations. Thirdly, and the most importantly, the constant accretion events of those galaxies can not only redistribute stars, but also introduce large amount of ex-situ stars to the system. while our results suggest this doesn't play a large role in the inner regions, continued study of this process in simulations will help understand how the chemical information of the ex-situ stars can help understand the galaxies evolution.

Unlike the dwarf galaxies, there are many observation and simulation data (e.g., IllustrisTNG) about those massive galaxies, which could provide us opportunity to

further explore their chemical evolution histories. Together next generation instrumentation and simulations will continue to provide further insight into the utility of stellar metallicity gradients as tracers of galaxy evolutionary processes.

"There is only one heroism in the world: to see the world as it is, and to love it."

Romain Rolland

List of Publications

1. **Zhuang Yulong**, Leaman Ryan, Pillepich Annalisa, van de Ven Glenn, Zibetti Stefano, Gallazzi Anna. The in-situ origin of galaxies' stellarmetallicity gradients. In preparation

2. **Zhuang Yulong**, Leaman Ryan, van de Ven Glenn, Zibetti Stefano, Gallazzi Anna, Zhu Ling, Falcón-Barroso Jesús and Lyubenova Mariya. A dynamical view on stellar metallicity gradient diversity across the Hubble sequence with CALIFA, MNRAS,483,1862Z

3. **Zhuang Yulong**, Zhang Fenghui, Anders Peter, Ruan Zhifeng, Cheng Liantao, Kang Xiaoyu. Effect of dynamical interactions on integrated properties of globular clusters, MNRAS,446,4260Z

Acknowledgements

First and foremost I want to thank my supervisors Ryan Leaman, Glenn van de Ven and Geneviève Parmentier. I truly appreciate their guidance, fruitful discussions, and the trust they have put in me, which allowed me to think and work on my own ideas. Secondly I want to thank my collaborators: Stefano Zibetti, Anna Gallazzi, Annalisa Pillepich, Ling Zhu, Anna Sippel, Alessandra Mastrobuono-Battisti, Jesus Falcon Barroso and Mariya Lyubenova, Christoph Engler, Kiyun Yun, Alina Böcker, Thijs Kouwenhoven, Maximilian Saßerath and the whole Galaxy Structure Dynamics group, Galaxies and Cosmology Theory group and Galactic Nuclei group for countless discussions, from which I learned a lot of things, not just limited to astrophysics. Thirdly I want to thank Ryan Leaman, Anna Sippel, Alessandra Mastrobuono-Battisti, Daniel Rahner, Neven Tomicic, Christos Vourellis, Christian Lenz, Hector Hiss and Katja Fahrion for helping me reading and correcting the thesis. In addition, I would like to extend my gratitude to Andreas Koch for agreeing to be my thesis referee and to Christian Fendt for supporting me after Glenn moved to Munich.

I am also extremely grateful to my friends: Daniel Rahner (Denn die Da!), Sebastian Bustamante, Kristian Ehlert, Christos Vourellis, Neven Tomicic, Sabina Puerckhauer, Riccardo Nanni, Giancarlo Mattia, Vincent Carpenter, Matteo Pais, Patrick Barth, Julian Penzinger, Jacob Isbell, Matthias Samland, Steffi Yen, Hector Hiss, Chrestian Lenz, Hans Baehr, Branislav Avramov, Felix Bosco, Alex Hygate, Mikhail Kovalev, Gigi Leung, Mayte Alfaro and Sarah Leslie and all the Ph.D. students at MPIA. Thanks for being so supportive all these years, may our friendship last forever.

Bibliography

Abdurro'uf Masayuki, A. (2018). "Evolution of spatially resolved star formation main sequence and surface density profiles in massive disc galaxies at 0 z 1: inside-out stellar mass buildup and quenching". In: 479, pp. 5083–5100. DOI: 10.1093/mnras/sty1771. arXiv: 1802.03782.

Allende Prieto, C. (2010). "The Stellar Population of the Thin Disk". In: *Chemical Abundances in the Universe: Connecting First Stars to Planets*. Ed. by K. Cunha, M. Spite, and B. Barbuy. Vol. 265. IAU Symposium, pp. 304–312. DOI: 10.1017/S1743921310000785. arXiv: 0911.3598.

Baldry, I. K. et al. (2004). "Quantifying the Bimodal Color-Magnitude Distribution of Galaxies". In: 600, pp. 681–694. DOI: 10.1086/380092. eprint: astro-ph/0309710.

Barrera-Ballesteros, J. K. et al. (2015). "Tracing kinematic (mis)alignments in CALIFA merging galaxies. Stellar and ionized gas kinematic orientations at every merger stage". In: 582, A21, A21. DOI: 10.1051/0004-6361/201424935. arXiv: 1506.03819.

Bellini, A. et al. (2010). "New Hubble Space Telescope WFC3/UVIS Observations Augment the Stellar-population Complexity of ω Centauri". In: 140, pp. 631–641. DOI: 10.1088/0004-6256/140/2/631. arXiv: 1006.4157.

Berentzen, I. et al. (2007). "Gas Feedback on Stellar Bar Evolution". In: *ApJ* 666, pp. 189–200. DOI: 10.1086/520531. eprint: astro-ph/0703028.

Bigiel, F. et al. (2008). "The Star Formation Law in Nearby Galaxies on Sub-Kpc Scales". In: 136, pp. 2846–2871. DOI: 10.1088/0004-6256/136/6/2846. arXiv: 0810.2541.

Bignone, L. A. et al. (2017). "Non-parametric morphologies of mergers in the Illustris simulation". In: 465, pp. 1106–1122. DOI: 10.1093/mnras/stw2788. arXiv: 1610.02416.

Binney, J. and S. Tremaine (1987). *Galactic dynamics*.

Blanton, M. R. et al. (2017). "Sloan Digital Sky Survey IV: Mapping the Milky Way, Nearby Galaxies, and the Distant Universe". In: 154, 28, p. 28. DOI: 10.3847/1538-3881/aa7567. arXiv: 1703.00052.

Brooks, A. et al. (2007a). "The Role of Cold Flows and Shock Heating in the Origin of Disk Galaxies". In: *American Astronomical Society Meeting Abstracts*. Vol. 39. Bulletin of the American Astronomical Society, p. 940.

Brooks, A. M. et al. (2007b). "The Origin and Evolution of the Mass-Metallicity Relationship for Galaxies: Results from Cosmological N-Body Simulations". In: 655, pp. L17–L20. DOI: 10.1086/511765. eprint: astro-ph/0609620.

— (2007c). "The Origin and Evolution of the Mass-Metallicity Relationship for Galaxies: Results from Cosmological N-Body Simulations". In: 655, pp. L17–L20. DOI: 10.1086/511765. eprint: astro-ph/0609620.

Bruzual, G. and S. Charlot (2003). "Stellar population synthesis at the resolution of 2003". In: 344, pp. 1000–1028. DOI: 10.1046/j.1365-8711.2003.06897.x. eprint: astro-ph/0309134.

Bundy, K. et al. (2015). "Overview of the SDSS-IV MaNGA Survey: Mapping nearby Galaxies at Apache Point Observatory". In: 798, 7, p. 7. DOI: 10.1088/0004-637X/798/1/7. arXiv: 1412.1482.

Bustamante, S. et al. (2018). "Merger-induced metallicity dilution in cosmological galaxy formation simulations". In: 479, pp. 3381–3392. DOI: 10.1093/mnras/sty1692. arXiv: 1712.03250.

Canzian, B., R. J. Allen, and R. P. J. Tilanus (1993). "Spiral structure of the giant galaxy UGC 2885 - H-alpha kinematics". In: 406, pp. 457–469. DOI: 10.1086/172457.

Carigi, L. (1994). "Chemical evolution of the solar neighborhood with yields dependent on metallicity". In: 424, pp. 181–188. DOI: 10.1086/173881.

Carroll, B. W. and D. A. Ostlie (2006). *An introduction to modern astrophysics and cosmology*.

Cassan, A. et al. (2012). "One or more bound planets per Milky Way star from microlensing observations". In: 481, pp. 167–169. DOI: 10.1038/nature10684. arXiv: 1202.0903 [astro-ph.EP].

Chabrier, G. (2003a). "Galactic Stellar and Substellar Initial Mass Function". In: 115, pp. 763–795. DOI: 10.1086/376392. eprint: astro-ph/0304382.

— (2003b). "The Galactic Disk Mass Function: Reconciliation of the Hubble Space Telescope and Nearby Determinations". In: 586, pp. L133–L136. DOI: 10.1086/374879. eprint: astro-ph/0302511.

Charlot, S. and S. M. Fall (2000). "A Simple Model for the Absorption of Starlight by Dust in Galaxies". In: 539, pp. 718–731. DOI: 10.1086/309250. eprint: astro-ph/0003128.

Chiappini, C., F. Matteucci, and R. Gratton (1997). "The Chemical Evolution of the Galaxy: The Two-Infall Model". In: 477, pp. 765–780. DOI: 10.1086/303726. eprint: astro-ph/9609199.

Chiappini, C., F. Matteucci, and D. Romano (2001). "Abundance Gradients and the Formation of the Milky Way". In: 554, pp. 1044–1058. DOI: 10.1086/321427. eprint: astro-ph/0102134.

Chiosi, C. (1980). "Chemical evolution of the galactic disk - The inflow problem". In: 83, pp. 206–216.

Ciotti, L. and G. Bertin (1999). "Analytical properties of the $R^{1/m}$ law". In: 352, pp. 447–451. eprint: astro-ph/9911078.

Cohen, J. G., J. P. Blakeslee, and A. Ryzhov (1998). "The Ages and Abundances of a Large Sample of M87 Globular Clusters". In: 496, pp. 808–826. DOI: 10.1086/305429. eprint: astro-ph/9709192.

Combes, F. (2014). "Gas Accretion in Disk Galaxies". In: *Structure and Dynamics of Disk Galaxies*. Ed. by M. S. Seigar and P. Treuthardt. Vol. 480. Astronomical Society of the Pacific Conference Series, p. 211. arXiv: 1309.1603 [astro-ph.CO].

Conselice, C. J. et al. (2016). "The Evolution of Galaxy Number Density at z 8 and Its Implications". In: 830, 83, p. 83. DOI: 10.3847/0004-637X/830/2/83. arXiv: 1607.03909.

Cook, B. A. et al. (2016). "The Information Content of Stellar Halos: Stellar Population Gradients and Accretion Histories in Early-type Illustris Galaxies". In: 833, 158, p. 158. DOI: 10.3847/1538-4357/833/2/158. arXiv: 1610.00014.

Cooper, A. P. et al. (2013a). "Galactic accretion and the outer structure of galaxies in the CDM model". In: 434, pp. 3348–3367. DOI: 10.1093/mnras/stt1245. arXiv: 1303.6283.

— (2013b). "Galactic accretion and the outer structure of galaxies in the CDM model". In: 434, pp. 3348–3367. DOI: 10.1093/mnras/stt1245. arXiv: 1303.6283.

da Cunha, E., S. Charlot, and D. Elbaz (2008). "A simple model to interpret the ultraviolet, optical and infrared emission from galaxies". In: 388, pp. 1595–1617. DOI: 10.1111/j.1365-2966.2008.13535.x. arXiv: 0806.1020.

Daflon, S. and K. Cunha (2004). "Galactic Metallicity Gradients Derived from a Sample of OB Stars". In: 617, pp. 1115–1126. DOI: 10.1086/425607. eprint: astro-ph/0409084.

Davies, R. L. and G. Illingworth (1983). "Dynamics of yet more ellipticals and bulges". In: 266, pp. 516–530. DOI: 10.1086/160799.

de Vaucouleurs, G. (1948). "Recherches sur les Nebuleuses Extragalactiques". In: *Annales d'Astrophysique* 11, p. 247.

Di Matteo, P. et al. (2009). "On the survival of metallicity gradients to major dry-mergers". In: 499, pp. 427–437. DOI: 10.1051/0004-6361/200911715. arXiv: 0903.2846.

El-Badry, K. et al. (2016a). "Breathing FIRE: How Stellar Feedback Drives Radial Migration, Rapid Size Fluctuations, and Population Gradients in Low-mass Galaxies". In: 820, 131, p. 131. DOI: 10.3847/0004-637X/820/2/131. arXiv: 1512.01235.

— (2016b). "Breathing FIRE: How Stellar Feedback Drives Radial Migration, Rapid Size Fluctuations, and Population Gradients in Low-mass Galaxies". In: 820, 131, p. 131. DOI: 10.3847/0004-637X/820/2/131. arXiv: 1512.01235.

Erb, D. K. (2008). "A Model for Star Formation, Gas Flows, and Chemical Evolution in Galaxies at High Redshifts". In: 674, pp. 151–156. DOI: 10.1086/524727. arXiv: 0710.4146.

Falcón-Barroso, J. et al. (2011). "An updated MILES stellar library and stellar population models". In: 532, A95, A95. DOI: 10.1051/0004-6361/201116842. arXiv: 1107.2303.

Falcón-Barroso, J. et al. (2017). "Stellar kinematics across the Hubble sequence in the CALIFA survey: general properties and aperture corrections". In: 597, A48, A48. DOI: 10.1051/0004-6361/201628625. arXiv: 1609.06446.

Fathi, K. et al. (2005). "A bar signature and central disc in the gaseous and stellar velocity fields of NGC 5448". In: 364, pp. 773–782. DOI: 10.1111/j.1365-2966.2005.09648.x. eprint: astro-ph/0509642.

Francis, K. J. et al. (2012). "The chemical composition of ultracompact dwarf galaxies in the Virgo and Fornax clusters". In: 425, pp. 325–337. DOI: 10.1111/j.1365-2966.2012.21465.x. arXiv: 1207.3382.

Fridman, A. M. and O. V. Khoruzhii (2003). "Progress in the Study of Galaxies: Structures, Collective Phenomena and Methods". In: 105, pp. 1–284. DOI: 10.1023/A:1023944520465.

Gallazzi, A. et al. (2005). "The ages and metallicities of galaxies in the local universe". In: 362, pp. 41–58. DOI: 10.1111/j.1365-2966.2005.09321.x. eprint: astro-ph/0506539.

Geach, J. E. et al. (2018). "Violent Quenching: Molecular Gas Blown to 1000 km s^{-1} during a Major Merger". In: 864, L1, p. L1. DOI: 10.3847/2041-8213/aad8b6. arXiv: 1807.09789.

Ghez, A. M. et al. (1998). "High Proper-Motion Stars in the Vicinity of Sagittarius A*: Evidence for a Supermassive Black Hole at the Center of Our Galaxy". In: 509, pp. 678–686. DOI: 10.1086/306528. eprint: astro-ph/9807210.

Gibson, B. K. et al. (2013a). "Constraining sub-grid physics with high-redshift spatially-resolved metallicity distributions". In: 554, A47, A47. DOI: 10.1051/0004-6361/201321239. arXiv: 1304.3020.

— (2013b). "Constraining sub-grid physics with high-redshift spatially-resolved metallicity distributions". In: 554, A47, A47. DOI: 10.1051/0004-6361/201321239. arXiv: 1304.3020.

Goddard, D. et al. (2017a). "SDSS-IV MaNGA: Spatially resolved star formation histories in galaxies as a function of galaxy mass and type". In: 466, pp. 4731–4758. DOI: 10.1093/mnras/stw3371. arXiv: 1612.01546.

Goddard, D. et al. (2017b). "SDSS-IV MaNGA: stellar population gradients as a function of galaxy environment". In: 465, pp. 688–700. DOI: 10.1093/mnras/stw2719. arXiv: 1612.01545.

González Delgado, R. M. et al. (2014). "Insights on the Stellar Mass-Metallicity Relation from the CALIFA Survey". In: 791, L16, p. L16. DOI: 10.1088/2041-8205/791/1/L16. arXiv: 1407.1315.

González Delgado, R. M. et al. (2015). "The CALIFA survey across the Hubble sequence. Spatially resolved stellar population properties in galaxies". In: 581, A103, A103. DOI: 10.1051/0004-6361/201525938. arXiv: 1506.04157.

Graham, A. W., H. Jerjen, and R. Guzmán (2003). "Hubble Space Telescope Detection of Spiral Structure in Two Coma Cluster Dwarf Galaxies". In: 126, pp. 1787–1793. DOI: 10.1086/378166. eprint: astro-ph/0308241.

Graham, A. W. et al. (2006). "Empirical Models for Dark Matter Halos. III. The Kormendy Relation and the $\log\rho_e$-$\log R_e$ Relation". In: 132, pp. 2711–2716. DOI: 10.1086/508992. eprint: astro-ph/0608614.

Greggio, L. and M. Tosi (1986). "Effects of overshooting on the chemical enrichment of the interstellar medium". In: 156, pp. L1–L4.

Harris, W. E. (1996). "A Catalog of Parameters for Globular Clusters in the Milky Way". In: 112, p. 1487. DOI: 10.1086/118116.

Hartwick, F. D. A. (2015). "A Multiple Burst Accretion Model to Describe the Metallicity Distributions and Stellar Mass-Metallicity Relation for Local Dwarf Galaxies". In: 150, 184, p. 184. DOI: 10.1088/0004-6256/150/6/184. arXiv: 1507.01551.

Herbst, E. (1995). "Chemistry in the Interstellar Medium". In: *Annual Review of Physical Chemistry* 46, pp. 27–54. DOI: 10.1146/annurev.pc.46.100195.000331.

Hirschmann, M. et al. (2014). "The influence of the environmental history on quenching star formation in a Λ cold dark matter universe". In: *MNRAS* 444, pp. 2938–2959. DOI: 10.1093/mnras/stu1609. arXiv: 1407.5621.

Ho, I.-T. et al. (2018). "Azimuthal variations of gas-phase oxygen abundance in NGC 2997". In: 618, A64, A64. DOI: 10.1051/0004-6361/201833262. arXiv: 1807.02043.

Ho, N. et al. (2015). "Metallicity Evolution of the Six Most Luminous M31 Dwarf Satellites". In: 798, 77, p. 77. DOI: 10.1088/0004-637X/798/2/77. arXiv: 1405.4424.

Holwerda, B. W. et al. (2014). "Morphological Parameters of a Spitzer Survey of Stellar Structure in Galaxies". In: 781, 12, p. 12. DOI: 10.1088/0004-637X/781/1/12. arXiv: 1309.1444.

Hopkins, P. F. et al. (2009). "Compact high-redshift galaxies are the cores of the most massive present-day spheroids". In: 398, pp. 898–910. DOI: 10.1111/j.1365-2966.2009.15062.x. arXiv: 0903.2479.

Hubble, E. (1926). "No. 324. Extra-galactic nebulae." In: *Contributions from the Mount Wilson Observatory / Carnegie Institution of Washington* 324, pp. 1–49.

Hubble, E. P. (1929). "A spiral nebula as a stellar system, Messier 31." In: 69. DOI: 10.1086/143167.

Husemann, B. et al. (2013a). "CALIFA, the Calar Alto Legacy Integral Field Area survey. II. First public data release". In: 549, A87, A87. DOI: 10.1051/0004-6361/201220582. arXiv: 1210.8150 [astro-ph.CO].

— (2013b). "CALIFA, the Calar Alto Legacy Integral Field Area survey. II. First public data release". In: 549, A87, A87. DOI: 10.1051/0004-6361/201220582. arXiv: 1210.8150 [astro-ph.CO].

Johnson, H. L. and W. W. Morgan (1953). "Fundamental stellar photometry for standards of spectral type on the revised system of the Yerkes spectral atlas". In: 117, p. 313. DOI: 10.1086/145697.

Kacharov, N. et al. (2017). "Prolate rotation and metallicity gradient in the transforming dwarf galaxy Phoenix". In: 466, pp. 2006–2023. DOI: 10.1093/mnras/stw3188. arXiv: 1612.01560.

Kauffmann, G. et al. (2003). "Stellar masses and star formation histories for 10^5 galaxies from the Sloan Digital Sky Survey". In: 341, pp. 33–53. DOI: 10.1046/j.1365-8711.2003.06291.x. eprint: astro-ph/0204055.

Kennicutt Jr., R. C. (1983). "The rate of star formation in normal disk galaxies". In: 272, pp. 54–67. DOI: 10.1086/161261.

— (1998). "The Global Schmidt Law in Star-forming Galaxies". In: 498, pp. 541–552. DOI: 10.1086/305588. eprint: astro-ph/9712213.

Kereš, D. et al. (2005). "How do galaxies get their gas?" In: 363, pp. 2–28. DOI: 10.1111/j.1365-2966.2005.09451.x. eprint: astro-ph/0407095.

Kirby, E. N. et al. (2013). "The Universal Stellar Mass-Stellar Metallicity Relation for Dwarf Galaxies". In: 779, 102, p. 102. DOI: 10.1088/0004-637X/779/2/102. arXiv: 1310.0814 [astro-ph.GA].

Kobayashi, C. (2004). "GRAPE-SPH chemodynamical simulation of elliptical galaxies - I. Evolution of metallicity gradients". In: 347, pp. 740–758. DOI: 10.1111/j.1365-2966.2004.07258.x. eprint: astro-ph/0310160.

Koudmani, S. et al. (2019). "Fast and energetic AGN-driven outflows in simulated dwarf galaxies". In: 484, pp. 2047–2066. DOI: 10.1093/mnras/stz097. arXiv: 1812.04629.

Krajnović, D. et al. (2005). "Dynamical modelling of stars and gas in NGC 2974: determination of mass-to-light ratio, inclination and orbital structure using the Schwarzschild method". In: 357, pp. 1113–1133. DOI: 10.1111/j.1365-2966.2005.08715.x. eprint: astro-ph/0412186.

Kroupa, P. (2001). "On the variation of the initial mass function". In: 322, pp. 231–246. DOI: 10.1046/j.1365-8711.2001.04022.x. eprint: astro-ph/0009005.

Lacey, C. G. and S. M. Fall (1985). "Chemical evolution of the galactic disk with radial gas flows". In: 290, pp. 154–170. DOI: 10.1086/162970.

Leaman, R. (2012). "Insights into Pre-enrichment of Star Clusters and Self-enrichment of Dwarf Galaxies from Their Intrinsic Metallicity Dispersions". In: 144, 183, p. 183. DOI: 10.1088/0004-6256/144/6/183. arXiv: 1209.4648 [astro-ph.GA].

Leaman, R. et al. (2013). "The Comparative Chemical Evolution of an Isolated Dwarf Galaxy: A VLT and Keck Spectroscopic Survey of WLM". In: 767, 131, p. 131. DOI: 10.1088/0004-637X/767/2/131. arXiv: 1302.1879.

Leaman, R. et al. (2017). "A unified model for age-velocity dispersion relations in Local Group galaxies: disentangling ISM turbulence and latent dynamical heating". In: 472, pp. 1879–1896. DOI: 10.1093/mnras/stx2014. arXiv: 1710.01317.

Lequeux, J. et al. (1979). "Chemical composition and evolution of irregular and blue compact galaxies". In: 80, pp. 155–166.

Liddle, A. (2003). *An Introduction to Modern Cosmology, Second Edition*, p. 188.

Loebman, S. R. et al. (2016). "Imprints of Radial Migration on the Milky Ways Metallicity Distribution Functions". In: 818, L6, p. L6. DOI: 10.3847/2041-8205/818/1/L6. arXiv: 1511.06369.

López-Corredoira, M. et al. (2018). "Disk stars in the Milky Way detected beyond 25 kpc from its center". In: 612, L8, p. L8. DOI: 10.1051/0004-6361/201832880. arXiv: 1804.03064.

Malinie, G. et al. (1993). "Inhomogeneous chemical evolution of the Galactic disk". In: 413, pp. 633–640. DOI: 10.1086/173032.

Marinacci, F. et al. (2018). "First results from the IllustrisTNG simulations: radio haloes and magnetic fields". In: 480, pp. 5113–5139. DOI: 10.1093/mnras/sty2206. arXiv: 1707.03396.

Markwardt, C. B. (2009). "Non-linear Least-squares Fitting in IDL with MPFIT". In: *Astronomical Data Analysis Software and Systems XVIII*. Ed. by D. A. Bohlender, D. Durand, and P. Dowler. Vol. 411. Astronomical Society of the Pacific Conference Series, p. 251. arXiv: 0902.2850 [astro-ph.IM].

Martin, G. et al. (2018). "The role of mergers in driving morphological transformation over cosmic time". In: 480, pp. 2266–2283. DOI: 10.1093/mnras/sty1936. arXiv: 1807.08761.

Martín-Navarro, I. et al. (2018). "Timing the formation and assembly of early-type galaxies via spatially resolved stellar populations analysis". In: 475, pp. 3700–3729. DOI: 10.1093/mnras/stx3346. arXiv: 1801.05486.

Matteucci, F. and P. Francois (1989). "Galactic chemical evolution - Abundance gradients of individual elements". In: 239, pp. 885–904. DOI: 10.1093/mnras/239.3.885.

Minchev, I. and B. Famaey (2010). "A New Mechanism for Radial Migration in Galactic Disks: Spiral-Bar Resonance Overlap". In: *ApJ* 722, pp. 112–121. DOI: 10.1088/0004-637X/722/1/112. arXiv: 0911.1794.

Minchev, I. and A. C. Quillen (2006). "Radial heating of a galactic disc by multiple spiral density waves". In: 368, pp. 623–636. DOI: 10.1111/j.1365-2966.2006.10129.x. eprint: astro-ph/0511037.

Minchev, I. et al. (2011). "Radial migration in galactic disks caused by resonance overlap of multiple patterns: Self-consistent simulations". In: 527, A147, A147. DOI: 10.1051/0004-6361/201015139. arXiv: 1006.0484.

Minchev, I. et al. (2012). "Evolution of galactic discs: multiple patterns, radial migration, and disc outskirts". In: 548, A126, A126. DOI: 10.1051/0004-6361/201219198. arXiv: 1203.2621.

Mo, H., F. C. van den Bosch, and S. White (2010). *Galaxy Formation and Evolution*.

Mollá, M., F. Ferrini, and A. I. Díaz (1997). "Evolution of Spiral Galaxies. VII. Time Evolution of the Radial Distributions of Abundances". In: 475, pp. 519–533. DOI: 10.1086/303550.

Mott, A., E. Spitoni, and F. Matteucci (2013). "Abundance gradients in spiral discs: is the gradient inversion at high redshift real?" In: 435, pp. 2918–2930. DOI: 10.1093/mnras/stt1495. arXiv: 1308.1549 [astro-ph.GA].

Naiman, J. P. et al. (2018). "First results from the IllustrisTNG simulations: a tale of two elements - chemical evolution of magnesium and europium". In: 477, pp. 1206–1224. DOI: 10.1093/mnras/sty618. arXiv: 1707.03401.

Navarro-González, J. et al. (2013). "Fully cosmological virtual massive galaxies at z = 0: kinematical, morphological and stellar population characterization". In: 436, pp. 3507–3524. DOI: 10.1093/mnras/stt1829. arXiv: 1309.7144.

Nelson, D. et al. (2018). "First results from the IllustrisTNG simulations: the galaxy colour bimodality". In: 475, pp. 624–647. DOI: 10.1093/mnras/stx3040. arXiv: 1707.03395.

Oey, M. S. (2000). "A New Look at Simple Inhomogeneous Chemical Evolution". In: 542, pp. L25–L28. DOI: 10.1086/312921. eprint: arXiv:astro-ph/0008302.

Oke, J. B. and J. E. Gunn (1983). "Secondary standard stars for absolute spectrophotometry". In: 266, pp. 713–717. DOI: 10.1086/160817.

Oogi, T. and A. Habe (2013a). "Dry minor mergers and size evolution of high-z compact massive early-type galaxies". In: 428, pp. 641–657. DOI: 10.1093/mnras/sts047.

— (2013b). "Dry minor mergers and size evolution of high-z compact massive early-type galaxies". In: 428, pp. 641–657. DOI: 10.1093/mnras/sts047.

Pagel, B. E. J. (1997). *Nucleosynthesis and Chemical Evolution of Galaxies*, p. 392.

Pakmor, R., A. Bauer, and V. Springel (2011). "Magnetohydrodynamics on an unstructured moving grid". In: 418, pp. 1392–1401. DOI: 10.1111/j.1365-2966.2011.19591.x. arXiv: 1108.1792 [astro-ph.IM].

Pilkington, K. et al. (2012a). "Metallicity gradients in disks. Do galaxies form inside-out?" In: 540, A56, A56. DOI: 10.1051/0004-6361/201117466. arXiv: 1201.6359.

Pilkington, K. et al. (2012b). "The distribution of metals in cosmological hydrodynamical simulations of dwarf disc galaxies". In: 425, pp. 969–978. DOI: 10.1111/j.1365-2966.2012.21353.x. arXiv: 1205.4796.

Pillepich, A. et al. (2014a). "Halo mass and assembly history exposed in the faint outskirts: the stellar and dark matter haloes of Illustris galaxies". In: 444, pp. 237–249. DOI: 10.1093/mnras/stu1408. arXiv: 1406.1174.

— (2014b). "Halo mass and assembly history exposed in the faint outskirts: the stellar and dark matter haloes of Illustris galaxies". In: 444, pp. 237–249. DOI: 10.1093/mnras/stu1408. arXiv: 1406.1174.

Pillepich, A. et al. (2018). "First results from the IllustrisTNG simulations: the stellar mass content of groups and clusters of galaxies". In: 475, pp. 648–675. DOI: 10.1093/mnras/stx3112. arXiv: 1707.03406.

Pipino, A., A. D'Ercole, and F. Matteucci (2008). "Formation of [α/Fe] radial gradients in the stars of elliptical galaxies". In: 484, pp. 679–691. DOI: 10.1051/0004-6361:20078121. arXiv: 0706.2932.

Planck Collaboration et al. (2014). "Planck 2013 results. XVI. Cosmological parameters". In: 571, A16, A16. DOI: 10.1051/0004-6361/201321591. arXiv: 1303.5076.

Planck Collaboration et al. (2016a). "Planck 2015 results. XIII. Cosmological parameters". In: 594, A13, A13. DOI: 10.1051/0004-6361/201525830. arXiv: 1502.01589.

Planck Collaboration et al. (2016b). "Planck intermediate results. XXIX. All-sky dust modelling with Planck, IRAS, and WISE observations". In: 586, A132, A132. DOI: 10.1051/0004-6361/201424945. arXiv: 1409.2495.

Portinari, L. and C. Chiosi (1999). "On star formation and chemical evolution in the Galactic disc". In: 350, pp. 827–839. eprint: astro-ph/9908326.

Prieto, J. L. et al. (2016). "MUSE Reveals a Recent Merger in the Post-starburst Host Galaxy of the TDE ASASSN-14li". In: 830, L32, p. L32. DOI: 10.3847/2041-8205/830/2/L32. arXiv: 1609.00013.

Quinn, P. J., L. Hernquist, and D. P. Fullagar (1993). "Heating of galactic disks by mergers". In: 403, pp. 74–93. DOI: 10.1086/172184.

Rodriguez-Gomez, V. et al. (2016). "The stellar mass assembly of galaxies in the Illustris simulation: growth by mergers and the spatial distribution of accreted stars". In: 458, pp. 2371–2390. DOI: 10.1093/mnras/stw456. arXiv: 1511.08804.

Rodriguez-Gomez, V. et al. (2017). "The role of mergers and halo spin in shaping galaxy morphology". In: 467, pp. 3083–3098. DOI: 10.1093/mnras/stx305. arXiv: 1609.09498.

Roediger, J. C. et al. (2012). "Stellar Populations and Radial Migrations in Virgo Disk Galaxies". In: 758, 41, p. 41. DOI: 10.1088/0004-637X/758/1/41. arXiv: 1201.6361.

Rogstad, D. H., I. A. Lockhart, and M. C. H. Wright (1974). "Aperture-synthesis observations of H I in the galaxy M83." In: 193, pp. 309–319. DOI: 10.1086/153164.

Rogstad, D. H., M. C. H. Wright, and I. A. Lockhart (1976). "Aperture synthesis of neutral hydrogen in the galaxy M33". In: 204, pp. 703–711. DOI: 10.1086/154219.

Rosales-Ortega, F. F. et al. (2012). "A New Scaling Relation for H II Regions in Spiral Galaxies: Unveiling the True Nature of the Mass-Metallicity Relation". In: 756, L31, p. L31. DOI: 10.1088/2041-8205/756/2/L31. arXiv: 1207.6216.

Roškar, R. et al. (2008). "Beyond Inside-Out Growth: Formation and Evolution of Disk Outskirts". In: 675, L65, p. L65. DOI: 10.1086/586734. arXiv: 0710.5523.

Ruiz-Lara, T. et al. (2017). "Observational hints for radial migration in disc galaxies from CALIFA". In: *ArXiv e-prints*. arXiv: 1705.02120.

Rupke, D. S. N., L. J. Kewley, and J. E. Barnes (2010). "Galaxy Mergers and the Mass-Metallicity Relation: Evidence for Nuclear Metal Dilution and Flattened Gradients from Numerical Simulations". In: *ApJL* 710, pp. L156–L160. DOI: 10.1088/2041-8205/710/2/L156. arXiv: 1001.1728.

Sakhibov, F. K. and M. A. Smirnov (1989). "Noncircular Gas Motion in the Spiral Galaxies NGC3031 NGC2903 and NGC925". In: 33, p. 476.

Salpeter, E. E. (1955). "The Luminosity Function and Stellar Evolution." In: 121, p. 161. DOI: 10.1086/145971.

Samland, M., G. Hensler, and C. Theis (1997). "Modeling the Evolution of Disk Galaxies. I. The Chemodynamical Method and the Galaxy Model". In: 476, pp. 544–559. DOI: 10.1086/303627.

Sánchez, S. F. et al. (2012a). "CALIFA, the Calar Alto Legacy Integral Field Area survey. I. Survey presentation". In: 538, A8, A8. DOI: 10.1051/0004-6361/201117353. arXiv: 1111.0962.

— (2012b). "CALIFA, the Calar Alto Legacy Integral Field Area survey. I. Survey presentation". In: 538, A8, A8. DOI: 10.1051/0004-6361/201117353. arXiv: 1111.0962.

Sánchez, S. F. et al. (2016). "CALIFA, the Calar Alto Legacy Integral Field Area survey. IV. Third public data release". In: 594, A36, A36. DOI: 10.1051/0004-6361/201628661. arXiv: 1604.02289.

Sánchez, S. F. et al. (2017). "The mass-metallicity relation revisited with CALIFA". In: 469, pp. 2121–2140. DOI: 10.1093/mnras/stx808. arXiv: 1703.09769.

Sánchez-Blázquez, P. et al. (2006). "Stellar populations of early-type galaxies in different environments. II. Ages and metallicities". In: 457, pp. 809–821. DOI: 10.1051/0004-6361:20064845. eprint: astro-ph/0604568.

Sánchez-Blázquez, P. et al. (2014). "Stellar population gradients in galaxy discs from the CALIFA survey. The influence of bars". In: 570, A6, A6. DOI: 10.1051/0004-6361/201423635. arXiv: 1407.0002.

Sandage, A. (1986). "Star formation rates, galaxy morphology, and the Hubble sequence". In: 161, pp. 89–101.

— (1989). "Edwin Hubble 1889-1953". In: 83, p. 351.

Schmidt, M. (1959). "The Rate of Star Formation." In: 129, p. 243. DOI: 10.1086/146614.

Schneider, P. (2015). *Extragalactic Astronomy and Cosmology: An Introduction*. DOI: 10.1007/978-3-642-54083-7.

Schödel, R. et al. (2002). "A star in a 15.2-year orbit around the supermassive black hole at the centre of the Milky Way". In: 419, pp. 694–696. DOI: 10.1038/nature01121. eprint: astro-ph/0210426.

Schoenmakers, R. H. M., M. Franx, and P. T. de Zeeuw (1997). "Measuring non-axisymmetry in spiral galaxies". In: 292, p. 349. DOI: 10.1093/mnras/292.2.349. eprint: astro-ph/9707332.

Schönrich, R. and P. J. McMillan (2017). "Understanding inverse metallicity gradients in galactic discs as a consequence of inside-out formation". In: 467, pp. 1154–1174. DOI: 10.1093/mnras/stx093. arXiv: 1605.02338.

Schroyen, J. et al. (2013a). "Stellar orbits and the survival of metallicity gradients in simulated dwarf galaxies". In: 434, pp. 888–905. DOI: 10.1093/mnras/stt1084. arXiv: 1306.4910.

Schroyen, J. et al. (2013b). "Stellar orbits and the survival of metallicity gradients in simulated dwarf galaxies". In: 434, pp. 888–905. DOI: 10.1093/mnras/stt1084. arXiv: 1306.4910.

Sellwood, J. A. and J. J. Binney (2002). "Radial mixing in galactic discs". In: *MNRAS* 336, pp. 785–796. DOI: 10.1046/j.1365-8711.2002.05806.x. eprint: astro-ph/0203510.

Shapley, H. and H. D. Curtis (1921). "The Scale of the Universe". In: *Bulletin of the National Research Council, Vol. 2, Part 3, No. 11, p. 171-217* 2, pp. 171–217.

Sijacki, D. et al. (2015). "The Illustris simulation: the evolving population of black holes across cosmic time". In: 452, pp. 575–596. DOI: 10.1093/mnras/stv1340. arXiv: 1408.6842.

Spitoni, E. et al. (2019). "Galactic Archaeology with asteroseismic ages: Evidence for delayed gas infall in the formation of the Milky Way disc". In: 623, A60, A60. DOI: 10.1051/0004-6361/201834188. arXiv: 1809.00914.

Springel, V. et al. (2018). "First results from the IllustrisTNG simulations: matter and galaxy clustering". In: 475, pp. 676–698. DOI: 10.1093/mnras/stx3304. arXiv: 1707.03397.

Steinmetz, M. (2012). "The Galactic thin and thick disk". In: *Astronomische Nachrichten* 333, p. 523. DOI: 10.1002/asna.201211698. arXiv: 1205.6098 [astro-ph.GA].

Strateva, I. et al. (2001). "Color Separation of Galaxy Types in the Sloan Digital Sky Survey Imaging Data". In: 122, pp. 1861–1874. DOI: 10.1086/323301. eprint: astro-ph/0107201.

Taylor, P., C. Kobayashi, and C. Federrath (2019). "The metallicity and elemental abundance maps of kinematically atypical galaxies for constraining minor merger and accretion histories". In: 485, pp. 3215–3223. DOI: 10.1093/mnras/stz630. arXiv: 1903.01597.

Thomas, D., C. Maraston, and R. Bender (2003). "Stellar population models of Lick indices with variable element abundance ratios". In: 339, pp. 897–911. DOI: 10.1046/j.1365-8711.2003.06248.x. eprint: astro-ph/0209250.

Thomas, D., C. Maraston, and J. Johansson (2011). "Flux-calibrated stellar population models of Lick absorption-line indices with variable element abundance ratios". In: 412, pp. 2183–2198. DOI: 10.1111/j.1365-2966.2010.18049.x. arXiv: 1010.4569.

Timmes, F. X., J. T. Lauroesch, and J. W. Truran (1995). "Abundance Histories for QSO Absorption-Line Systems". In: 451, p. 468. DOI: 10.1086/176235. eprint: astro-ph/9504031.

Tinsley, B. M. (1980). "Evolution of the Stars and Gas in Galaxies". In: 5, pp. 287–388.

Tissera, P. B. et al. (2016a). "The gas metallicity gradient and the star formation activity of disc galaxies". In: 456, pp. 2982–2992. DOI: 10.1093/mnras/stv2736. arXiv: 1511.08227.

Tissera, P. B. et al. (2016b). "The stellar metallicity gradients in galaxy discs in a cosmological scenario". In: 592, A93, A93. DOI: 10.1051/0004-6361/201628188. arXiv: 1604.08116.

Tremonti, C. A. et al. (2004). "The Origin of the Mass-Metallicity Relation: Insights from 53,000 Star-forming Galaxies in the Sloan Digital Sky Survey". In: 613, pp. 898–913. DOI: 10.1086/423264. eprint: astro-ph/0405537.

Turner, D. G. (2014). "An eclectic view of our Milky Way galaxy1". In: *Canadian Journal of Physics* 92, pp. 959–963. DOI: 10.1139/cjp-2013-0429. arXiv: 1310.0014.

van den Bergh, S. (2003). "History of the Local Group". In: *arXiv Astrophysics e-prints*. eprint: astro-ph/0305042.

van den Bosch, R. C. E. et al. (2008). "Triaxial orbit based galaxy models with an application to the (apparent) decoupled core galaxy NGC 4365". In: 385, pp. 647–666. DOI: 10.1111/j.1365-2966.2008.12874.x. arXiv: 0712.0113.

Vazdekis, A. et al. (1997). "A New Chemo-evolutionary Population Synthesis Model for Early-Type Galaxies. II. Observations and Results". In: 111, pp. 203–232. DOI: 10.1086/313008. eprint: astro-ph/9701036.

Villalobos, Á. and A. Helmi (2008). "Simulations of minor mergers - I. General properties of thick discs". In: 391, pp. 1806–1827. DOI: 10.1111/j.1365-2966.2008.13979.x.

Vogelsberger, M. et al. (2014a). "Introducing the Illustris Project: simulating the coevolution of dark and visible matter in the Universe". In: 444, pp. 1518–1547. DOI: 10.1093/mnras/stu1536. arXiv: 1405.2921.

Vogelsberger, M. et al. (2014b). "Properties of galaxies reproduced by a hydrodynamic simulation". In: 509, pp. 177–182. DOI: 10.1038/nature13316. arXiv: 1405.1418.

Walcher, C. J. et al. (2014). "CALIFA: a diameter-selected sample for an integral field spectroscopy galaxy survey". In: 569, A1, A1. DOI: 10.1051/0004-6361/201424198. arXiv: 1407.2939.

Weinberger, R. et al. (2018). "Supermassive black holes and their feedback effects in the IllustrisTNG simulation". In: 479, pp. 4056–4072. DOI: 10.1093/mnras/sty1733. arXiv: 1710.04659.

White, S. D. M. and M. J. Rees (1978). "Core condensation in heavy halos - A two-stage theory for galaxy formation and clustering". In: 183, pp. 341–358. DOI: 10.1093/mnras/183.3.341.

Williams, B. F. et al. (2009). "The Detection of Inside-Out Disk Growth in M33". In: 695, pp. L15–L19. DOI: 10.1088/0004-637X/695/1/L15. arXiv: 0902.3460 [astro-ph.CO].

Worthey, G. (1994). "Comprehensive stellar population models and the disentanglement of age and metallicity effects". In: 95, pp. 107–149. DOI: 10.1086/192096.

Zahid, H. J. et al. (2014). "The FMOS-COSMOS Survey of Star-forming Galaxies at z ˜ 1.6. II. The Mass-Metallicity Relation and the Dependence on Star Formation Rate and Dust Extinction". In: 792, 75, p. 75. DOI: 10.1088/0004-637X/792/1/75. arXiv: 1310.4950.

Zaritsky, D., R. C. Kennicutt Jr., and J. P. Huchra (1994). "H II regions and the abundance properties of spiral galaxies". In: 420, pp. 87–109. DOI: 10.1086/173544.

Zheng, Z. et al. (2017a). "SDSS-IV MaNGA: environmental dependence of stellar age and metallicity gradients in nearby galaxies". In: 465, pp. 4572–4588. DOI: 10.1093/mnras/stw3030. arXiv: 1612.01523.

— (2017b). "SDSS-IV MaNGA: environmental dependence of stellar age and metallicity gradients in nearby galaxies". In: 465, pp. 4572–4588. DOI: 10.1093/mnras/stw3030. arXiv: 1612.01523.

Zhu, L. et al. (2017). "The stellar orbit distribution in present-day galaxies inferred from the CALIFA survey". In: *ArXiv e-prints*. arXiv: 1711.06728.

Zhu, L. et al. (2018a). "Morphology and kinematics of orbital components in CALIFA galaxies across the Hubble sequence". In: 479, pp. 945–960. DOI: 10.1093/mnras/sty1521. arXiv: 1806.02886.

Zhu, L. et al. (2018b). "Orbital decomposition of CALIFA spiral galaxies". In: 473, pp. 3000–3018. DOI: 10.1093/mnras/stx2409. arXiv: 1709.06649.

— (2018c). "Orbital decomposition of CALIFA spiral galaxies". In: 473, pp. 3000–3018. DOI: 10.1093/mnras/stx2409. arXiv: 1709.06649.

Zhu, L. et al. (2018d). "The stellar orbit distribution in present-day galaxies inferred from the CALIFA survey". In: *Nature Astronomy* 2, pp. 233–238. DOI: 10.1038/s41550-017-0348-1. arXiv: 1711.06728.

Zhu, L. et al. (2018e). "The stellar orbit distribution in present-day galaxies inferred from the CALIFA survey". In: *Nature Astronomy* 2, pp. 233–238. DOI: 10.1038/s41550-017-0348-1. arXiv: 1711.06728.

Zhuang, Y. et al. (2019). "A dynamical view on stellar metallicity gradient diversity across the Hubble sequence with CALIFA". In: 483, pp. 1862–1880. DOI: 10.1093/mnras/sty2916. arXiv: 1810.12223.

Zibetti, S. et al. (2017). "Resolving the age bimodality of galaxy stellar populations on kpc scales". In: 468, pp. 1902–1916. DOI: 10.1093/mnras/stx251. arXiv: 1701.06570.

Zschaechner, L. K. et al. (2018). "Spatially Resolved ^{12}CO(21)/^{12}CO(10) in the Starburst Galaxy NGC 253: Assessing Optical Depth to Constrain the Molecular Mass Outflow Rate". In: 867, 111, p. 111. DOI: 10.3847/1538-4357/aadf32. arXiv: 1809.01160.